Cardiff University

Electroabsorption modulators and laser diodes for free space optics and on-chip applications

---

Benjamin Cosimo Maglio

A thesis submitted as partial fulfilment for the degree of

Doctor of Philosophy

School of Physics & Astronomy

June 2022

Abstract

Theoretical predictions corroborated with experimental observations of III-V compound semiconductor normal-incidence electroabsorption modulators and edge-coupled modulators and lasers are described. Application of such devices to free space optical communication and photonic integrated circuits respectively are considered. These are of interest collectively for extending present capabilities in wireless and on-chip communication techniques.

Free space optical communication offers a high-speed, secure alternative to wireless radio frequency communication, without spectrum licensing nor excessive infrastructure requirements. Laser transceivers, although presently in operation in ground-satellite and satellite-satellite communication cannot be supported in miniaturized systems due to size, weight, and power constraints. Quantum well modulating retroreflectors offer an alternative, though few studies have considered optimization of the epi-structures for this particular application.

Monolithic integration of III-V alloys on silicon substrates is currently being explored as a method of increasing on-chip optoelectronic integration. Active photonic components such as lasers and modulators are required. Quantum dot lasers offer low threshold current densities, temperature insensitivity, and resilience to dislocation induced degradation from lattice mismatch between III-V alloys and silicon. Nevertheless, doping strategies (p-type modulation and n-type direct) are required to correct carrier occupation imbalances and enhance performance.

A modelling routine for calculating absorption in quantum well and dot heterostructures is corroborated with experimental measurements. Measurement validated predictions of the quantum confined Stark effect in quantum wells are used to propose novel epi-structures, for application to retroreflective free space optics. Expected improvements in the extinction ratio and insertion loss are reported.

Predictions of gain and the quantum confined Stark effect in InAs quantum dots show potential improvements through p-type modulation doping in lasers and modulators operating at 1310nm. Calculations of n-type direct doped InAs quantum dots highlight possible mechanisms of enhanced laser operation, with further enhancements using both p-type modulation and n-type direct doping, so-called “co-doped” quantum dot devices.

Acknowledgements

I would like to express gratitude to my supervisor Professor Peter M. Smowton. Firstly, for offering me the opportunity to pursue scientific research. Secondly, for consistent support over the last four years through our regular discussions. Finally, for granting me the trust and patience work remotely through so many time zones.

Thanks are owed to my supervisors at Airbus for taking me on as a PhD student for this project. Particularly to Dr. Crisanto Quintana for working with me on developing new concepts for retroreflective free space optics and triathlon motivation. I would also like to thank Yoann Thueux and Dr. Gavin Erry for interviewing me, discussing engineering problems, and for always finding me a desk when visiting AWIC.

I would like to thank Professor Jonathan F. Holzman of the Integrated Optics Laboratory at the University of British Columbia Okanagan (UBCO), for your help developing my proposal, for welcoming me into your lab, and for excellent hiking recommendations around British Columbia. While at UBCO I had the pleasure of working with a fantastic lab. Special thanks to the FSO group Alex MacGillivray, Ilija Hristovski, and Matthias Jenne, and of course the Terahertz folks, Mike Mitchell and Isaac Spotts.

Next I would like to acknowledge Dr. Malcolm Watson from AVoptics not only for continuous guidance on operating modulator devices, but assistance in collecting and delivering those devices to Canada during the pandemic. Thank you to the Research Institutes of Sweden, particularly Dr. Qin Wang, Dr. Duncan Platt, and Dr. Darius Jakonis for enthusiastic advice and instruction on using their devices. Additionally, thank you to Grahame Faulkner and Professor Dominic O’Brien at the University of Oxford for granting me access to test these devices.

I am very grateful to the many people in the School of Physics & Astronomy at Cardiff University who helped me during my PhD, my undergraduate degree, and as a technician. I would like to acknowledge everyone within the optoelectronics group for assistance, collaboration, and discussion. A special thanks to Dr. Sam Shutts for all of your help at the start my PhD, and for being a great climbing and running partner whenever we found time. I’d like to thank Lydia Jarvis for constant back and forth about doped InAs quantum dots as well as hiking and gardening discussions. Thanks to Josie Nabialek and Basmah Almagwashi for some great morning chats. I would also like to thank the technical and administrative support staff within the School of Physics & Astronomy.

The support from my friends and family has been amazing. Thanks to my mother and father, Leslie and Alessandro, and my brother and sister, Vincent and Ellena. I am so appreciative of being able to work from home in Christchurch, and I appreciate all of the teas, coffees, and beers. Thanks to my in-laws for always offering me a place to stay and making me feel so welcome in Wyoming. A special thanks to my sister in law Jaik and the Terry’s, Jacob, Milo, and Thea, for letting me stay in your basement. I would like to thank my friends, in and out of Cardiff, for providing a whole lot of fun and laughs. I would also like to acknowledge my good friend Brad Saunders for his exceptional hospitality and always letting me stay in his home whenever I was in Cardiff during the last year of my PhD.

Finally, I would like to acknowledge my wife Jazlynn and our dog Jordy Nelson, who have been the best companions I could have ever wished for. Nelson has provided us with unrestrained affection and an innate ability to sense stress or alert us to when the working day is done. Jaz has been my rock, not only helping me better myself as a scientist, but providing perfect company when hiking, camping, gardening, foraging, and through many, many hours of driving. Jaz has been a real inspiration to me since I met her in 2014, and it has been nothing short of an adventure completing our PhDs together.

This research was funded by the Engineering and Physical Sciences Research Council industrial case award 2036167 and sponsored by Airbus UK.

Publications, presentations, patents, & funding

Publications

B. Maglio, L. Jarvis, M. Tang, H. Liu and P. M. Smowton, "Modelling the effects of p-modulation doping in InAs/InGaAs quantum dot devices," *Opt Quant Electron [Under review] – B. M performed calculations and wrote the manuscript with support from P. M. S, L. J characterised samples, M. T and H. L conducted epitaxy, P. M. S supervised the findings of this work. All authors contributed to the final manuscript.*

A. C. MacGillivray, N. I. Lesack, I. R. Hristovski, M. F. Jenne, B. C. Maglio, S. Gorgani, and J. F. Holzman, "Band edge absorption Characteristics under unified Einstein/ Franz-Keldysh models," *Physical Review B,* https://doi.org/10.1103/PhysRevB.105.155203 – *A. C. M took the lead in writing the manuscript, N. I. L, I. R. H, and J. F. H. conceived of the presented idea and took preliminary measurements, M. F. J and J. F. H developed analytical calculations and theoretical formalism, B. C. M, A. C. M, M. F. J, and I. R. H contributed to planning, fabrication of devices, experimental setup and data collection. All authors contributed to the final manuscript.*

H. Deng, L. Jarvis, Z., Li, Z, Liu, M. Tang, K. Li, B. Maglio, S. Shutts, J. Yu, L. Wang, S. Chen, C. Jin, P. M. Smowton, A. Seeds, H. Liu, "The role of different types of dopants in 1.3 µm InAs/GaAs quantum-dot lasers", *J. Phys. D: Appl. Phys,* https://doi.org/10.1088/1361-6463/ac55c4 – *H. D, Z. L, M. T, K. L, J. Y, S. C, A. S and H. L were involved in epitaxial development and material characterisation of devices. J. Y, L. W, and C. J were involved in the fabrication and some preliminary characterisation of devices, L. J, Z. L, S. S were involved in further fabrication and final characterisation of devices, B. M conducted numerical calculations. P. M. S and B. C interpreted numerical results. All authors contributed to the final manuscript and theoretical understanding.*

B. Mariana, M. Benjamin, and C. C. Pablo Alejandro, "Latest advances in optical frequency combs based on quadratic non-linearity," *IET Optoelectron.*, vol. 14, no. 3, pp. 143–147, Jun. 2020, https://doi.org/10.1049/iet-opt.2019.0078 – *B. M took the lead writing the manuscript under supervision from C. C. P. A. M. B assisted with translations, proof reading and final corrections to the manuscript.*

Presentations & conference proceedings

B. Maglio, A. C. MacGillivray, C. Quintana, Y. Thueux, M. Watson, D. Jakonis, Q. Wang, D. Platt, J. F. Holzman, P. M. Smowton, "Modelling electroabsorption modulators for retroreflective free space optical communication," *2022 Semiconductor Integrated Optoelectronics (SIOE)*

B. Maglio, L. Jarvis, M. Tang, H. Liu, P. M. Smowton, "Predicting limitations to the performance of p-modulation doped InAs/InGaAs quantum dot lasers and modulators," *2022 Semiconductor Integrated Optoelectronics (SIOE)*

B. Maglio *et al*., "The limits to peak modal gain in p-modulation doped indium arsenide quantum dot laser diodes," *2021 IEEE Photonics Conference (IPC)*, 2021, pp. 1-2, https://doi.org/10.1109/IPC48725.2021.9592852

B. Maglio, L. Jarvis, M. Tang, H. Liu and P. M. Smowton, "Modelling the effects of p-modulation doping in InAs quantum dot devices," *2021 International Conference on Numerical Simulation of Optoelectronic Devices (NUSOD)*, 2021, pp. 21-22, https://doi.org/10.1109/NUSOD52207.2021.9541500

J. Mahoney, P. M. Smowton, B. Maglio, L. Jarvis, C. Allford, S. Shutts, M. Tang, H. Liu, and N. Abadía, "QCSE and Carrier Blocking in P-modulation Doped InAs/InGaAs Quantum Dots," in Conference on Lasers and Electro-Optics, OSA Technical Digest (Optical Society of America, 2021), https://doi.org/10.1364/CLEO_AT.2021.JTu3A.167

B. Maglio, N. Abadía, P. M. Smowton, C. Quintana, G. Erry, Y. Thueux, “Designing optimized retro-reflecting electroabsorption modulators for free space optical datalinks”, *SIOE – Poster Session, Cardiff University School of Physics and Astronomy, Apr. 2019.*

B. Maglio, “Communicating with Light”, 3MT Three Minute Thesis Competition, Mar. 2019

Patents

British Patent 2115386.1 – Benjamin C. Maglio, Crisanto Quintana, Peter M. Smowton – *Filed* Oct. 2021

Funding

EPSRC Industrial Case Award (2036167), Airbus UK – Apr. 2018

UKRI-Mitacs UK-Canada Globalink Doctoral Exchange Scheme (NERC-519344) – Sept. 2021

**Lead author/presenter is underlined.*

Contents

List of figures

List of tables

Chapter 1 Introduction

1.1 Motivation

Continued research and development is essential to meet an ever growing demand for data transfer coupled with continuing miniaturization of the relevant technology. The increasing number of bits we wish to send wirelessly from shrinking platforms like small unmanned aerial vehicles (UAVs) and nano-satellites requires size, weight and power efficient optical communication.

Photonics has been an active field of study since the 1960s and huge strides have been made internationally to use related technology, not only for scientific research, but in telecommunication, aerospace, medical, and energy industries. Photonics was conceived in the wake of the first semiconductor-based light sources, alongside the invention of the laser diode and optical fibers. These technologies have provided the world with unprecedented increases in data transfer and ultimately, the creation of the internet that we know today.

As the advent of the fiber optics industry provided huge advances in technological capabilities we are again on the cusp of a new step forward, this time with photonic wireless, indoor and outdoor communication, as well as photonic integrated circuits. In each, the higher frequency radiation used significantly increases bandwidth. III-V compound semiconductors offer optical band gaps spanning a wide range of the visible and infrared spectrum, and can be combined into a number of ternary and quaternary alloys for creating photonic components composed of intricate heterostructures, exhibiting tunable and quantum mechanical properties. III-V alloys currently offer one of the most convincing methods of achieving this step towards photonic communication.

Wireless communication has developed in tandem, predating the laser diode, with the conception of radar systems. These systems, like many still today, communicate data through broadcasting radio signals isotropically, with the exception of 5G and 6G using beamforming techniques to direct signals. Though increased frequencies through these newer generations have made large increases in data transfer possible, this region of the electromagnetic spectrum is becoming saturated. Spectrum licenses are needed to prevent interference as data transfer speeds plateau, with increasing fears over data jamming and security.

Free space optical (FSO) communication is a line of sight method of wireless data transfer utilizing the higher frequencies available from photonics operating in directional beams. Minimal infrastructure is required, and optical transceiver specifications can be scaled depending on the application. An example of a portable, bi-directional optical transceiver for small UAVs is shown in fig. 1.1, courtesy of AVoptics Ltd. A continuous wave laser beam will interrogate a UAV, with a high frequency detector reading returned data. This is interpreted through a portable control panel containing programmed firmware for pointing and tracking, data logging, and bit error correction.

Fig. 1.1 – Free space optical transceiver station from AVoptics Ltd.

FSO communication does not require a spectrum license, offers higher speed data transfer, and does not require significant changes to existing infrastructure in the same way as laying optical fiber lines. Equally, as a line of sight is needed between the transmitter and receiver, it is intrinsically more secure and difficult to jam. This method is already in use, particularly in satellite communication systems. Other examples, from the UK's CableFree FSO range offer data rates of up to 1.5Gbps, Canada's fSONA's SONAbeam® 10G-E+ with 10Gbps, and of course USA's Starlink offering satellite FSO internet with download speeds between 100 and 200Mbps in remote locations.

The other aspect of the limits to data capacity occur on the micro-chip level. To combat the problems arising with integrated circuits, primarily, transistor proximity and bond wire resistance, photonic integrated circuits (PICs) may offer the solution.

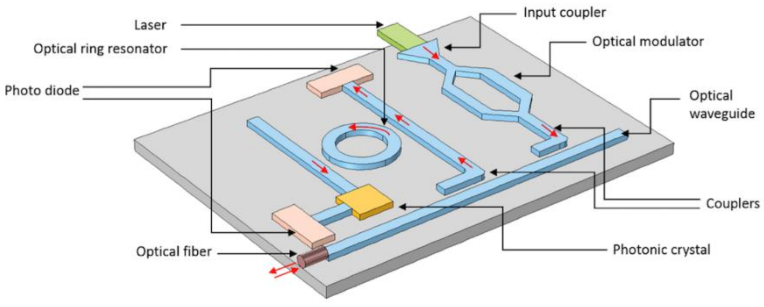

Fig. 1.2 – Diagram of a photonic integrated circuit from Saleh and Teich[1].

In this approach, light provides the carrier signal, channeled through low loss structures called waveguides. The silicon manufacturing industry provides the scale and potential for mass-producing high quality wave guided circuitry, though it’s indirect band gap prevents practical light generation. Therefore, monolithically integrating III-V alloys, with optical band gaps, on silicon substrates can provide high performance active components (lasers, modulators, detectors) with low loss passive components (waveguides, filters, attenuators). Fig. 1.2 shows a diagram of a PIC from [1].

1.1.1 Retroreflective free space optical communication

In each of the aforementioned FSO communication examples a laser and detector are used on either side of the communication channel. The problem arises when our portable devices become too small to mount and power a laser, not to mention coarse and fine tracking systems. In this instance a modulating retroreflector (MRR) may offer high speed data download for compact devices. An example is shown in fig. 1.3 with a MRR module contained within the total payload for an octocopter drone, from AVoptics Ltd.

Fig. 1.3 – Octocopter drone with MRR for free space optical communication, from AVoptics Ltd.

Optical intensity modulators are devices able to imprint data onto continuous wave beams requiring only a fraction of the power of a laser, by varying the transmissivity of the device. Many optical modulators, particularly for this application can be composed of semiconductors. In FSO, where a 1550nm operating wavelength is the industry standard, III-V alloys (such as InGaAs) offer lightweight and low footprint, high speed operation. Reductions in the power consumption can be achieved by creating quantum wells (sandwiching narrow layers of low and high band gap semiconductors together).

A retroreflector is an amalgamation of lenses and mirrors which returns incident light directly back at the direction it arrived. The combination of the two can provide a low power device with a small footprint, mounted on board compact, wireless devices, capable of returning high speed data back to a receiver, as shown in fig. 1.4. This creates an asymmetric data link. Many aspects of this technology have been considered, including pointing and tracking, optical setup, and quantum encryption[2]–[6]. Nevertheless, the epi-structure associated with the modulator remains understudied, with possible enhancements to low extinction ratios and high insertion losses allowing for vast improvements in the transmission distance and link reliability.

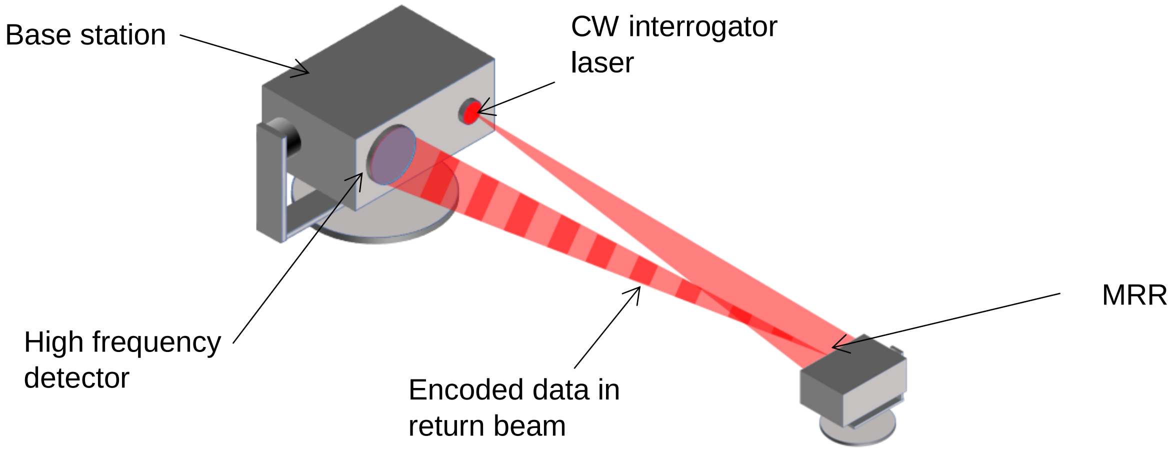

Fig. 1.4 – Diagram of a modulating retroreflector based free space optical communication asymmetric data down link.

1.1.2 Monolithically integrated quantum dots

For future on-chip platforms investment into all necessary components is required, including both passives and actives. Nevertheless, active components for emission and manipulation of light, such as lasers and modulators offer particular challenges. Additionally, by incorporating III-V alloys on silicon substrates problems are encountered regarding the mismatch in lattice constant between the crystals. This difference causes misfit dislocation defects at the interface between substrate and epi-structure, with threading dislocations propagating through the structure from these origins. The dislocations cause degradation in both device performance and lifetime. The quantum wells mentioned in section 1.1.1 are particularly sensitive to these dislocations, as entire layers may be impacted. Quantum dots, semiconductor nanoparticles, offer a resilience owing to their non-planar geometries, among other benefits such as temperature insensitive threshold current and increased modulation bandwidth[7]–[9].

Quantum dots offer another challenge due to the large differences in effective masses associated with III-V alloys, such as InAs, leading to asymmetric carrier occupation and poor transport to the allowed hole energy states. Whereas in quantum wells strained layers may be incorporated to alleviate this, strain is a requirement in the quantum dot formation process and other options are required. Doping strategies, such as p-type modulation doping or n-type direct doping, have shown promise[8], [10]–[12]. In either case, modulators have not received the same level of study, with only Mahoney et al. considering p-type modulation doped modulators in [13]. The more recent n-type direct doping technique still requires extensive study to evaluate the potential benefits to lasers and modulators.

Furthermore, it is highly likely that photonic integration and FSO will entwine. This will provide efficient, high speed, internal microprocessors and external, low power, secure wireless communication systems. Therefore, each facet offers a valuable contribution towards the future body of knowledge that will be leveraged to make this technology a reality. In this thesis, quantum well electroabsorption modulators for FSO and quantum dot laser diodes and modulators for PICs are analysed and modelled to influence epitaxial design decisions.

1.2 Thesis structure

Subsequently, in chapter 2, the background theory necessary for conducting measurements and devising models for the following chapters is highlighted. Particular attention is paid to calculation of full device band structures using Nextnano software[14], in addition to absorption calculations for both quantum wells and quantum dots[15]–[17].

In chapter 3, the current state of the art is evaluated. Present as of the date of submission, performance metrics for quantum well and alternative MRR technologies are collated. Additionally, current capabilities and important parameters for InAs quantum dots are described, including p-type modulation and n-type direct doping strategies.

Chapter 4 combines spectroscopic and temperature dependent measurements of current state of the art modulators for retroreflective FSO from [2]–[4]. This is followed by a semi-empirical modelling routine imposed for the corresponding epi-structure. The model is then utilized to evaluate potential materials, compositions, and quantum well dimensions to enhance current performance capabilities. Strain-balancing calculations are incorporated prior to a final comparison of the modelled absorption spectra for the current state of the art with proposed epi-structures.

In chapter 5, the modelling routine is extended to analyse grown quantum dot structures unintentionally doped and with p-type modulation doping. By comparison to absorption measurements taken by fellow PhD student Joe Mahoney, modelled results are used to predict modulator and laser performance. Subsequently, band structure calculations are employed to calculate variations in p-type modulation doping and with the inclusion of the n-type direct doping technique. Through the analysis of a range of band structure parameters as a function of n-type doping concentration, possible mechanisms for device improvement are discussed. Finally, the combined results are used to suggest the implications of p-type modulation and n-type direct co-doping.

Conclusions of this work as well as considerations for future investigation are discussed in the final chapter.

Chapter 2 Background Theory

In this chapter, methods and principles required for modelling absorption, electroabsorption and gain in quantum well (QW) and quantum dot (QD) heterostructures are outlined. Band structure calculations and solutions to Maxwell's equations are combined with experimentally determined sample parameters to calculate absorption, gain, and the quantum confined Stark effect (QCSE).

2.1 Full device band structure calculations

Full device band structures were calculated using a self-consistent Schrödinger-Poisson-current continuity solver with a single-band effective mass approximation (EMA) from Nextnano, under zero, reverse and forward bias. Equations were discretized prior to solving along user defined grid points and then solved using a finite difference method[18]. The band alignment in this software was calculated using average valence band energies derived from Van De Walle and Martin's model solid theory (MST) as proposed in [19]–[21]. The effects of parallel biaxial and perpendicular uniaxial, homogeneous strain were calculated using material lattice and elastic constants, as well as conduction and valence band deformation potentials similarly to in [22]. Many of the material parameters used in the software database were gathered from Vurgaftman and Meyer's work[23], though specific exceptions are shown as annotations within the full software database.

Solutions were found iteratively, switching between self-consistent Schrödinger-Poisson and current continuity equations respectively. The charge distribution used in the Poisson equation to solve for the potential was defined by donor and acceptor concentrations, in addition to conduction and valence band occupation probabilities given by, the initially fixed quasi-Fermi levels, calculated using Fermi-Dirac statistics. Bound energy states and wavefunctions were then calculated for this initial band potential using the Schrödinger equation, allowing for a new charge distribution including quantized states to be found. This loop was repeated until a self-consistent Schrödinger-Poisson solution was found. Next, the potential and quantized states were fixed while the current continuity equation was solved for new quasi-Fermi level solutions, providing a new charge distribution and re-initiating the first loop. This process was then repeated until a self-convergence criterion for both the Schrödinger-Poisson and the current continuity solver was reached. This solving procedure is displayed in fig. 2.1.

e was elementary charge, ρ was the charge density distribution, with N_d and N_a the ionized donor and acceptor concentrations respectively. ε was the material permittivity and φ was the electrostatic potential. $\hbar$ was the Dirac constant (or reduced Planck constant), m^* was the carrier effective mass, with ψ_i and E_i the eigenfunction and eigenvalue for bound states of subband index i. V was the electronic potential. ϵ_n and ϵ_p were values used for the self-convergence criterion, defined in the software equivalent to the maximum acceptable change in electron and hole densities. μ_n and μ_p were the carrier mobilities for electrons and holes respectively. R was a generation or recombination dominant term depending on whether it was positive or negative. Finally, ϵ_{Ee} and ϵ_{Eh} were the last self-consistence criterion for maximum acceptable energy change and k indicated the iteration step.

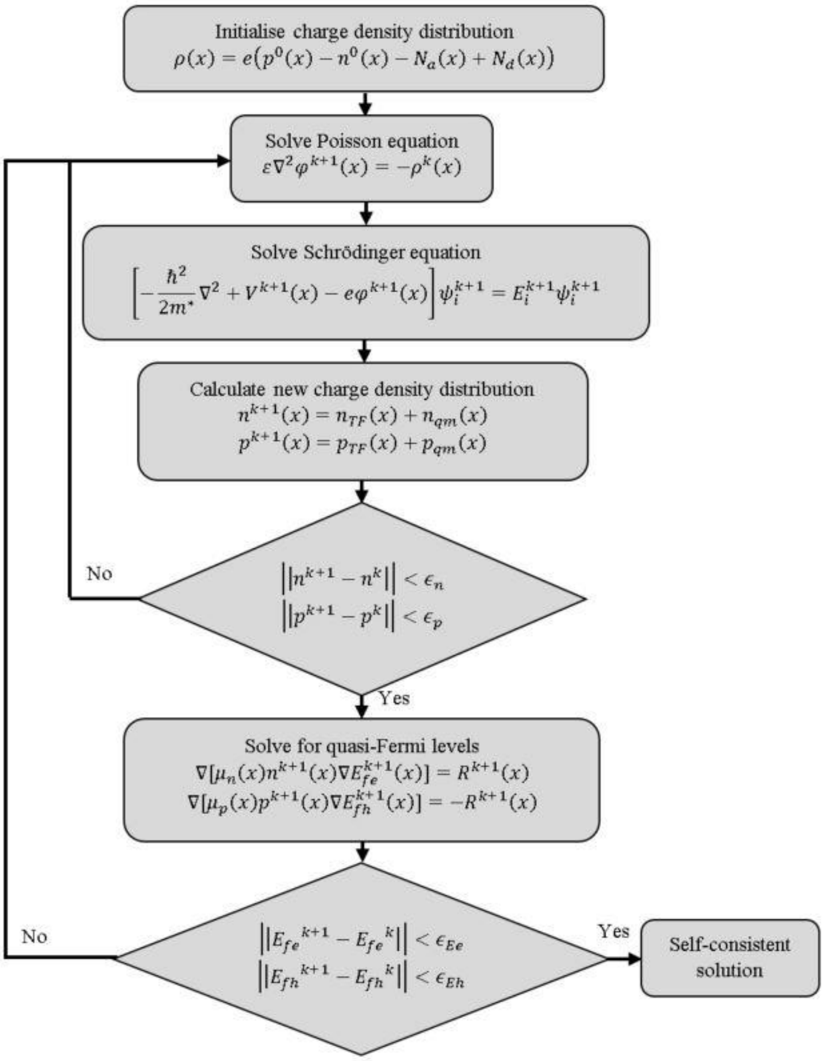

Fig. 2.1 – Flow chart diagram of iteration scheme used in Nextnano software for self-consistent calculation of solutions to the Schrödinger-Poisson-current continuity equations.

Carrier densities were calculated classically and quantum mechanically across the full device. As the EMA was invoked only parameters evaluated at $\boldsymbol{k} = 0$, the extrema of the Γ-valley were considered. The Thomas-Fermi approximation was used for classical free-carrier charge densities, shown in eq. 2.1 and 2.2. The remaining quantum mechanical charge densities were calculated for each subband in eq. 2.3 and 2.4.

$$n_{TF}(x) = \sum g_c N_c(x) \mathrm{F}_{1/2}\left(\frac{-E_c(x)-V(x)+E_{Fe}(x)}{k_b T}\right) \qquad (2.1)$$

$$p_{TF}(x) = \sum g_v N_v(x) \mathrm{F}_{1/2} \left(\frac{E_v(x) + V(x) - E_{Fh}(x)}{k_b T} \right) \tag{2.2}$$

The sum extended over the material appropriate conduction and valence band edges as a function of position, x, which was defined in the graphical user interface (GUI) via a material and mesh grid input. g_c and g_v, accounted for the spin and valley degeneracies calculated in the conduction and valence bands respectively. $N_c(x)$ and $N_v(x)$, were the effective density of states as a function of position across the full device, accounting for the density of states near the band edge, relating to an effective mass tensor in the x direction. $\mathrm{F}_{1/2}$, was the numerically solved Fermi-Dirac integral of order 1/2, which provided the population of these states. $E_c(x)$ and $E_v(x)$ were the conduction and valence band edges across the device. $E_{Fe}(x)$ and $E_{Fh}(x)$, were the electron and hole quasi-Fermi levels as a function of position. k_b was the Boltzmann constant and T the temperature, generally set to a room temperature of 294K. For the quantum mechanical carrier densities, values were summed across calculated subbands with index i. Here, $|\psi_i(x)|^2$ was the probability density from the wavefunction for a given subband.

$$n_{qm}(x) = \sum_i g_c N_c |\psi_i(x)|^2 \mathrm{F}_{1/2} \left(\frac{-E_i + E_{fe}(x)}{k_b T} \right), \tag{2.3}$$

$$p_{qm}(x) = \sum_i g_v N_v |\psi_i(x)|^2 \mathrm{F}_{\frac{1}{2}} \left(\frac{E_i - E_{fh}(x)}{k_b T} \right) \tag{2.4}$$

The bulk effective density of states, defined in eq. 2.5, corresponded to the density of states at the band minima. This was related to the density of states effective mass, m^*_{DOS} shown in eq. 2.6, the average of the effective mass tensor, with prefactor of 2 accounting for spin degeneracy.

$$N(x) = 2 \left(\frac{m^*_{DOS}(x) k_b T}{2\pi\hbar^2} \right)^{3/2} \tag{2.5}$$

$$m^*_{DOS}(x) = \left(m^*_x(x) \cdot m^*_y(x) \cdot m^*_z(x) \right)^{1/3} \tag{2.6}$$

A band structure containing two GaAs-AlGaAs QWs following the structure defined by Miller et al. in [25] (shown in fig. 2.2) is calculated as an example in fig. 2.3. As normal incident illumination is considered for QWs, slab structures are considered for all calculations rather than waveguided devices.

1000nm p-GaAs
1300µm p-Al$_{0.3}$GaAs/GaAs SL
550nm Al$_{0.3}$GaAs/GaAs SL
9.4nm GaAs QW
20nm Al$_{0.3}$GaAs/GaAs SL
9.4nm GaAs QW
550nm Al$_{0.3}$GaAs/GaAs SL
1300nm n- Al$_{0.3}$GaAs/GaAs SL
300nm n-GaAs
n-GaAs substrate

Fig. 2.2 – Example QW slab epi-structure as given in [25]. SL denotes a superlattice region, with n and p representing a 10^{18}*cm*$^{-3}$ *concentration of p-type or n-type dopant.*

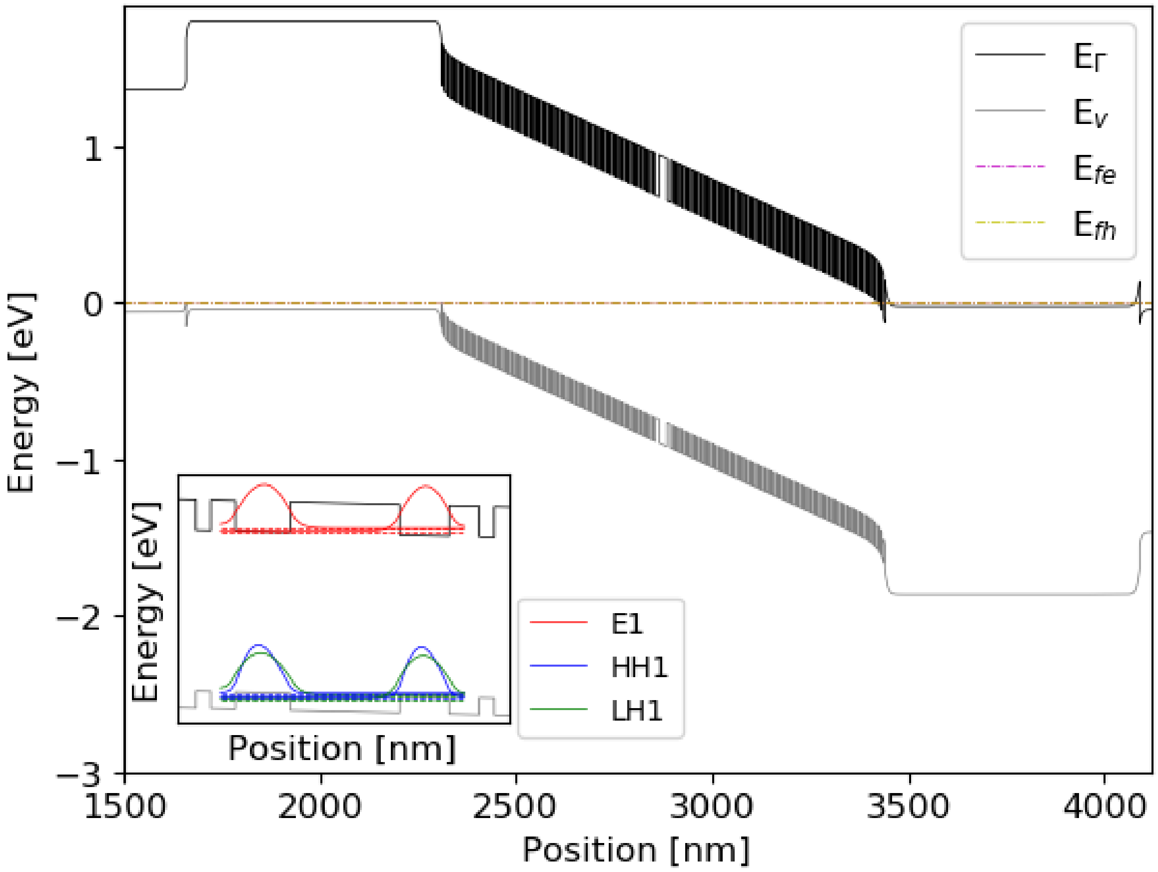

Fig. 2.3 – Band structure calculated for GaAs-AlGaAs QW slab structure as in [25]. Inlay shows ground state energies and wavefunctions of electron, heavy and light hole bands.

In general, only layer thicknesses were used as structural inputs corresponding to a wafer epi-structure, creating one dimensional band structures as shown in fig. 2.3. Therefore only the effective mass in the direction of growth was used in the Schrödinger equation to calculate bound states and wavefunctions. As a result, it was possible to create an effective mass tensor ellipsoid by altering the in-plane effective masses of certain materials, influencing the effective density of states in these layers. This allowed control of the effective density of states used in the previous equations, as an approximation for more complex structures such as QDs which require additional dimensions for increased confinement and correspond to a growth density. This simplification allowed for calculation of a full device including a dot layer within the Schrödinger-Poisson-current continuity solver by equating the effective density of states in that region to the dot density in that layer. This altered the isotropic effective mass tensor used for calculations of QWs to an effective mass tensor ellipsoid as shown in fig. 2.4. Further detail is discussed in Chapter 5. For additional information about the Nextnano modelling procedure, see [26], [27].

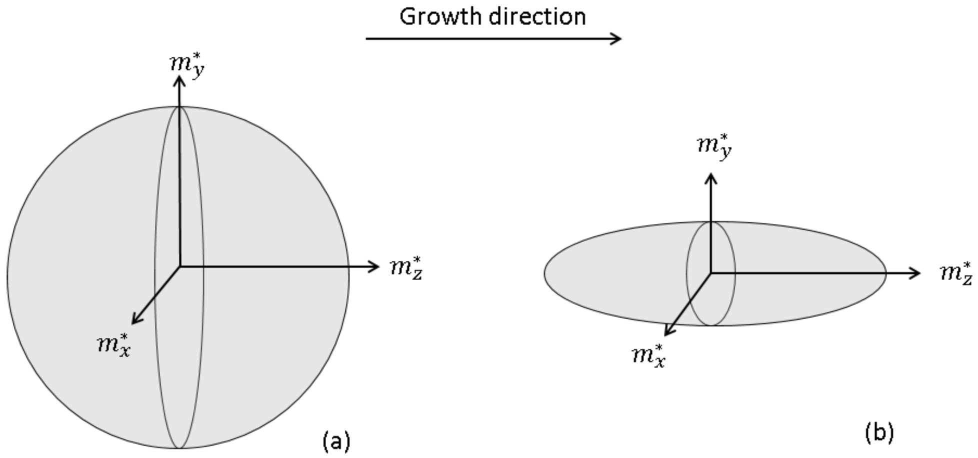

Fig. 2.4 – (a) Isotropic (b) ellipsoidal effective mass tensors.

Nextnano was used to calculate homogeneous strain effects on band alignment, yet an understanding of individual and full layer strain with composition and thickness was important to avoid the formation of defects and dislocations in real materials. The lattice mismatch strain, as described by Ayers[28], was evaluated in eq. 2.7. This described the expected percentage strain for two crystals.

$$f = \frac{a_s - a_e}{a_e} \tag{2.7}$$

Here, a_s was the relaxed lattice constant of the substrate and a_e was the relaxed lattice constant of the epilayer. The strain was either tensile or compressive depending on whether a_e was smaller than or larger than a_s respectively. Additionally, the parallel and perpendicular strain were calculated, with material parameters from [21], [22] and [23].

Eq. 2.8 can be used to calculate the in-plane lattice constant $a_{\parallel}$ resulting from two epi-layers subscripted 1 and 2. The in-plane lattice constant is generally considered that of the substrate in a full structure. The in-plane biaxial strain $\epsilon_{\parallel}$ can then be calculated from eq. 2.9 for either layer, a_i. The perpendicular lattice constant $a_{i\perp}$ for that layer can be calculated from eq. 2.10, and the uniaxial strain $\epsilon_{i\perp}$ in eq. 2.11.

$$a_{\parallel} = \frac{a_1 G_1 h_1 + a_2 G_2 h_2}{G_1 h_1 + G_2 h_2} \tag{2.8}$$

$$\epsilon_{\parallel} = \frac{a_{\parallel}}{a_i} - 1 \tag{2.9}$$

$$a_{i\perp} = a_i \left[1 - D_i \left(\frac{a_{\parallel}}{a_i} - 1\right)\right] \tag{2.10}$$

$$\epsilon_{i\perp} = \frac{a_{i\perp}}{a_i} - 1 \tag{2.11}$$

G and h were the shear modulus and layer thicknesses respectively. $D^{001} = 2(c_{12}/c_{11})$ was a constant related to elastic constants dependent on the orientation of the interface and material, described in [21]. $\epsilon_{\perp}$ combined with $\epsilon_{\parallel}$ represented the strain tensor, which was minimized to find materials and dimensions for epitaxy with minimal dislocations in the crystal lattice.

Strain balancing is a technique used when growing large period multiple QWs or superlattices to reduce the average strain throughout the full epi-structure. As the substrate tends to set the in-plane lattice constant, by combining materials whose strain will give a $a_{\parallel}$ equal to the substrate lattice constant, strain is compensated. This is generally done by implementing a layer of material with lattice mismatch of opposite sign calculated using eq. 2.7. For example, for higher gallium content InGaAs growth on InP substrates, higher indium content InGaAs or InAlAs may be used to compensate the strain[29], [30]. This is similarly done for InGaAs on GaAs substrates using GaAsP[31], [32].

2.2 Eigenmode Analysis

When light-matter interactions in semiconductors were evaluated, particularly for waveguided structures, such as photonic integrated circuitry, it was important to calculate the mode field profiles, which were used to calculate optical confinement. This was conducted in the MODE waveguide simulation suite from Lumerical, in particular, using the finite domain eigenmode expansion solver. This involved defining geometries of the epitaxial layer thicknesses and waveguide dimensions. The problem was discretized along a Cartesian mesh, with fully vectorised electric and magnetic field wave equations solved using Maxwell’s curl equations in eq. 2.12, at each mesh point for a local cross section of the device, at a single frequency.

$$\nabla \times \boldsymbol{E} = -\frac{\partial \boldsymbol{B}}{\partial t} \qquad ; \qquad \nabla \times \boldsymbol{B} = \mu_0 \boldsymbol{J} + \mu_0 \epsilon_0 \frac{\partial \boldsymbol{E}}{\partial t} \tag{2.12}$$

$\boldsymbol{E}$ and $\boldsymbol{B}$ were electric and magnetic field vectors. μ_0 and ϵ_0 were the permeability and permittivity of free space respectively. t was time, and $\boldsymbol{J}$ was the current density, though mobile charge carriers were not considered in these calculations. Geometry input via a GUI required real refractive indices of each material layer at a single frequency. These were defined by [33], [34], and averaged in the software between mesh points. The procedure for solving the fully vectorised electric and magnetic fields across the mesh grid is shown in [35], returning normalized electric field E_x, E_y, E_z, and magnetic field B_x, B_y, B_z, components at each grid point. The mesh grid, refractive index, and calculated mode profile are shown in fig. 2.5.

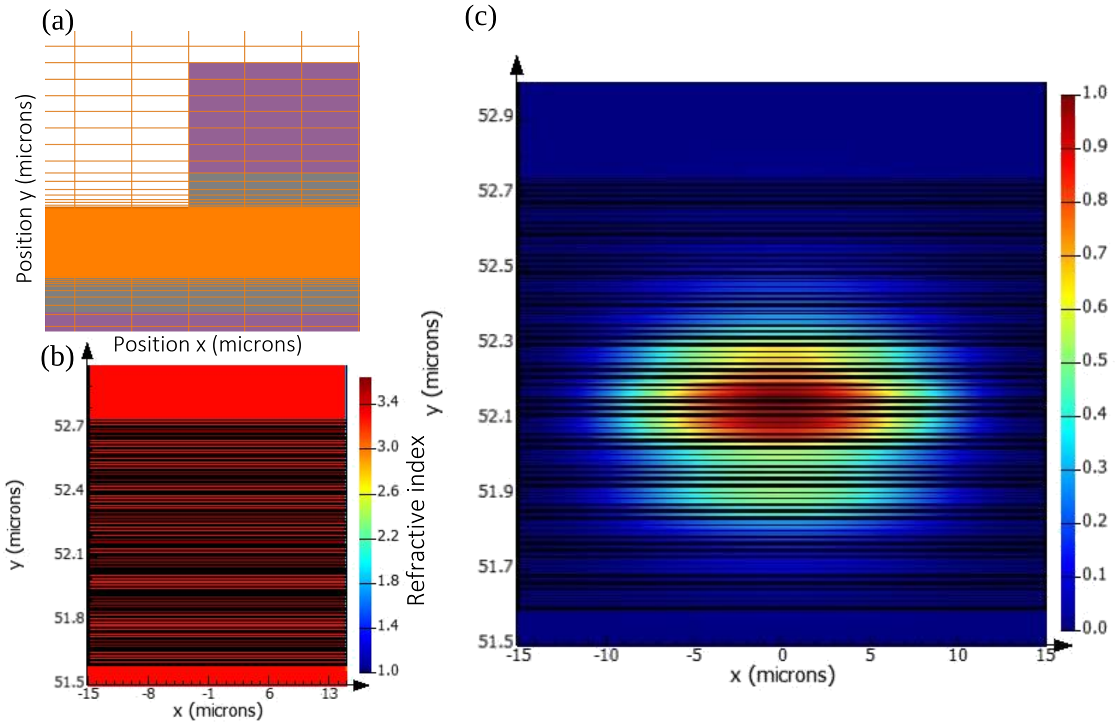

Fig. 2.5 – (a) Mesh grid, (b) real refractive index, and (c) calculated fundamental optical mode for GaAs-AlGaAs QW slab structure[25].

After calculating allowed optical modes in the waveguide, the integral of the electric field of a given cross section over that of the full device provided the optical confinement factor, in eq. 2.13.

$$\Gamma = \frac{\int_{-\frac{L}{2}}^{\frac{L}{2}} E^2(x)dx}{\int_{-\infty}^{\infty} E^2(x)dx} \tag{2.13}$$

This allowed calculation of optical confinement weightings at each relevant layer. Γ was the optical confinement factor, L was the thickness of the element, and E was the magnitude of the electric field vector as a function of x.

2.3 Absorption and gain

The preceding outputs were combined to calculate material and modal absorption and gain in QWs and QDs. Beginning with the optical absorption coefficient, a dimensionless fractional change in energy due to absorption by a single QW[16], and then the optical gain coefficient are separately described.

2.3.2 The absorption coefficient

The optical absorption coefficient is a measure of the fraction of light absorbed by a material across a unit distance. This is often described classically by Beer's law, which can be found by considering the incremental change in optical intensity through an incremental slice of an optical medium[36]. The absorption coefficient is independent of the optical intensity, but directly proportional to the natural logarithm of the power transmitted over the power incident on the medium.

$$I(x) = I_0 e^{-\alpha x} \tag{2.14}$$

$I(x)$ was the optical intensity at a position x, I_0 was the incident optical intensity or at a position $x = 0$, and α was the absorption coefficient. The absorption coefficient in semiconductors is strongly influenced by the density of states in that material or structure as this defines the number of possible states which may absorb a photon. Here, only interband absorption between valence and conduction bands was considered.

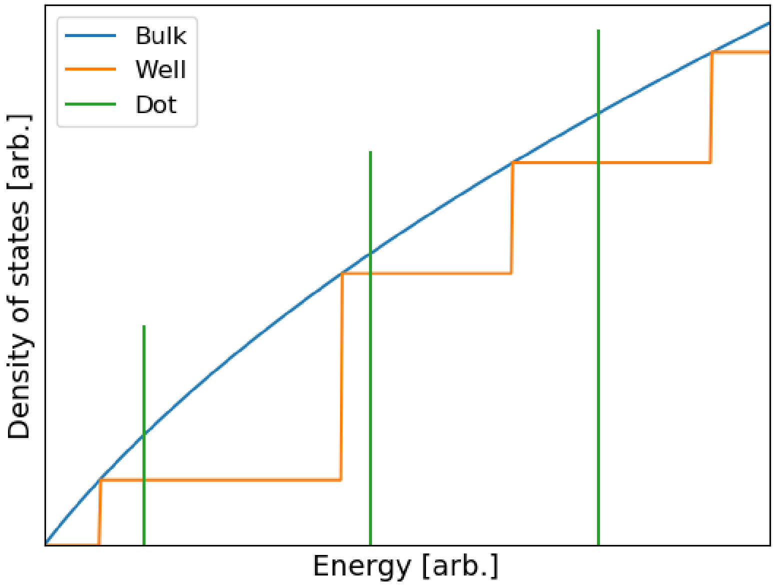

Fig. 2.6 – Schematic diagram of density of states as a function of energy above a band edge for a bulk semiconductors, QWs, and QDs.

Fig. 2.6 shows the density of states as a function of energy from the band edge for bulk semiconductors, QWs, and QDs. The density of states of bulk material, QWs, and QDs can be described by the relationship with energy from the band edge. In bulk material, the density of states increased with the square root of the energy, equal to zero at the band edge due to zero state occupation within the forbidden band gap between the valence and the conduction band, though this can change with electric field and temperature[37]. In QWs, there are quantized states due to one dimensional confinement but continua of states in the plane of the well This has a Heaviside step relationship between the density of states and energy. QDs experience confinement in all three dimensions and have completely quantized states. Delta functions show the relationship between energy and the density of states. In a real structure this density of states will also be related to the size distribution of the QDs grown in a layer. Therefore, the delta functions become broadened and finite, and can be modelled with a Gaussian size distribution of Lorentzian functions. The magnitude of the density of states will depend on the density of dots grown, with degeneracy increasing with each bound state.

Absorption is also dependent on whether states are occupied. A likelihood of occupation can be calculated using Fermi-Dirac statistics when a structure is in thermal or quasi-thermal equilibrium[38]. In this case an electron and hole quasi-Fermi level are assumed to represent the energy at which there is a 50% probability of occupation.

The equations described in subsequent sections were originally derived from time-dependent perturbation theory, with a good explanation given by Chuang in [17]. The inclusion of the Coulomb interaction in QWs was incorporated through a Green's-function approach in [15], again by Chuang. The final expressions are used through this thesis, and the exciton Green's-function approach is described with more detail in appendix A1.

2.3.3 Absorption in QWs

Initially, Chuang describes absorption in QWs, similarly to the density of states, modelled as a Heaviside step function. A reduced density of states with proportionality to the thickness of the QW in eq. 2.15 related to the effective mass of each subband involved in the transition provided a quantification of the number of transitions possible for a given material and QW dimension.

$$\alpha(\hbar\omega) = C_0 \sum_{c,v} |I_{cv}|^2 |M|^2 \rho_r^{2D} H\left(\hbar\omega - E_{c,v}\right)(f_v - f_c) \tag{2.15}$$

$$C_0 = \frac{\pi e^2}{n_r c \epsilon_0 m_0^2 \omega} \qquad \rho_r^{2D} = \frac{m_r^*}{\pi \hbar^2 L_z}$$

C_0 is derived from the time averaged Poynting vector (the cross product of the electric and magnetic fields perturbing the electronic structure)[17]. n_r was the real refractive index of the medium, c the speed of light in a vacuum, ϵ_0 the vacuum permittivity, and ω the photon energy frequency. $|I_{cv}|^2$ was the wavefunction overlap integral between the conduction and valence band states c, v. $|M|^2$ was the basis function matrix element derived from time dependent perturbation theory. The basis function matrix element has been well determined through band structure calculations to be almost constant for many III-V alloys[16]. These matrix elements were written in terms of a P parameter by Kane[39] as $P = (\hbar/m_0)|M|^2$ or in terms of energy through $E_p = 2Pm_0/\hbar^2$. ρ_r^{2D} was the reduced density of states for a QW of thickness L_z, with m_r^* the reduced effective mass, $1/m_r^* = 1/m_e^* + 1/m_h^*$. m_e^* and m_h^* were the electron and hole effective mass respectively. H was the Heaviside step function. $E_{c,v}$ was the Interband transition energy.

$(f_v - f_c)$ was the difference in probability of occupation with an electron between the valence and conduction bands describing the level of depletion, and given in eq. 2.16. If the conduction band was fully depleted and the valence was fully occupied $(f_v - f_c) = 1$, maximum absorption could occur. Whereas, if the conduction band state c was not fully depleted, or the valence band state v not fully occupied, blocking of carriers would occur reducing the overall absorption magnitude.

$$f_{c,v} = \frac{1}{1+exp\left(\frac{E_{c,v}-E_{fc,v}}{kT}\right)} \tag{2.16}$$

$E_{fc,v}$ was the quasi-Fermi level energy for either the electrons or holes. This was a sufficient description for rudimentary modelling, however, QWs may display exciton resonances due to Coulomb attraction between electrons and holes creating bound states. Excitons may occur above room temperature near to and below the transition energy, provided high quality material growth[40]. Consideration of the bound and continuum of states is required in realistically predicting electroabsorption. For this, expressions derived using a Green's-function approach in [15] and tabulated in [17] are considered in eq. 2.17. Further detail is given in appendix A1.

$$\alpha(\hbar\omega) = C_0 \frac{2}{L_z} \gamma_{cv} M_b^2 |I_{cv}|^2 \frac{k_0^2}{2\pi R_y} \times \left[4 \sum\nolimits_n |a_0 \phi(0)|^2 \frac{R_y \Gamma_b}{\left(E_{c,v} - E_B - \hbar\omega\right)^2 + {\Gamma_b}^2} \right.$$
$$\left. + \int_0^\infty \frac{dE_{cv}}{\pi} |\phi(0)|^2 \frac{\Gamma_b}{\left(E_{c,v} - \hbar\omega\right)^2 + {\Gamma_b}^2} \right] (f_v - f_c) \tag{2.17}$$

a_0 was the exciton Bohr radius, shown in eq. 2.18, with $k_0 = 1/a_0$. R_y was the exciton Rydberg energy, shown in eq. 2.19, which was used to calculate the exciton binding energy E_B. These related to the properties of exciton resonances for the semiconductor arising from Coulomb interaction between the electron and hole. The interaction was described spatially by a_0 and related to the reduced effective mass between electron and hole.

$$a_0 = \frac{4\pi\varepsilon\hbar^2}{m_r^* e^2} \tag{2.18}$$

$$R_y = \frac{m_r^* e^4}{2\hbar^2 (4\pi\varepsilon)^2} \tag{2.19}$$

E_B described the reduction in the transition energy due to the Coulomb attraction between the bound electron-hole state, which was $-R_y$ for a 3D exciton and $-4R_y$ for a pure 2D exciton. $|\phi(0)|^2$ was the oscillator strength approximated by the Sommerfeld enhancement factor, shown in eq. 2.20, with $1 \leq s \leq 2$, with $s = 2$ for a pure 2D exciton and $s = 1$ for a 3D exciton. With $ka_0 = \sqrt{E_t/R_y}$, where E_t was the difference between the transition energy and the band gap energy[15].

$$|\phi(0)|^2 \cong \frac{s_0}{1+e^{-\frac{2\pi}{ka_0}}} \tag{2.20}$$

The bulk matrix element related to the Kane energy parameter was $M_b^2 = (m_0/6)\, E_p$ which was multiplied by a polarization, band dependent prefactor, γ_{cv}. Each degenerate valence band had a momentum matrix element dependent on the incidence angle of the electric field and the electronic wave vector expressed in spherical coordinates. In bulk semiconductors this is often isotropic[17], [39] and can be averaged. In a QW, an average was taken across the *x-y* plane, assuming the growth axis was in the *z*-dimension. The light-matter interaction is considered for transverse electric (TE) polarization along either the *x* or *y* direction, or transverse magnetic (TM) polarization with electric field orientated in the *z* direction.

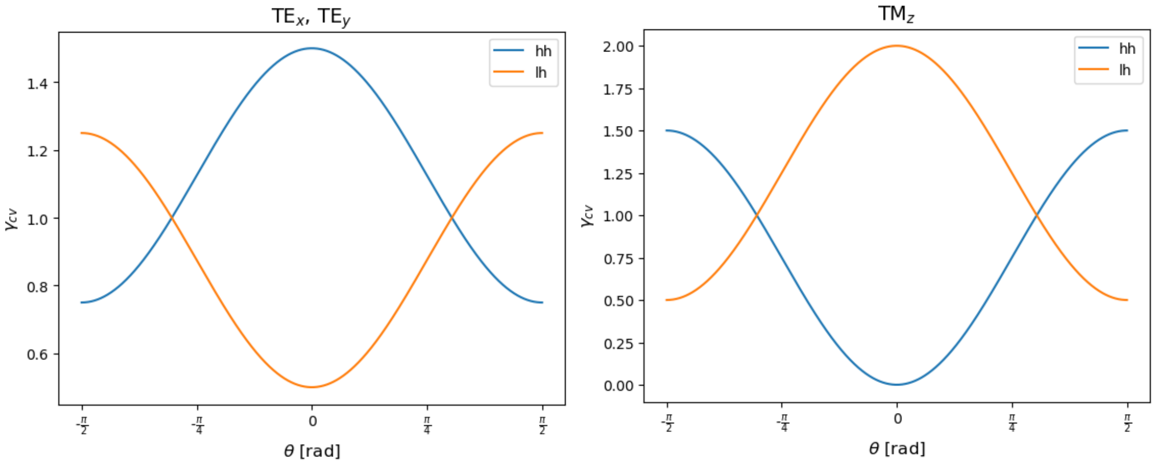

Fig. 2.7 – Prefactor for TE for x and y, and TM for z oriented polarization varying angle θ.

This yielded the following relationships from [17] for heavy and light holes, shown in fig. 2.7:

$$\gamma_{TE-HH} = \frac{3}{4}(1 + \cos^2\theta) \tag{2.21}$$

$$\gamma_{TE-LH} = \frac{5}{4} - \frac{3}{4}\cos^2\theta$$

$$\gamma_{TM-HH} = \frac{3}{2}\sin^2\theta$$

$$\gamma_{TM-LH} = \frac{1+3\cos^2\theta}{2}$$

For TE polarization, γ_{cv} was $3/2$ and $1/2$, and for TM polarization, 0 and 2 for heavy holes and light holes respectively, when $\theta = 0$.

Γ_b combined the homogeneous and inhomogeneous broadening energy and was calculated using eq. 2.22. The broadening in both continuum and bound state contributions are commonly modelled as Lorentzian functions[17], though Gaussian functions[41] and hyperbolic secant functions[42] have been used if the experimentally observed absorption tail decays more sharply.

$$\Gamma_b = \Gamma_0 + \frac{\Gamma_{ph}}{exp\left(\frac{\hbar\omega_{LO}}{k_b T}\right) - 1} \tag{2.22}$$

Γ_0 accounted for additional half width at half maximum (HWHM) of the inhomogeneous broadening linewidth induced by scattering via interface surface roughness and well width fluctuation, which have been experimentally observed to be exacerbated with an applied electric field[41]. The remaining term described the temperature dependent homogeneous longitudinal optical (LO) phonon scattering with $\hbar\omega_{LO}$ the LO-phonon energy, and Γ_{ph} was the HWHM of phonon broadening linewidth. The values of these could be found from fitted experimental data and calculations in the literature[10],[17],[19],[21]. Stevens et al[41] used a convolution of two Gaussians to describe the homogeneous and inhomogeneous broadening distributions giving a larger value than suggested by Chemla et al[24]. Though it is prudent to consider experimental observations when selecting a broadening distribution.

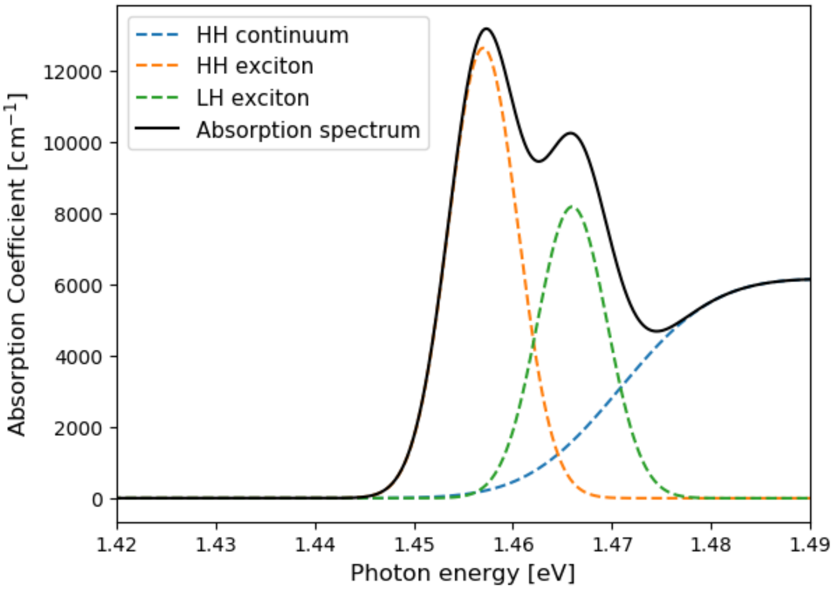

Fig. 2.8 – Calculated absorption spectrum (solid line) for GaAs-AlGaAs QW slab structure[25], with exciton and continuum contributions (dashed lines). Gaussian distributions have been used to represent the homogeneous broadening.

The exciton and continuum contributions are shown in fig. 2.8, combined to give the resulting absorption spectrum for the GaAs-AlGaAs QW[25], in this case Gaussian distributions were used to represent excitons, similarly to Chemla et al.[24].

2.3.4 Fractional change in energy due to QW absorption

For applications at normal incidence to the QW layers, it may not be appropriate to use the absorption coefficient for comparison between different structures due to the dependence on the width of the QW, L_z. According to Blood, Beer's law requires proportionality to the thickness of an element, however, at normal incidence, where the element is often given as L_z, this becomes undefined due to tunneling of carriers into the barrier[16].

Moreover, when comparing structures containing QWs of differing dimensions or shapes, potentially due to intermixing, or for band alignments where carriers are in separately confined layers, the absorption coefficient is not appropriate[43], as Beer's law does not scale with the thickness of the element. At normal incidence the magnitude of light absorbed is related to the number of subbands with transition energy less than the photon energy. Therefore, the fractional change in energy due to absorption by transitions between a single pair of sub-bands for a single well was used[16]. This was derived by Blood providing eq. 2.23.

$$\gamma_{well} = \frac{\Delta S}{S} = \frac{4\pi\hbar}{\epsilon_0 cn(h\nu)}\left(\frac{e}{2m_0}\right)^2 |M_T|^2 \rho_{trans} \tag{2.23}$$

Here S was the time averaged flux of incident photons, and ΔS was the change in this flux upon transmission through a QW. $|M_T|^2$ was the transition matrix element equal to that previously defined as $\gamma_{cv} M_b^2 |I_{cv}|^2$, containing the polarization, band dependent prefactor, bulk matrix element, and wavefunction overlap integral. ρ_{trans} was the transition density, a function of the effective masses of each band for two spins, sometimes referred to the reduced density of states, given by eq. 2.24.

$$\frac{1}{\rho_{trans}} = \pi\hbar^2\left(\frac{1}{m_e^*} + \frac{1}{m_h^*}\right) \tag{2.24}$$

This value provided the density of states available for transitions through the absorption of photons without including a dependence on the thickness of the element as in the previously defined notation. However, this description only gives the fractional change in energy through a QW, without consideration of the intricacies of exciton resonances nor broadening mechanisms. It was important to remove the thickness dependence from eq. 2.17 as in 2.23, to be able to compare absorption spectra of various heterostructures.

In [16], Blood calculates γ_{well} for the first two subbands of a typical GaAs QW, including a cumulatively summed Lorentzian broadening term, similarly to Chuang in eq. 2.17, which accounted for the continuum of states contribution.

Blood maintains the majority of the terms outside the parentheses, excluding the thickness of the element L_z. Broadening terms and the exciton contribution are presented eq. 2.25. The calculated fractional change in energy due to absorption between subbands in a GaAs-AlGaAs QW, including Coulomb attraction, as shown in fig. 2.9.

$$\gamma_{well} = \frac{4\pi\hbar}{\epsilon_0 cn(h\nu)}\left(\frac{e}{2m_0}\right)^2 |M_T|^2 \rho_{trans} \times \left[\sum_n |\phi(0)|^2 \frac{R_y\Gamma_\mathrm{b}}{\left(E_{c,v}-E_B-\hbar\omega\right)^2+{\Gamma_\mathrm{b}}^2}\right.$$

$$\left. + \int_0^\infty \frac{dE_{cv}}{\pi} |\phi(0)|^2 \frac{\Gamma_\mathrm{b}}{\left(E_{c,v}-\hbar\omega\right)^2+{\Gamma_\mathrm{b}}^2}\right] (f_v - f_c) \tag{2.25}$$

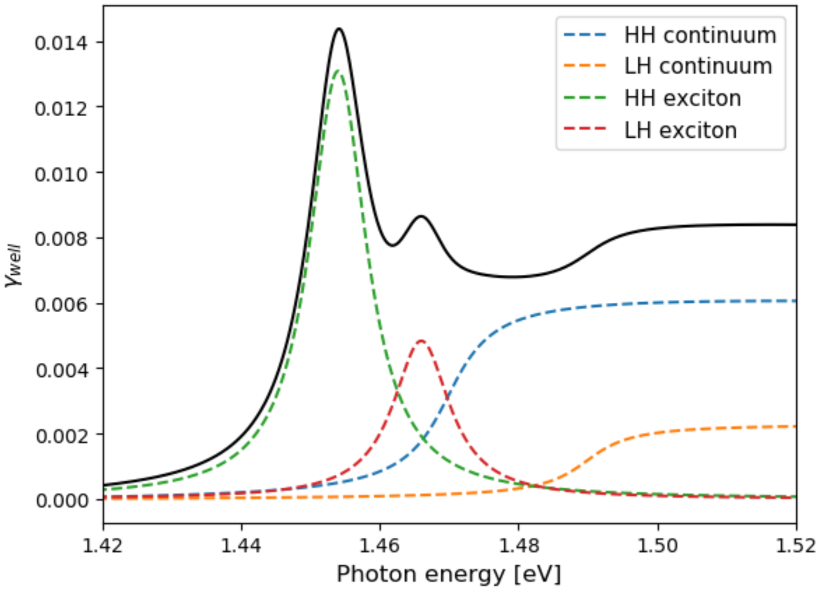

Fig. 2.9 – Calculated γ_{well} spectrum (solid line) for GaAs-AlGaAs QW slab structure[25] using fraction absorbed per well[16], with exciton and continuum contributions (dashed lines). Lorentzian distributions have been used to represent homogeneous broadening.

A cornerstone of this description was that the fraction of energy absorbed at a given photon energy is proportional not to the thickness of the element, but to the number of transitions between subbands of energy separation below a given photon energy. Therefore, this metric could be used for comparison of QWs of differing dimension, band alignment, and shape, particularly for normal incidence where Beer's law is not appropriate and the absorption coefficient may become undefined.

2.3.5 Absorption in QDs

QDs are confined in all dimensions and therefore have no interaction with a continuum of states in the same way as QWs. The dots considered in this thesis were grown using self-assembly, specifically the Stranski-Krastanov growth mode. In this growth technique a thin strained layer (often GaAs or InGaAs in many III-V devices) is grown acting as a nucleation layer for material grown subsequently above a critical thickness. The subsequent material will coalesce into three dimensional islands or nanoparticles and a wetting layer, this is known as the Stranski-Krastanov transition[44]. Finally a capping layer, of the same material as the nucleation layer, is grown to incase the QDs providing a potential barrier. The material used as the barrier will have a larger band gap energy than the QDs. If sufficiently narrow the material surrounding the QD will form a QW improving confinement[45], referred to as dots-in-a-well (DWELL). If a DWELL is used there will be a further barrier material of even higher band gap energy to separate the DWELL layers.

As a result of self-assembly the QDs have a probabilistic size distribution. This size distribution is inhomogeneously broadened as a Gaussian function. Though this does not directly translate to the energy distribution required for absorption modelling, it is a suitable approximation[16]. Hence, the layer of QDs grown is treated as an ensemble. The delta-like functions shown in fig. 2.6 experience homogeneous broadening, due to carrier scattering mechanisms, which is commonly modelled by a Lorentzian function[17]. However, as with the QW, depending on the structure and experimental observations, it may be more appropriate to use a Gaussian, secant, or secant squared function[16], [46], [47] to represent the homogeneous broadening of the absorption spectrum for each dot size. This is shown in fig. 2.10 with the energy distribution modelled using eq. 2.26.

$$P(E_i) = \frac{1}{\sigma\sqrt{2\pi}} exp\left(\frac{-(E_i - E_0)^2}{\sigma_E^2}\right) \tag{2.26}$$

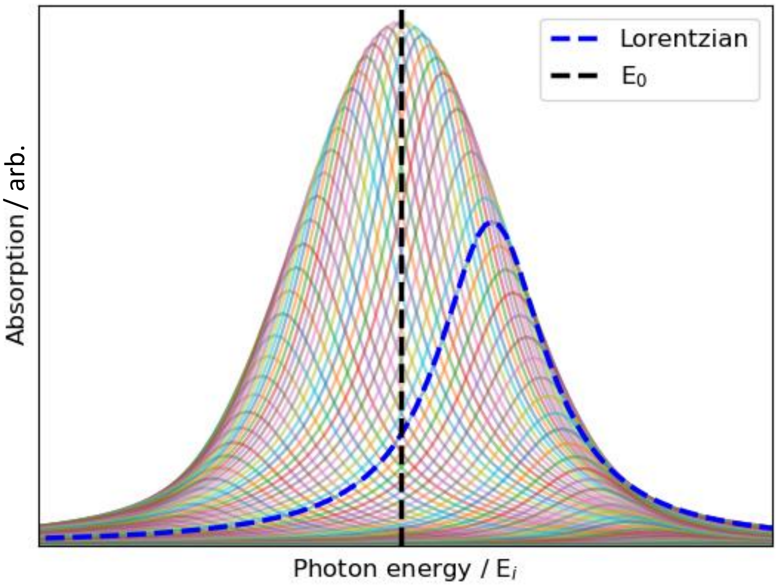

Fig. 2.10 – Inhomogeneously broadened energy distribution of Lorentzian functions representing the inhomogeneously broadened QD sizes in the ensemble.

$P(E_i)$ was the probability of a dot with a size resulting in a ground state energy equal to photon energy E_i. E_0 was the mean dot ground state energy and equivalent to the most prominent dot size coalesced during growth. σ_E was the standard deviation in the distribution of energy states which relates to the level of inhomogeneous broadening encountered in the dot size distribution. The absorption coefficient contains a cumulative sum of all contributing dot sizes at each photon energy.

Chuang[17] and Blood[16] provide excellent descriptions of QD dynamics including absorption and gain, though Chuang is primarily followed here. QD devices are uncommonly used as larger area normal incidence devices, as they provide significantly less interaction area compared with QWs. As wave-guided structures an interaction length will include many QDs, thus the absorption coefficient is a valid and useful metric. The absorption coefficient for a QD ensemble is shown in eq. 2.27.

$$\alpha(\hbar\omega) = C_0 \Gamma \sum_{cv} \int_0^{\infty} dE \, |I_{ov}|^2 M_b^2 D(E) L(E-\hbar\omega)(f_v - f_c) \tag{2.27}$$

$$L(E-\hbar\omega) = \frac{1}{\pi}\frac{\gamma}{\left(E_{c,v}-\hbar\omega\right)^2+\gamma^2} \qquad D(E) = \frac{2N_{dot}^{2D}}{L_{dot}}\frac{1}{\sqrt{2\pi}\sigma}\exp\left(-\frac{\left(E-E_{c,v}\right)^2}{2\sigma^2}\right)$$

Here, Γ was the optical confinement factor describing the overlap of the optical mode with the QDs, which was calculated through eigenmode analysis highlighted in section 2.2. This provided a measure of the modal absorption that would be present in a real device allowing comparison with experimental measurements. Omitting this provides the material absorption as described for QWs. The homogeneous Lorentzian broadening distribution $L(E-\hbar\omega)$ was characterized by the FWHM of 2γ which is proportional to the carrier scattering rate in the structure. $D(E)$ described the inhomogeneous broadening and contains a Gaussian function. N_{dot}^{2D} was the areal dot density and L_{dot} was the height of the dot. σ was the standard deviation of the inhomogeneous broadening distribution and describes the variation in energy due to the differences in dot growth sizes.

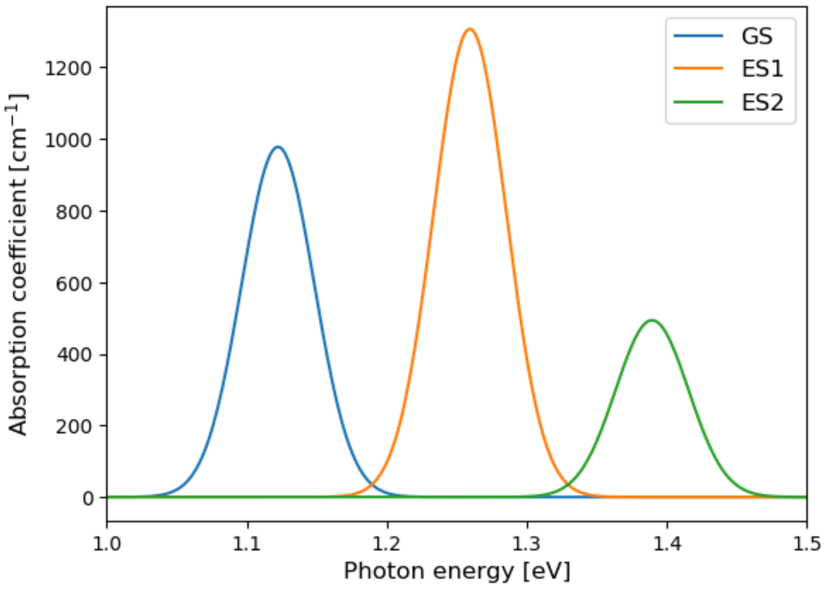

Fig. 2.11 – QD absorption contributions from ground (E1-HH1), first (E2-HH2) and second (E3-HH3) excited states utilizing material parameters listed in [17].

This related to the energy broadening of both electrons and holes by $\sigma^2 = \sigma_c^2 + \sigma_v^2$. E was the energy of the transition for a particular dot size, giving the difference from the mean transition energy $E_{c,v}$. The resulting absorption from ground (E1-HH1), first (E2-HH2) and second (E3-HH3) excited states are shown in fig. 2.11. The light hole to conduction band transitions occur at significantly higher photon energy due to a lower effective mass and are not included here.

Experimental observation of some III-V compound semiconductor QDs, particularly InAs, demonstrate two distinctive dot size distributions at higher growth temperatures, becoming multimodal at lower growth temperatures[48]. This has been observed by atomic force microscopy, photoluminescence, and transmission electron microscopy measurements[49]. As a result it may be useful to invoke a bimodal approximation when modelling the absorption and gain of particular materials, deriving a ratio between large and small dot distributions dependent on experimental data of real samples.

This is shown in [50] by fitting experimental data with Gaussians to approximate the density of large and small QDs. Fig. 2.12 demonstrates a bimodal dot size distribution approximation using the data from fig. 2.11, with a ratio between large dots (LDs) and small dots (SDs) equal to 60:40 in this example.

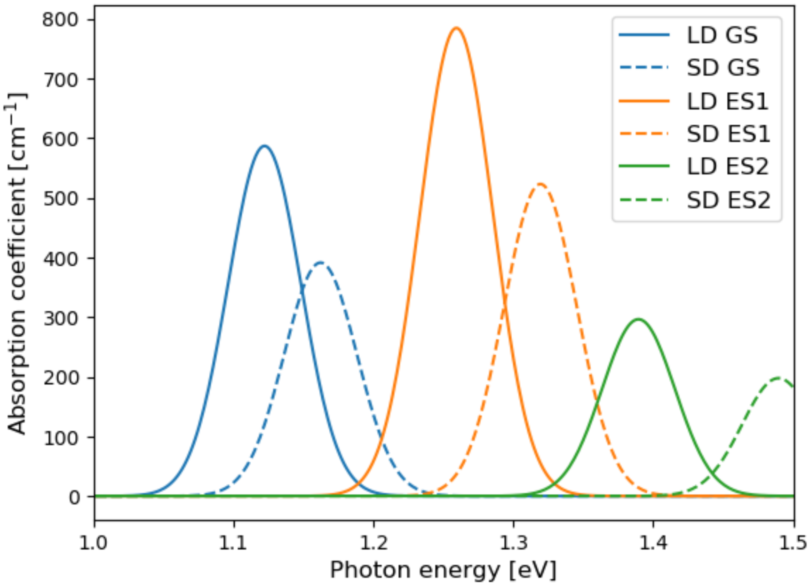

Fig. 2.12 – QD absorption contributions from ground, first and second excited states assuming a bimodal dot size distribution approximation, with large dots (LD) and small dots (SD).

In this approximation the ratio of the area under the curves should be maintained for all transitions, though, due to the change in confinement the energy separation between LD and SD contributions will increase with transition index.

2.3.6 Electroabsorption in quantum wells and quantum dots

Prior to this section the framework for calculation of absorption spectra in QWs and QDs has been outlined. For modulators, how the absorption spectra change when an external electric field is applied, demonstrates the efficacy of the devices. This is known as electroabsorption, which utilizes the quantum confined Stark effect (QCSE) in QWs and QDs. The QCSE is the major principle behind the operation of optical intensity modulators, where at a single wavelength, transmission of light through a device can be increased or decreased depending on whether an electric field is applied. This yields highs and lows in the transmission spectrum, corresponding to lows and highs in absorption spectrum respectively. This method can be used to modulate the intensity of an incident beam to imprint data upon it in the form of “ons” and “offs” or “1s” and “0s”.

It is possible to calculate the QCSE by applying a reverse bias in band structure calculations described in section 2.1. Under reverse bias, the electron and hole wavefunctions are shifted spatially to opposite sides of the quantum confined structure reducing the overlap integral $|I_{ov}|^2$, thus reducing the absorption strength.

The electric field deforms the band potential and generally reduces the band gap, shifting the absorption edge to longer wavelengths. These band structure changes are shown in fig. 2.13, with the absorption spectra under zero and non-zero reverse bias conditions calculated using eq. 2.17, and shown in fig. 2.14. Fig. 2.14 shows the change in absorption spectrum under reverse bias with the absorption edge shifted to a lower photon energy and peak absorption reduced. In QDs the peak absorption will vary less due to higher associated confinement energy and reduced dimensions, similarly to narrow QWs[51]. There is also variability in the wavefunction overlap integral in QDs not only due to changes in size, but also shape[52].

Key metrics used to define the performance of modulator devices can be explained via reference to fig. 2.14. Firstly, the extinction ratio, defined as the power transmitted when the device is switched on to the power transmitted when the device is switched off or $ER = P_1/P_0$. This does not necessarily correspond to whether the electric field is on or off, but whether a device is operated for maximum or minimum transmitted power respectively, at a single wavelength or photon energy. Commonly quoted in units of decibels, $ER = 10\log_{10}(P_1/P_0)$, provides a metric of modulation depth.

The insertion loss is the fraction of power removed from the incident signal after transmission through the modulator, when biased for minimum absorption. This is the ratio between the input power and output power at maximum transmission operation, calculated in units of decibels as $IL = 10\log_{10}(P_t/P_i)$[53].

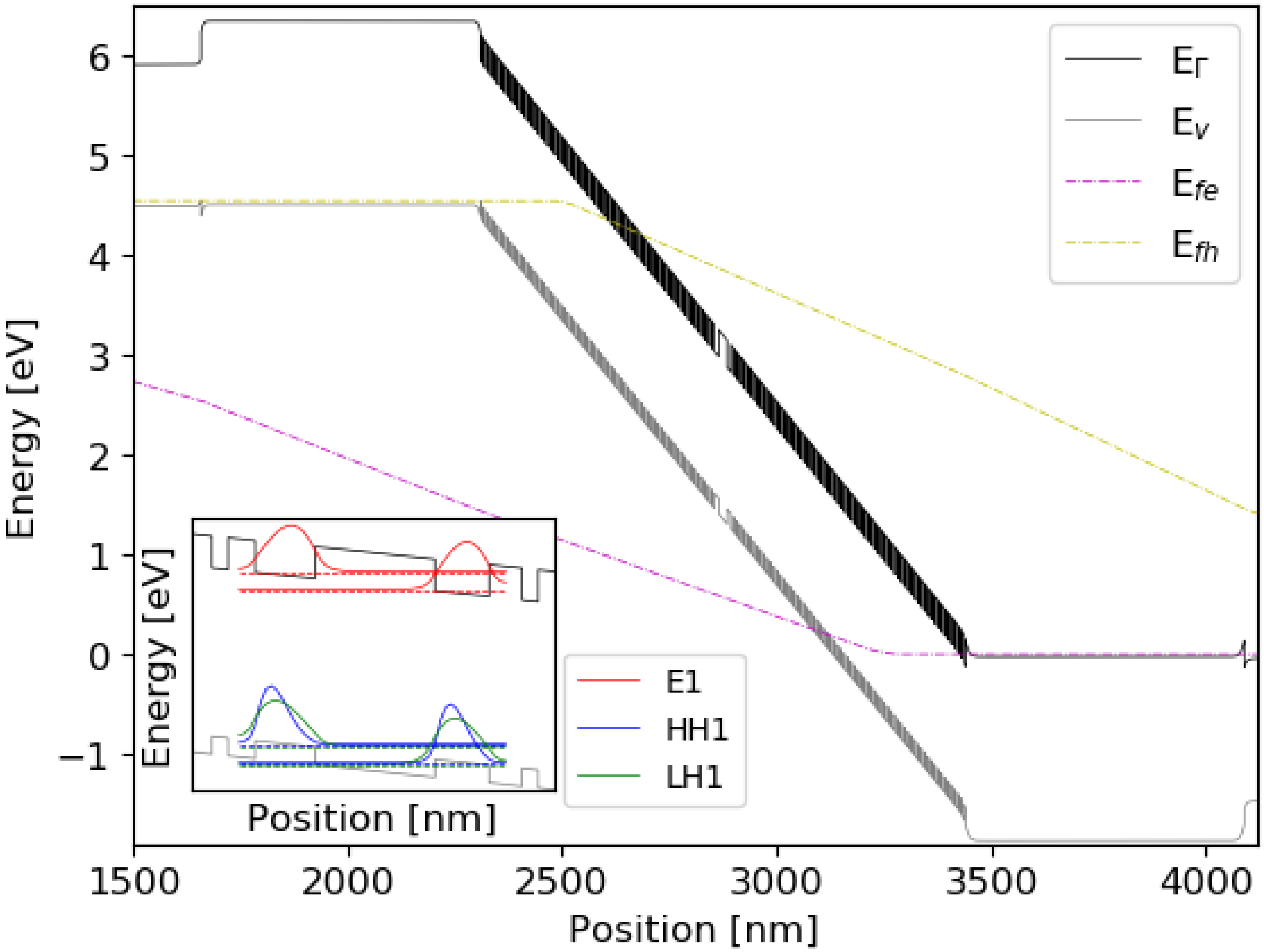

Fig. 2.13 – Calculated band alignment for GaAs-AlGaAs slab structure[25] *under reverse bias. The inlay shows the distorted band potential and shifted electron and hole wavefunctions.*

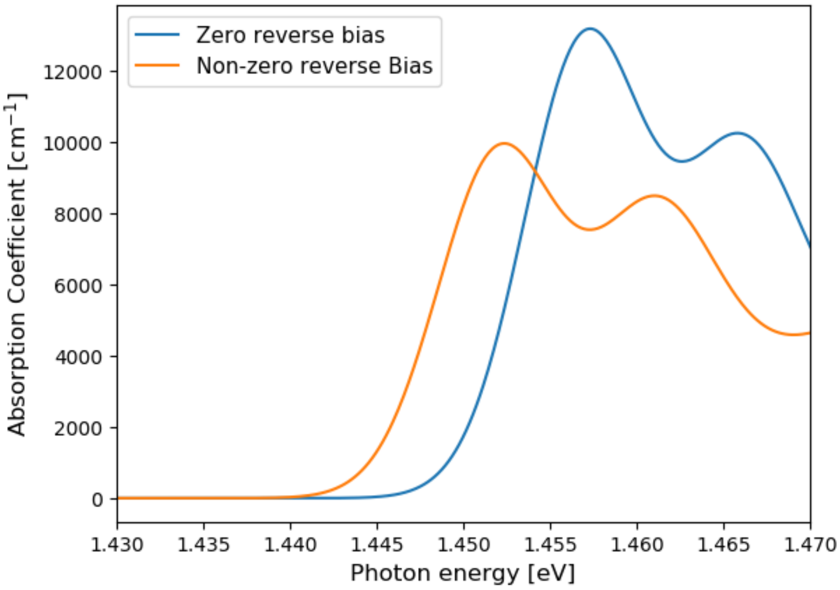

Fig. 2.14 – Quantum confined Stark effect in GaAs-AlGaAs QW slab structure[25] with absorption spectra under zero and non-zero applied reverse bias conditions.

These metrics are often scaled by the interaction length of the device, so the ratio between the ER and IL is defined as the figure of merit (FoM), to compare structures of varying dimensions, $FoM_1 = ER/IL$[54] is defined as the first FoM. However, Chin describes the importance of a second FoM[55] defined by the change of absorption coefficient with electric field strength, $FoM_2 = \Gamma\Delta\alpha/F$[56]. F is the electric field strength and Γ the optical confinement factor. Both metrics offer comparison between differing structures, which will be of utmost importance in subsequent chapters, though FoM_2 may be neglected for FoM_1 if the electric fields and optical confinement factors are comparable.

Additionally, the speed of modulation at which the device can be operated offers information on the data transmission capabilities. This is commonly given as the modulation bandwidth frequency describing the switching time between ons and offs per second. This is measured using swept frequency characterization methods, measuring the magnitude of the modulated signal as the frequency is increased until this magnitude is halved[53]. The data rate can be quoted as a measure of the number of bits transmitted per second. Data rate is generally quoted as an experimentally achieved data transmission speed, whereas the bandwidth gives the maximum capabilities possible.

2.3.7 Gain in QWs and dots

The material gain of a medium is an important characteristic in describing possible amplification available for a device, particularly in laser diodes. The gain coefficient is the negative of the absorption coefficient, and vice versa. This is because the occupation probabilities are reversed to describe the inversion of electrons to a higher energy state rather than the depletion. For QWs this yields the following notation in eq. 2.28.

$$g(\hbar\omega) = C_0 \sum_{c,v} |I_{cv}|^2 |M|^2 \rho_r^{2D} H\left(\hbar\omega - E_{c,v}\right)(f_c - f_v) \tag{2.28}$$

Similarly to eq. 2.15, this was summed across relevant transitions energies to provide the gain spectrum. The Heaviside step function may be replaced by a cumulatively summed Lorentzian as previously described to provide broadening considerations. If $(f_c - f_v) < 0$, the equation is describing loss or absorption, whereas if$(f_c - f_v) > 0$ it describes gain. Otherwise at $(f_c - f_v) = 0$ the material is at its transparency point. QDs follow the same progression, with the gain coefficient shown in eq. 2.29.

$$g(\hbar\omega) = C_0 \sum_{cv} \int_0^\infty dE\, |I_{ov}|^2 M_b^2 D(E) L(E - \hbar\omega)(f_c - f_v) \tag{2.29}$$

In both instances the optical confinement factor, Γ, can be applied to calculate the proportion of optical overlap with the inverted layer or region giving the modal gain, which will be more appropriate for comparison to experimental results.

The value of gain is heavily dictated by the population inversion of carriers and thus can be described simply by replacing all remaining terms with G_{max}, as in eq. 2.30.

$$g(\hbar\omega) = G_{max}(f_c - f_v) \tag{2.30}$$

The gain available is dependent upon the material parameters described, the population inversion of carriers, and the density of states available. Therefore QW lasers offer higher G_{max} due to significantly higher density of states compared with QDs. The QD density of states is directly proportional to density of dots in the layer. Fig. 2.15 shows the GaAs-AlGaAs QW structure described under forward bias. Under this condition the bands are flattened and the wavefunction overlap integral is near to unity.

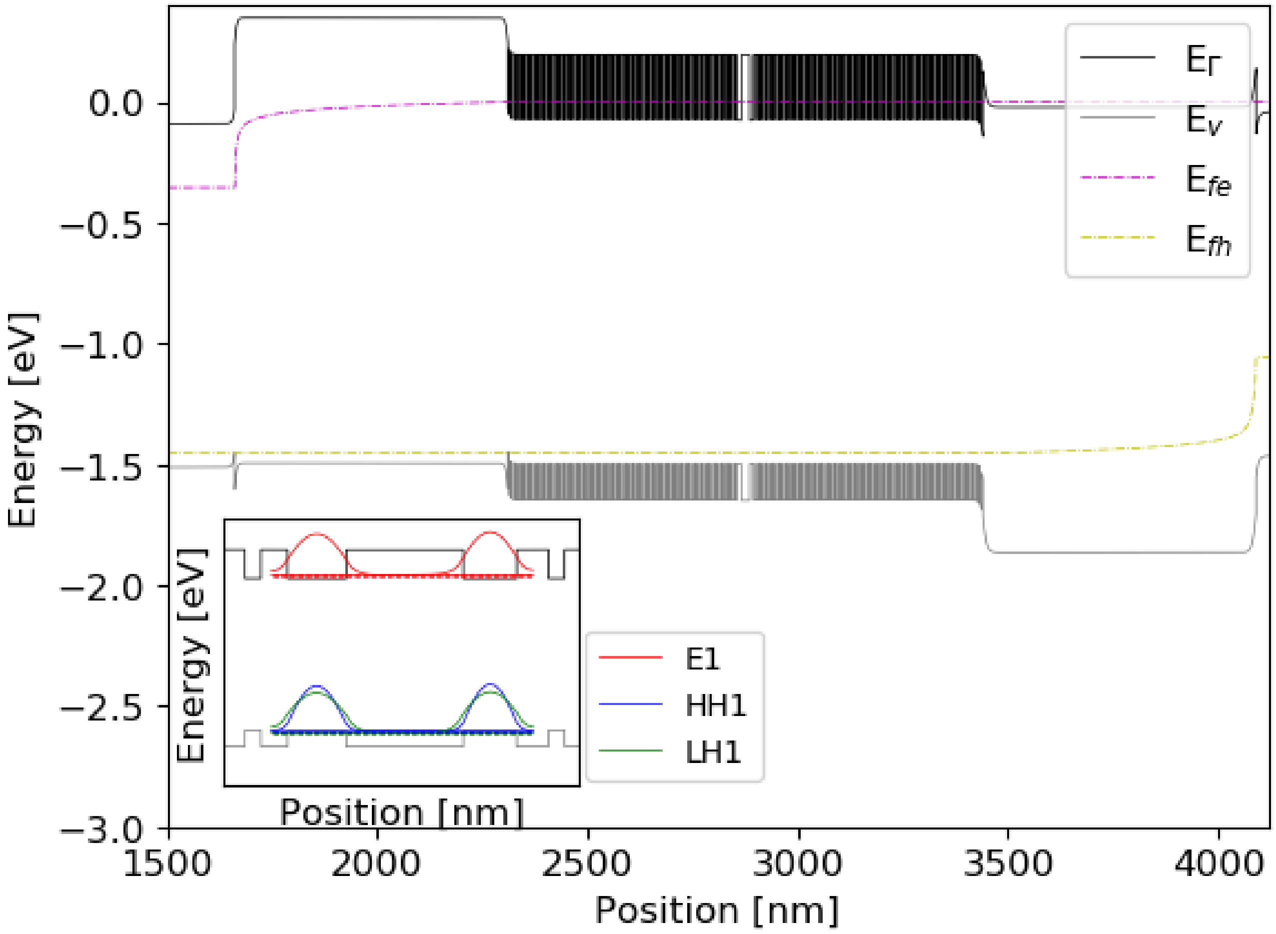

Fig. 2.15 – Calculated band alignment for GaAs-AlGaAs slab structure[25] under forward bias. Inlay shows the electron and hole wavefunctions.

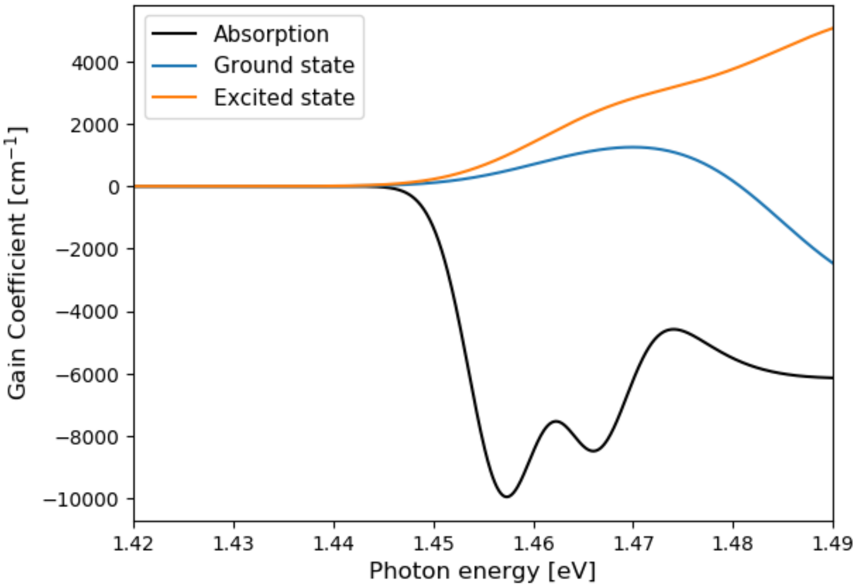

Fig. 2.16 – Calculated gain coefficient for GaAs-AlGaAs slab structure[25] under zero and two forward bias conditions showing ground state and excited state gain contributions.

Fig. 2.16 shows typical gain spectra calculated for a GaAs QW. The progression is shown from full carrier depletion or absorption (considered loss in terms of amplification), to population inversion of the ground state, and finally of the first excited state. There is an increase in the photon energy where the peak gain occurs, which gives a blue-shift in the emission wavelength compared with the absorption spectrum. There is a further blue-shift from ground state to first excited state dominated gain. There are strong similarities compared with QD gain spectra.

2.4 Summary

The background theory required for conducting semi-empirical modelling of band structures and light-matter interactions of QWs and QDs has been outlined. Full device band structure calculations using Nextnano software have been described, with the use of an effective mass tensor ellipsoid to equate the effective density of states in a region to the QD density. Lumerical's eigenmode expansion solver has been outlined for the calculation of an optical mode within a geometry. By applying optical mode weightings, modal absorption and gain can be calculated providing comparison between experimental data.

QW absorption equations derived by Chuang in [15], [17] have been discussed, with exciton contributions modelled as broadened Lorentzian functions, and a continuum of states contribution integrated over all states. For normal incidence applications, Beer's law is not appropriate for comparison as the interaction length is defined as the thickness of the element. In QWs this is undefined due to tunneling, and does not scale directly. Conversely, Blood has shown that the absorption is proportional to the number of transitions between subbands below a given photon energy[16], [43] rather than the well thickness. Therefore, Chuang and Blood's methodologies have been combined to include exciton and continuum of states contributions while removing the dependence on the thickness of the element.

The quantum confined Stark effect observed through variations in the absorption spectra for QWs and QDs has been discussed. The Stark effect can be exploited to create efficient optical intensity modulators. Finally, through population inversion, represented by the positions of the quasi-Fermi levels under forward bias, the gain coefficient can be calculated for QWs and QDs, to evaluate the efficacy for amplification as a laser cavity.

Chapter 3 State-of-the-art

Preceding the research, development, and design of novel semiconductor heterostructure devices, it is prudent to provide a benchmark of similar, current technology. Through this process it is possible to explain and highlight key performance metrics, and devise a specification for project outcomes. This may be reflected upon in later chapters and used as a method of comparison between different device structures.

This chapter will be divided into two main sections, the first considering modulating retroreflector (MRR) devices for free space optical (FSO) communication. The second concerns wave-guided quantum dot modulators and lasers for application to photonic integrated circuits (PICs). MRRs can be applied to real-time free space transmission of high definition (HD) video, for search & rescue, and defense applications. In addition, there are multiple applications in the aerospace industry, with Airbus concerned with the potential of offloading high volumes of telemetry data from inflight aircraft. The metrics for this section will be subsequently tabulated. The quantum dot devices will be discussed primarily from the perspective of research, with operational principles outlined and notable demonstrations listed.

3.1 Modulation schemes

For signal modulation, not only in FSO, there are a number of techniques that can be employed to encode data onto a signal which are important for the context of this chapter. Generally, modulation can be initially separated by whether the carrier signal is uninterrupted or discretized which can be referred to as a continuous-wave (CW) or analog carrier, and a pulsed or digital carrier, respectively. A CW interrogating laser is considered, so only analog carrier techniques were considered here. A diagram of modulation scheme categories is shown in fig. 3.1.

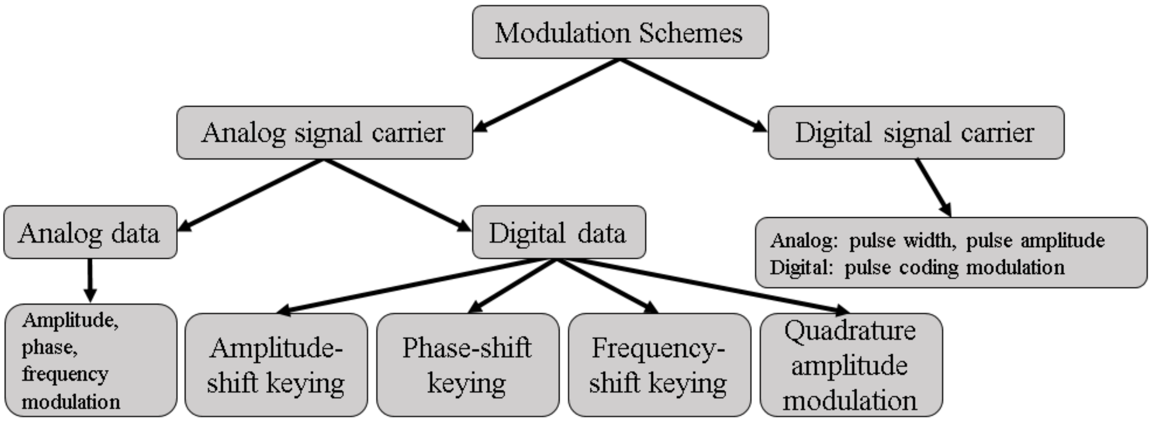

Fig. 3.1 – Modulation schemes categorized by carrier-type and then data-type.

The method of encoding data is then split between analog and digital depending on whether a continuous or binary form of data is required. Continuous methods can be associated with analog radio transmission such as amplitude, frequency, and phase modulation and will not be considered further for this application. Digital data modulation techniques, amplitude, frequency, or phase shift keying (ASK, FSK, or PSK) and quadrature amplitude modulation (QAM) may then be considered. In each form of shift keying, binary data corresponds to a value of amplitude, frequency, or phase, with the number of levels depending on the sensitivity of detection available.

For example, ASK may utilize only 0% and 100% amplitudes corresponding to 0 and 1 bits respectively. This is known as on-off-keying (OOK), the simplest form of ASK, and widely used in MRR for FSO[3], [57]. Nevertheless, more complex schemes can be used, such as 0%, 25%, 75%, and 100% amplitude, corresponding to 00, 01, 10, and 11. Through this method it is possible to transfer a higher number of bits per second. FSK uses the same methodology, though is less commonly used for these applications. This is similar to PSK, where the phase is used to transmit data in comparison to a reference. Here, in-phase signals represent a 0, and anti-phase signals a 1. Though this can also be employed in quadrature to transmit at higher data rates, as shown in fig. 3.2.

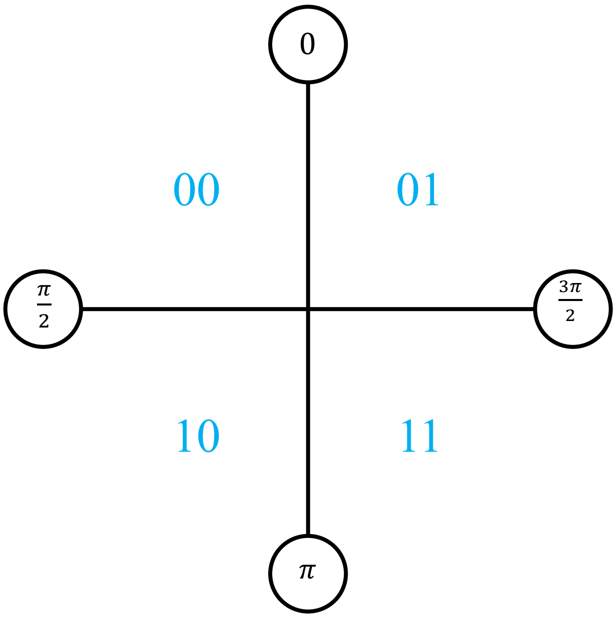

Fig. 3.2 – Quadrature phase-shift keying (QPSK) modulation scheme phase diagram.

Finally, QAM considers two signals out of phase by 90º which can be amplitude modulated, combined to be transmitted through a single channel, then de-modulated and compared once received. As the waves are orthogonal they do not interact. This operates similarly to combined ASK and PSK, with 00, 01, 10, and 11 giving the simplest constellation of transmitted signals. If further levels of amplitude and phase are used exceptionally high data rates can be achieved. This has been demonstrated using 1024-QAM, transmitting

60Gbps[58]. However, the focus of this chapter will be predominantly on the simpler OOK and PSK modulation techniques with the proposed devices.

3.2 Modulating retroreflectors

FSO communication has been discussed in chapter 1, though to reiterate, due to technological miniaturization in wireless mobile platforms, MRRs have been proposed. MRRs can remove size, weight, and power consumption (SWaP), in addition to complexity, whilst maintaining high speed optical data download, creating asymmetric data links. When MRRs are intercepted by a continuous wave laser beam they are able to reflect directly back at the incidence angle and modulate the beam, while imprinting data. Henceforth, eliminating the need for an onboard laser with associated temperature control, constant current source, and full tracking system, allowing for stricter SWaP constraints. MRRs are composed of two components, modulators and retroreflectors, which will be considered separately. Many of the modulators described below provide limited bandwidths, making them unsuitable for HD video transmission (approximately 1Mbps for HD and >35Mbps for 4K).

3.2.2 Retroreflector classification

There are two methods of retroreflection, classified by corner-cube and cat's-eye retroreflectors, as shown in fig. 3.3. The corner-cube, composed of three square perpendicular mirrors, offers high extinction ratios (ERs) through three reflections and six light passes, when modulators are mounted on each mirror[59] opposed to only one in front of the aperture[60].

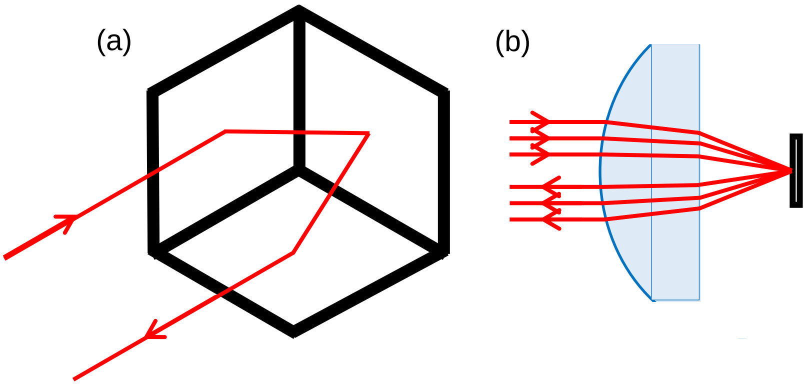

Fig. 3.3 – Diagrams of (a) corner-cube retroreflector and (b) cat's-eye retroreflector.

Corner-cubes are significantly less complex to fabricate and may offer a wide field of view[61] if the mirrors are large enough. However this configuration has fundamental limitations on modulation speed[62], primarily due to either the size or driving power required to provide significant modulation to the device. Modulation can be achieved by using a liquid crystal (LC) cell in front of the retroreflector offering data rates up to 10Kbps, or using a controllable micro-electromechanical systems (MEMS) mirror in one of the faces of the retroreflector with data rates up to 1Mbps.

The cat's-eye retroreflector design can vary more, though these are primarily a set of focusing optics and a single mirror[60]. Generally, cat's-eyes offer considerably higher speed due to a significant reduction in the modulator size, which is beneficial for capacitive devices. Size reduction is also beneficial for lowering power consumption. Speed can be further increased by pixelating modulators, though this can require greater fabrication intricacy and potentially reduce the final device yield. However, the reduction in modulator size and the use of lenses can reduce the field of view and increase spherical aberrations[60] resulting in increased divergence and a higher bit-error rate in the returned signal.

3.2.3 Electroabsorption modulators

Electroabsorption modulators (EAMs) are semiconductor devices which modulate the intensity of light transmitting through them. This occurs due to the Franz-Keldysh effect in bulk semiconductors and the quantum confined Stark effect (QCSE) in quantum wells (QWs) – see chapter 2. The QCSE for a QW is demonstrated in fig. 3.4.

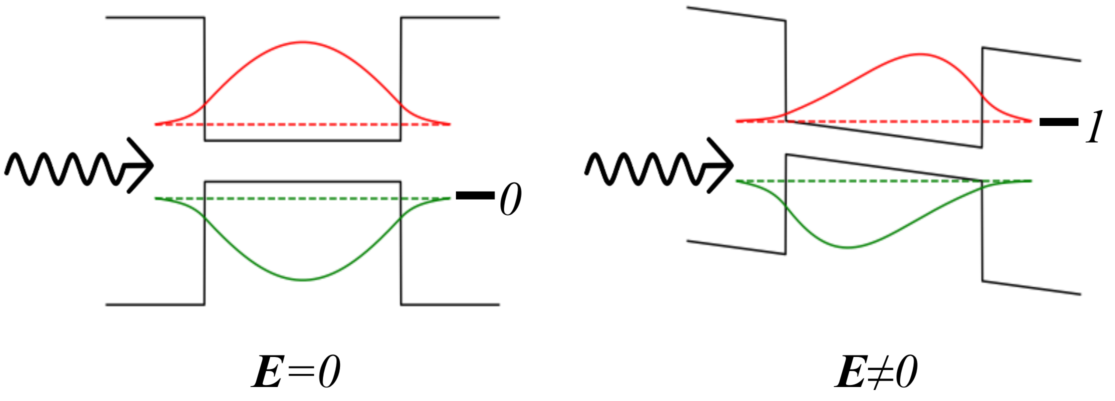

Fig. 3.4 – Diagram of quantum well conduction valence band with zero and non-zero applied electric field.

Through the application of an electric field, the absorption spectrum of the semiconductor is altered, either increasing or decreasing the amount of light absorbed at a given wavelength. This results in regimes of high and low transmission which can be used for ASK modulation of an incident optical signal. Fig. 3.4 shows potential conditions for modulation in a QW, with high overlap between the hole and electron wavefunctions and therefore high absorption with zero applied electric field, transmitting a low or 0 signal. Under a non-zero applied electric field, wavefunction overlap is reduced, so absorption is low, transmitting a high or 1 signal. This is accompanied by a reduction in the transition energy between these states, redshifting the absorption spectra, further increasing the effect.

EAMs have been used extensively as MRRs previously, notably from the United States Naval Research Laboratory (NRL). Additionally, the Research Institutes of Sweden (RISE), some of which has been in collaboration with Oxford University and Airbus UK. In these examples multiple quantum well (MQW) structures have been used as the absorption medium of the intrinsic layer, sandwiched between p-type and n-type doped cladding layers, forming a PIN diode mounted behind a cat's-eye optical setup. The PIN diode allows for an electric field to be easily applied to the QWs. Benefits including low operating voltages[63], especially when compared to bulk semiconductors, and high speed outdoor data links of up to 500Mbps[4] have made MQW EAMs extensively utilized for MRRs. MQW EAMs are capacitance limited devices dictated by a time constant, RC, though resistance is often not the limiting factor. Devices have potential data rates up to Gbps[64].

Early publications propose either GaAs-AlGaAs[65]–[67] or InGaAs-AlGaAs[60], [68] based MQWs grown on GaAs substrates. Coupled InGaAs-InAlAs MQWs grown on InP substrates are now commonly used[69], [70]. This material system better targets the eye-safe wavelength of 1550nm, now an industry standard for FSO data links. These coupled quantum wells (CQWs) have demonstrated a stronger QCSE when compared to single QW alternatives[71], which is proposed to be an effect of closely spaced energy levels and the presence of previously forbidden transitions caused by asymmetry in the band structure under reverse bias[72]. The development of these CQW EAMs is evident through the suggested references, with the most recent publications highlighting the current technological capabilities.

Comparison of these MRRs is not straightforward, due to variation in the operation conditions. The dimensions of the repeating periods within the intrinsic region are consistent between both NRL and RISE devices, with two 6.4nm InGaAs QWs separated by a 1.5nm InAlAs coupling layer, and 4.8nm InAlAs barriers[57], [73]. In each structure QWs and barriers have compositions $In_{0.58}GaAs$ and $In_{0.43}AlAs$ respectively. It should be noted that the composition reported in [73] is a misprint, with the InGaAs and InAlAs compositions reversed, this has been confirmed through private communication with RISE.

The significant difference between these modulators is the number of repeating periods of QWs. NRL's device contains 160 periods resulting in an ER of 7.5dB under a 10V reverse bias, though an ER of 15dB and insertion loss (IL) of 12dB was achieved by packaging two modulators together and driving them simultaneously at 1MHz[6]. Note, this publication studied quantum key distribution encryption using MRR technology, which requires a high ER, and the authors were not concerned with reductions in IL or enhancements in modulation speed. NRL have reported data rates of 45[16] and 70Mbps[15] in previous works using an 80 period device of the same structure in outdoor and indoor demonstrations respectively. In [57] an ER of 1.7dB with ILs up to 4.5dB, depending on the wavelength in the C-band, under a 6V reverse bias was reported. This highlights the need for improved ER and reduced IL at 1550nm.

RISE use 80 QW periods, yielding an ER of 6dB under a 12V bias, with an IL of 3dB[73] though this has not been replicated. RISE, Oxford University and Airbus UK report data rates of up to 500Mbps with an outdoor link distance of 560m with the same structure[4], though this was achieved with an ER of <1dB and an IL of 11.5dB under a 6V bias.

There is some uncertainty in these values due to the variety of operating conditions, including the link distance and whether the link is kept under laboratory conditions or exposed to atmospheric turbulence. NRL provide single-pass values in [57], whereas RISE, Oxford University and Airbus UK report the double-pass values for ER and IL.

3.2.4 Micro-electromechanical systems modulators

Micro-electromechanical systems (MEMS) can be used to modulate light signals by changing the geometry of a material by exposing it to an electromotive force. For retroreflective FSO data links MEMS mirrors are appropriate as they provide a large reflective surface and have been successfully incorporated into corner-cube retroreflector configurations[74], [75] resulting in a wide field of view and no required consideration of optical alignment or aberrations. MEMS mirrors are planar materials capable of efficiently reflecting light, which deform under bias, scattering the incident light rather than returning a coherent signal. A diagram of a MEMS mirror is shown in fig. 3.5.

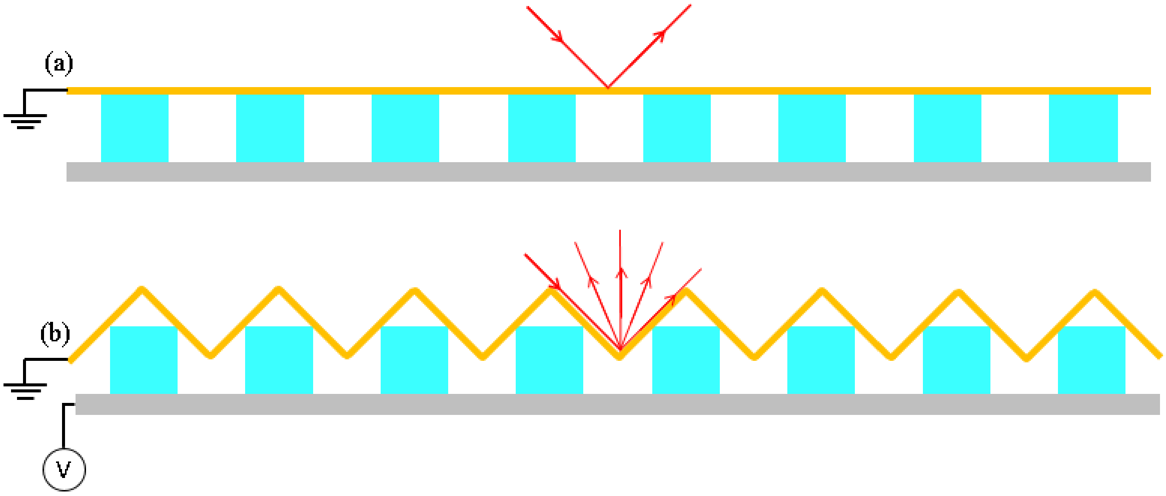

Fig. 3.5 – Diagrams of a MEMS mirror (a) in off state with no applied bias, thus acting as a planar surface with high reflectivity, (b) in on state with an electromotive force acting causing a corrugated surface and scattering incident light.

The mirror deformation provides on and off signals to transmit data. Opposed to some alternatives, MEMS mirrors can operate across a wide band of optical wavelengths providing increased versatility[76] for a range of applications.

ERs of up to 10dB have been reported[77] with data rates at 1Mbps demonstrated through a 7.7m water tank[78]. These devices are primarily limited by the range of motion (or stroke) available for deformation of the mirror[79], though it has been shown that viscous air damping between the mirror surface and electrode can also limit performance[80].

Voltages over 50V are commonly used to create a significant electromotive force and to reduce the response times, though devices only requires microwatts of power to maintain the on state[76]. However, the major limitation of these devices is operation only within the KHz range[76], [77], [81], which is insufficient for contemporary data transference requirements.

The MGR6N MEMS Grating Modulator from Thorlabs is an example of a commercially available product, with an ER up to 20dB and an operational frequency range between 0-200kHz, with a field of view of 10º. This was manufactured by Boston Micromachines Corporation, who have dominated the market for MEMS products, particularly modulators. MEMS mirrors clearly offer useful properties for particular applications such as LIDAR or FSO transmission of audio, however, the kHz bandwidth is limiting for uses requiring the transfer of real-time video, especially for proposed search and rescue applications (where live multispectral video transmission could be beneficial).

3.2.5 Electro-optic modulators

Electro-optic (EO) materials exhibit optical property changes under an applied electric field. Commonly this term refers to the changes in the refractive index or birefringence, rather than absorption (as in EAMs) though these are inherently linked. When the refractive index of a material varies linearly under an electric field, this is known as the Pockel's effect. The Kerr effect relates the refractive index change to the square of the electric field requiring exceptionally high field strengths to observe similar effects, thus inappropriate with the SWaP constraints associated with MRR applications.

EO modulators can utilize changes in refractive index or the polarization dependence of the crystals. The latter may be unsuitable for FSO due to the reduction in the returned signal by selecting only a single polarization. Additionally, maintaining a consistent polarization for a moving platform may be challenging. The change in refractive index causes changes in the phase of light which can be split along two crystals under the same or differing electric fields, and recombined to constructively or destructively interfere, resulting in highs and lows in the intensity of the transmitted signal. This method is similar to that of the EAMs modulating intensity, and using the OOK modulation scheme. Devices can be operated for longitudinal or transverse propagation as shown in fig. 3.6. A single crystal can be used to transmit data simply by the phase of the light which allows for PSK based modulation schemes.

A common EO material is lithium niobate ($LiNbO_3$) which has received attention for phase modulation, an example with a 111Gbps data rate using differential quadrature PSK has been demonstrated[82]. An ER of 25dB and IL of 7.9dB is reported.

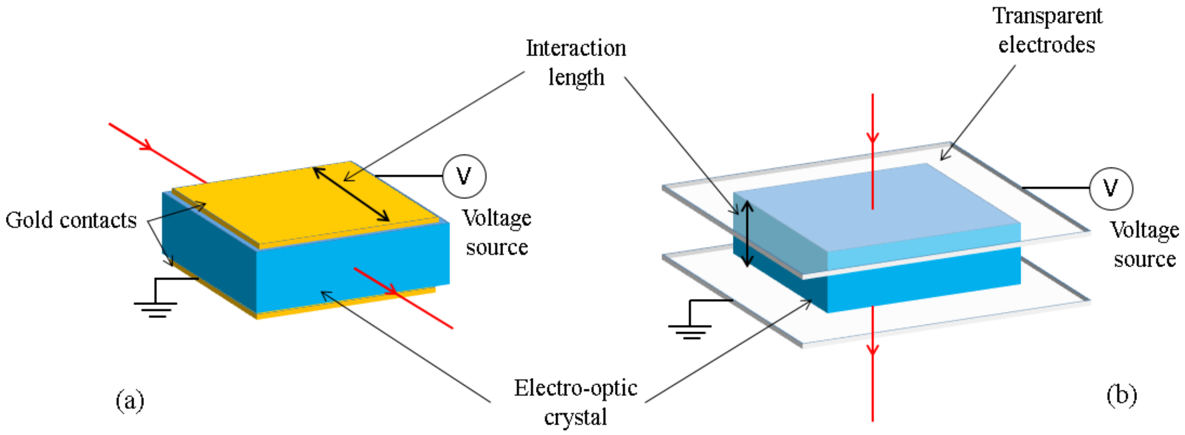

Fig. 3.6 – EO modulator operated for (a) longitudinal and (b) transverse operation.

$LiNbO_3$ EO modulators are prevalent in the fiber optics industry, though these are designed to be longitudinally propagating devices, in which light must be coupled to the width of a fiber. For MRRs this is extremely undesirable due to the challenging optical design required and the large interaction lengths needed to impart suitable levels of modulation. Moreover, there are significant limitations on the device power consumption due to the kilovolt magnitude electric fields necessary to achieve modulation. Alternatives include AlInGaAs-based MQWs demonstrated as a free space transceiver module but with an ER of <1dB[83], which demonstrates one of the limitations to this technology, at normal incidence there is not a significant interaction length to impart enough phase change to function effectively as a MRR in longer range FSO data links.

3.2.5.2 Metal-ferroelectric nanocomposites

A novel approach to EO modulation involves composite nanoparticle-embedded ferroelectric thin films. These consist of a ferroelectric medium, an example being lead zirconate titanate (PZT), embedded with metal nanoparticles, forming a nanocomposite material[84], with the nanoparticles exhibiting tunability of the local surface plasmon resonances[31], allowing for a wide range of operating wavelengths. PZT embedded with TiO_2 coated Ag nanoparticles was first proposed in [85] for application to a MRR for FSO with a calculated ER of 17.5dB for +/-2V bias. Though these are only predictions, very high performance is suggested. The limiting factor for this technology, similarly to EAMs is the frequency dependence on capacitance of the device, in addition to possible piezoelectric induced volume changes which may cause deformation of the nanoparticles[86]. These studies have only considered simulated data[84], [85], [87], with no MRR devices fabricated to this date. Though sample PZT films have been fabricated[88], [89] the techniques for developing modulating retroreflectors still appear to be in their infancy.

3.2.6 Acousto-optic modulators

Acousto-optic modulators (AOMs) operate via the acousto-optic (AO) effect, the changing of the refractive index through mechanical strain[90]. The mechanical strain is applied to an AO material such as crystalline quartz or tellurium dioxide using a piezoelectric transducer driven at radio frequencies. The resulting sound waves create periodic gratings within the crystal dictated by the points of compression and rarefraction of the pressure wave, diffracting incident light into several orders, as shown in fig. 3.7. This technology has seen a lot of development for beam steering applications[91]–[93] rather than for MRRs for FSO.

AOMs for FSO are already commercially available with Brimrose offering a variety of AOMs across a wide spectral range of 200-1600nm, with modulation bandwidths up to 400MHz. The diffraction efficiency varies from around 25-80%, potentially limiting the ER at a 1550nm operating wavelength and with active apertures as small as 0.025mm would require significant capture and focusing of incident light. Besides, the power required for the RF driver can be up to 55W which is beyond reasonable overall power consumption for the MRR, with additional drawbacks similarly to the EO modulators, large interaction lengths required for suitable modulation and difficulties with optical system design.

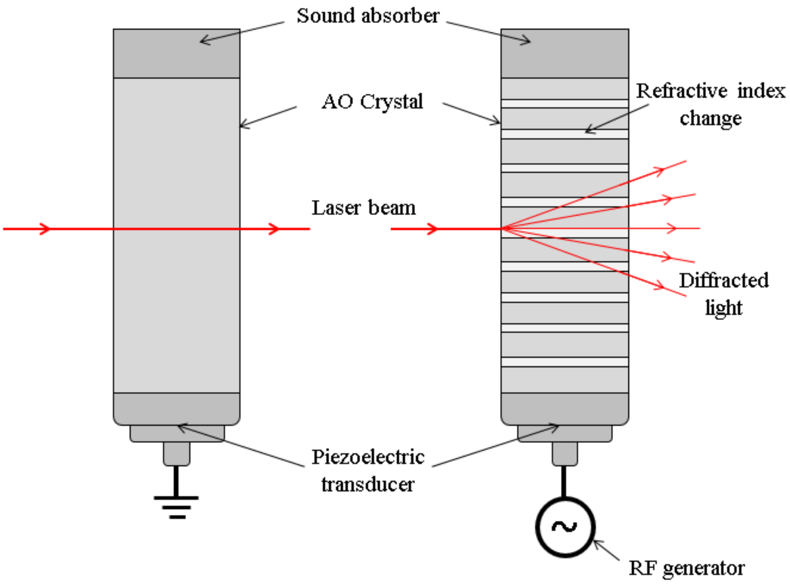

Fig. 3.7 – Diagram of AO effect utilized as a modulator. AO crystal appears transparent until a RF signal applied to a piezoelectric transducer creates pressure waves across the crystal diffracting an incident beam.

3.2.7 Liquid crystal modulators

Liquid crystals (LCs) are a state of matter between the liquid and solid state phase, which exhibit crystalline order in molecular orientation, but not in position. LC molecules are anisotropic in dimension and can exhibit birefringence, as such acting like EO modulators.

By applying an electric field to liquid crystals it is possible to change the orientation of the molecules[94]. The birefringence exhibited in LCs will rotate the polarization of the incident light by altering the phase of the incident light, however, when the electric field is applied this rotation does not occur due to the variation in the orientation of the molecules. As a result, a modulator can be made by sandwiching a LC first by transparent electrodes, such as indium tin oxide (ITO), and then by a pair of orthogonal polarizers. Under zero applied electric field the LC will rotate the polarization of the incident light so it is accepted by the second polarizer appearing transparent. Under a non-zero applied electric field, this will not occur, and light will be rejected by the second polarizer, as shown in fig. 3.8. This acts as a shutter providing on and off states for modulation.

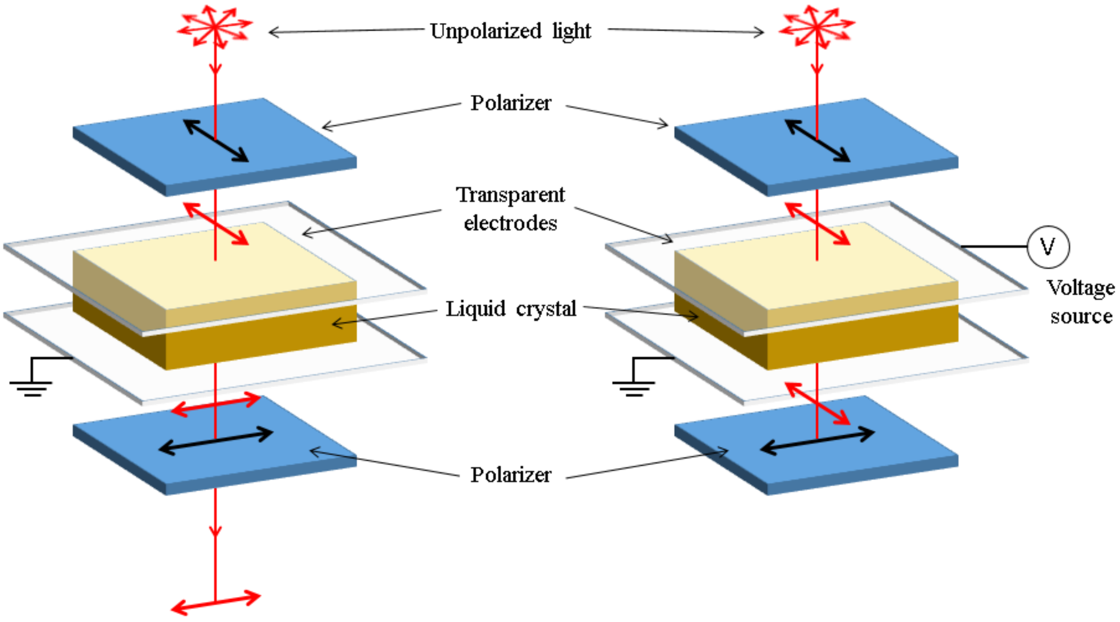

Fig. 3.8 – Diagram of LC-based modulator, utilizing polarization rotation when unbiased. When voltage source is on, an electric field orientates LC molecules preventing polarization rotation acting as a shutter.

As a result it is possible to achieve very high ERs using LCs although this is inversely proportional to switching speed, with only kHz modulation bandwidths available. Thorlabs offer a free space LC modulator with wavelength range 1050-1620nm with close to 100% modulation depth at low modulation bandwidth (e.g. <20Hz) though this reduces significantly over 1kHz. Additionally, the viscosity of the LC is temperature dependent[95] and can have impacts on the switching speed, which is undesirable for outdoor FSO data links.

3.2.8 Comparison

Though there are many options available as potential MRRs for FSO, it is evident that the low modulation speeds achievable in MEMS, and LCs severely limit their efficacy for applications requiring real-time transmission of high-definition or even multi-spectral video.

AOMs offer high speed modulation though the power consumption associated with the RF generators are significantly higher than what would be acceptable for these applications. The EAM and EOM each provide desirable characteristics, with potentially higher ERs and modulation bandwidths available with EO materials. Magneto-optic modulating devices have also been proposed in [96] though no performance metrics have yet been measured for this comparison, and no commercially available MRRs examples have been found.

Table 3.1 – Comparison of modulator technologies for MRR FSO applications.

	Technique-scheme	**Data rate / Mbps**	**ER / dB**	**IL /dB**	**FoM**	**Voltage / V**
RISE/Airbus UK[4]	EAM-OOK	500	0.97-6	3-11.5	0.1-2	12
NRL[5], [6], [57]	EAM-OOK	<75	<15	<12	1.25	10
Boston Micro-machines	MEMS-OOK	<0.2	20	<4%	-	<200
$LiNbO_3$[82]	EOM-QPSK	111Gbps	>25	7.9	3.2	5
Brimrose	AOM-ASK	<400	30	3	-	-
Thorlabs	LC-OOK	<0.001	>2	1-2	-	2.5

A table of appropriate metrics is shown in table 3.1, note these have been tabulated to best represent the capabilities possible from certain technologies. Many metrics are coupled (e.g. bandwidth, ER, and IL), with a variety of different demonstration conditions, such as data link distance, therefore this is only an overview. The figure of merit (FoM) is defined as the ratio between ER and IL.

Unfortunately the power consumption required in conventional EO devices, as intended for fiber applications is higher than allowable within strict SWaP constraints for small UAVs. There is also a risk removing too much light by using polarization selection techniques, increasing the effective IL, for a mobile platform operating at significant link distances. $LiNbO_3$, among other materials is well-established in fiber applications, though it would not be practical to attempt to couple light into a fiber sized opening over FSO on a moving platform. At normal incidence a very thick layer of EO material with additional power consumption would be required to generate large enough electric fields to induce a significant phase change and impart modulation. To achieve a reasonable field of view, the area of the EO material would also need to be large, increasing electric field generation requirements further.

Metal-ferroelectric nanocomposites appear to have many benefits not only for MRRs but for low SWaP beam steering applications, however, the practicality of manufacturing and fabricating a final device from this technology is unclear due to it being in its early stages. Additionally, there are issues due to the piezoelectric effect in these materials which causes deformation to the nanoparticles and the optical properties of the device, degrading return signals, which would require characterization to quantify. EAMs remain interesting devices to study for this application as minimal research on the epitaxial design has been considered, with the literature demonstrating this through almost identical structures used by major contributors and little evidence of optimisation. Therefore, it may be possible to raise the current performance limit by determining new optimal materials, compositions, dimensions, and QW period number for a novel EAM device structure.

Therefore, we define a rudimentary specification to surpass a figure of merit of 2 between ER and IL, in addition to maintaining or enhancing the data rate of 500 Mbps for applied voltages of < 12V, with a minimum of 35Mbps for lower applied voltages to cope with 4K video transmission. This corresponds to the top end of the range given from Airbus UK and RISE.

3.3 Quantum dots & photonic integrated circuits

The importance of photonic integration was discussed in chapter 1, particularly focusing on the benefits achievable through leveraging the silicon manufacturing industry to produce large scale and inexpensive substrates[97].

Quantum dots offer benefits over quantum wells as monolithically integrated laser sources with lower threshold current densities[46], reduced temperature sensitivity[98], and a greater tolerance to threading dislocation defects incurred during epitaxy of particular semiconductors on silicon substrates owing to non-planar geometries.

A dot layer shown by atomic force microscopy (AFM) and threading dislocations propagating through an epi-structure from transmission electron microscope (TEM) are shown in fig. 3.9 (images provided by UCL). The TEM image shows a cross section of threading dislocations, a dislocation density is used to define the extent of these over a single device or wafer. III-V compound semiconductors can provide high electron mobilities and direct band gaps at telecommunication wavelengths[99], with InAs/InGaAs quantum dots demonstrating high performance for 1.3μm laser emission.

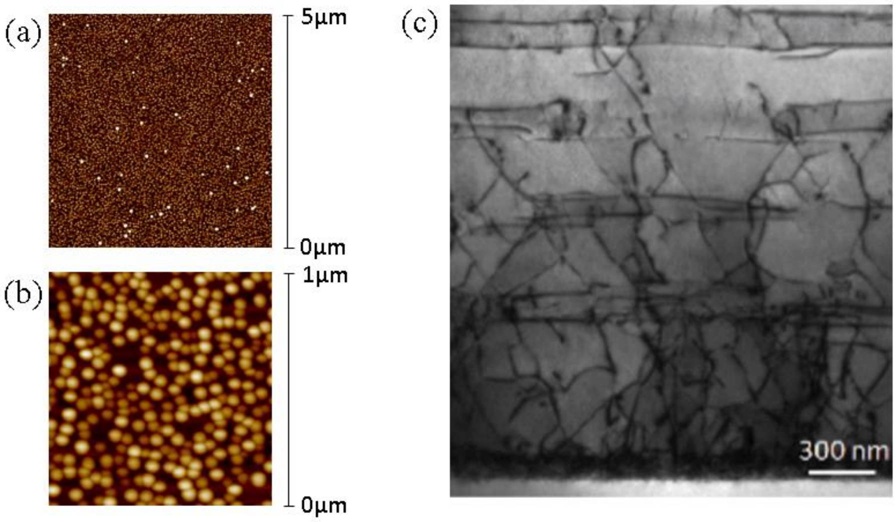

Fig. 3.9 – AFM image of quantum dots with (a) 5μm scale and (b) 1μm scale. (c) TEM image of threading dislocations propagating through heterostructures from misfit formation during epitaxy of III-V alloys on silicon substrate. Images from UCL.

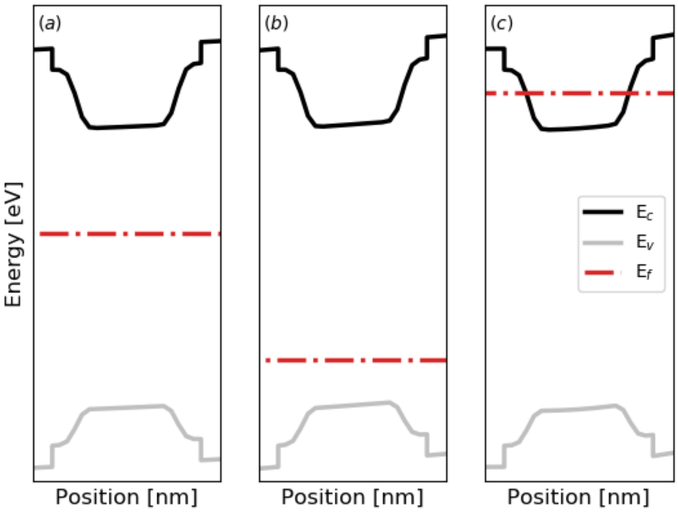

Fig. 3.10 – Schema for conduction and valence band energies E_c and E_v, and Fermi level E_f, for (a) undoped, (b) p-modulation doped, and (c) n-direct doped quantum dots under zero bias.

III-V compound semiconductors suffer from large differences between electron and hole effective masses[100] resulting in imbalanced carrier occupation between conduction and valence bands[101]. This causes asymmetric movement of the quasi-Fermi levels leading to poor ground state operation in lasers[7]. Example dot band structures are shown in fig. 3.10. These are calculated by equating the effective density of states to the measured density of dots in a layer multiplied by a factor of two for spin degeneracy, following the mass tensor ellipsoid theory in section 2.1 and shown in fig. 2.3.

Although this may be corrected for in quantum wells through the inclusion of either compressive or tensile strained layers (depending on the alloy) in self-assembled quantum dots the strain profile is an integral part of the Stranski-Krastanov growth mode[7] and cannot be manipulated as a design parameter.

One solution is p-type modulation doping: growing a narrow layer of p-type dopant within the barrier region of the waveguide core proximally to the quantum dot layer. This provides a reservoir of acceptors, which are used to populate the highest valence band states[47], correcting the asymmetry, as shown in fig. 3.10. An additional, more contemporary technique uses n-type direct doping: introducing n-type impurities directly into the quantum dots during their formation. Data has showed preferential incorporation during the assembly step of the growth process[102], with reported improvements in the linewidth enhancement factor and predictions of increased electron confinement and differential gain[103]. A schematic diagram, demonstrating the movement in the Fermi level, is shown in fig 3.10. With p-type modulation doping, the quasi-Fermi levels are lowered towards the valence band, due to state filling from the reservoir of holes. In fig. 3.10 the Fermi level is calculated to be raised though further analysis is required to understand the occupation characteristics of this doping strategy. Benefits of n-type direct doping are attributed to increases in conductivity and electron confinement.

3.3.2 P-type modulation doping

P-type modulation doping has been examined in InAs/InGaAs quantum dot lasers both theoretically and experimentally, demonstrating temperature insensitive threshold current densities, increased modal and differential gain, and improved ground state operation[8], [47], [104]. Yet, there have been observations of saturation in these enhancements above given levels of p-type modulation doping concentration, with the dominant mechanism behind this the subject of dispute. Saturation has been attributed to increased carrier scattering rates and nonradiative recombination mechanisms[11], with Kim and Chuang emphasizing particular enhancements in Auger recombination rates[47]. Increased free carrier absorption was suggested as a possible mechanism in [105], and significant reductions in the electron population in the conduction band as a result of increased potential barriers between subsequent quantum dot layers was highlighted in [101]. Optimisation of the doping concentration and position remains challenging, with difficulties associated in decoupling effects of p-type modulation doping from an assortment of variations during epitaxy, including dot size distributions[106], interdiffusion between dots and the surrounding material[107], as well as carrier induced index changes[108]. It has also been suggested that it is difficult to control the precise number of doped carriers in the modulation doping technique[102].

The QCSE, principally responsible for the operation of EAMs, has been well characterized in undoped InAs/InGaAs quantum dots, with Stark shifts of around 20meV and data rates of 2.5Gbps demonstrated[109]. However, to our best knowledge only [13] (with more recently updated results in [110]) has conducted a comparative study investigating the differences in the QCSE between undoped and p-modulation doped InAs/InGaAs quantum dots. In this work, measurements of absorption under reverse biased voltage swings between 0 and 10V, across a temperature range between 25 °C and 100 °C, were compared for nominally identical epitaxial structures, except for inclusion of p-type modulation doping in one of the samples. A maximum ER of 12dBmm^{-1} was measured in the undoped structure, yet the p-type modulation doped structure displayed a figure of merit of up to three times that of the undoped. An understanding of the QCSE in p-type modulation doped QDs will surely be essential for future monolithic integration of EAMs with laser diodes. As use of PICs proliferates it will be essential to combine external modulators with optimized laser sources[111].

3.3.3 N-type direct doping

The technique of directly doping quantum dots with n-type impurities is less established than p-type modulation doping, though several reports have demonstrated promising characteristics for laser performance. The n-type dopant (Si has commonly been used for InAs/InGaAs quantum dots) can be incorporated during several phases of the quantum dot growth, nucleation, assembly, or the self-limiting step. Inoue et al. reported preferential incorporation during the assembly step, with the electrical conductivity measured using conductive atomic force microscopy[102]. This study also reports an enhancement of almost five times the low temperature photoluminescence (PL) intensity in direct doped samples, and a reduction in quenching of this intensity with temperature, remaining double that of the undoped when measured at room temperature.

In [10] similar observations in PL intensity and stability at room temperature were reported, in addition to indications of reduced nonradiative recombination due to the excess of electrons neutralizing electron trap recombination centers. Results from [112] suggest benefits of Si-doped InAs/GaAs quantum dots for application to solar cells concluding that the impurities assist strain relaxation and reduce possible nonradiative centers in addition to enhancing PL intensity. Others have observed benefits which apply directly to laser diodes[12], [103] and with Wang et al. describing improvements to the output power and the spectral width of InAs/GaAs quantum dot based superluminescent diodes[113]. Importantly, improvements in differential gain and the linewidth enhancement factor have been demonstrated in [52], with Inoue et al. suggesting precise incorporation of impurities is possible through the direct doping technique[102]. To our best knowledge, no examples of measured or modelled n-type direct doped quantum dot EAMs have been reported, though correspondingly to p-modulation doping, it is an important consideration for monolithic integration of high performance externally modulated lasers.

3.3.4 Quantum dot laser diodes

Fully comparing the plethora of quantum dot laser diodes currently within the remits of research and development would be unnecessary for the scope of this thesis, however, outlining relevant performance metrics, and providing examples of work at the cutting edge is valuable. P-type modulation doped and n-type direct doped quantum dot lasers remain novel and have not yet reached commercial viability. There are 1310nm emitting InAs/GaAs quantum dot-based lasers available offering up to 2.5Gbps modulation capabilities from QDLaser, and another designed for continuous wave operation from Innolume GmbH.

Gain, or the amplification of light is a useful metric for the material capabilities as a lasing cavity medium. Gain may be initially calculated as the material gain (described in chapter 2), the amplification exhibited from a material with a given set of parameters and a particular population inversion.

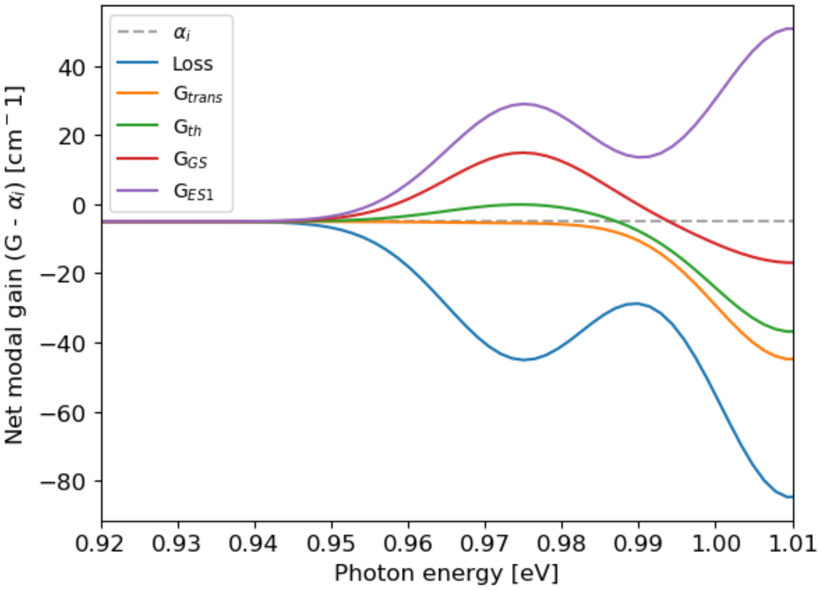

Fig. 3.11 – Net modal gain for a variety of conditions. Absorption or loss shown under zero bias, transparency gain G_{trans}, equal to α_i, threshold gain G_{th} equal to 0 cm^{-1}, and ground state and first excited state dominated gain.

However, in optically confining structures (wave-guides) only a fraction of the optical mode overlaps with this gain medium and so the optical confinement factor must be included to provide the modal gain. Modal gain is significantly more relevant to real devices. It must be noted that the level of gain is also dependent on the cavity length, the number of quantum dot layers, and the internal optical loss α_i, so these should be kept consistent in comparisons. The contributions to the net amount of gain generated under different conditions is demonstrated in fig. 3.11.

Additionally, quantum dot lasers are especially desirable due to the increased confinement and so fully quantized energy states (see chapter 2) providing specific output wavelengths. However, it is important to note that the specific wavelength is reliant on the ground state mode of operation which can change to the excited state quickly in undoped lasers[49]. Maximov et al. demonstrated a ground state modal gain > 40 cm^{-1} for a ten-layer structure with an enhanced optical confinement factor through high Al concentration cladding layers[114]. In [115] a modal gain of > 50 cm^{-1} was measured with a nine-layer structure, and a modal gain of > 40 cm^{-1} for a seven-layer structure was reported in [116], though these showed poorer internal optical loss than in [114].

The differential gain is also a valuable parameter for comparison of laser and amplifier structures. This describes the rate of change of modal gain with increasing injection current above transparency, in units of cm^{-1}/mA. High differential gain can often signify reductions in the linewidth enhancement factor (depending on refractive index changes[47]) which can lead to low frequency chirp and signify an increased modulation bandwidth. In [47] Kim and Chuang have demonstrated enhancements in differential gain in p-modulation doped InAs/InGaAs quantum dot lasers through experimental measurements and a theoretical model. In [52] Qiu et al. found similar results for n-direct doped InAs/InGaAs, both operating around 1.3μm. Moreover, both studies suggested increased differential gain in doped quantum dots lead to improvements in the linewidth enhancement factor (LEF), the ratio of the difference between the real and imaginary parts of the refractive index, and the corresponding carrier density[117], which is often related through the differential gain and refractive index changes. The LEF can help determine the chirp, changes in the central output wavelength, in a pulsed signal. Reductions in the chirp are important for high speed modulation.

Another important metric for quantifying laser performance is the threshold current density. This value describes the current flowing through a given cross section (length × width of stripe contact[118]) to achieve a quasi-Fermi level separation producing threshold gain (shown in fig. 3.11), or when gain matches the optical losses of a cavity[16], given in units of A/cm^2. This is a more meaningful metric compared with the operating current, which is dependent on the device geometry and fabrication[118], though to be a sufficient description of a device, a knowledge of the structure and dimension is required[16]. Therefore it must be noted that threshold current I^{th}, and threshold current density J^{th}, can broadly be related by the cavity length L_c, and the contact width w, as shown in eq. 3.1.

$$J^{th} = \frac{I^{th}}{L_c w} \tag{3.1}$$

Though a greater number of QD layers can be used to increase total gain this requires increased carrier injection to populate the excited state, therefore some key examples showing low threshold current densities utilize only a single layer of dots. In [119] an ultra-low threshold current density of 32.5 A/cm^2 is reported from continuous wave operation of a single layer of InAs quantum dots, with a 9.2mm cavity length and 20µm stripe width with uncoated facets. A threshold current density of 10.4 A/cm^2 was measured by Deppe et al. in [120] for a single InAs quantum dot layer in a 1.6 cm-long cavity with a broad area device with 120µm wide stripe, with a very low internal loss of 0.25cm^{-1}. Multi-layer structures providing increased modal gain will encounter higher threshold current densities. Nevertheless, Zhang et al. [11] showed a reduced threshold current densities in five-layer InAs/InGaAs quantum dot structures compared with equivalent unintentionally doped structures. Whereas, Smowton et al.[7] demonstrated that this may be compromised by increases in nonradiative recombination associated with p-modulation doping.

3.3.5 Quantum dot electroabsorption modulators

The QCSE responsible for operation in EAMs has been well characterised in undoped InAs/InGaAs QDs, demonstrating maximum Stark shifts (shown in fig. 3.12) and data rates of 20meV and 2.5 Gbps respectively[109]. A 3dB bandwidth of 3.3GHz with a voltage swing of 0 to 6V, was demonstrated by Lin et al.[121].

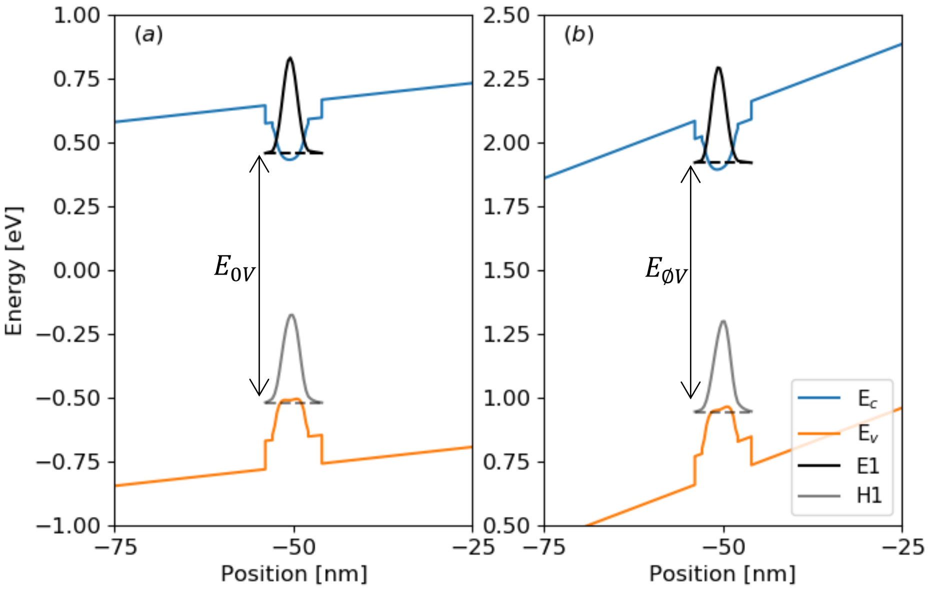

Fig. 3.12 – Quantum dot potential under (a) zero and (b) non-zero bias. Stark shift is calculated from the difference between the zero and non-zero biased transition energies, $E_{0V} - E_{\emptyset V}$*. With* $E1$ *and* $H1$ *the electron and hole ground state energies respectively.*

Malins et al. investigated electroabsorption as well as electrorefraction, observing a Stark shift of 15meV, but with ILs up to 21dB, and 0.001 refractive index change below the bandgap suggesting potential for electro-optic modulators[122]. ERs of 10dB for a voltage swing of 0 to 10V were originally measured by Nqo et al. in [111], with an ER and IL of 13dB and 14.8dB subsequently measured in [123] for 10-layer structures in each study. Finally, Le Boulbar et al. characterised a near constant ER of 4.1dBm^{m-1} between 25 °C and 125 °C[124], suggesting temperature insensitivity across a wide range.

To our best knowledge, only Mahoney et al. has directly compared measurements of the QCSE in undoped and p-modulation doped InAs/InGaAs quantum dot structures [13] (with updated results in [110]). A maximum ER of 12dBmm^{-1} was measured for a voltage swing of 0 to 10V in the undoped structure, yet with the p-doped structure presenting up to three times the figure of merit (ER/IL) across a wide temperature range between 21 °C and 100 °C. This was primarily attributed to carrier blocking reducing the level of depletion of electrons in the conduction band, and ultimately reducing the IL of the devices. Yet, there has not been a study modelling the QCSE in p-modulation doped InAs/InGaAs quantum dots, which will likely provide further insight not only on the characteristics of modulating devices but generally on the material system as a whole.

The QCSE in n-type directly doped InAs/InGaAs quantum dots has not been studied. An understanding of the QCSE in p-modulation doped and n-direct doped QDs will be essential for monolithic integration of high performance EAMs with doped lasers. As the field expands, combining external modulation with optimised laser sources[111], will be critical to PIC development.

3.3.6 Summary

There are potentially major prospects for the study and understanding of both the operation of lasers and modulators with p-type modulation doping or n-type direct doping, and potentially the combined effects of both of these techniques. Due to the novelty and continued dispute over the benefits and trade-offs of these techniques, there is scope for studying how these effects manifest within real and simulated structures providing insight for the application to monolithically integrated devices. Furthermore, the performance metrics highlighted in the previous section will be used as tools for comparison in equivalent structures, maintaining device length, number of quantum dot layers, and considering internal optical losses, rather than defining a distinct specification.

Chapter 4 Surface-normal quantum well electroabsorption modulators

This chapter describes the experimental procedure and results from transmission measurements of state of the art modulating retroreflector (MRR) devices from [2] and [3]. Further analysis outlines the characterization of the extinction ratio (ER), insertion loss (IL), and figure of merit (FoM) as a function of wavelength. Additionally, a transmission experiment is devised at a fixed wavelength of 1550nm across a 20ºC temperature range. Subsequently, variations in ER, IL, and FoM above room temperature at 1550nm are reported. Spectral measurements are then compared to the results of a semi-empirical modelling routine to corroborate methodology outlined in chapter 2. Utilizing these calculations, a novel quantum well (QW) structure is presented with predicted benefits in ER, IL, and FoM. The active region of the final epi-structure is reported with calculated strain compensation layers.

4.1 State of the art devices

The two state of the art electroabsorption modulators (EAMs) described here were developed in a collaboration between Airbus UK, the University of Oxford, and Research Institutes of Sweden (RISE). The epi-structure of the EAMs is shown in fig. 4.1.

Device 1 was designed for UAV to ground communication[2], and device 2 was designed for inter-satellite applications[3]. Molecular beam epitaxy for both device wafers was conducted at IQE, with fabrication and packaging at RISE. Growth and device fabrication by IQE and RISE was completed prior to the electro-optic measurements completed by the candidate in this chapter. Each device had epitaxial designs similar to devices first reported by the United States Naval Research Laboratory (NRL)[57], as shown in fig. 4.1. The active region consisted of 80 repeating periods of coupled 6.4 nm $In_{0.58}GaAs$ quantum wells either side of a narrow 1.5 nm $In_{0.43}AlAs$ coupling layer, and separated by 4.8 nm $In_{0.43}AlAs$ barriers to prevent the formation of mini bands between adjacent periods. Devices 1 and 2 are distinguished by the size of EAM region and defined by individual pixel dimensions.

Devices contained 36 pixels, with 1x1mm and 250x250μm pixels in devices 1 and 2 respectively[2], [3]. This is shown with a scale of ≈10:1 in fig. 4.2. Gold bonding pads and wires are shown in fig. 4.2 with pixels as purple.

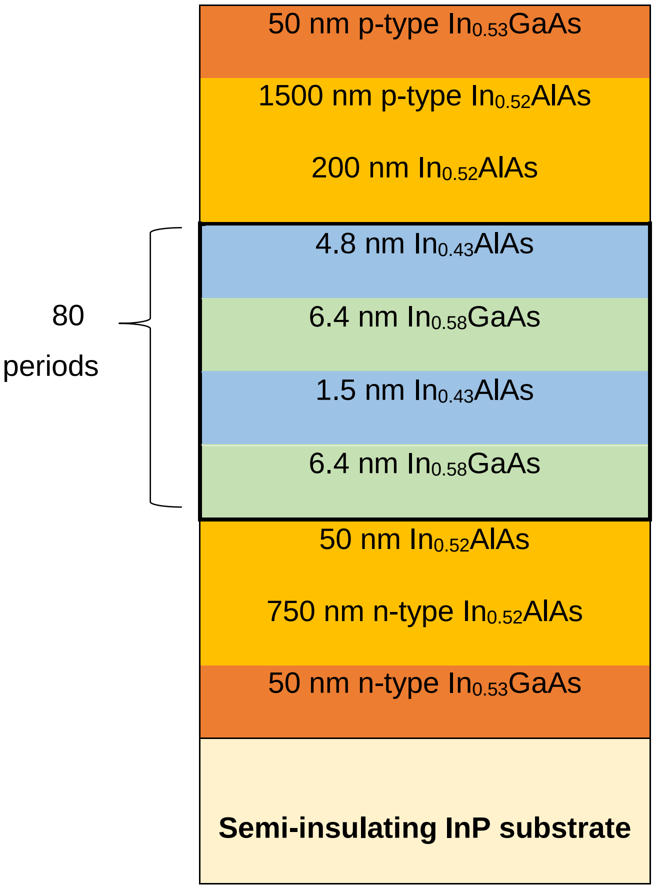

Fig. 4.1 – Schematic diagram of state of the art epi-structure developed by RISE[73] following [57], p and n-type dopant concentrations are 3x10^{18}cm^{-3}.

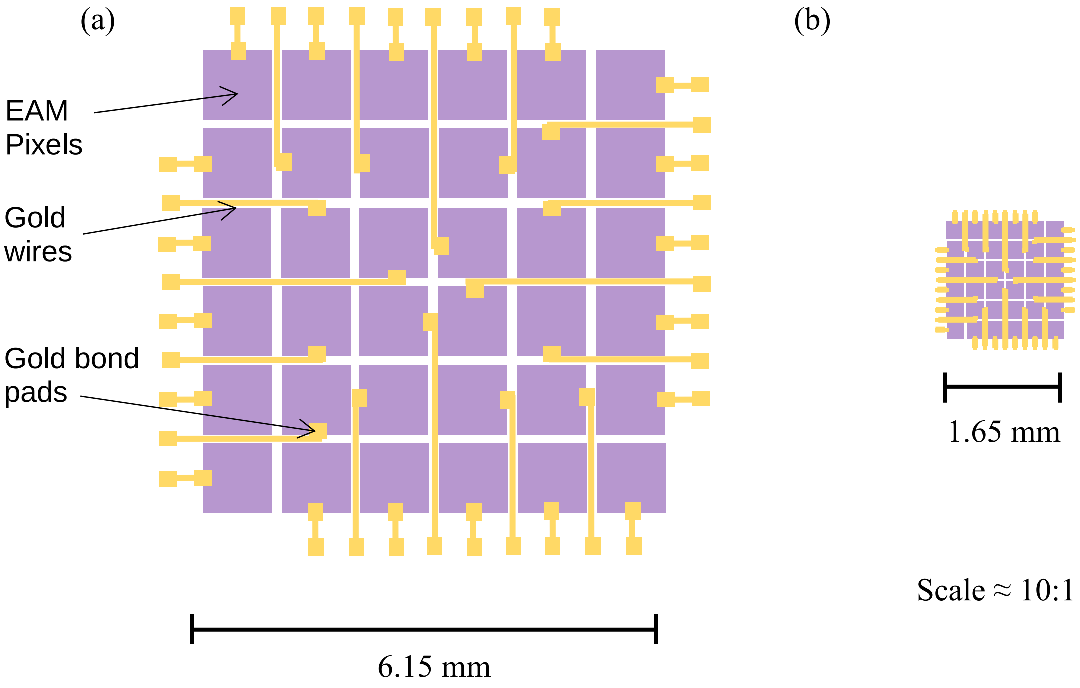

Fig. 4.2 – 10:1 scale schematic diagram of pixel layout, gold bond wire and pad design in (a) device 1, and (b) device 2.

Device 1 required a 10MHz modulation bandwidth and a large field of view (FOV) to maintain communication during rapid movement of the UAV. Device 2 required a 100MHz modulation bandwidth or higher, though a significantly reduced FOV for satellite applications. The maximum modulation bandwidth was determined by the device time constant and primarily the capacitance C, given by eq. 1. With the equally thick depletion region d, the modulation frequency was determined by the pixel area A. ε was the dielectric constant. Device 1 was used here unless otherwise specified, as increased area improved transmission by simplifying optical alignment

$$C = \frac{\varepsilon A}{d} \tag{1}$$

Final devices were prepackaged on PCBs, as shown in fig 4.3, with drivers used for biasing the EAM pixels. External pins were used with insulation-displacement connectors to provide power to drivers, apply an electric field, and monitor approximate temperature. Drivers were connected via gold wires to bonding pads against the p-contact, with the n-contact pad etched through the active region of the EAM, as shown in fig. 4.3. Gold sputtering was used to fabricate the back mirror so devices could be operated as retroreflectors with optics assembled in front of the EAMs.

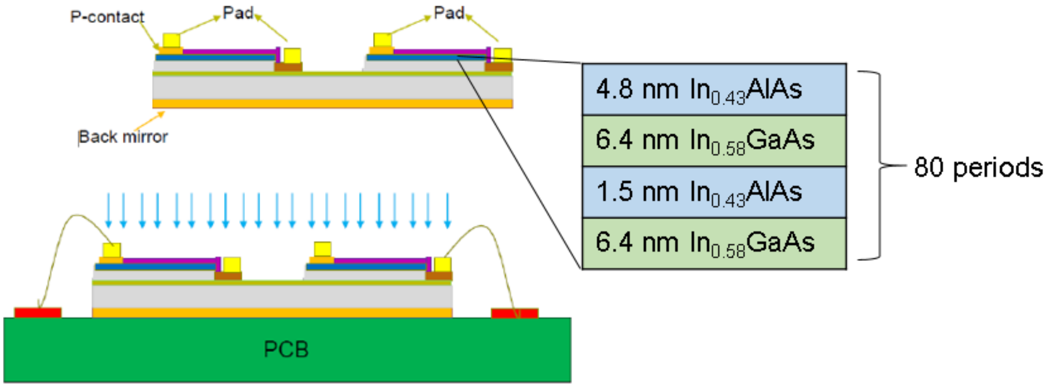

Fig. 4.3 – Schematic diagram of fabricated EAM pixels mounted on PCBs, with the active region highlighted.

Temperature was monitored by a voltage divider from a thermistor mounted proximally to the EAM pixels, with a voltage-temperature relationship shown in fig. 4.4.

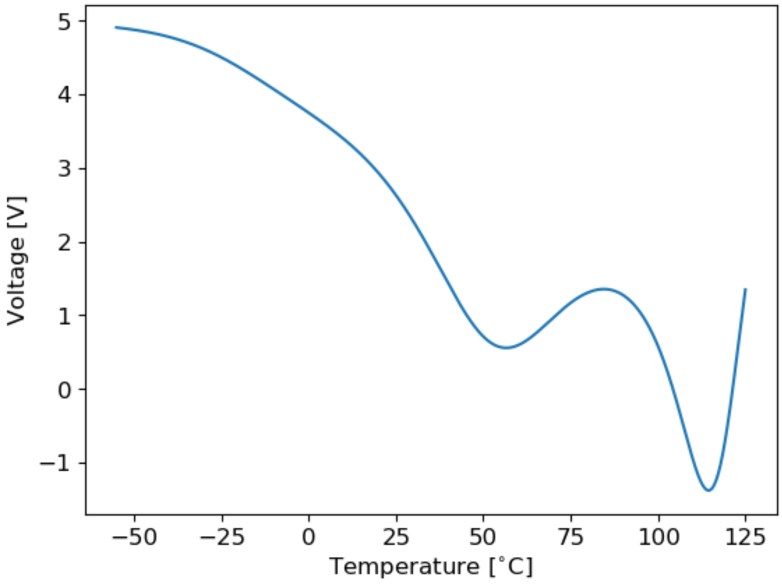

Fig. 4.4 – Output voltage versus temperature of a NTC standard series thermistor from TDK electronics, with 5V bias.

An NTC standard series thermistor from TDK electronics was used, with the temperature relationship provided from the Mouser data sheet. The voltage output from the divider, was then calculated by the ratio in eq. 2. The data in fig. 4.4 was provided by RISE.

$$V_2 = \frac{V_1 R_{fit}}{(R_{fit}+R_{ref})} \tag{2}$$

V_2 was the voltage output from the thermistor voltage divider, V_1 was the potential difference across the voltage divider, which was set to 5V. R_{fit} was the fitted resistance at given temperature and R_{ref} was the reference resistance at 25ºC, equal to 10KΩ. This provided an approximate monitor for heating effects, though, there was likely a temperature gradient between the pixel and thermistor, in addition to some latency in the response.

4.2 Experimental methodology

An experiment to measure transmission as a function of wavelength was used to characterize the IL, ER, and FoM. Secondly, heating effects observed when the EAM was continuously biased, required a separate methodology considering temperature variation. Due to the back mirror incident light was reflected with a double pass through the EAM pixels. Characterization was conducted without cat’s-eye retroreflective optics to separate the beam path and necessary apparatus.

4.2.1 Transmission measurements

Transmission measurements as a function of wavelength were taken at a 90º angle between the incident and transmitted beam due to the back mirror reflection as shown in fig. 4.5. This allowed for full characterization of IL, ER, and FoM. The experimental setup is shown in fig. 4.5.

Devices were illuminated by a M1550L3 31mW broadband infrared LED from Thorlabs, with a 1550nm center wavelength, and thermally stabilized output via a heat sink. The spectral response of the source is shown inset in fig. 4.5. The emission significantly diverged, so light was first captured with a Newport 10 x magnification microscope objective, then collimated with a biconvex spherical lens from Thorlabs with 1000 - 1700nm anti-reflection coating. Collimating lenses are represented with the stabilized source, shown in fig. 4.5.

Two aspheric condenser lenses were used to focus the collimated light onto the EAM pixels then capture and focus the reflected light into a SMA-type multimode optical fiber connected to a spectrum analyser. By focusing the light to a smaller spot size on the pixels, reflections from the gold bonding area surrounding the EAM were significantly minimised.

The device and the optical fiber were mounted on linear XYZ translation stages to optimise light focused on EAM pixels and coupled into the fiber prior to recording data. Device 1 was used due to its larger area, with device 2 demonstrating increased losses from scattering, reflection, and fiber coupling. Biasing pins were connected to a dual channel power supply providing 5V board power, and a variable EAM bias. A second dual channel power supply was used to bias the thermistor voltage divider circuit, with the output shown on a multimeter to observe sufficient cooling time between measurements.

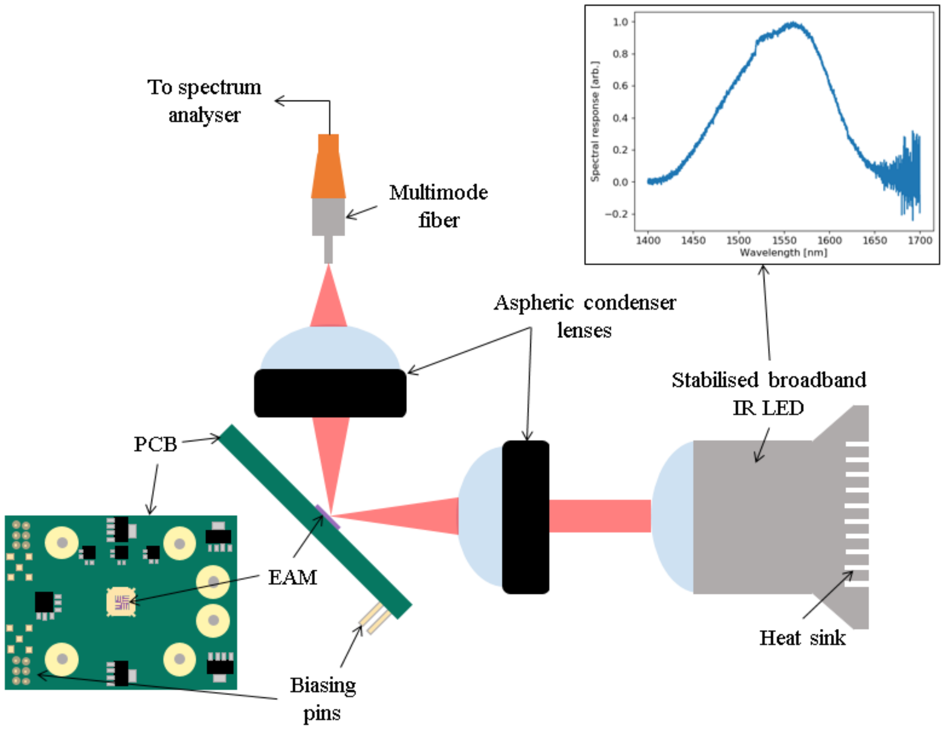

Fig. 4.5 – Schematic diagram of experimental apparatus for measurement of transmission as a function of wavelength.

The optical fiber was connected to a Yokogawa AQ6370 spectrum analyser providing power measurements as a function of wavelength with a resolution of 0.02nm. The spectrum analyser's internal chopper was used during measurements. This minimised stray light from the monochromator within the spectrum analyser, and reduced noise in the measured signal. The sample was replaced by a silver mirror to measure the spectral response of the broadband IR LED across the same optical path length.

Background measurements were taken with the LED covered, prior to measuring the spectral response of the LED which provided the incident power on the sample. The spectral response was recorded before and after recording sample measurements though no significant change in incident power was observed. The mirror was replaced by the sample and the XYZ stage position re-optimised. Transmission measurements with a double pass through the sample were taken with 1V reverse bias increment steps between 0V and 7V. Though 7V was the maximum voltage able to be supplied to the pixels, 6V operating voltage was quoted in the literature[57], [73]. RISE found a voltage drop between the pins and the pixels.

The drivers drew currents of up to 1A, heating the devices. To mitigate this, the thermistor was monitored and allowed to return to its initial temperature between subsequent measurements, with a fan behind the EAM pixels to assist heat dissipation. The full scan time of the spectrum analyser for wavelength range 1400nm to 1700nm was only ≈ 2.5s, and could be reduced by lowering the wavelength resolution to 1nm, though some broadening effects were still expected from the heating of the pixels. Measurements were repeated five times for each reverse bias voltage to calculate errors as the range from the mean. The transmittance T, was then calculated using eq. 3.

$$T = \frac{P_t}{P_i} \tag{3}$$

Where P_t was the transmitted power and P_i the incident power. The absorbance was then calculated using eq. 4.

$$A = -\log_{10}\left(\frac{P_t}{P_i}\right) \tag{4}$$

The IL and ER were then calculated in eq. 5 and 6 in units of decibels.

$$IL = -10\log_{10}(T_{ON}) \tag{5}$$

$$ER = -10\log_{10}\left(\frac{T_{ON}}{T_{OFF}}\right) \tag{6}$$

T_{OFF} was the transmittance when the device was operated for minimum transmission (equating to an OFF in the modulated signal) and T_{ON} was the value of the transmittance when the device was operated for the maximum transmission (equating to an ON in a modulated signal). Finally, the FoM was the ratio between ER and IL.

4.2.2 Temperature measurements

Due to the current drawn by the pixel drivers and noticeable effects of heating, a second experiment was set up to analyse the relationship between temperature, ER, IL, and FoM at 1550nm. The apparatus is shown in fig. 5.6. A LDM1550 compact 1550nm laser diode module from Thorlabs was used to illuminate the pixels. Biconvex lenses were used to focus the laser beam onto the pixels and then the active area of a Thorlabs DET20C biased InGaAs photodetector. Current generated at the photodetector was output to a transimpedance amplifier with 200μA/V sensitivity, then input to the first channel of a Tektronix 2014c oscilloscope. The thermistor output was connected to the second channel of the oscilloscope, with data from both channels synchronously recorded by a data acquisition script written in Python taking the mean of the trace every second. The incident power was measured before and after by replacing the sample with a silver mirror. No significant changes were observed in the output power of the laser diode module during the experiment. The incident power was calculated from the measured voltage at the photodetector (4.95V), with a 500μA/V transimpedance amplifier sensitivity. A responsivity of 0.95 from the photodetector datasheet, resulted in a 2.4mW incident power.

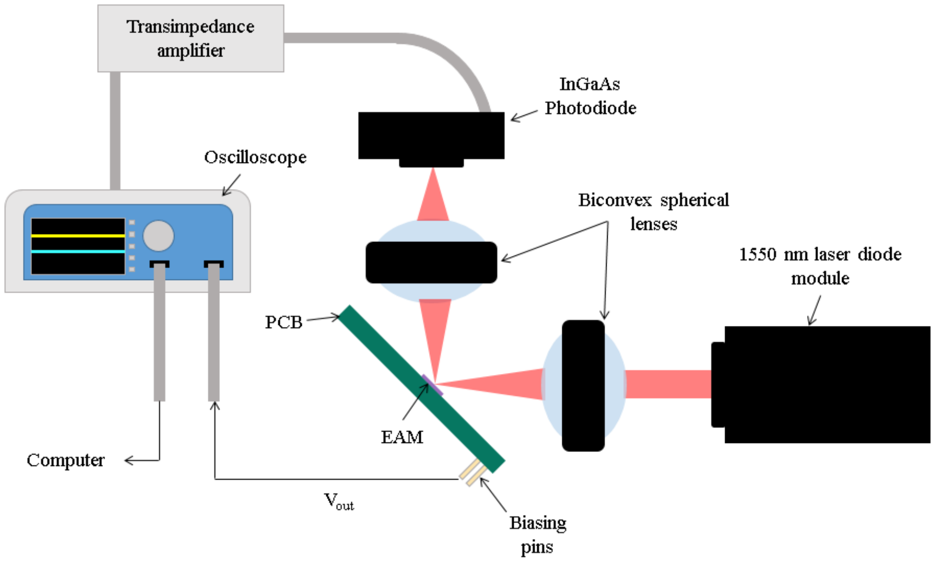

Fig. 4.6 – Schematic diagram of experimental apparatus for measuring transmittance at 1550nm as a function of temperature and reverse bias.

Photodetector voltage and temperature were recorded unbiased prior to each applied reverse bias from 1V to 6V in 1V increments. Measurements were taken as a function of time until the trace stabilized showing when the temperature of the pixels had equalized. Subsequently, the reverse bias was removed and data acquisition continued until photodetector voltage and temperature readings returned to initial values. The procedure was repeated with errors calculated as the standard deviation. Transmission as a function of both reverse bias and temperature was calculated at 1550nm. Further analysis provided the dependence of the ER, IL, and FoM with temperature.

4.3 Experimental results

In this section, measurements of transmission as a function of wavelength and electric field are reported with absorbance, ER, IL, and the FoM, analysed over a spectral range of 1450-1650nm. Subsequently, measurements of transmission at a wavelength of 1550nm, as a function of temperature and electric field are reported, with absorbance, ER, IL, and the FoM calculated between 20-40ºC. Finally, the results and possible implications are discussed.

4.3.1 Transmission results

The measured transmitted power is shown in fig. 4.7 with a 0-7V reverse bias and incident power P_i, of the LED. The units of power are nano-watts due to the low power from the broadband LED and additional losses from free space transmission, reflection, and coupling. This initially produced a poor signal to noise ratio (SNR) particularly at the edges of the LED spectrum as shown in fig. 4.5. This was mitigated by averaging five samples at each wavelength step during the measurement, and subtracting a background measurement. The resulting signals are shown in fig. 4.7 with good SNR up to 1650nm.

Repeated measurements allowed the derivation of errors in the data, taking the mean averages of five measurements, the minima, and the maxima. Finally, a Butterworth filter from the scipy signal processing library was implemented to provide final spectra.

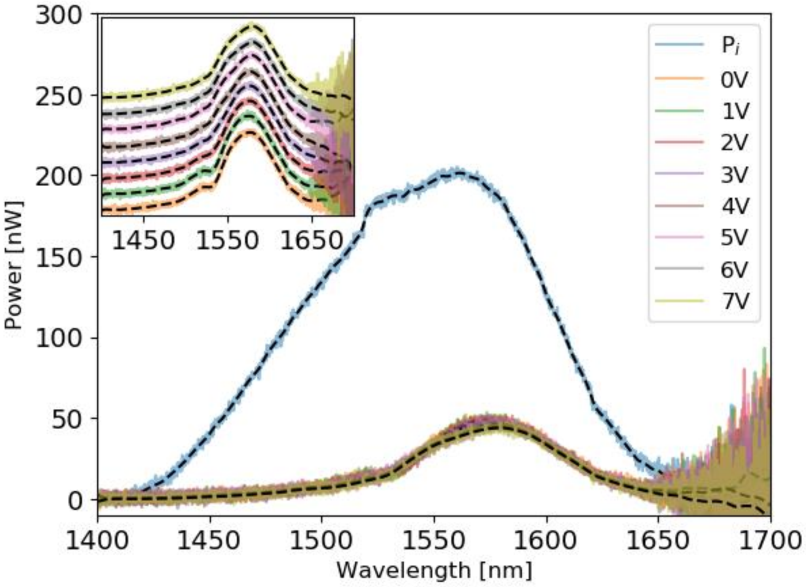

Fig. 4.7 – Incident and transmitted power measured as a function of wavelength. Transmitted power offset in the inset. Filtered signal shown by dashed line.

The inset of fig. 4.7 has been offset for clarity. In fig. 4.7, a shift in the peak transmitted power and alteration to the shape of the spectral response with increased reverse bias, is indicative of the QCSE. This was attributed to a shift in the band edge of the EAM under increasing applied electric field. Reduced definition in the spectra is attributed predominantly to a reduction in the wavefuntion overlap, as well as broadening from the applied electric field and temperature increases during the measurement.

Device 2 was measured following the same methodology, though the SNR was significantly poorer due to the active area of the device. Though the shape of the transmission spectrum was similar, heating occurred significantly faster. This caused more broadening of the spectrum and therefore was not included in this section.

The shift in band edge was also shown when calculated as transmittance in fig. 4.8, with reductions near 1515nm and 1565nm, and increases at 1540nm as the reverse bias voltage was increased. The reductions were attributed to the variation in wavefunction overlap and redshifting of allowed, and previously forbidden transitions in the coupled quantum wells (CQWs) consistent with [71], [72], [125].

Measurements reported in [3], [57], [73] included temperature control, whereas the change in temperature during the measurement here may have caused additional broadening. This effect has negative implications for low SWaP aerospace applications and will be discussed in subsequent sections.

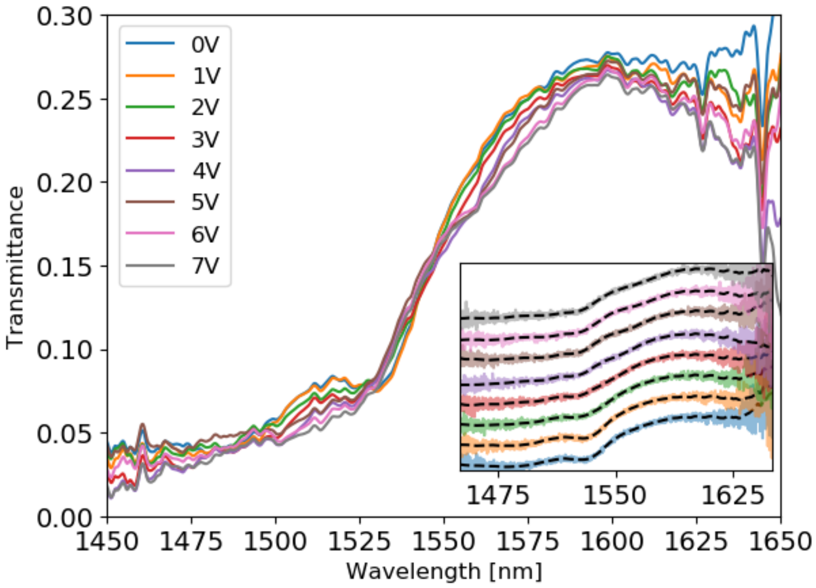

Fig. 4.8 – Filtered transmittance measurements under 0V – 7V reverse bias. Original (shaded) and filtered (dashed) signal is shown offset in the inset.

The absorbance was calculated using eq. 4 and is shown in fig. 4.9. A minimum absorbance of around 0.57 is attributed partly to losses when measuring the EAMs as discussed in section 4.2.1, though it is indicative of high IL. The absorbance was subtracted by the minimum value of 0.57 in fig 4.10 for subsequent comparison with calculated modelled data. This reduced the offset of minimum absorbance to zero, and will be discussed in following sections.

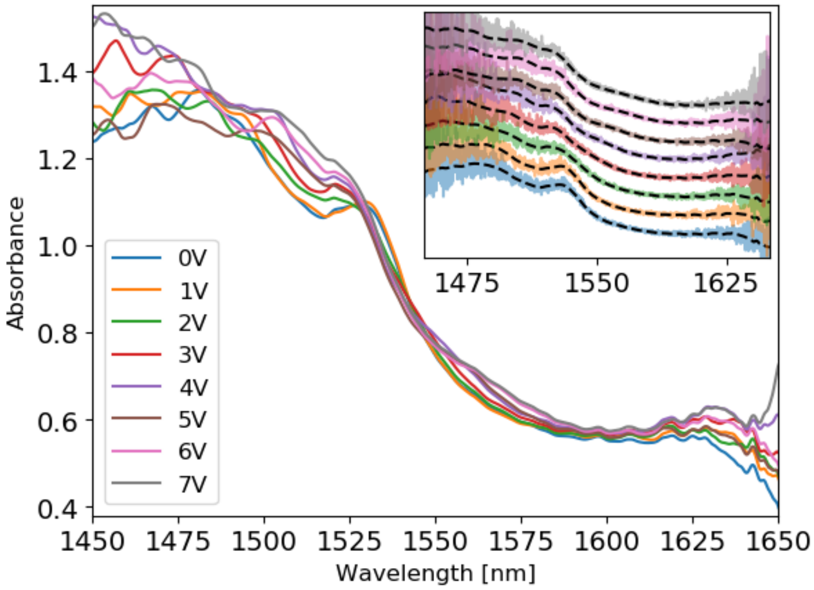

Fig. 4.9 – Filtered absorbance measurements under 0V – 7V reverse bias. Original (shaded) and filtered (dashed) signal shown offset in the inset.

Fig. 4.9 and 4.10 show excitonic resonance peaks for ground state and first excited heavy hole to electron transitions (E1-HH1 and E2-HH2) under zero bias, around 1525nm and 1485nm respectively. There is a redshift and reduction in magnitude of this ground state peak with increasing reverse bias visible in the inset, with an increase in absorbance around 1565nm. A forbidden transition is evident at 1520nm under increasing reverse bias. The redshifting of the E2-HH2 transition and appearance of the E1-HH2 transition increases the magnitude of absorbance at 1520nm. This may give the illusion of excitons encroaching on each other, through redshifting of one and blue shifting of the other. However this is because of a redshift and a strong reduction in overlap of the E1-HH1 transition, which can be seen at 1575nm, accompanied by an increase in the E1-HH2 overlap. The ambient temperature was measured as ≈ 20ºC, with excitons still distinct up to 25ºC, which is suggestive of high exciton binding energies and weak phonon-electron coupling[126].

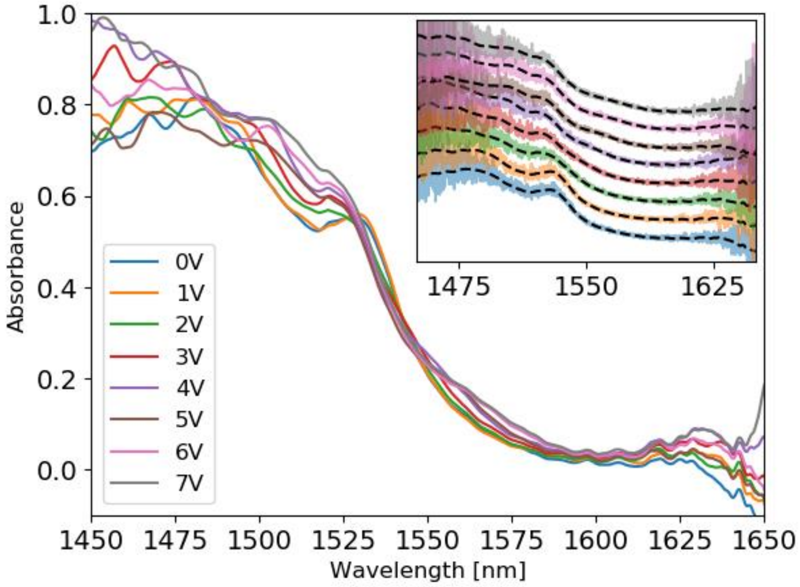

Fig. 4.10 – Offset filtered absorbance measurements of device 1 under 0V – 7V reverse bias. Original (shaded) and filtered (dashed) signal shown offset in the inset.

Fig. 4.11 shows the unbiased absorbance and under 3V and 6V reverse bias with minimum absorbance subtracted. Fig. 4.12 shows the subsequently calculated ERs. A peak ER of 1.45dB is shown at 1508nm in fig 4.12 corresponding to the appearance of the forbidden E1-HH2 transition evident in fig. 4.11. This appears to be the most significant peak, though it occurs at a wavelength with significantly higher absorbance and thus IL. There is a second peak of 0.57dB at 1532nm, and third lower peak of 0.51dB at 1565nm, shown in fig. 4.12.

The second and third peaks may be lowered due to additional broadening from temperature increases during the measurement. The second and third peaks are limited by the precise movement of the bound states and reliant on a narrow region of the absorbance spectrum shown in fig. 4.11. Whereas, the peak at 1508nm, occurs across a broader region of the spectrum. Quintana et al. reported a contrast ratio of 1.25:1 (≈0.97dB) occurring at 1540nm whilst employing temperature control[127], which may correspond to the redshifted peak of 0.51dB at 1565nm.

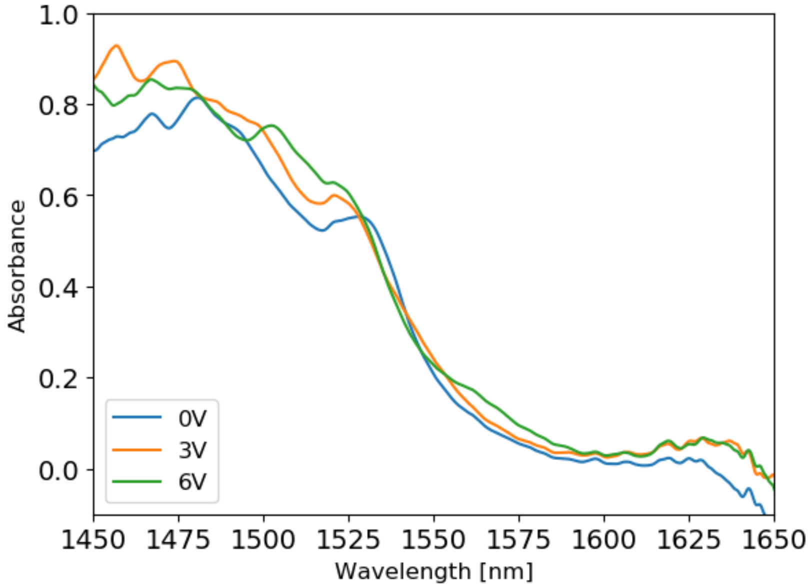

Fig. 4.11 – Offset absorbance measured under 0V, 3V, and 6V reverse bias.

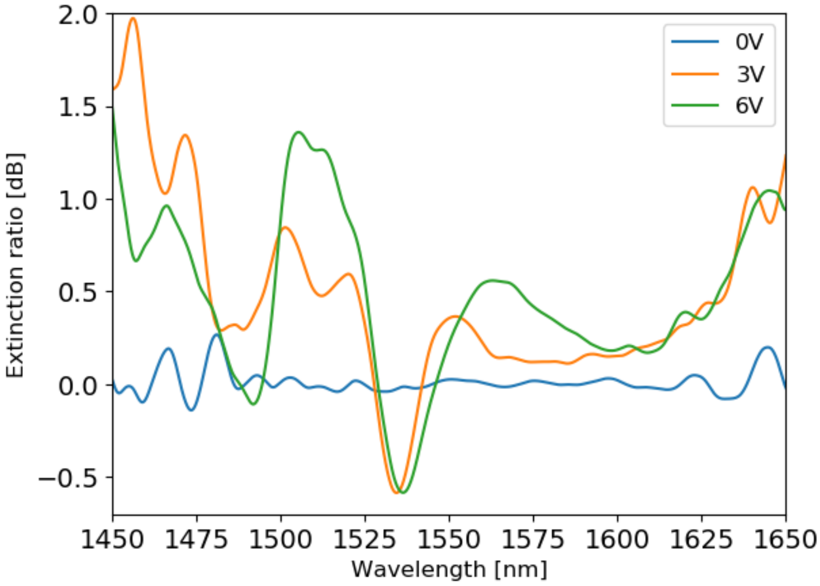

Fig. 4.12 – Extinction ratio under 0V, 3V, and 6V reverse bias.

The IL, calculated from data shown in fig. 4.9, was 7.34dB at 1550nm. An IL of 9.17dB corresponded to the 0.57dB ER peak at 1532nm. At 1532nm, a FoM of 0.062 was calculated. This is comparable to the FoM reported in [127], with ER of 0.97dB and IL of 11.5dB, with a calculated FoM of 0.082 obtained at 1540nm under a 6V reverse bias. This reduction in the FoM is attributed to broadening from increased temperature during the measurement and may also be indicative of a voltage drop between the drivers and pixels giving a reduction in the applied electric field.

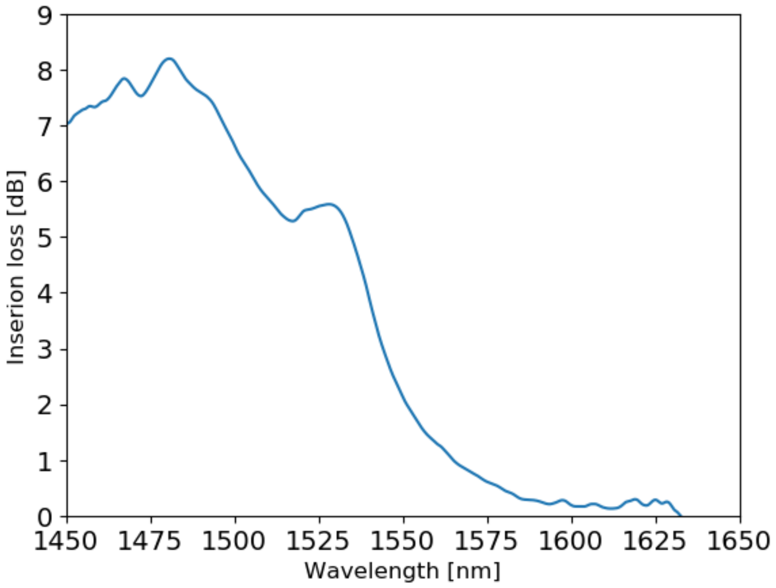

Fig. 4.13 – Normalized IL from 0V absorbance measurement.

The IL, with minimum equated to zero, is shown in fig. 4.13, with a value of 2.1dB at 1550nm. This adjusted spectrum was used to calculate the FoM, for the purpose of subsequent comparison with model results. The FoM was calculated under 3V and 6V reverse bias, shown in fig. 4.14. Under 6V reverse bias peaks of 0.2 and 0.16 were observed at 1510nm and 1535nm respectively. An additional peak in the FoM of 0.18 is shown at 1565nm. Nonetheless, these results highlight the importance of heat dissipation for these devices, which may be impractical as stricter SWaP requirements for the payload are employed.

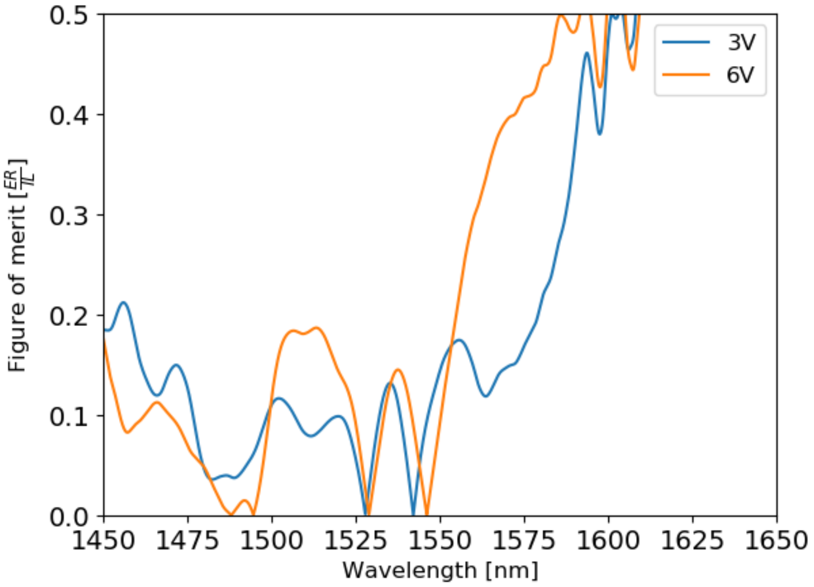

Fig. 4.14 – FoM under 3V and 6V reverse bias.

4.3.2 Temperature Results

Measurements of transmittance as a function of temperature and reverse bias voltage at a single wavelength of 1550nm were taken following the methodology outlined in section 4.2.2. A maximum temperature increase of 15ºC was observed. As in [127], consideration of the impact of temperature was necessary for aerospace applications with -100ºC to 100 ºC temperature ranges.

The voltage outputs of the thermistor and the photodetector were recorded simultaneously, though we only report the temperature here, as shown in fig. 4.15, with the voltage referring to the photodetector response. The voltage response from the photodetector is shown in fig. 4.16 with the data offset for clarity.

For each measurement, the EAM was initially unbiased for around 10 seconds from time = 0 in fig 4.15 and 4.16, to establish initial conditions. After time = 10s a reverse bias was applied and the current drawn by the drivers heated the EAM. The current drawn under each reverse bias is shown in table. 4.1, and indicated the magnitude of the heating. This is shown in fig. 4.15 by the rate of temperature increase for each measurement.

Table 4.1 – Current drawn by pixel drivers under applied reverse bias voltages.

Reverse bias voltage / V	**Driver current / A**
1	0.00
2	0.13
3	0.67
4	0.80
5	0.88
6	0.97

Fig 4.15 shows the increase in temperature as current is drawn by the drivers. With comparison to fig. 4.16, the voltage response from the photodetector was monitored across a temperature range under each reverse bias at 1550nm.

The reverse bias was removed when the temperature appeared to stabilize. This removed the current supply and the EAM was allowed to cool to the initial temperature. Therefore, for each measurement an equal temperature range both under reverse bias and unbiased was recorded.

Measurements were taken for both devices with similar trends in the outcomes, though results from device 2 are presented here, as the smaller pixel size had a more significant response to the temperature change.

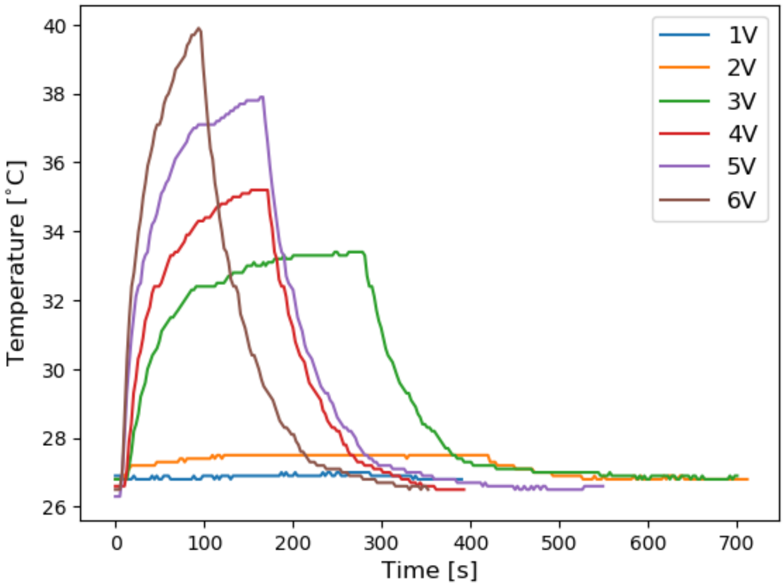

Fig. 4.15 – Thermistor equivalent temperature versus time elapsed, with bias removed at peak in temperature.

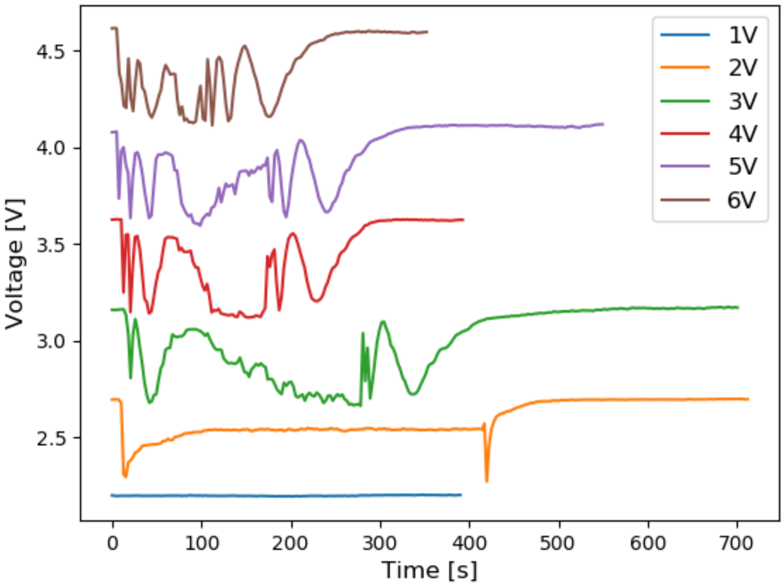

Fig. 4.16 – Photodetector voltage for each applied reverse bias offset from 1V.

The photodetector voltage response in fig. 4.16 showed differing relationships between measurements while the reverse bias was applied. This difference was attributed to the temperature effects as well as differences in the QCSE due to the magnitude of the electric field. There were clear correlations during the final part of the measurement, once the bias was removed, with all measurements experiencing only heating effects over different temperature ranges. Under a 1V reverse bias effects were negligible with no current drawn and very little electric field applied across the EAM.

The unbiased and biased parts of the photodetector voltage response in fig. 4.16 were decoupled and compared as a function of temperature, shown in fig. 4.17 and 4.18 respectively. As mentioned in section 4.2.2 errors were calculated from the standard deviation of repeated measurements, and spline functions were used to fit the data to assist with interpolation. Points are shown in red if not within error of the spline function. Fig 4.17 shows consistency between the unbiased measurements, with a maximum temperature of 39.8ºC when under 6V reverse bias. 6V data was used in further analysis providing the greatest temperature range, and the optimum mode of operation suggested by RISE. There was an ambient temperature of 26.4ºC during these measurements.

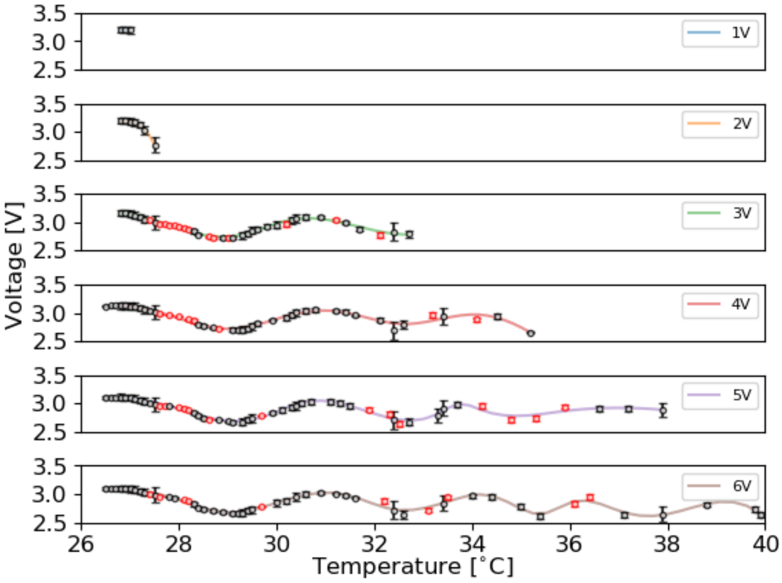

Fig. 4.17 – Photodetector voltage response as a function of temperature under 0V reverse bias with splines fitted for interpolation. Labels refer to reverse voltage applied during measurement.

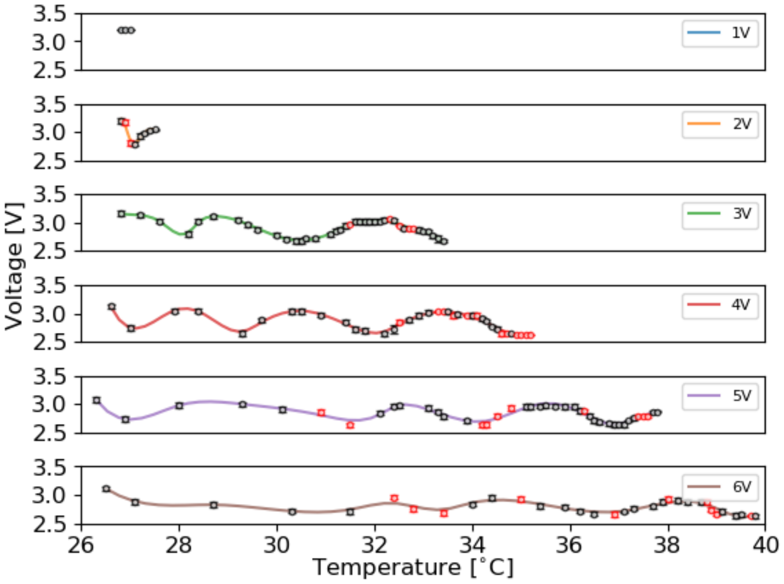

Fig. 4.18 – Photodetector voltage for transmitted signal versus temperature under each applied reverse bias (before reverse bias was removed), with splines fitted for interpolation.

The changes observed in fig. 4.17 are attributed to a reduction in the band gap, increased homogeneous broadening, and a reduction in the exciton binding energy associated only with temperature changes. Fig. 4.18 showed the photodetector voltage response as a function of temperature and reverse bias. The data in Fig. 4.18 show evidence of the same temperature changes in addition to varying strengths of the QCSE, dependent on the magnitude of the applied reverse bias. This showed variation between each reverse bias due to temperature and electric field induced effects as reported in [126], [128], [129].

The oscillatory behavior was attributed to band gap reduction, increased homogeneous broadening, and a reduction in the exciton binding energy in addition to Stark effects, including the appearance of forbidden transitions. These caused increases and decreases in the absorbance of the EAM at 1550nm, depending on the position and magnitudes of the relevant excitons. The absorbance (shown in fig. 4.19) was calculated using eq. 4, with the incident power of the laser measured by replacing the EAM with a mirror. Unbiased absorbance and under a 6V reverse bias was calculated as a function of temperature in fig. 4.19.

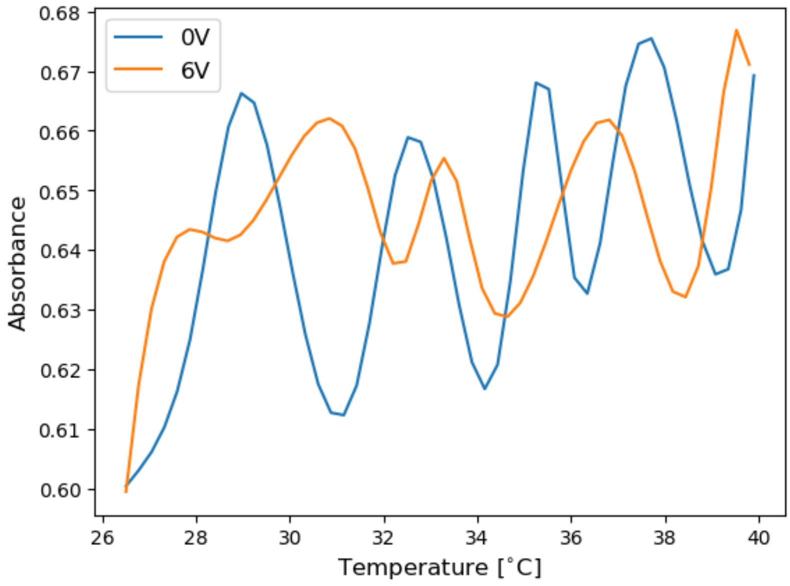

Fig. 4.19 – Absorbance as a function of temperature under 0V and 6V reverse bias.

An overall increase in absorbance was observed in fig. 4.19, with similar oscillatory behaviour to the photodetector voltage response in fig. 4.17 and 4.18. This upward trend is attributed to shrinking of the band gap, redshifting the absorption edge and generally increasing absorption.

The ER between 6V and unbiased absorbance, as a function of temperature is shown in fig. 4.20, calculated using eq. 6. Over < 2ºC at the thermistor, the ER may be reduced to zero, making the EAM totally ineffectual. The reduced ER occurs at points where the 6V biased and 0V unbiased absorbance data intersect in fig. 4.19.

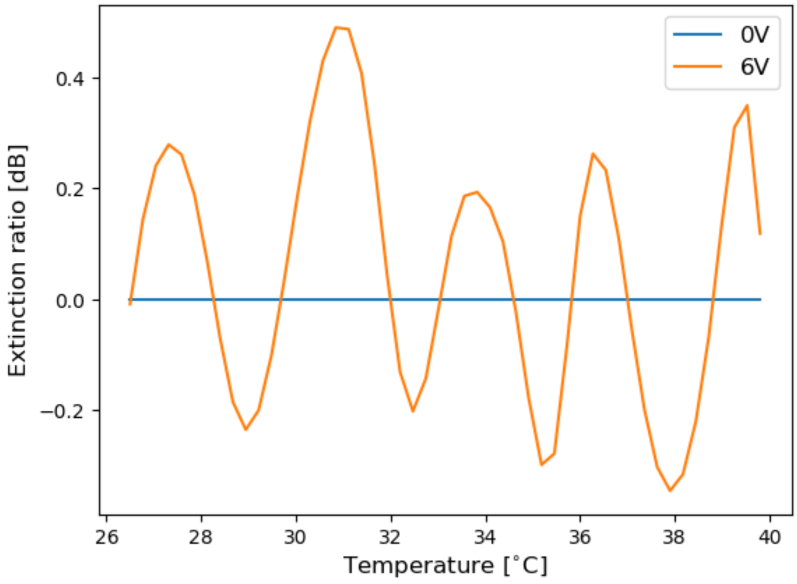

Fig. 4.20 – Extinction ratio as a function of temperature under 0V and 6V reverse bias.

At these intersections, for a given temperature, the QCSE may cause no difference in 6V biased and 0V unbiased absorbance at 1550nm. The ER at 31ºC is nearly double that measured in fig. 4.12.

The IL is shown in fig. 4.21. The IL tends to increase with temperature which is indicative of band gap reduction and increased broadening, following the absorbance in fig. 4.19. The fluctuations in IL, which can vary by 0.65dB over only a 2ºC temperature change, can be attributed to the shift in exciton resonance, caused by both reduction of the band gap and the exciton binding energy.

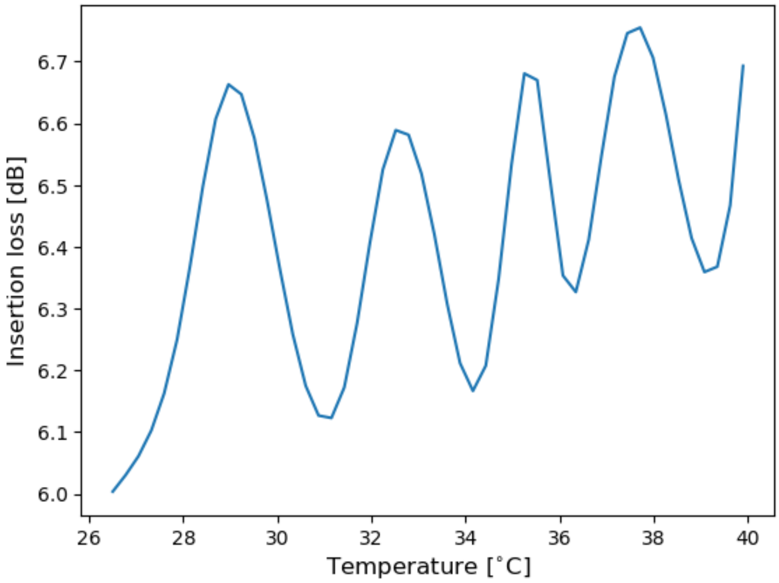

Fig. 4.21 – Insertion loss as a function of temperature under 0V reverse bias.

The FoM is shown in fig. 4.22. The FoM is dependent on the highly fluctuating IL and ER. There is a peak in FoM occurring at 31ºC, where the high ER and low IL coincide. There is consistent oscillatory behavior in the FoM, with an increased number of minima resulting from intersections in the unbiased and 6V reverse biased absorbance spectra, and the fluctuating ER and IL.

Under reverse bias, the temperature effects are accompanied by the QCSE, with a similar increasing trend, but additional shifts due to electrostatic effects. This is due to the electric field deformation on the band structure leading to redshifted symmetric transitions, and the appearance of antisymmetric, forbidden transitions. Intersections between biased and unbiased absorption at 1550nm reduce the ER to zero making the EAM ineffectual.

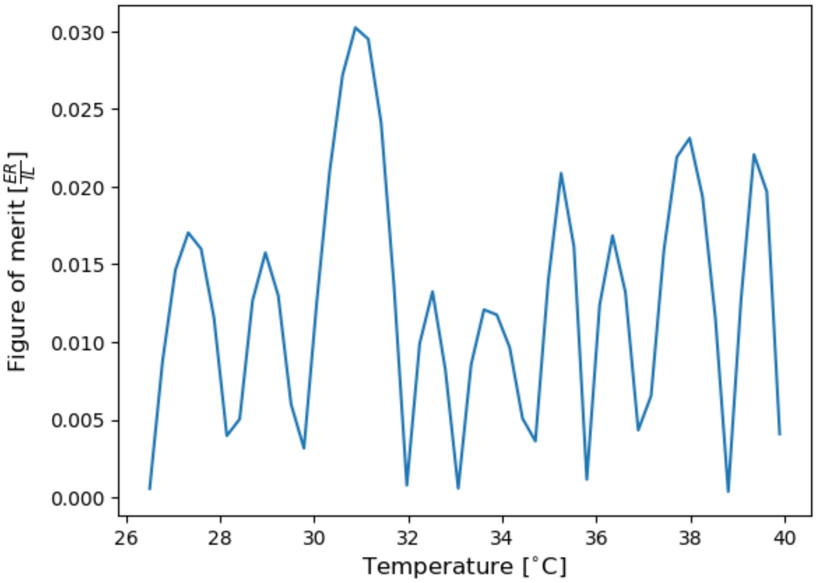

Fig. 4.22 – Figure of merit as a function of temperature under a 6V reverse bias swing.

Though this appears to occur over a 15ºC temperature range, the large variation in IL and ER signify a much greater temperature variation, with a peak ER temperature shift of 0.7nm/ºC measured in [127]. This may be caused by poor thermal contact between the thermistor and the EAM. Nevertheless, for aerospace applications, a temperature range of -100ºC to 100ºC is desirable, though this is unrealistic without external temperature control, unless the reliance on closely spaced and forbidden transitions can be eliminated.

4.4 Computational modelling

To understand the limitations and improvements possible by changing the epi-structure of the state of the art devices in [2], [4], [57], [73], a modelling approach following the theory outlined in chapter 2 was employed. Full device band structure calculations via a Schrödinger-Poisson-current continuity solver from Nextnano, with a single band effective mass approximation were used to calculate band alignment, bound energy levels, and wavefunctions. An externally applied static electric field was simulated through a potential difference across the structure to calculate the QCSE. The absorbance was then calculated using equations outlined by Chuang[15], [17]. Subsequently, the fraction of light absorbed, γ_{well} described by blood[16] was calculated for comparison with proposed alternative epi-structures.

4.4.1 Band structure calculations

Band diagrams were determined for the epi-structure shown in fig. 4.1. Full device band diagrams under 0V and 6V reverse bias are shown in fig. 4.23 and 4.24. The detail of the band diagrams under 0V and 6V for a single CQW period are shown in fig. 4.25 and 4.26, with relevant bound energy states and wavefunctions. Bound energy states and wavefunctions were compared for QWs at the center of the structure, and adjacent to the p-type and n-type cladding respectively, to approximate inhomogeneous broadening caused by variations in the electric field across the structure.

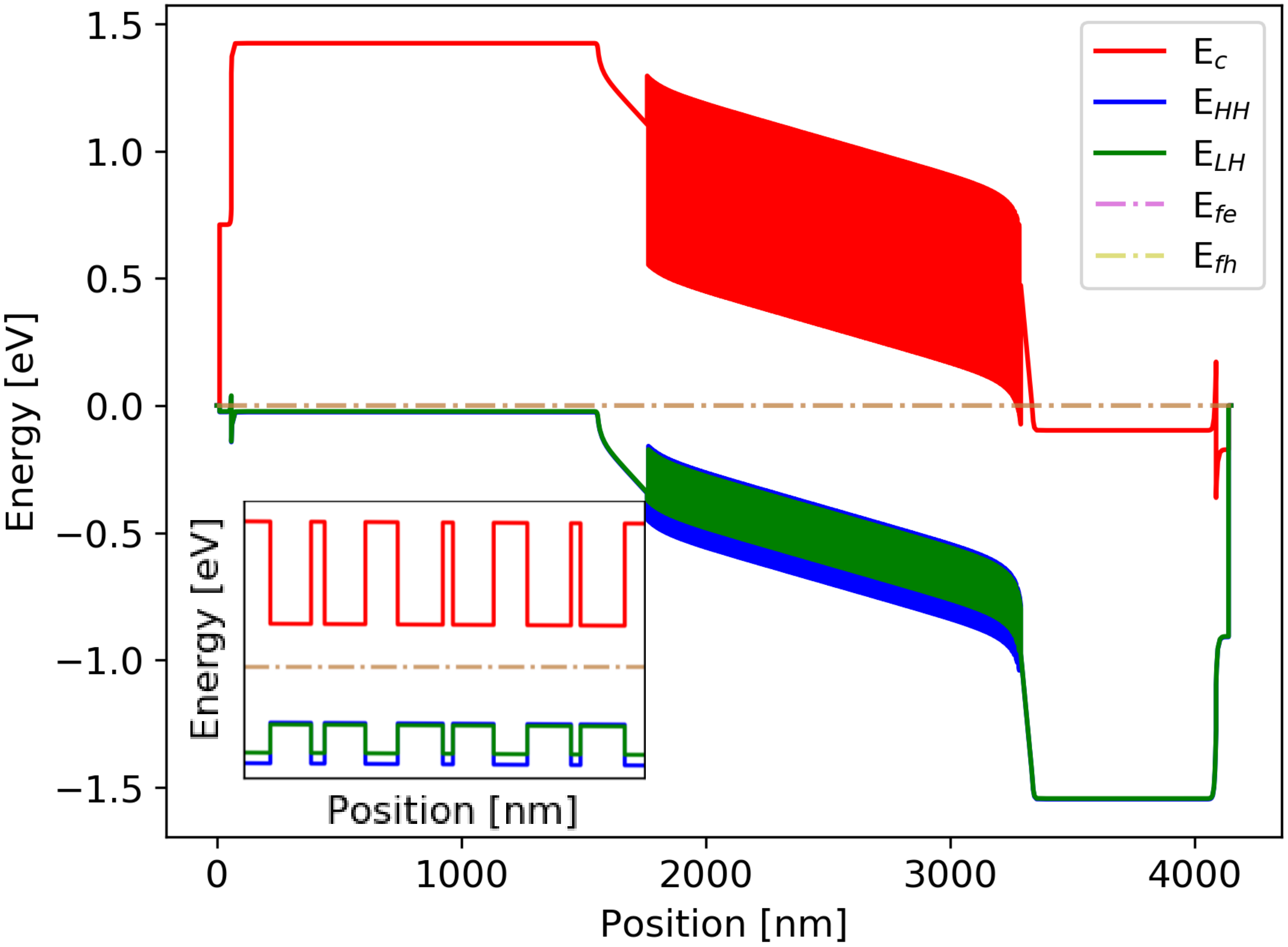

Fig. 4.23 – Full device band structure unbiased calculated for CQW slab structure, with three periods shown in the inset.

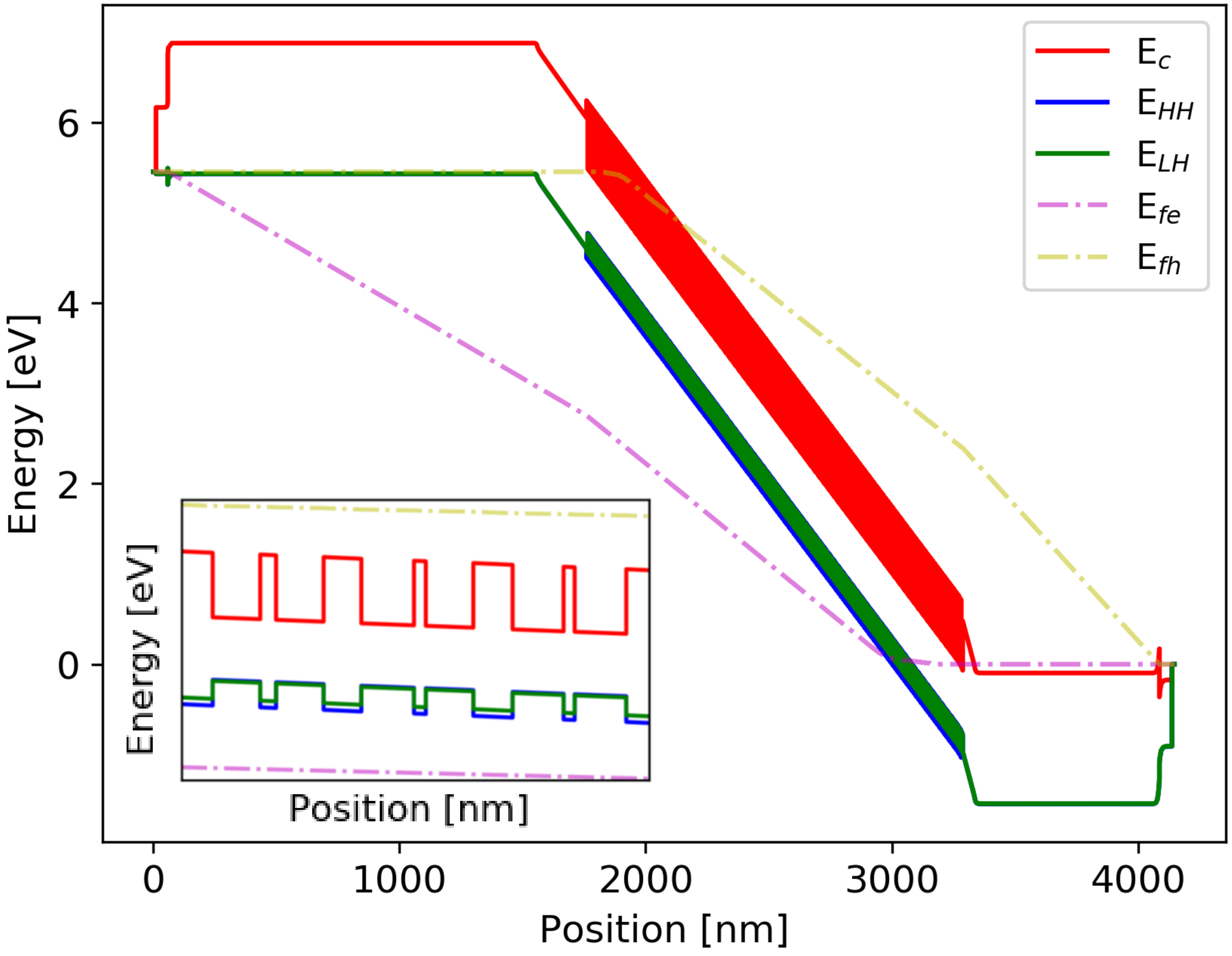

Fig. 4.24 – Full device band structure under 6V reverse bias calculated for CQW slab structure, with three periods shown in the inset.

Fig. 4.23 shows the full unbiased band diagram. In fig. 4.23 there is strong uniformity in the potential near the center of the intrinsic region, with less uniformity adjacent to the n-side and p-side cladding shown through band bending. The biased band diagram is shown in fig 4.24, with the potential across the intrinsic region showing higher uniformity with the conduction band almost fully depleted, based on the relative positions of the quasi-Fermi levels. Comparing the insets in fig 4.23 and 4.24, there is an increase in the slope of the CQWs due to the electrostatic potential causing the QCSE.

Fig. 4.25 shows an unbiased CQW. Coupling between carriers through the 1.5nm barrier in the unbiased structure, show the wavefunctions distorted away from a symmetrical solution, as described in [71], [72], [125]. There is initially strong overlap between the first light hole and electron wavefunctions, though the overlap between the E1-HH1 wavefunctions is only around 50%. This is due to the higher effective mass of the heavy hole reducing tunnelling through the barrier.

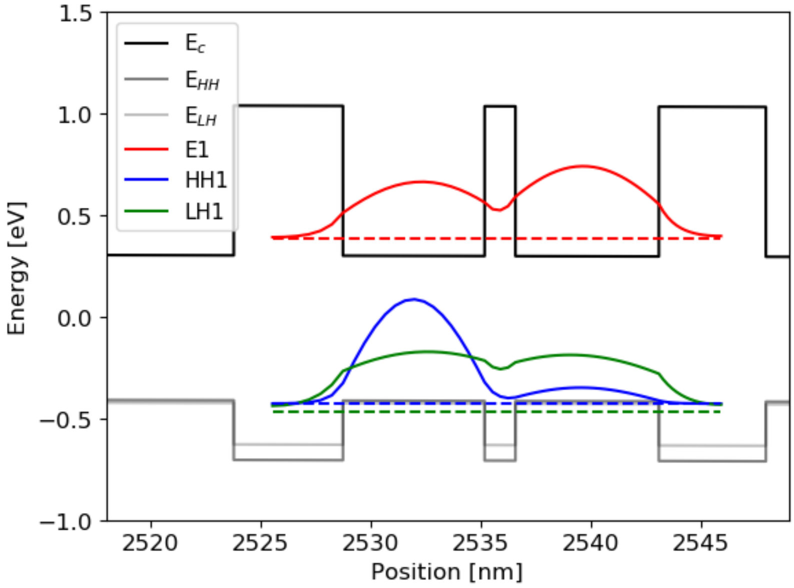

Fig. 4.25 – Band diagram for CQW under zero reverse bias with ground state electron, heavy and light hole bound states and wavefunctions.

Fig. 4.26 shows the CQW band structure under 6V reverse bias. The electron and heavy hole first excited states are shown here to demonstrate the increase in wavefunction overlap with the ground states. The HH1 wavefunction is now almost completely confined in the left hand side well with high overlap with E2. Additionally, the HH2 wavefunction overlaps strongly with the E1, leading to high absorption from nominally forbidden transitions E1-HH2 and E2-HH1. In fig. 4.26 the energy levels have been shifted for visual clarity, however, HH1 and HH2 are very closely spaced. There are similar effects for the light hole. Yet, the effects of the light hole are less distinct than the heavy hole, as the lower effective mass enhances the tunnelling and occupation in adjacent wells (similarly to the electron) so overlap varies less. Additionally, light hole-electron transitions absorb at higher photon energies and have a lower absorption magnitude near the band edge. Hence, the light hole absorption contributes less to the observed QCSE in these structures.

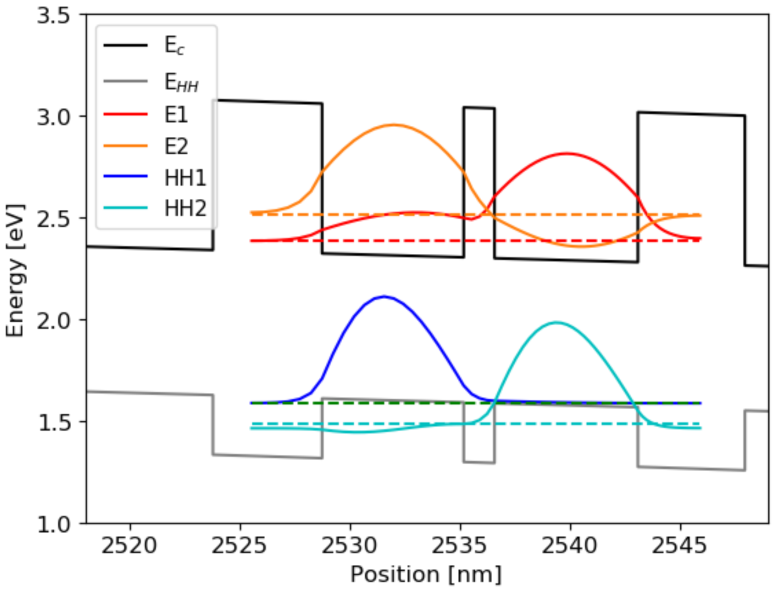

Fig. 4.26 – Band diagram for CQW under 6V reverse bias with ground and first excited electron and heavy hole bound states and wavefunctions. Excited states are shifted in energy for clarity.

4.4.2 Absorption calculations

To calculate absorbance with comparison to measurements, equations derived by Chuang's exciton Green's function method[15], [130] and Beer's Law (described in chapter 2) with outputs from the band structure calculations are used. Material parameters are based on those in Vurgaftman and Meyer[23]. Calculated exciton Rydberg energies and Bohr radii for heavy and light holes respectively are shown in table. 4.2. The heavy hole excitons are significantly stronger due to a lower exciton Bohr radius, and the higher exciton Rydberg energy results in a greater exciton binding energy.

Table 4.2 – Exciton Rydberg energies and Bohr radii used in absorption calculation for state of the art EAM.

Parameter	**Value**
Heavy hole exciton Rydberg energy / R_y	5.02 meV
Light hole exciton Rydberg energy / R_y	3.62 meV
Heavy hole exciton Bohr radius / a_0	17.9 nm
Light hole exciton Bohr radius / a_0	24.9 nm

Comparison between measurements are made with an offset for minimum absorbance equated to zero, as described in section 4.3.1. Calculated absorbance with comparison to unbiased, and under 3V and 6V reverse bias experimental data is shown in fig. 4.27, 4.28, and 4.29. The model matched the experimental data well when unbiased at 20ºC. Under applied reverse bias some differences between experimental and calculated data were initially observed, which were attributed to changes in the temperature during the measurement and a lower electric field strength supplied to the EAM than expected. In fig 4.28, calculations under 2V reverse bias and a temperature of 22ºC, consistent with the estimated temperature increase during the measurement. In fig 4.29, a 4V reverse bias and a temperature of 24ºC, consistent with the temperature increase during the measurement, were used. This corresponded to electric field strengths of 14.2KV/cm and 24.3KV/cm, for 3V and 6V reverse bias measurements respectively, and demonstrates the expected voltage drop between supply and the pixels, as observed by RISE.

The exciton binding energy was used as a fitting parameter aligning the E1-HH1 exciton to the experimental data in fig. 4.27. This was equal to $2.8R_y$ (with the calculated exciton Rydberg energy shown in table 4.2), falling between the 3D and 2D exciton binding energies, R_y and $4R_y$ respectively, similarly to [130]. This is referred to as quasi-2D excitonic behavior which is expected in QWs above room temperature[17].

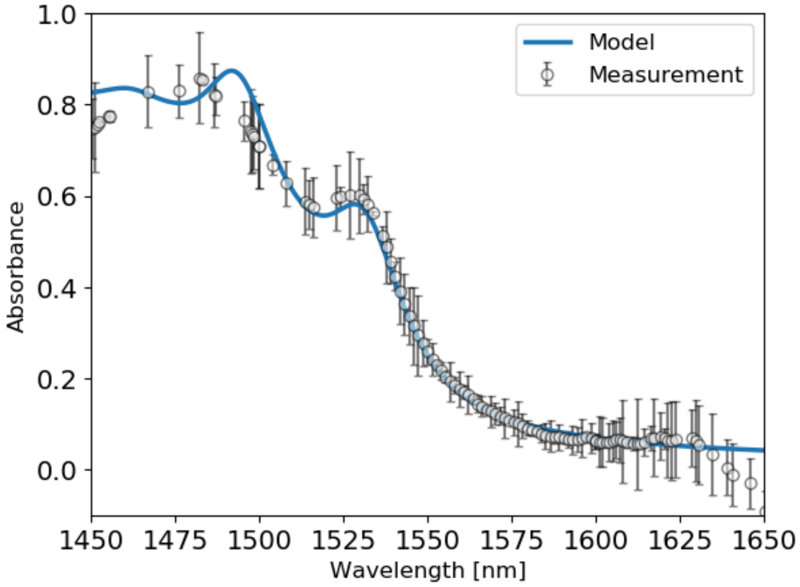

Fig. 4.27 – Modelled unbiased absorbance compared to measurement at 20ºC.

The exciton resonance peak positions and magnitudes are captured well by the model, with the E1-HH1 magnitude very close to the mean of the measured values. The absorption tail is also well represented, with the measurement reducing below zero above 1625nm. As discussed, this is due to significant degradation in the SNR due to the lowering of spectral response from the IR-LED at these wavelengths.

In fig. 4.28, there are some departures from the model at the shortest and longest wavelengths, similarly, due to SNR. Band edge absorption is well predicted using the corrected electric field strength. Under this reverse bias, the overlap in E1-HH1 and E1-HH2 transitions are decreasing and increasing respectively, resulting in broadening of the absorption edge. The E1-HH1 transition has redshifted to near 1550nm with the wavefunction overlap reduced by a factor of two.

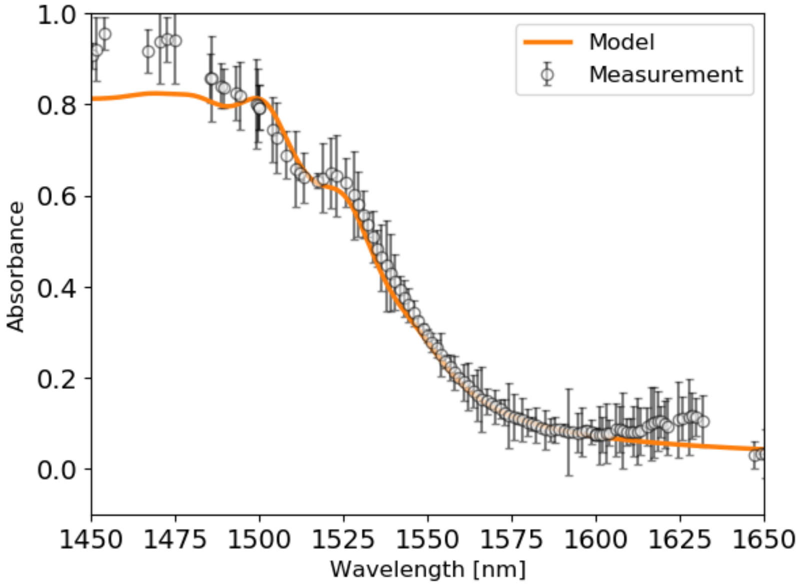

Fig. 4.28 – Absorbance modelled under 2V reverse bias compared to 3V measurement at 22ºC.

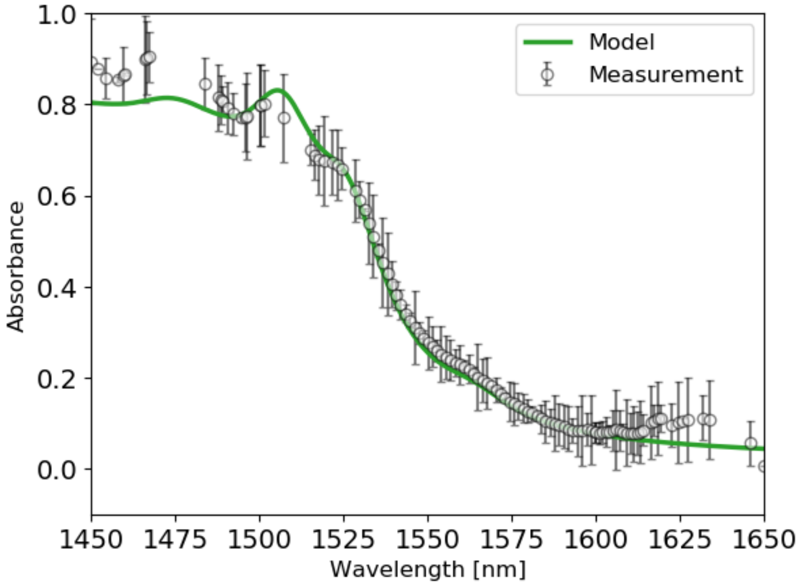

Fig. 4.29 – Absorbance modelled under 4V reverse bias compared to 6V measurement at 22ºC.

In fig. 4.29, the absorption edge is well modelled with the electric field strength correction, where departures between experimental and calculated data at longer and shorter wavelengths are again attributed to the SNR. Under 4V reverse bias, the E1-HH1 overlap has significantly decreased and redshifted to around 1565nm, which is captured well by the model. The E1-HH2 and E2-HH1 are more strongly overlapping and providing peaks in absorbance between 1510nm and 1530nm.

Fig. 4.30 shows the calculated absorbance with electric field corrections for unbiased, 3V, and 6V reverse biased data. The redshift in the E1-HH1 with increasing reverse bias is shown at the absorption edge, with the magnitude reducing dramatically with the wavefunction overlap.

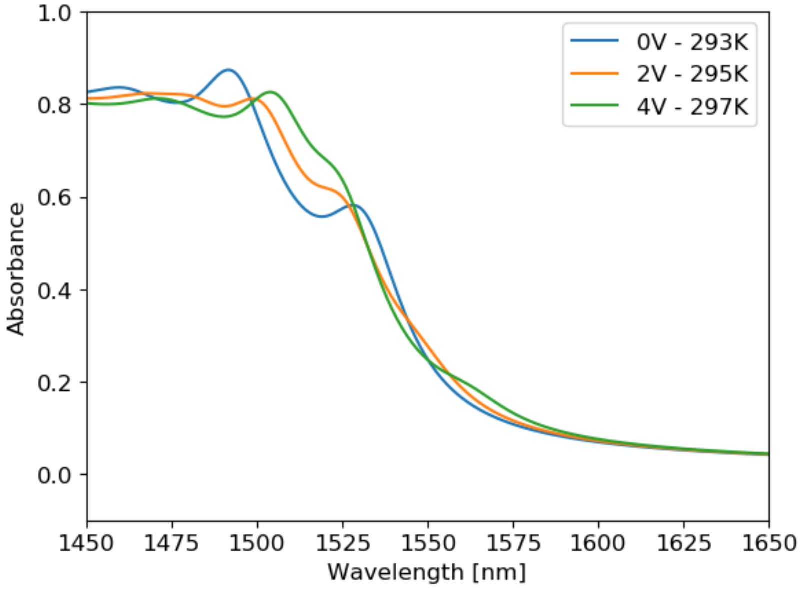

Fig. 4.30 – Calculated absorbance spectra under 0V, 2V, and 4V reverse bias with measurement temperatures.

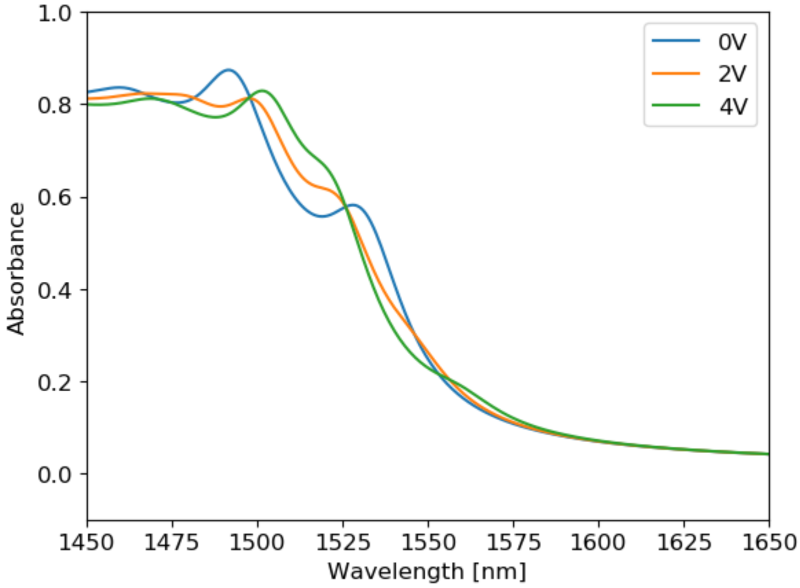

Fig. 4.31 – Calculated absorbance spectra under 0V, 2V, and 4V reverse bias at 20ºC.

The calculation was repeated at 20ºC, assuming no variation in temperature under different reverse bias, with absorbance shown in fig. 4.31. The absorbance calculated at 20ºC, shown in fig 4.31, has only subtle differences. The most predominant difference at 20ºC is the reduction in redshift at the absorption edge. This can be seen from the increased separation between curves at 1540nm in fig. 4.31, in comparison to fig. 4.30. There is also reduced separation between the unbiased absorption tail and the decreasing E1-HH1 transition under a 4V reverse bias, shown in fig. 4.31. The ER was calculated with electric field strength and temperature corrections and shown in fig 4.32.

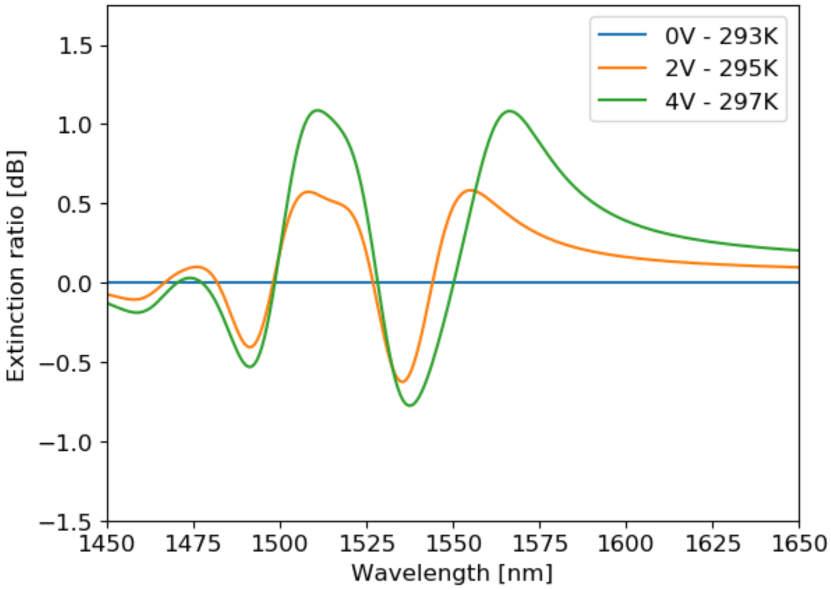

Fig. 4.32 – Calculated extinction ratio under 0V, 2V, and 4V reverse bias, with measurement temperatures.

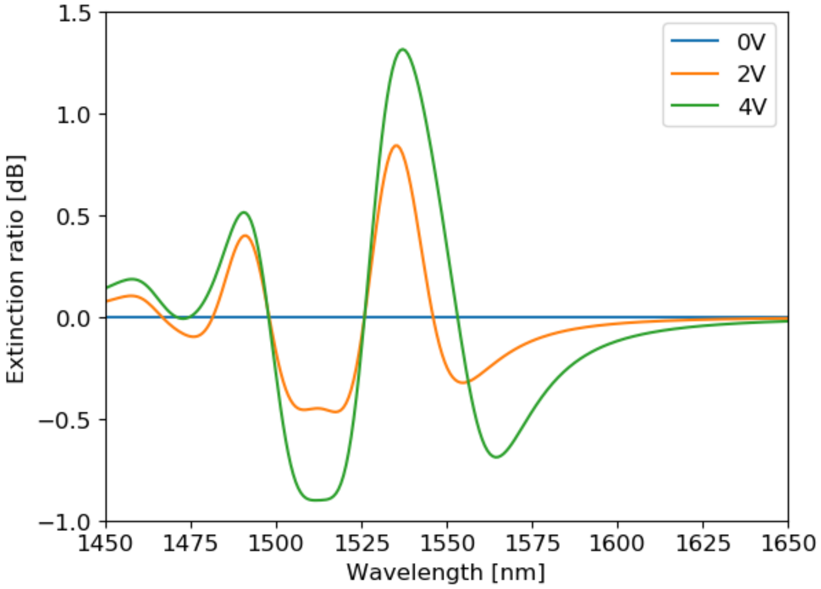

Fig. 4.33 – Calculated extinction ratio under 0V, 2V, and 4V reverse bias at 20ºC.

Fig 4.32 shows a similarly measured ER peak of just over 0.5dB at 1532nm, with a slightly underestimated ER peak just above 1dB at 1508nm. Fig. 4.33 shows the ER calculated at 20ºC but under the same reverse bias conditions as fig. 4.32. The ratio has been inverted in fig. 4.33 making the highest ER peak positive in fig. 4.33. Comparing fig. 4.32 to fig 4.33, a higher ER is shown if the temperature is maintained at 20ºC across all reverse bias conditions. Therefore, if temperature stabilisation was employed to maintain the material at 20ºC improved performance could be achieved.

Fig. 4.33 shows a strong ER peak of 1.27dB at 1530nm at 20 ºC. This is consistent with the 0.97dB ER measured at 1540nm by the University of Oxford[127] at 23ºC. This peak occurs from the separation in the declining overlap and redshifting E1-HH1 transition and increasing overlap of the E1-HH2 transition. Comparing fig. 4.32 and 4.33, this ER peak is significantly degraded over a 4ºC temperature increase, which is not appropriate for any practical application. This appears to be due to a narrow part of the spectrum responsible for the QCSE, with reliance on very closely spaced and forbidden transitions. Additionally, the ER dependence on precise redshifting and overlap changes of closely spaced transition energies will be more sensitive to growth induced variations and defects.

Fig. 4.34 shows the optical IL calculated from the unbiased absorbance. At 1550nm there is a 2.2dB IL, which is consistent with the offset IL in fig. 4.13. This is combined with the ER in 4.32 to model the FoM measured in section 4.3.1. The calculated FoM is shown in fig. 4.35.

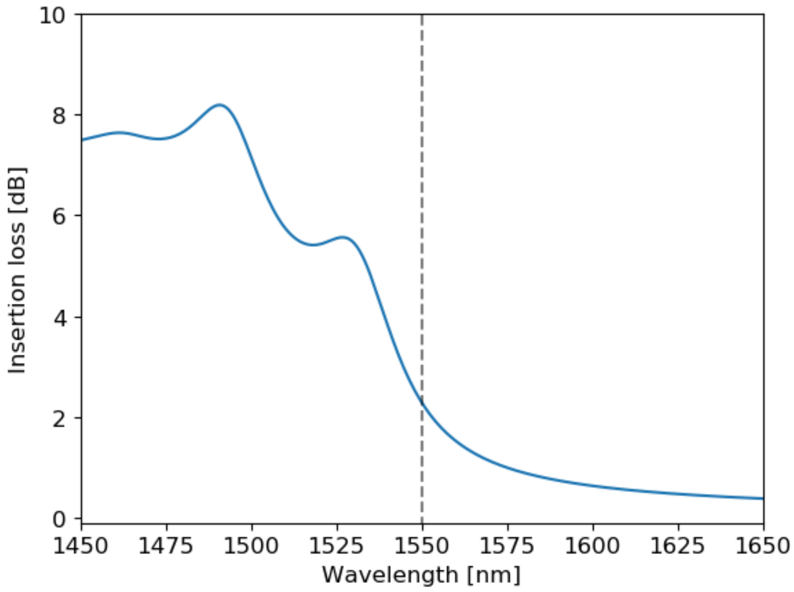

Fig. 4.34 – Calculated IL from unbiased absorbance. 1550nm operating wavelength is shown by vertical dashed line.

The FoM, shown in fig. 4.35 is consistent with the measurement in fig. 4.14, with only some minor departures attributed to the low SNR in the experimental data at the shortest and longest wavelengths. FoMs of almost 0.2 for relevant wavelengths are shown in fig 4.35.

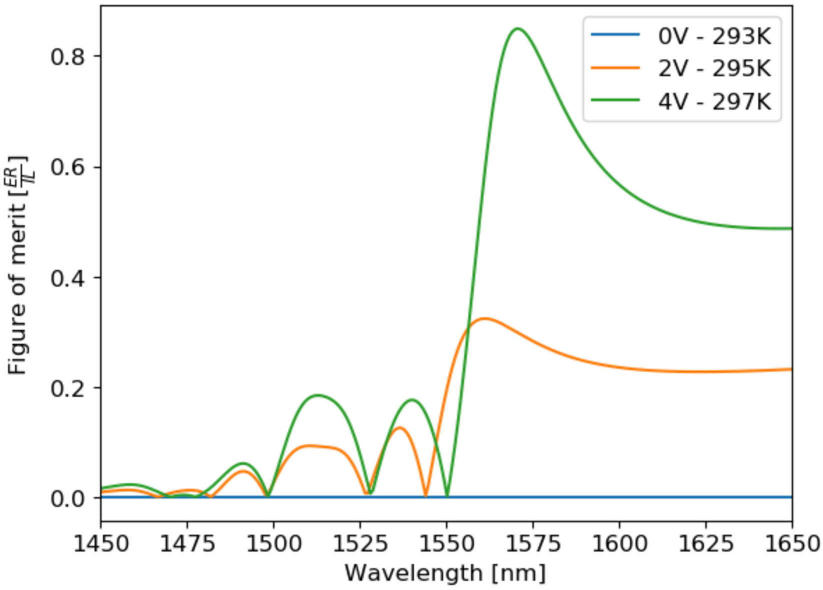

Fig. 4.35 – Calculated figure of merit under 0V, 2V, and 4V reverse bias, with measurement temperatures.

Fig. 4.36 shows the unbiased FoM and under 2V and 4V reverse bias calculated at 20ºC. A significant effect of maintaining constant temperature is the reduction in the large FoM at 1575nm, which is caused by the additional temperature induced redshift of the E1-HH1 transition. There is a larger peak FoM of 0.3 at 1535nm, highlighting the degradation due to an apparent temperature increase of 4ºC.

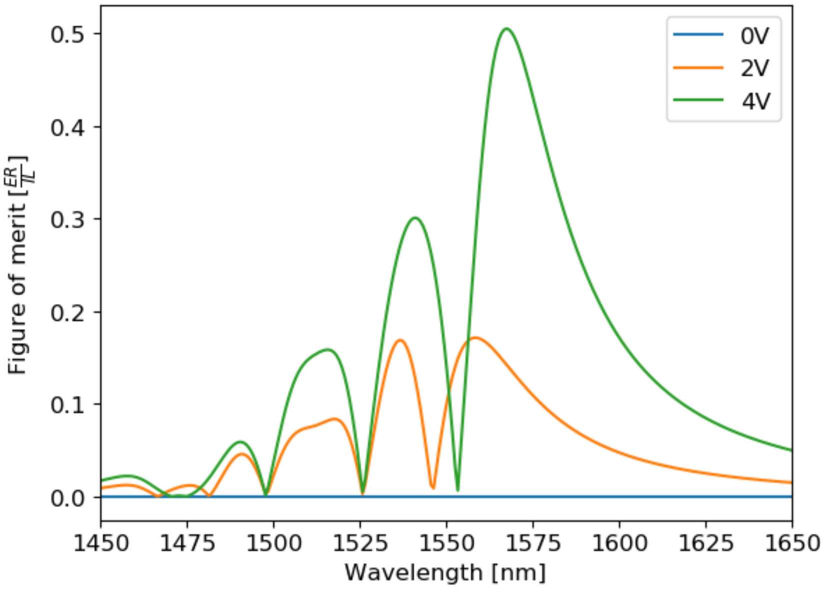

Fig. 4.36 – Calculated figure of merit under 0V, 2V, and 4V reverse bias at 20ºC.

4.5 Novel epi-structures

The limitations observed in the previous sections highlight the necessity for the design of new epi-structures. CQWs display a strong dependence on closely spaced and forbidden transitions requiring a high degree of temperature control for successful operation. The system would only function at specific wavelengths which may lead to declining performance with broadening caused by well width fluctuations and defects incurred during growth.

Further, operation is strongly limited by the magnitude of IL arising from high overlap between wavefunctions. Though a strong QCSE has been identified in CQWs[71], for long distance outdoor data links this may not be the optimal approach. Due to the narrow operating regions and intersections observed between unbiased and biased absorbance spectra it may be necessary to continually invert corresponding 1 or 0 signals, as shown by the nodes in the ER spectra in fig. 4.20. Additionally, at room temperature, a 0 signal can correspond to unbiased operation, whereas it may be energetically favourable to allow for maximum transmission or a 1 signal when the EAM is not consuming power.

Reductions in IL and increases in ER will yield benefits in performance, however, particular attention to the positioning and movement of energy levels may offer benefits and flexibility for operation in long distance FSO data links, in a variety of environments. To analyse the potential of new structures, materials, compositions, band alignment, and quantum well dimensions, will be used as design parameters.

4.5.1 Material selection

Evaluating the limitations observed through measurement and modelling of the current state of the art structures was used as a starting point for selecting relevant materials for novel epi-structures. FSO demands operational wavelengths of 1550nm (or C-band) so few material combinations are appropriate. Generally, InP-based devices are used at this wavelength, and improvements may still be possible through variation of the composition and dimension of existing CQWs.

GaAs-based devices have been shown for use in the O-band with alloys including InGaAs-GaAsSb showing potential[131]–[133]. However additional alloying (to form quaternaries) or dilute incorporation of nitrides, bismides, or phosphides are required to extend operation to 1550nm[134]–[136]. A significant benefit of considering InGaAs-GaAsSb QWs is the type-II band alignment, resulting in spatial separation of electrons and holes within different layers. This acts to reduce the wavefunction overlap and IL, provided a significant QCSE can still be achieved.

InGaAs-GaAsSb can be grown on InP substrates and if strain balancing is incorporated because of the large number of quantum well periods expected for this application. This has been shown in type-II superlattice photodetectors[137]. Therefore, we considered altering existing CQWs, and InGaAs-GaAsSb type-II QWs on both GaAs and InP substrates with strain compensation.

4.5.2 Quantum well dimension & composition

To explore potential geometries, unbiased band structure calculations were conducted for state of the art CQWs, and InGaAs-GaAsSb on GaAs and InP substrates with variation of the composition and QW dimensions. The cut-off wavelength, equivalent to the ground state transition energy and the corresponding wavefunction overlap was evaluated. This is shown in fig. 4.37-4.42 with the 1550nm cut-off displayed as a contour. Specific composition and dimension ranges were selected to prioritise regions displaying the 1550nm operating cut-off from initial calculations. Fewer suitable regions were identified for the GaAs-based structures without very thick well dimensions, further reducing the energy level separation.

For consistency, structures were calculated maintaining equal intrinsic thickness to the state of the art p-i-n device. P-type and n-type dopant concentrations were kept constant so the built-in electric field was preserved in all calculations. Strain balancing would likely be necessary and suitable combinations could then be specifically tuned using barrier materials. For InP-based structures InAlAs could be used for strain compensation[30], [138], [139], and GaInP or GaAsP for GaAs-based structures[31], [32], [140].

The wavefunction overlap was calculated to indicate suitability of the structure for low IL. If the wavefunction overlap was too high, the IL would remain high. However, if the wavefunction overlap was too low, the confinement between carriers may inhibit appreciable QCSE. The cut-off wavelength provided an estimate of the operational wavelength, corresponding first interband transition, where the greatest changes in electroabsorption will occur. However, the exciton binding energy will cause resonance at wavelengths greater than this value, and would require further evaluation after appropriate structures were identified.

The analysis of variation in the state of the art CQW structures is shown in fig. 4.37 and 4.38, with the 1550nm contour across all combinations, yet, the overlap remaining high, indicating strong type-I band alignment. This suggested limited reductions in the IL would be achievable. Considering the band diagrams themselves, another limitation was the closely spaced and forbidden transitions. To reduce this it is possible to reduce the thickness of the hole confining layer to increase separation between the states. Due to the strong coupling required in these structures by reducing the thickness in one layer, the ground state hole wavefunction is forced into the other layer, again increasing the overlap. Though, by decreasing the electron confining layer or both simultaneously, carriers were confined to smaller dimensions with the overlap and IL increasing. This suggested limited improvements possible with the original structure.

Due to the significantly lower lattice constant of the substrate In the GaAs-based structures, there were prominent strain effects. Though this may be offset through strain balancing, large QWs were needed to provide the 1550nm cut-off, as shown in fig. 4.40. Furthermore, the high confinement of carriers lead to exceedingly low wavefunction overlaps with a maximum of around 18%. Though this is promising for low IL, the QCSE is degraded by inhibited tunneling into adjacent layers.

The InP-based wavefunction overlap and cut-off wavelength are shown in fig. 4.41 and 4.42. The 1550nm transition wavelength is observed across all structural combinations, with a wide range of degrees of wavefunction overlap. InP-based structures required significantly narrower QW dimensions, providing increased confinement and thus greater energy separation between transitions. With $In_{0.40}GaAs$-$GaAsSb_{0.40}$ QWs, wavefunction overlap of less than 50% was possible depending on the QW dimensions.

Selecting asymmetric QW dimensions could provide further benefits through additional separation between the hole energy levels. By increasing the electron confining InGaAs layer to 3nm and reducing the hole confining GaAsSb layer to less than 2nm, good QCSE is expected. Yet, further analysis was required to calculate strain compensation layers in addition to simulation of the QCSE.

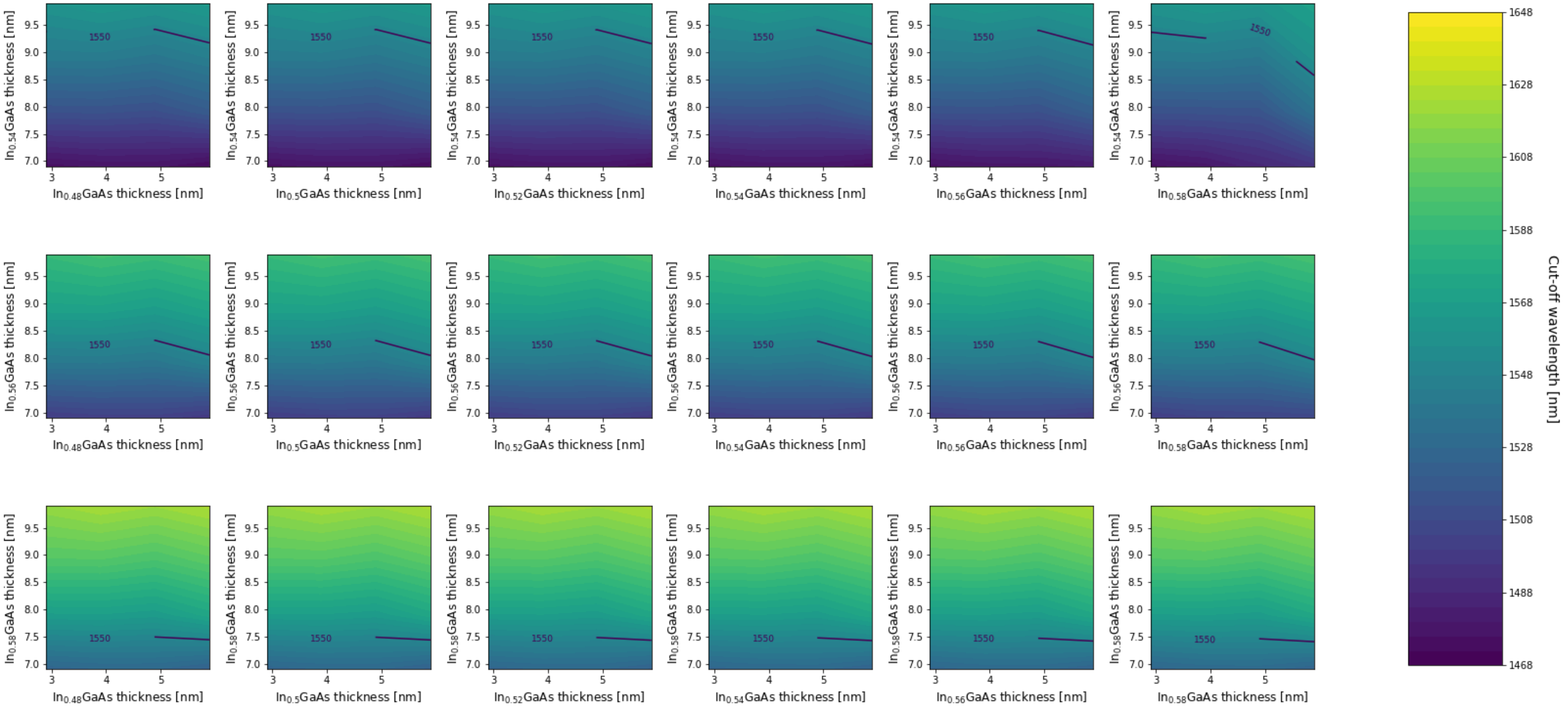

Fig. 4.37 – Cut-off wavelength calculated for varying InGaAs-InGaAs coupled quantum well thickness and composition on InP substrate.

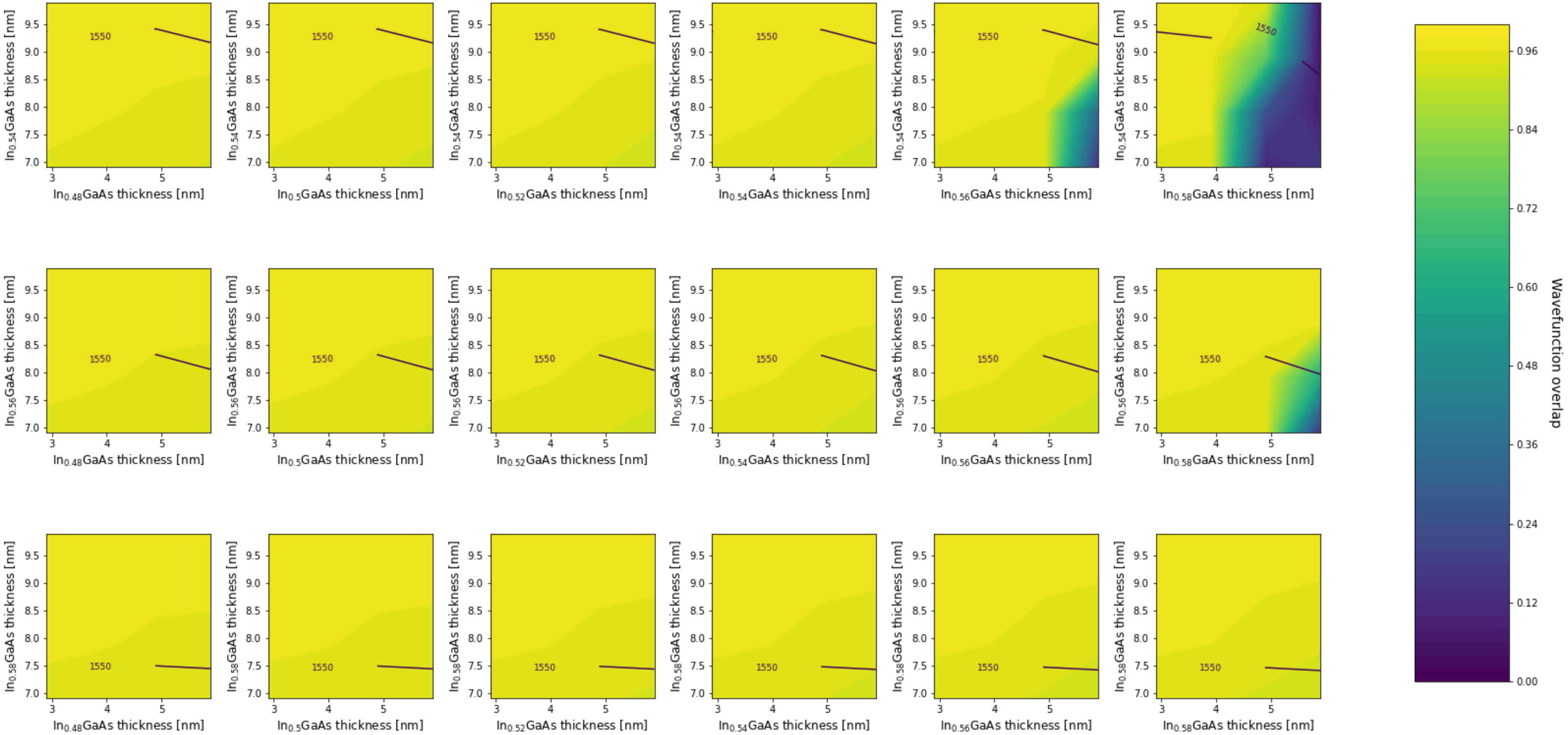

Fig. 4.38 – Wavefunction overlap calculated for varying InGaAs-InGaAs coupled quantum well thickness and composition on InP substrate.

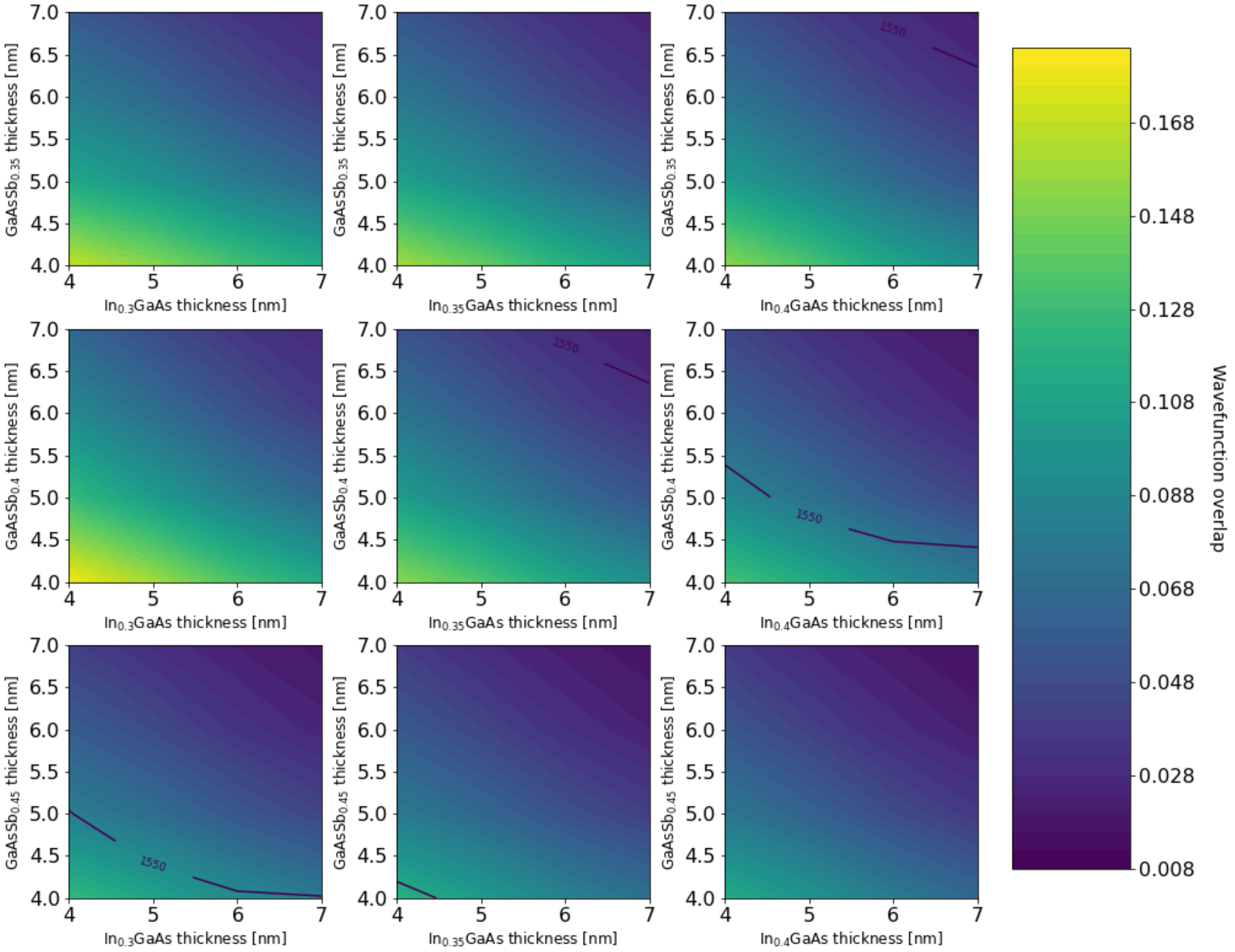

Fig. 4.39 – Wavefunction overlap calculated for varying InGaAs-GaAsSb quantum well thickness and composition on GaAs substrate.

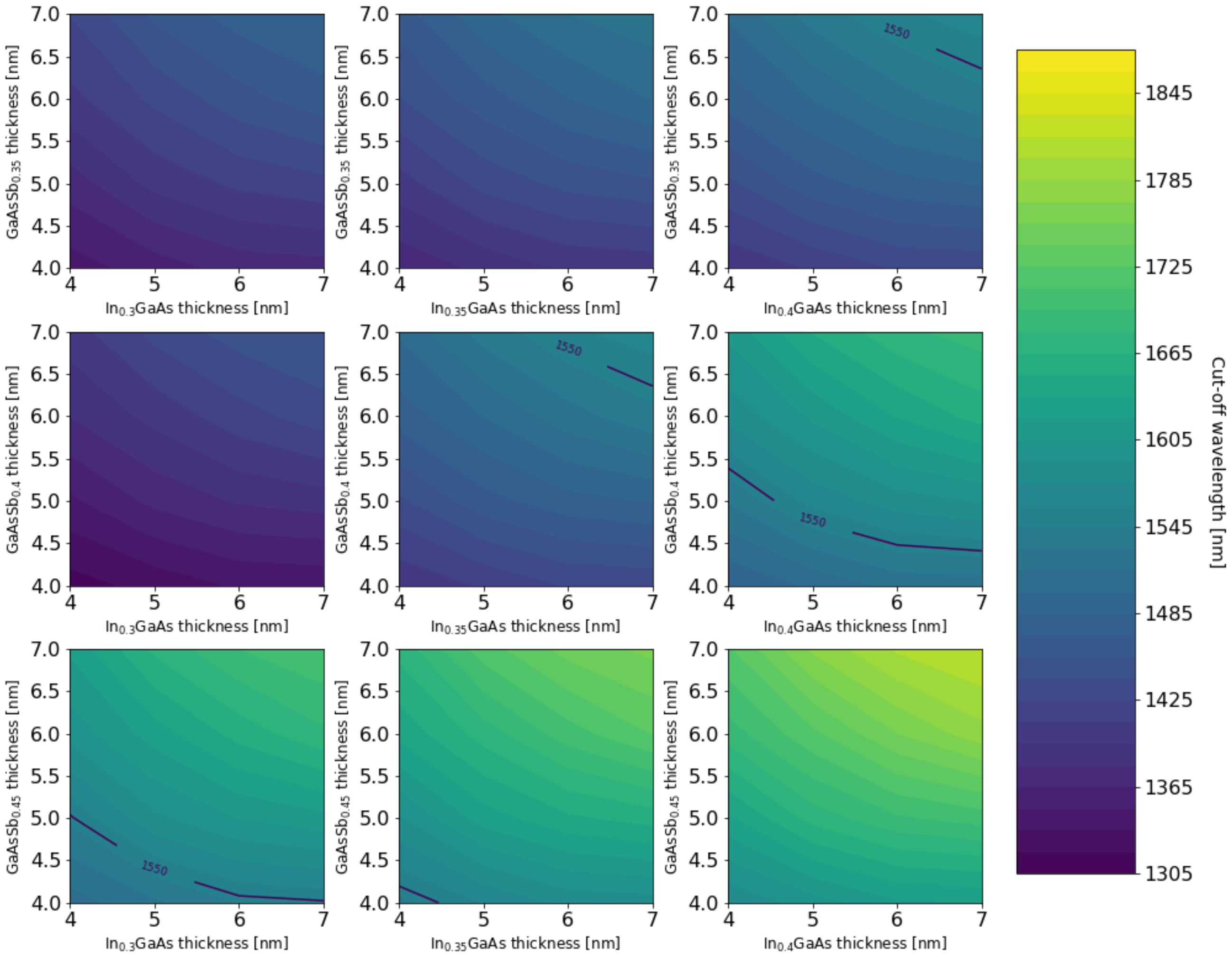

Fig. 4.40 – Cut-off wavelength calculated for varying InGaAs-GaAsSb quantum well thickness and composition on GaAs substrate.

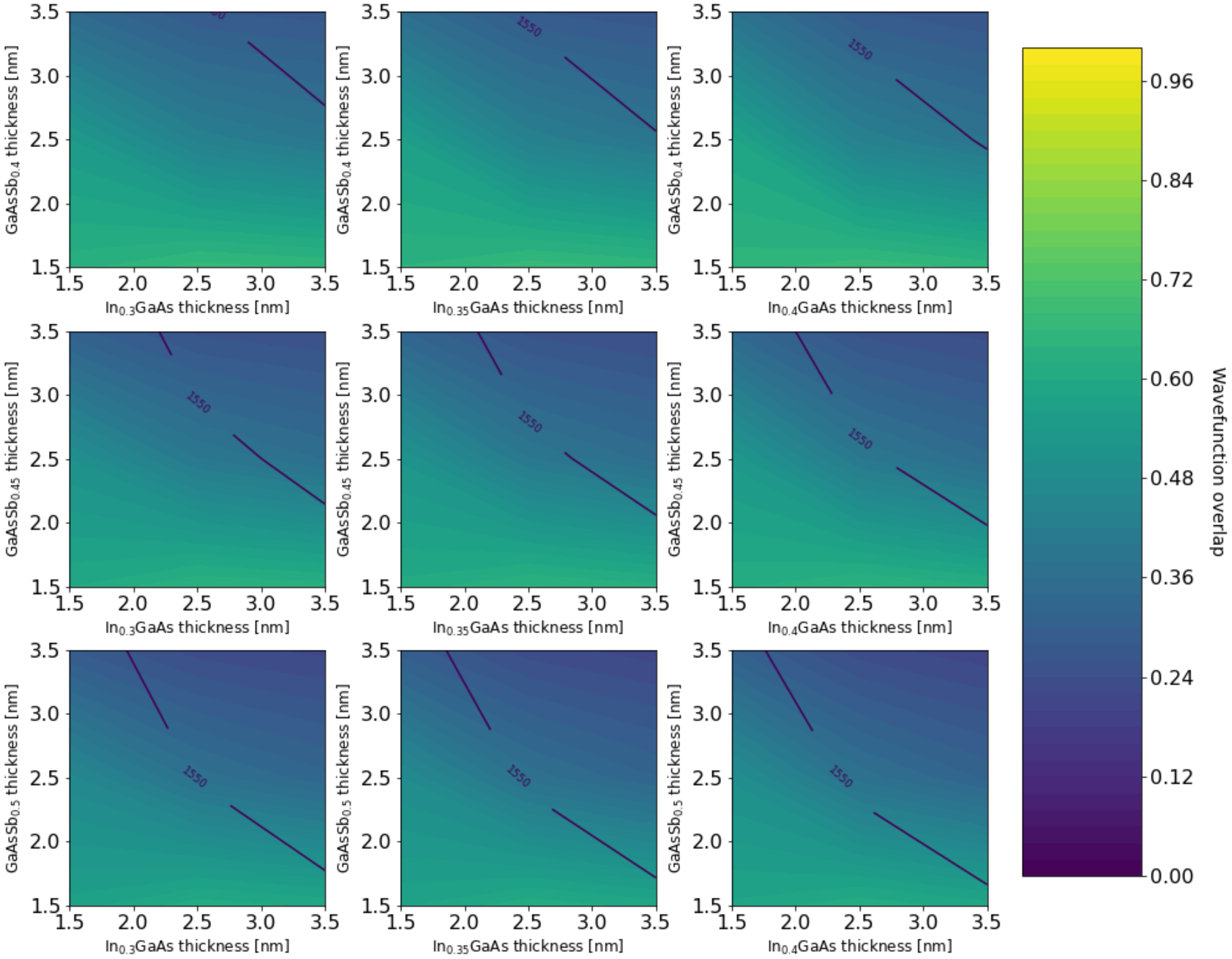

Fig. 4.41 – Wavefunction overlap calculated for varying InGaAs-GaAsSb quantum well thickness and composition on InP substrate.

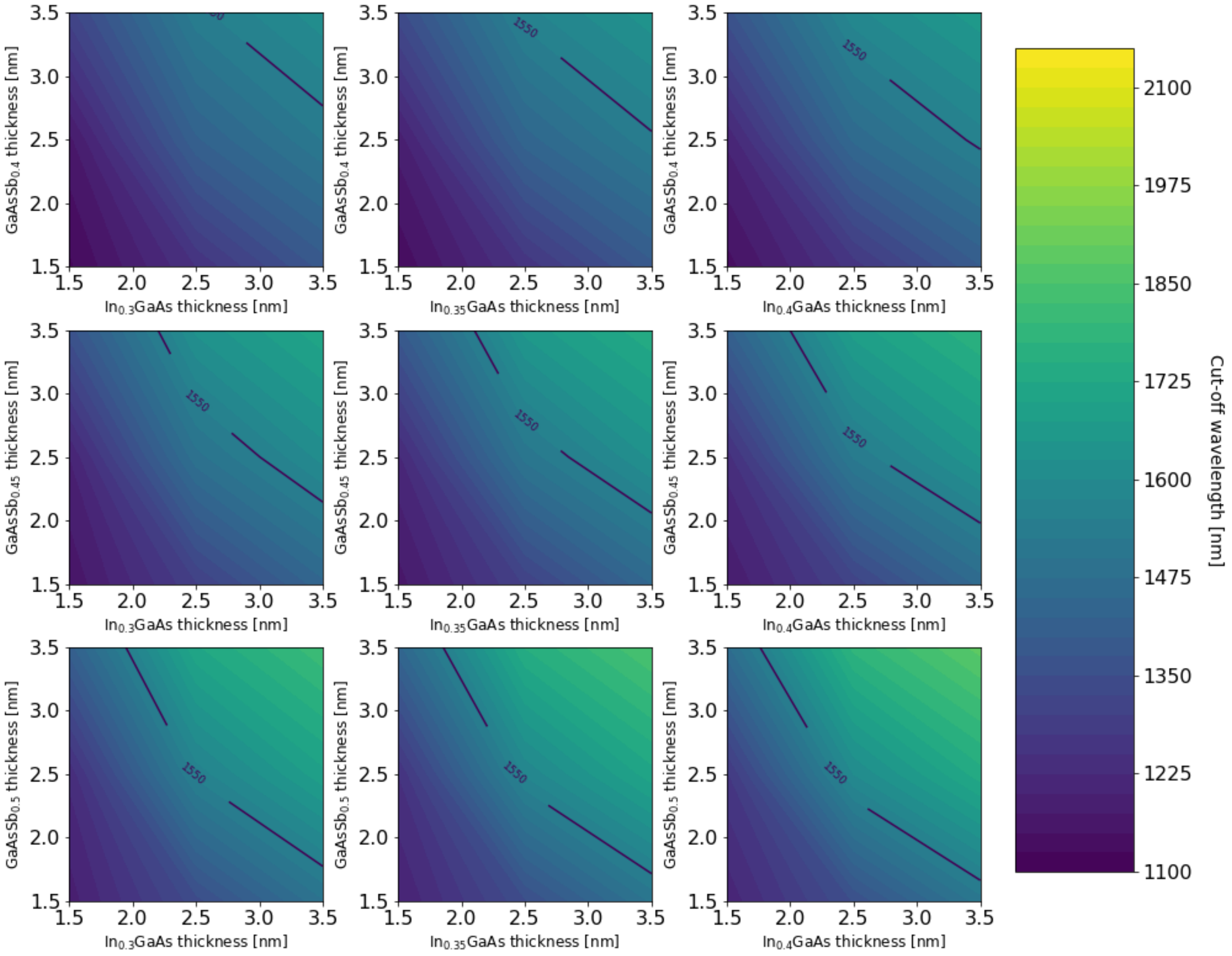

Fig. 4.42 – Cut-off wavelength calculated for varying InGaAs-GaAsSb quantum well thickness and composition on InP substrate.

4.5.3 Strain balancing

Strain balancing calculations were conducted with equations using elastic coefficients and shear moduli derived by Van de Walle[21] and collated by Krijn[22] (in chapter 2). By varying the indium content and barrier thickness for strain compensation, the in-plane lattice constant $(a_{||})$ was to be equated to the lattice constant of the InP substrate. By equating $a_{||}$ to the lattice constant of the substrate, the in-plane biaxial strain is minimized providing high quality material growth. This is shown in fig. 4.43. A structure composed of 3nm $In_{(0.40)}GaAs$ and 2nm $GaAsSb_{(0.4)}$ was used. Using the relationship shown in fig. 4.43, an indium composition between 0.55 and 0.65 is identified and used with a layer thickness between 30nm and 3nm.

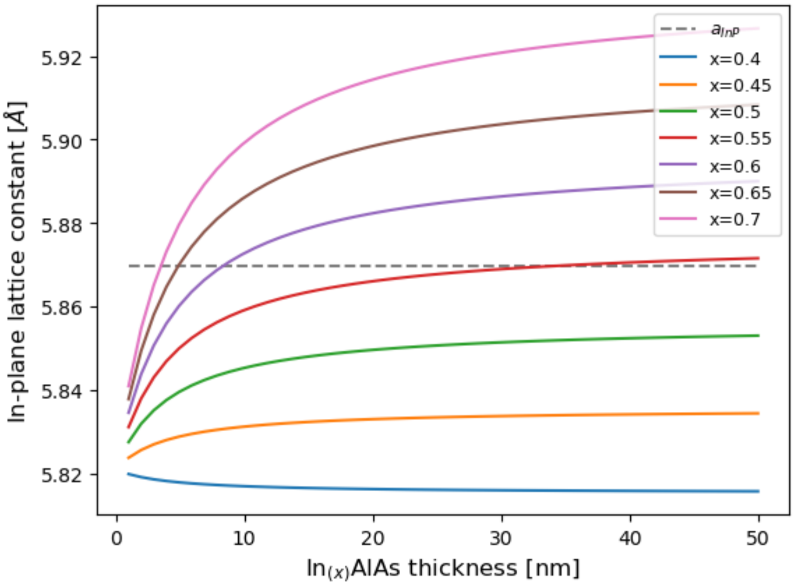

Fig. 4.43 – In-plane lattice constant calculated for 3nm $In_{(0.40)}GaAs$ and 2nm $GaAsSb_{(0.40)}$ quantum wells with varying indium composition and thickness for InAlAs barriers.

By increasing the InAlAs barriers it is possible to reduce the indium composition. However, for the same intrinsic region thickness, this reduces the total amount of material imparting modulation on an incoming beam. By increasing the indium composition the thickness of the strain compensation layer can be reduced. If the barrier thickness is too low, coupling between the QWs can occur and change the absorption characteristics. Coupling between adjacent QWs is undesirable, as the wavefunction overlap and cut-off wavelength may be significantly altered, possibly reducing the QCSE. An indium content of 0.60, with layer thickness of 7nm was used as a starting point to further study the suitability within the structure. Reducing the QWs to 2.7nm and 1.5nm for InGaAs and GaAsSb respectively maintained a cut-off wavelength slightly below 1550nm, to allow for exciton resonance.

Further analysis was conducted by simulating x-ray diffraction (XRD) in X'pert Epitaxy software for the 2.7nm $In_{0.40}GaAs$, 1.5nm $GaAsSb_{0.40}$, and $In_{0.60}AlAs$ structure. The XRD simulation is shown in fig. 4.44 for two barrier thicknesses and InP substrate. For comparison the epi-structure was considered the same as described in section 4.5.3, with the narrower $In_{0.40}GaAs$-$GaAsSb_{0.40}$ QWs requiring 100 periods compared to 80 in the CQWs. This maintained the intrinsic thickness and built-in potential.

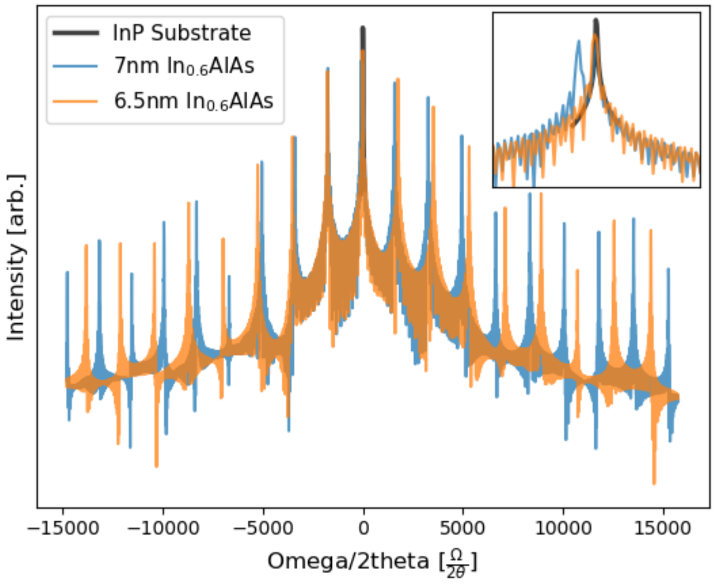

Fig. 4.44 – Simulated XRD for 100 period QW structure with two InAlAs barrier thicknesses, for 2.7nm $In_{(0.40)}$*GaAs and 1.5nm* $GaAsSb_{(0.40)}$*. The highest peaks and InP substrate are shown in the inset.*

The 7nm barrier thickness did not align with the InP peak, so a second simulation with decreasing strain compensation provided by the InAlAs barrier was conducted. This aligned well with the InP substrate, as shown in the inset of fig. 4.44. Re-calculating the operating wavelength, a final structure with 2.7nm $In_{(0.43)}GaAs$, 1.5nm $GaAsSb_{(0.40)}$ was found to be most suitable with 6.5nm $In_{(0.60)}AlAs$ strain compensation barriers. This increase in indium content, may further relax strain in the structure with a slightly narrower barrier required. Nevertheless, it is important to note that further study of the epitaxy of these materials would be required to achieve high quality growth, and appropriately tune, through iterative growth calibration steps, the strain compensation layer with the QW parameters.

Specifically, attention to the variation of growth temperature will be required between the indium based alloys and the GaAsSb due to the antimony content[29], [141], [142], which may affect the interface quality.

4.5.4 Type-II quantum confined Stark effect

Full device band structures were modelled following the procedure highlighted in section 4.4.1. QCSE calculations were repeated slightly varying the QW compositions, with 2.7nm $In_{(0.43)}GaAs$ and 1.5nm $GaAsSb_{(0.40)}$ showing the best performance at 1550nm. Thus an iterative process between strain compensation and QW parameters must be employed during epitaxy, with feedback to the model for parameters such as the exciton binding energy. Full devices are shown unbiased and under reverse bias in fig. 4.45 and 4.46. Unbiased and reverse biased QWs with calculated wavefunctions and bound energy states are shown in fig. 4.47 and 4.48. Calculated exciton Rydberg energies and Bohr radii for heavy and light holes respectively are shown in table. 4.3.

There is a slight reduction in the exciton Rydberg energy for both heavy and light holes with this structure compared to the state of the art CQWs, which will result in lower exciton binding energies. Nonetheless, this difference may be negligible depending on how near to pure 2D behavior the excitons are in grown structures. An increase in exction binding energy from $2.8R_y$ to $2.93R_y$ will provide equivalence between CQW and type-II structures. Incidentally, the exciton Bohr radius is increased, though further characterization of grown structures is necessary for realistic comparison. In these calculations, an exction binding energy of $2.8R_y$ is assumed.

Table 4.3 - Exciton Rydberg energies and Bohr radii used in absorption calculation for type-II EAM.

Parameter	**Value**
Heavy hole exciton Rydberg energy / R_y	4.79 meV
Light hole exciton Rydberg energy / R_y	3.11 meV
Heavy hole exciton Bohr radius / a_0	17.3 nm
Light hole exciton Bohr radius / a_0	26.6 nm

From fig. 4.45, consistency with fig. 4.23 is evident with equivalent intrinsic thickness and approximately equal built-in potential. The inset of fig. 4.45 shows the type-II band alignment, with holes confined to the narrow GaAsSb QW and electrons confined in the InGaAs QW. The reduction in thickness from 6.4nm to 1.5nm of the hole confining layer increases the separation between ground and first excited state transitions and suppresses the forbidden transitions observed in the CQWs. The full band diagram under reverse bias is shown in fig. 4.46.

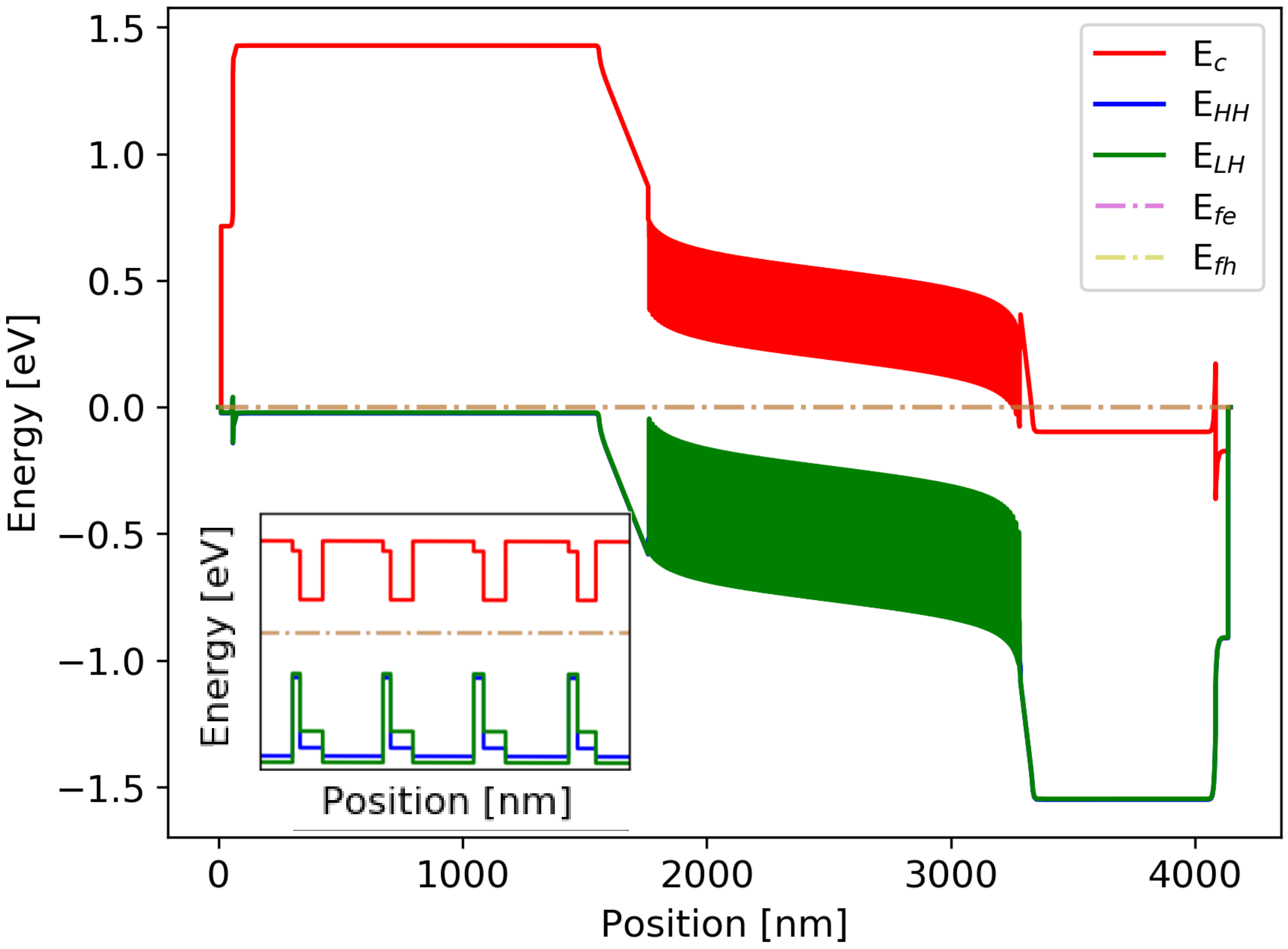

Fig. 4.45 - Full device band structure unbiased calculated for type-II QW slab structure, with four periods shown in the inset.

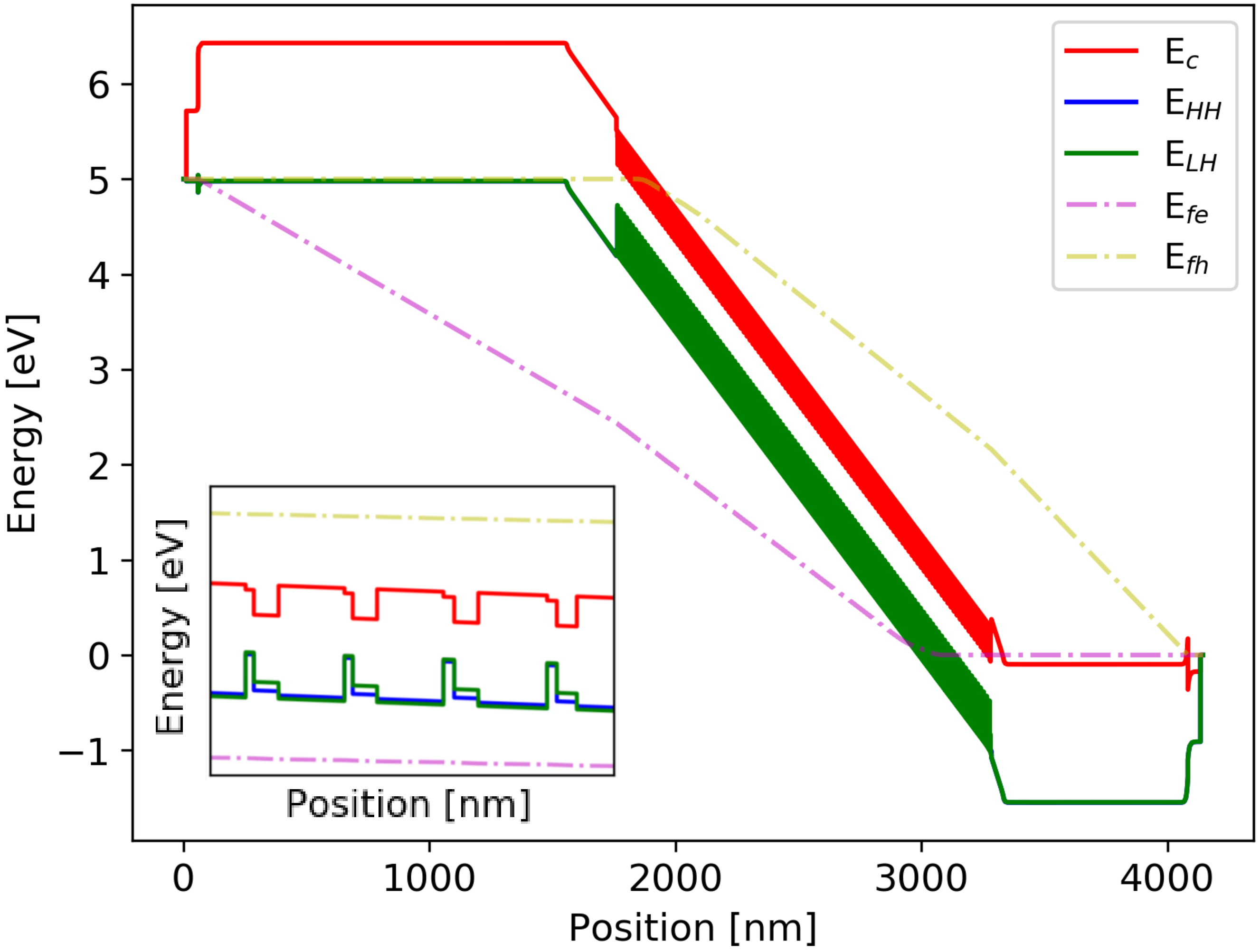

Fig. 4.46 - Full device band structure under 6V reverse bias calculated for type-II QW slab structure, with four periods shown in the inset.

Under reverse bias, only small differences in the wavefunction overlap are expected, but a large redshift in the transition energy. This is primarily due to the narrow QW dimensions.

Fig. 4.47 shows the unbiased QW, with the first bound states and wavefunctions for electron, heavy and light holes. In addition to increasing the separation between the ground and first excited heavy hole state, there is a large separation between the ground state heavy and light holes. This is due to the small QW thickness for the lower effective mass associated with the light hole.

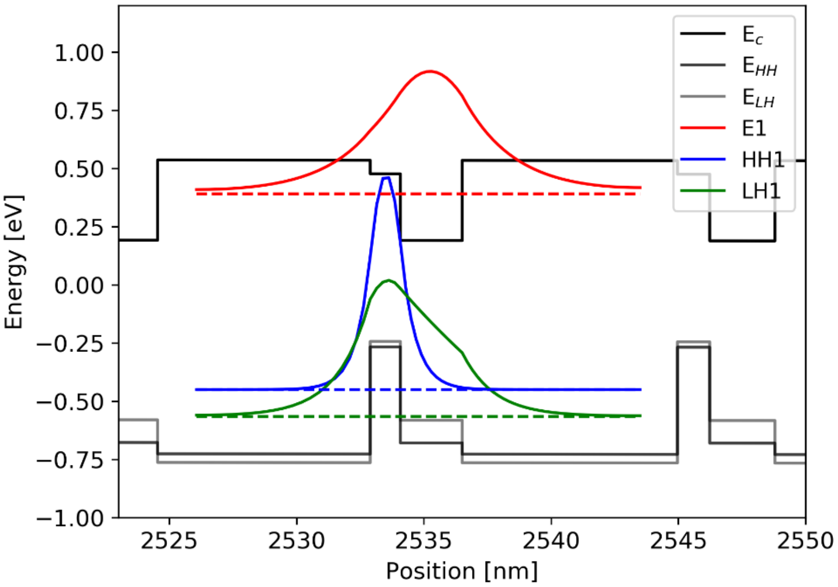

Fig. 4.47 - Band diagram for type-II QW under zero reverse bias with ground state electron, heavy and light hole bound states and wavefunctions.

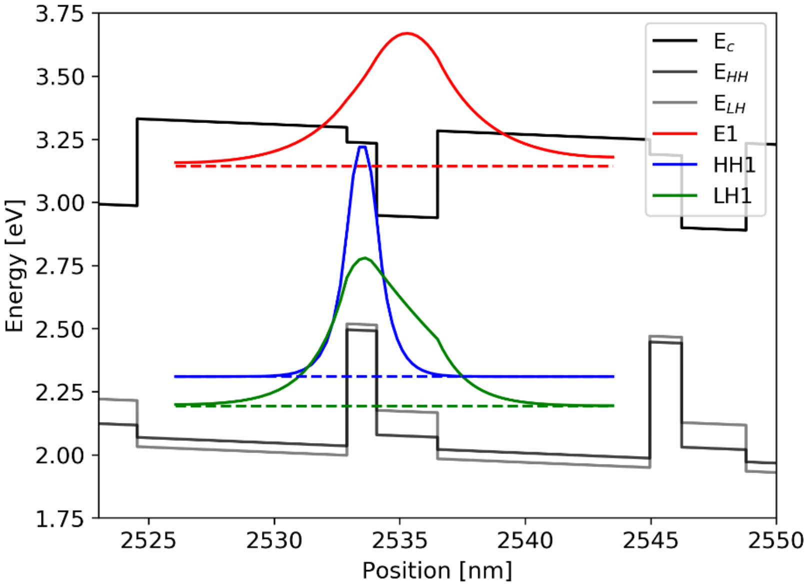

Fig. 4.48 - Band diagram for type-II QW under reverse bias with ground state electron, heavy and light hole bound states and wavefunctions.

This is expected to be beneficial for MRR FSO applications by removing the combined absorption from many overlapping exciton and continuum contributions. The narrow GaAsSb layer has benefits, though may be vunerable to reduced interface quality due to growth temperature changes[142], or more significant broadening from well width fluctuations.

Fig. 4.48 shows the QW under reverse bias, with the first bound states and wavefunctions for electrons, heavy and light holes. There are negligible changes in the overlap of the wavefunction but significant reduction in the transition energy compared to the unbiased case, which will redshift the absorption spectrum.

4.5.5 Fraction of light absorbed

As discussed in chapter 2, the absorption coefficient or absorbance is unsuitable for comparisons between structures with different geometries and band alignment because the well width is undefined, particularly at normal incidence. Therefore, the fraction of light absorbed by a QW (γ_{well}) as described by Blood[16], [43] is used. The inclusion of bound and continuum of states contributions follows Chuang[15] [130]. Fig. 4.49 and 4.50 show the γ_{well} (for a single QW) as a function of wavelength calculated for state of the art CQWs and type-II QWs respectively. The ERs are shown in the insets of fig. 4.49 and 4.50.

In fig. 4.49 and 4.50, γ_{well} is calculated for 0V unbiased, and under 3V and 6V reverse bias. Each reverse bias voltage has equivalent electric fields strengths of 22 kV/cm and 41 kV/cm, with less than 2 kV/cm between the CQWs and type-II QWs. Here, calculations at a constant temperature are used, and assuming no voltage drop under 3V and 6V reverse bias.

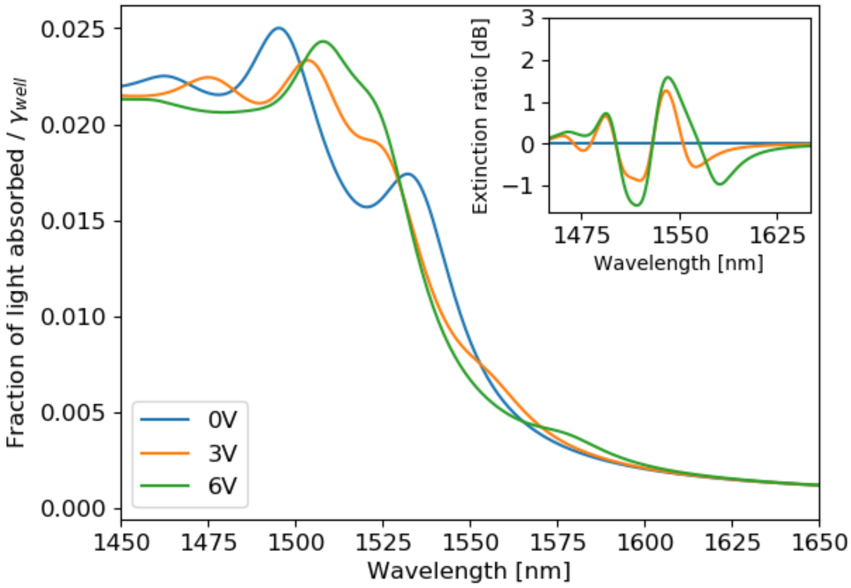

Fig. 4.49 – Fraction of light absorbed by state of the art CQW under 0V, 3V, and 6V reverse bias. ER is shown in the inset.

Fig. 4.49 shows a peak ER of 1.57dB for the CQW under 6V reverse bias and a γ_{well} magnitude of 0.0084 at 1550nm. Fig. 4.50 shows a peak ER of 2.96dB for the type-II QW under 6V reverse bias and a γ_{well} magnitude of 0.0018 at 1550nm.

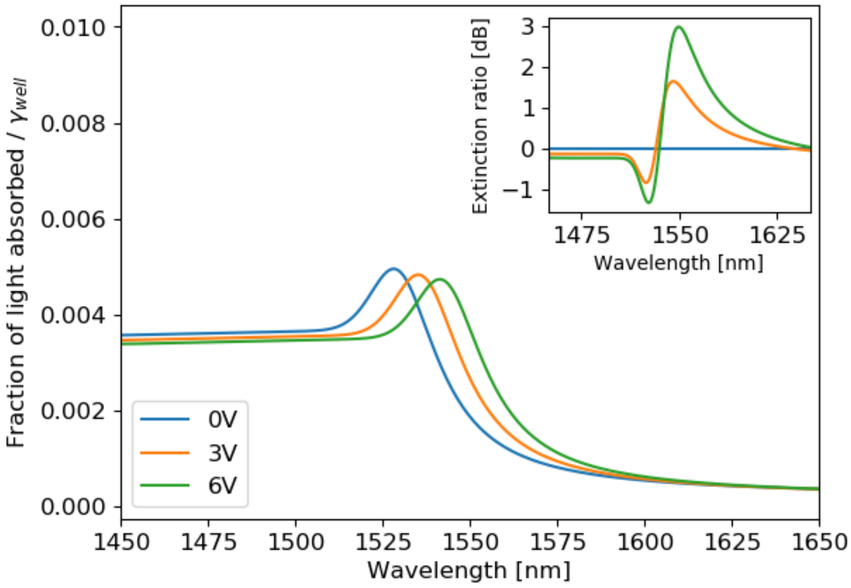

Fig. 4.50 – Fraction of light absorbed by type-II QW under 0V, 3V, and 6V reverse bias. ER is shown in the inset.

The unbiased γ_{well} is multiplied by the relative number of periods in each intrinsic region to provide an estimate of the fraction of light absorbed through a device, shown in fig. 4.51. This is used as a metric for the comparative optical IL between the two EAM structures. At 1550nm, the magnitude of the scaled γ_{well} in type-II QWs is approximately 30% that of the CQWs.

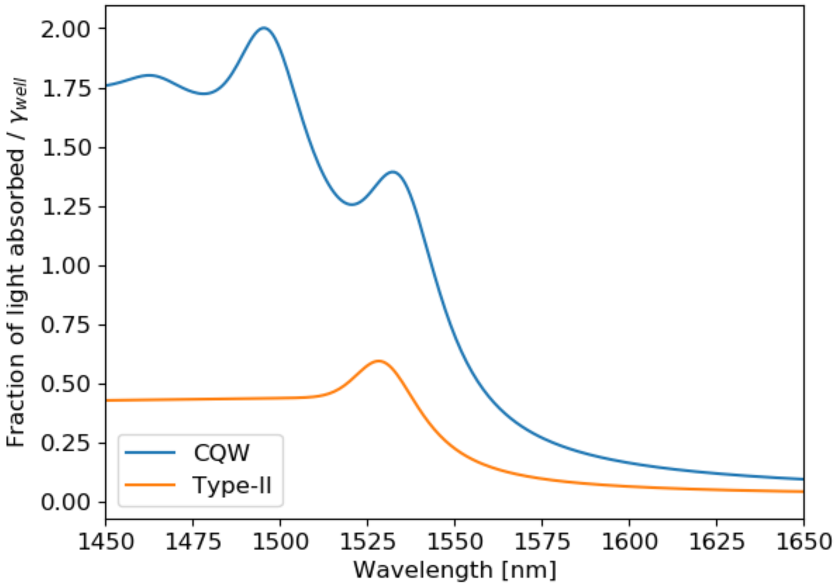

Fig. 4.51 – Fraction of light absorbed for 80 periods of the state of the art CQWs and 120 periods of the type-II QWs.

The calculated FoM for the CQWs and type-II QWs is shown in fig. 4.52. To maintain comparable magnitudes a normalization is applied to equate the FoM at 1550nm to that calculated in section 4.4 and verified by measurements in section 4.3 for CQWs.

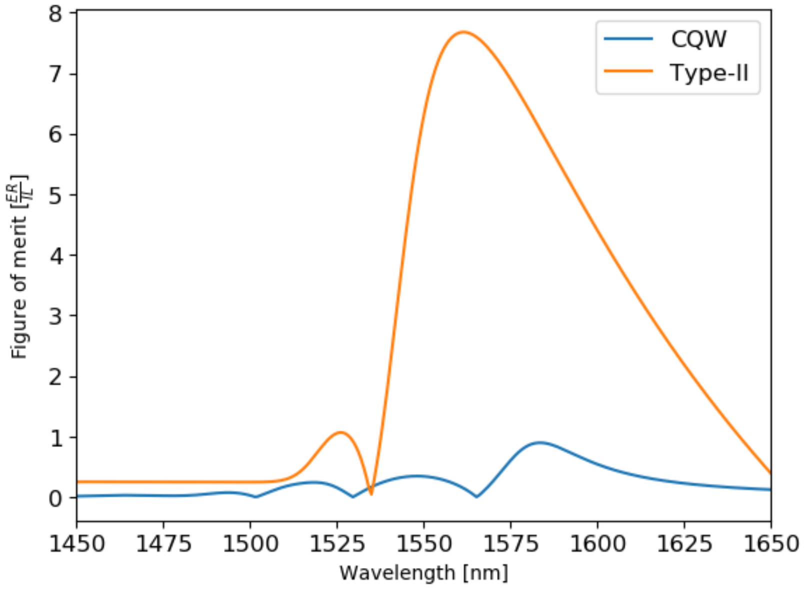

Fig. 4.52 – FoM calculated for state of the art CQWs and type-II QWs under 6V reverse bias voltage swing. Normalization to modelled and measured FoM is applied to both structures.

Fig. 4.52 demonstrates an enhancement in the FoM in type-II QWs over ten times that of the CQWs, accompanied by broadening of a single peak above 1535nm. This improvement is yielded in part through the significant reductions possible in the unbiased γ_{well}, which leads to a reduced optical IL, as shown in fig. 4.51. This is predominantly due to reductions in the wavefunction overlap due to spatial separation of carriers into adjacent layers (an effect arising from type-II band alignment).

Additionally, a significant improvement in the peak ER is predicted, with almost a factor 2 increase in type-II QWs compared with CQWs, as shown in fig. 4.49 and 4.50. This increase is primarily due to the large redshift in the ground state transition wavelength caused by the narrow QWs. It is also noted that the reduction and asymmetry in the type-II QW dimensions significantly increase the separation between bound energy states, particularly for holes. This provides a broadening of the ER spectrum and a reductions in the density of intersections between the unbiased and biased absorption spectra (shown in fig. 4.50), particularly at the band edge. The breadth in the ER and hence the FoM, may assist temperature dependent operation, because of the reduction of these intersections. SWaP capacity required for onboard temperature controls may then be reduced. Smaller and lighter Peltier elements may be used for example, with a lower power onboard fan required.

Although, this appears to be a vast improvement, additional features are important to note for the epitaxy and subsequent characterization of this structure. Firstly, the strain compensation layers must be correctly implemented, which will require a series of growth steps and calibration. This may also necessitate review of the current modelling parameters for example to update the exciton binding energy. Due to the increased number of periods and the small dimension of the QWs, there may be additional inhomogeneous broadening incurred through well-width variation. These factors may reduce the improvement seen in the peak ER.

Furthermore, the significant increase in the FoM shown in fig. 4.52 is heavily influenced by the low IL. Though low IL is desirable for long range FSO applications, if too low insufficient modulation will be imparted on the incident beam. Therefore, additional periods or stacked devices (as in [6]) may be necessary to impart appropriate modulation depending on the application. Through addition of further periods the risks of increased broadening, through well width fluctuations and electric field inhomogeneity, may be increased. On the other hand, the low IL and high ER are advantageous giving flexibility in epitaxial design depending on the particular FSO application. By increasing the periods, the intrinsic region is increased and thus the capacitance of the EAM is reduced. This may provide an increased modulation bandwidth for equivalent or even enhanced ER and IL.

4.6 Conclusion

State of the art CQW EAMs for retroreflective FSO applications have been analysed both experimentally and computationally. Using IR spectroscopic measurements the absorption spectrum has been characterized, with the ER, IL, and FoM calculated. Subsequently, transmission measurements over a range of temperatures at 1550nm were taken. Both experiments demonstrate limitations in the current design, with low ER and high IL degrading the FoM, and significant variation with temperature increases. With a 6V reverse bias voltage swing, the ER declines to 0 due to intersections of the biased and unbiased absorption spectra as temperature is increased. This has implications for the level of temperature control required on UAV payloads.

Through comparisons to transmission measurements, a semi-empirical modelling routine has been developed and validated. Using this model, the unbiased and reverse biased band structure and absorption have been evaluated. Temperature sensitivity and low ER was attributed to closely spaced and forbidden transitions. This led to a narrow region of the spectrum responsible for modulation near 1550nm. The CQW structure was shown to be susceptible to degradation in performance (particularly ER) with variations in growth and temperature.

Subsequently, type-II band alignment was exploited to improve EAM structures for MRR applications. InGaAs-GaAsSb on both GaAs and InP substrates were analysed unbiased to evaluate the cut-off wavelength and wavefunction overlap. GaAs-based structures were limited by wider QWs needed to meet the operating wavelength requirements, causing closely spaced energy levels. Reduced tunneling of carriers into adjacent layers lowered the IL but inhibited the desired changes from the QCSE.

An InP-based structure composed of 2.7nm $In_{0.43}GaAs$ and 1.5nm $GaAsSb_{0.40}$ QWs was proposed. InAlAs barriers were used for strain compensation, with composition and thickness approximated by equating the in-plane lattice constant of the epi-structure to the substrate. A 6.5nm thick $In_{0.60}AlAs$ barrier was confirmed optimum using simulated XRD peaks. Nevertheless, further epitaxial study is needed. The narrow QWs may be vulnerable to broadening from reduced interface definition caused by large growth temperature differences between antimonide and indium based alloys. Further, an iterative calibration approach may be required to achieve strain balancing whilst maintaining the desired operating wavelength.

Band structure and absorption calculations were used to compare the proposed type-II structure to the current state of the art CQWs. The fraction of light absorbed by a single QW was utilized to remove dependence on the well width, which is undefined in the type-II band alignment. The reduction in the wavefunction overlap provided significant reductions in the optical IL, and a broader ER spectrum was achieved. This should be more robust to temperature changes. A peak ER of 2.96dB in the type-II structure is obtained compared to 1.57dB in the CQW structure. This yielded a significant increase in the EAM FoM.

Further development, iterating between grown test structures and the semi-empirical model will be required to manufacture a high quality EAMs, and should lead to a design with significant benefits for applications in retroreflective FSO. In addition to improvements in IL, ER, and FoM, there is flexibility in design for future applications including modulation speed. By matching either the IL or the ER of the state of the art, it is possible to increase the intrinsic region thickness of the device and reduce the capacitance. Therefore, higher data rates may be achievable for equivalent if not enhanced IL or ER compared with the state of the art CQWs.

Chapter 5 Quantum dot laser diodes & electroabsorption modulators

In this chapter, a modelling routine for predicting the performance of quantum dot (QD) laser and modulator devices, with and without the inclusion of p-type modulation doping is described, with outputs discussed. Sample dependent parameters are extracted from absorption measurements and used to calculate the modal absorption coefficient prior to prediction of the quantum confined Stark effect (QCSE) and peak modal gain.

The modelling routine is then used to consider optimization of the movement of the global quasi-Fermi levels under forward bias, for p-type modulation doping at varying proximity to the dot layer. This can be used to observe some general trends and influence future growth of potentially impactful QD devices.

Finally, band diagrams with n-type direct doping and so called co-doping (including both n-type direct doping and p-type modulation doping) are analysed. Direct and co-doping techniques require further growth, fabrication, and characterization (particularly absorption spectra) to give a more complete theory, provide suitable parameters for use within this semi-empirical modelling routine, and to evaluate the viability for modulators.

5.1 Quantum dot epi-structures

Nominally identical InAs/InGaAs QD structures were considered, except for the inclusion of p-doping, shown in fig. 5.1. Wafers were grown by molecular beam epitaxy at University College London (UCL).

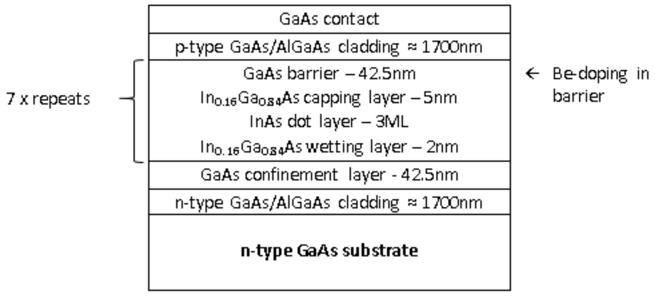

Fig. 5.1 – Epi-structure of measured and modelled QD structures with seven InAs/InGaAs DWELL layers and GaAs spacers in the active region, with cladding composed of GaAs/AlGaAs.

Active regions consisted of seven dots-in-a-well (DWELL) layers of InAs QDs within $In_{0.16}Ga_{0.84}As$ QWs. GaAs spacers separated each DWELL, with a 10nm layer of Beryllium doped GaAs grown within the center of the spacer in the p-doped samples. The waveguide core and cladding layers were composed of GaAs/$Al_{0.4}Ga_{0.6}As$, with superlattices for enhanced electrical conduction through interfaces. A dot areal density of $5 \times 10^{10} cm^{-2}$ was determined by atomic force microscopy (AFM) of an uncapped sample, with nominal modulation doping corresponding to 10 holes per dot (hpd). Samples were fabricated into segmented contact devices with modal absorption measured using the segmented contact method[143] by fellow PhD student Joe Mahoney.

5.2 Modelling procedure & assumptions

To allow for the calculation of the full device shown in fig. 5.1, including the cladding and all seven independent dot layers within a fully self-consistent Schrödinger-Poisson-current continuity equation solver (theory in chapter 2), additional assumptions were necessary and are highlighted here.

5.2.1 Band structure calculations

Full device band structure calculations were conducted via a self-consistent Schrödinger-Poisson-current solver from Nextnano[14]. A single band effective mass approximation (EMA) was used to compute bound states and wavefunctions in the DWELL layers, with resulting band diagrams shown in fig. 5.2 and 5.3 without and with p-modulation doping respectively. Quasi-Fermi levels were calculated by solving the current continuity equations for electrons and holes with a simple drift-diffusion transport model. The band alignment was calculated from average valence band energies with considerations of homogeneous strain through deformation potentials defined from a density functional theory approach developed in [21], [144], [145]. Material parameters in the Nextnano database were generally from [23], evaluated at $\boldsymbol{k} = 0$, the extrema of the Γ-valley with isotropic, parabolic effective masses assumed in the EMA.

The current continuity equations, balancing generation and recombination processes[146] (radiative, Shockley-Read-Hall, and Auger), were solved using a simple drift-diffusion transport approach[14], neglecting the peculiarities of quantum transport as in [101] and differing from the traditional rate equation models in previous work[8], [9]. Hence, it was possible to model the entire structure within a fully self-consistent Schrödinger-Poisson-current continuity equation solver, recalculating the band structure and quasi-Fermi levels for each step under reverse or forward bias. This method allowed for the assessment of the position, movement, and separation of the global quasi-Fermi levels, describing population and depletion of carriers in calculated states, for temperatures between 200-300K where quasi-thermal carrier distributions have been experimentally observed in InAs QDs[38]. Yet, as subsequently described, further approximations were necessary to maintain realistic outputs.

A one-dimensional geometry was employed, modelling the band structure as a function of the growth direction (along the z-axis), hence, only the layer thickness and the average dot height were required as structural inputs. This removed quadratic or even cubic dependencies on the computation times for two and three dimensional structures respectively. QD regions were initially predicted with QW-like properties, due to only one dimension of confinement available. Further approximations were input via the QD layer material parameters to correct the effective density of states, effective mass, and band gap energy to reflect experimental measurements.

The effective density of states, used to calculate band edge densities and hence critical to the magnitudes of the generation/recombination processes involved in the current continuity equations, was initially predicted as a QW, following eq. 5.1.

$$N_{eff}(z,T) = \frac{m^*_{DOS}(z)}{\pi\hbar^2} k_b T \tag{5.1}$$

The temperature dependent effective density of states, N_{eff}, was given as a function of both growth direction z and temperature, T. m^*_{DOS} was the density of states effective mass, calculated using eq. 5.2, with $\hbar$ and k_b the reduced Planck constant and Boltzmann constant respectively.

$$m^*_{DOS}(x) = \left(m^*_x(x) \cdot m^*_y(x) \cdot m^*_z(x)\right)^{1/3} \tag{5.2}$$

m^*_{DOS} described the average of the effective mass tensor relating the effective mass m^* along each axis, for a given band. In the EMA, bands are considered parabolic and isotropic near the band edge, with $m^*_x = m^*_y = m^*_z$. Although only the z-dimension was evaluated by the Schrödinger-Poisson equations, the current continuity equations required an average of all dimensions via m^*_{DOS}. The in-plane effective masses m^*_x, m^*_y were reduced to alter the effective density of states while not impacting calculations of band alignment and quantization. Therefore, an effective mass tensor ellipsoid was employed, as described in chapter 2, equating the effective density of states in the QD regions to twice that of the dot density (accounting for spin degeneracy) observed during epitaxy. This reduction corrected the recombination/generation magnitudes in the QD regions and provided realistic calculation of the movement of the global quasi-Fermi levels across the full structure.

To replicate the three experimentally observed QD absorption peaks and the corresponding nearly equally spaced transition energies, a parabolic potential was created by varying the composition of $In_{(x)}Ga_{(1-x)}As$ between x=0.16 at the well and x=1.0 at the center of the QD region. This was suggested by Blood as a method of representing the confining potential in the plane of self-assembled QDs in 3D calculations and in one dimension is a suitable approximation to predict near equally spaced transition energies, corresponding to the experimentally observed absorption peak separation[16].

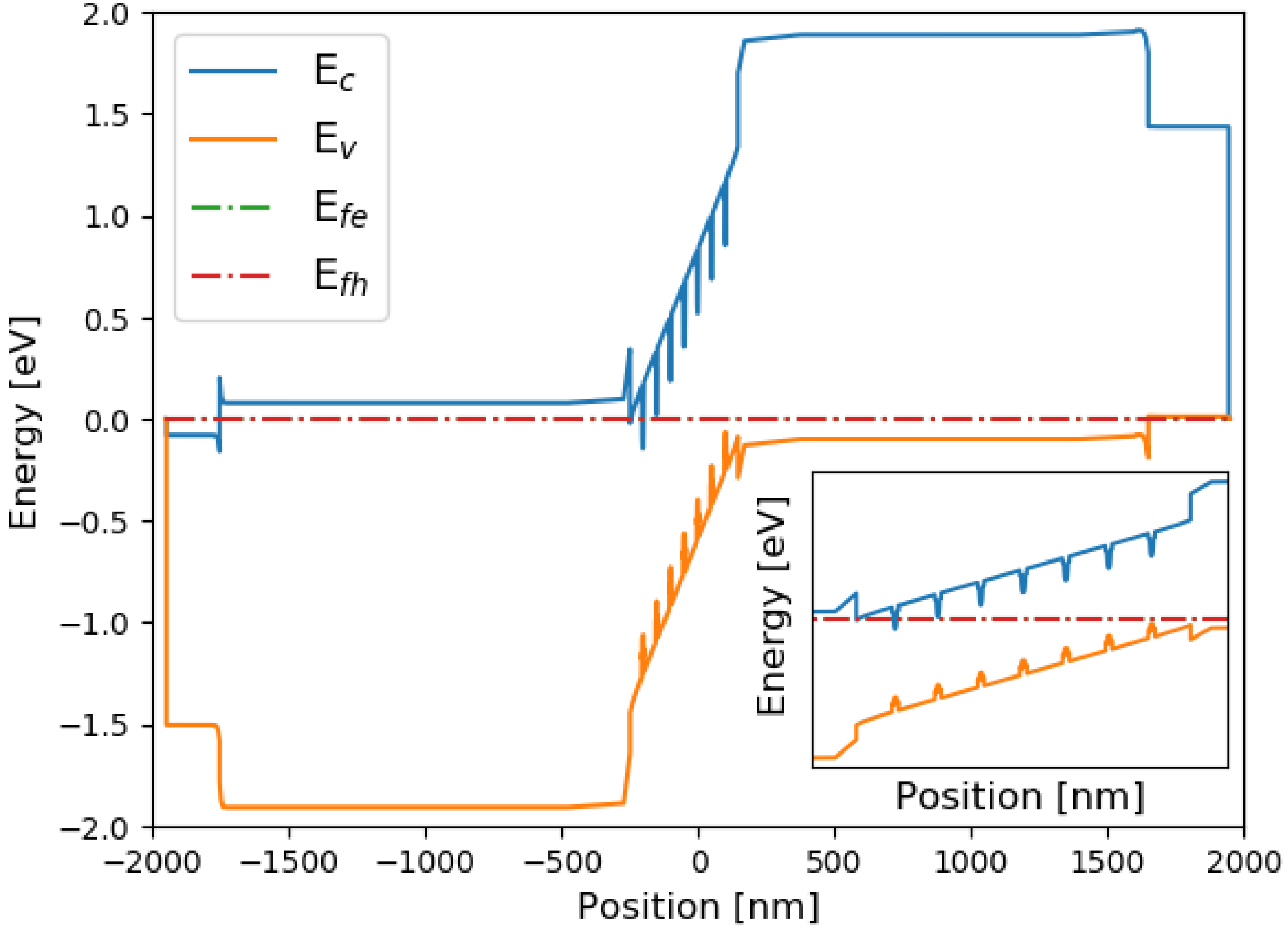

Fig. 5.2 – Full device band diagram calculated in Nextnano for undoped structure including corrections, with active region shown in inlay. Conduction band Ec, valence band, Ev, and overlapping electron and hole quasi-Fermi levels, Efe and Efh respectively.

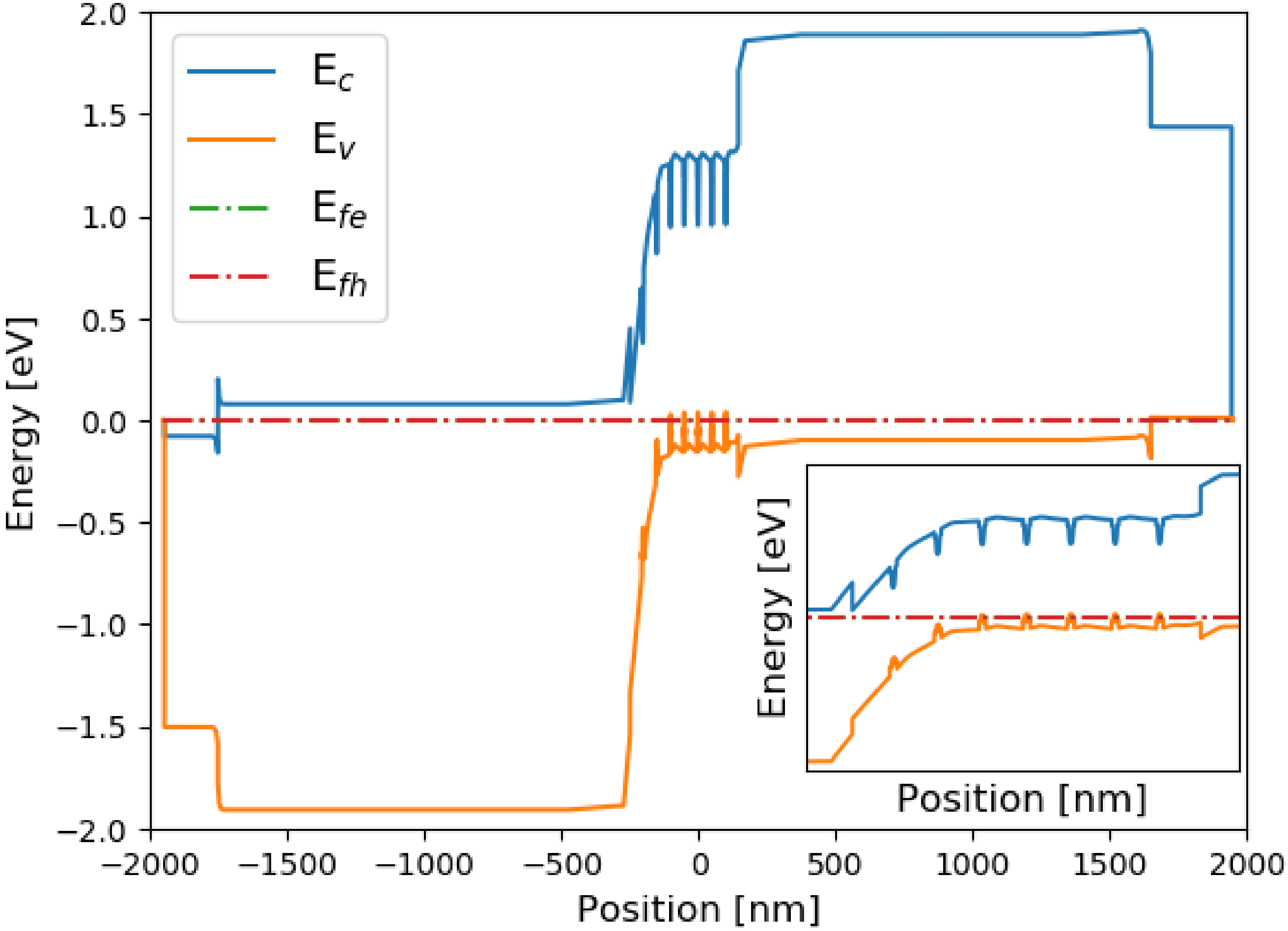

Fig. 5.3 – Full device band diagram calculated in Nextnano for p- doped structure including corrections, with active region shown in inlay

A further correction, this time to the effective mass in the growth direction m_z^* was used to match the energy separation between the absorption peaks.

Nextnano calculated homogeneous strain but was unable to capture the intricacies of a non-uniform strain distribution in a region with only one dimensional confinement[148], therefore an additional correction was made to the band gap energy to match the experimentally observed ground state transition energy ≈ 0.98eV, similarly to [47]. Three electron and twelve hole states were calculated in each dot layer.

The resulting one dimensional confining potentials were shallow, and while predicting the transition energies well, the wavefunction overlap integral was not suitable for prediction of the QCSE. Capturing a realistic approximation for the overlap with only a single dimension available for confinement required a separate analysis, to consider the wavefunctions in a deeper potential, matching the barrier energy in [47]. The confinement potential was inversely related to the size (Bohr radius) of the dot in [149], hence a deeper potential was required to approximate the increased confinement associated with a three dimensional quantum dot. This yielded average overlap integrals across all seven layers of 95% and 94% under zero bias, decreasing at the same rate to 90% and 89% under a 5V reverse bias, for undoped and p-doped structures respectively. The 1% variation between the undoped and p-doped values can be observed in fig. 5.2 and 5.3, with the undoped showing a consistent built in potential across all dot layers. The p-doped structure showed uniform, flattened bands adjacent to the p-type cladding with overlap ≈ 100%, whereas the layer adjacent to the n-type cladding layer is highly distorted with significantly lower overlap leading to the average values quoted above.

Under forward bias, the bands flattened and overlap was ≈ 100% for all layers in both structures. The high overlap was attributed to the narrow confining potential in the z-direction, which is consistent with measurements of narrow quantum wells in [51].

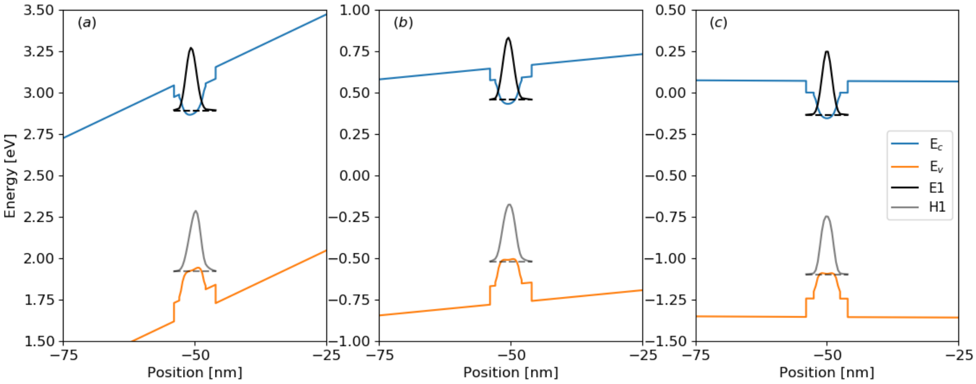

Fig. 5.4 – Calculated electron (E1) and hole (H1) ground state energy levels and wavefunctions for the undoped structure in the conduction and valence band under (a) reverse bias, (b) zero bias, and (c) forward bias conditions.

Undoped and p-doped structures were simulated under reverse, zero, and forward bias to predict the QCSE, modal absorption, and peak gain respectively, with the central dot layer shown in fig. 5.4 and 5.5 respectively.

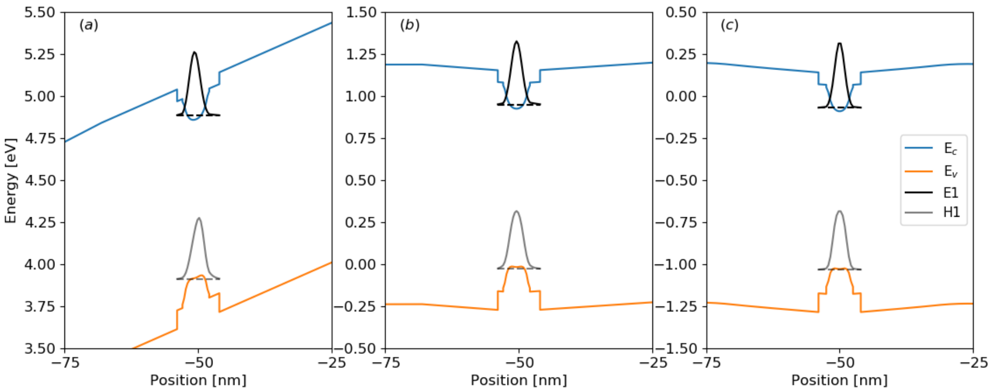

Fig. 5.5 – Calculated ground state energy levels and wavefunctions for the p-doped structure in the conduction and valence band under (a) reverse bias, (b) zero bias, and (c) forward bias conditions.

5.2.2 Optical confinement weighting

Optical confinement factor weightings at each layer of dots was determined using an eigenmode expansion solver from Lumerical (theory in chapter 2), with the mode profile and weightings as percentages shown in fig. 5.6. This permitted calculation of modal absorption and gain, which was directly comparable to experimental measurements. A layer thickness of 3MLs was used for the QD layers, equal to the quantity of InAs deposited during epitaxy. Note, this differed from the 5nm thickness used in the full device band structure calculations, which referred to the mean height of the QDs observed during AFM. InAs dot layers, shown in the table of fig. 5.6, were labelled as deposited, 1 through to 7.

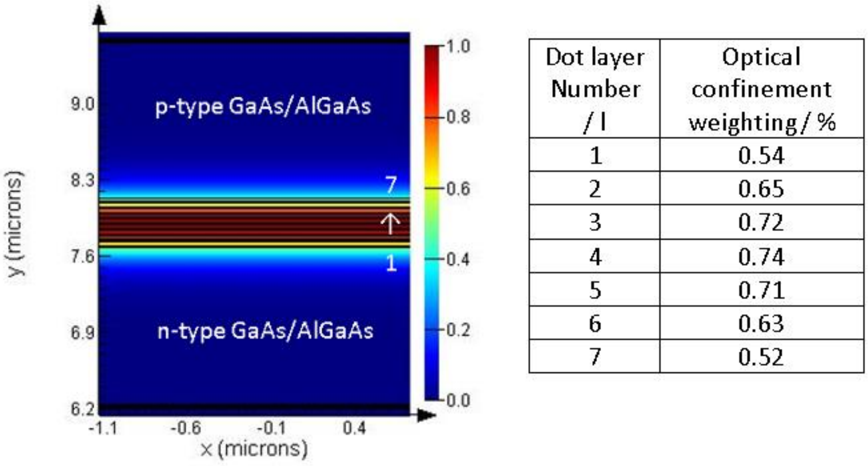

Dot layer Number / l	Optical confinement weighting / %
1	0.54
2	0.65
3	0.72
4	0.74
5	0.71
6	0.63
7	0.52

Fig. 5.6 – Optical confinement weighting at each layer of dots, where layer 1 is adjacent to the n-side, calculated in Lumerical's MODE waveguide simulator suite device width scaled here to clearly distinguish active region layer structure.

A total optical confinement factor of ≈ 4.5% was calculated.

5.2.3 Fitting experimental absorption spectra

Measured absorption spectra were fitted with Gaussian functions representing the inhomogeneously broadened ground and first excited state transitions, as shown in fig. 5.7 and 5.8. These measurements were taken by Mahoney.

Internal optical losses of < 1 cm^{-1} were extracted for each sample and the combined homogeneous and inhomogeneous broadening was approximated from the extracted standard deviations. InAs QDs have been shown to exhibit two distinct size distributions under higher growth temperatures, becoming multimodal at lower temperatures[48]. Here a bimodal dot size distribution was observed to provide the best fit with absorption data, similarly to [150]. Measurements using AFM, photoluminescence, and transmission electron microscopy methods have found similar conclusions for InAs QDs[151]. The ratio of the large dot (LD) to small dot (SD) densities from the area under the fitted Gaussians[50] was determined assuming bimodality.

Additionally, the separation between LD and SD ground state energy was identified and used to approximate the size difference in terms of the height of the dot. This was used to calculate the difference in energy shift experienced by the SD under forward and reverse bias following the same procedure in Nextnano described previously.

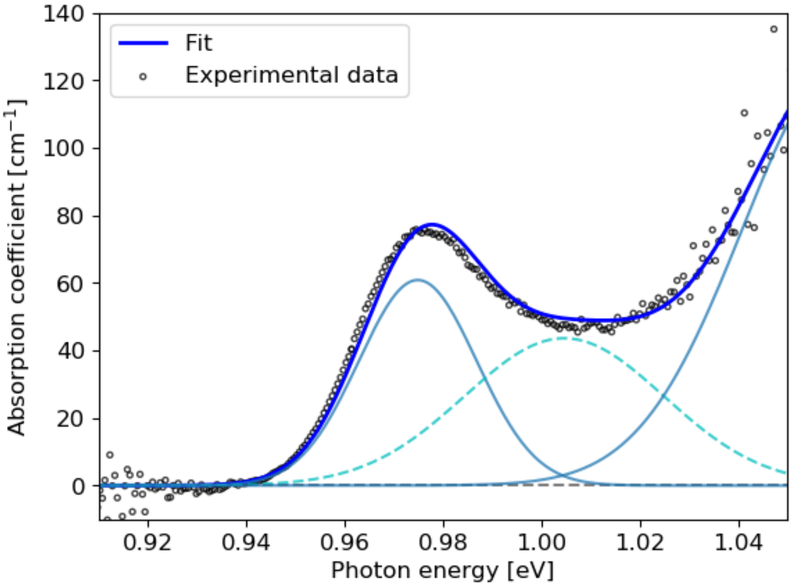

Fig. 5.7 – Fitted experimental data for modal absorption coefficient against photon energy for the undoped structure. LD ground and excited state, and SD ground state fitted functions represented by solid and dashed lines respectively. Measurements taken by Joe Mahoney.

The bimodal ratios calculated from fitted data were ≈41:59 and ≈63:37, between large to small dot distributions for undoped and p-doped structures respectively. This difference may have resulted from variation in growth temperatures between undoped and p-doped wafers during epitaxy[48], though it is also possible that inclusion of the dopant impurities themselves may have affected the growth conditions.

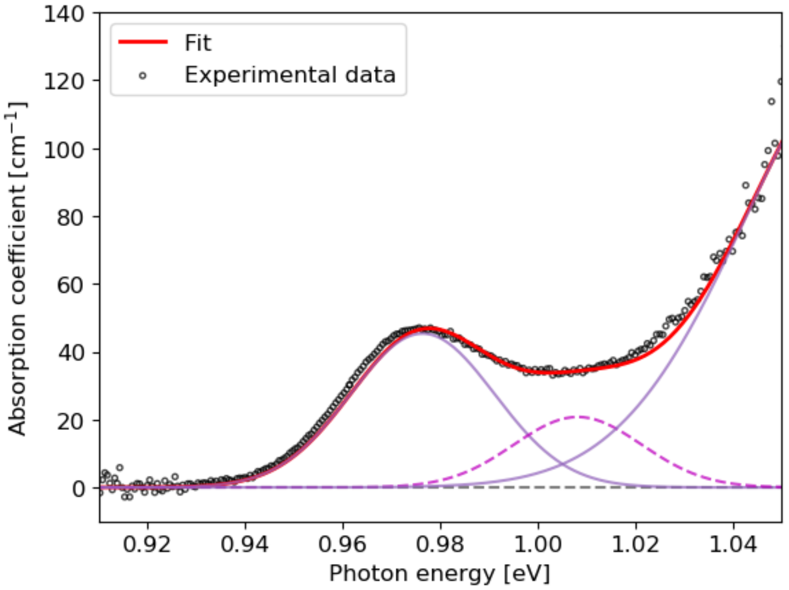

Fig. 5.8 – Fitted experimental data for modal absorption coefficient against photon energy for p-modulation doped structure. LD ground and excited state, and SD ground state fitting functions represented by solid and dashed lines respectively. Measurements taken by Joe Mahoney.

The energy separation between ground state absorption peaks for LD and SD was fitted as 30meV and 32meV for undoped and p-doped structures respectively.

5.2.4 Absorption & gain calculation

Preceding data from Nextnano, Lumerical, combined with parameters extracted from fitted absorption data were used within a Python script developed for calculating absorption and gain, similarly to [46], using eq. 5.3 (extended from eq. 2.27 in chapter 2). Reverse and forward bias conditions employed in the band structure calculations were used to predict the QCSE and gain spectra respectively.

$$\alpha(\hbar\omega) = \sum_l \sum_D \sum_{nm} \frac{\Gamma_l \pi e^2 \hbar M_b^2 |I_{ov}|^2 N_{L,S} s_i}{c m_0 \varepsilon_0 n_r L_z E_{nm}} S(E_{nm}) G(E_{nm})(f_v - f_c) \tag{5.3}$$

Modal absorption as a function of photon energy was first calculated by summing for all transitions in the QD region, with n and m the energy levels in the conduction and valence band respectively. These were summed for D dot size contributions LD and SD, and at each layer of the structure, l. Here, *e* represented the elementary charge, c, the speed of light in a vacuum and m_0 the electron rest mass. The areal dot densities for LDs and SDs were $N_{L,S}$. s_i was the degeneracy of the transition (2 and 4 for ground and first excited state respectively). The real refractive index was n_r, dot height L_z, and M_b^2 was the bulk matrix element relating to the Kane energy parameter ($M_b^2 = \frac{m_0}{6}E_p$). Γ_l was the optical confinement layer weighting. $f_v - f_c$ was the difference in valence and conduction state electron occupation probabilities, calculated using Fermi-Dirac statistics with the corresponding quasi-Fermi level energies, resulting in modal gain once population inversion was achieved. The wavefunction overlap integral was $|I_{ov}|^2$.Homogeneous $S(E_{nm})$, and inhomogeneous $G(E_{nm})$, broadening distributions were modelled as hyperbolic secant as in [16], [46], and Gaussian distributions respectively as functions of the transition energy E_{nm}, as shown in eq. 5.4 and 5.5.

$$S(E_{nm}) = sech\left(\frac{E_{nm}\tau}{\hbar}\right) \tag{5.4}$$

$$G(E_{cv}) = \frac{1}{\sqrt{2\pi\sigma}}e^{-\frac{(E_{cv}-\hbar\omega)^2}{2\sigma^2}} \tag{5.5}$$

Here, τ was the time between dephasing events. Inhomogeneous broadening was modelled as a Gaussian function, where σ was the standard deviation in transition energies due to dot size variation during growth. σ was assumed constant for both structures at ≈ 22meV in the fitting procedure. There was a calculated decrease of ≈ 35fs in τ between undoped and p-doped structures respectively. The extinction ratio (ER) and insertion loss (IL) were evaluated from 0-5V reverse biased structures in units of dBmm^{-1} in eq. 5.6 and 5.7, with the FoM taken as the ratio between ER and IL.

$$ER = -0.434\alpha_{ON} + 0.434\alpha_{OFF} \tag{5.6}$$

$$IL = -0.434\alpha_{OFF} \tag{5.7}$$

5.3 Absorption and the quantum confined Stark effect

The calculated modal absorption under zero bias was compared to experimental data to verify the modelling procedure prior to simulating structures under applied reverse and forward bias to predict the QCSE and gain respectively. The inhomogeneous broadening and dot density was assumed to be constant in these calculations, based on AFM and PL measurements carried out after growth at UCL. Appropriate replication of the band edge absorption, though with some departure at the first excited state was observed in fig. 5.9 and 5.10.

Additionally, modal absorption was calculated a second time, in this instance with the degree of depletion fixed to $f_v - f_c = 1$. The difference between the two calculations indicated the magnitude of the effects of state-filling and resulting carrier blocking of the absorption process, which has been thought to be important for p-doped structures[13], and was evident in the calculated band structures (shown in fig. 5.2 and 5.3).

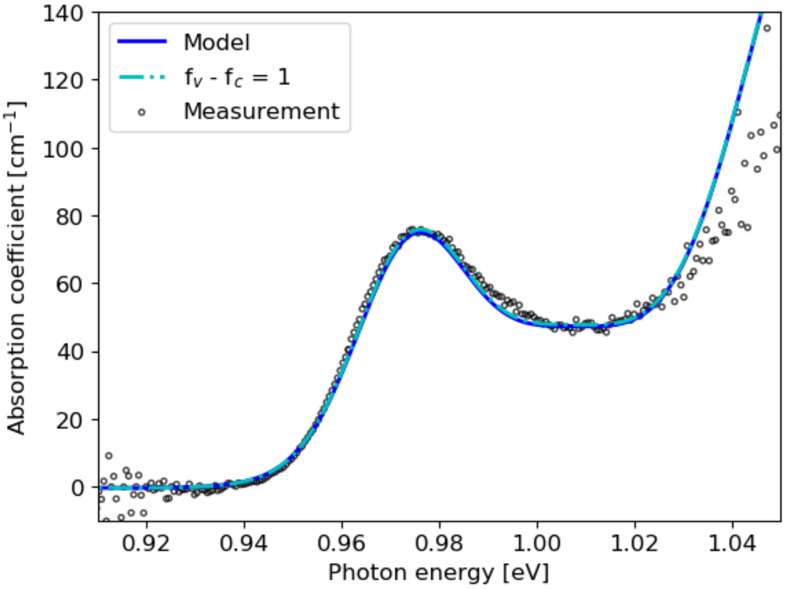

Fig. 5.9 – Modelled and experimentally measured modal absorption coefficient against photon energy for undoped structure. Model run a second time with fv - fc = 1 to evaluate the role of carrier blocking overlaps original spectrum. Measurements taken by Joe Mahoney.

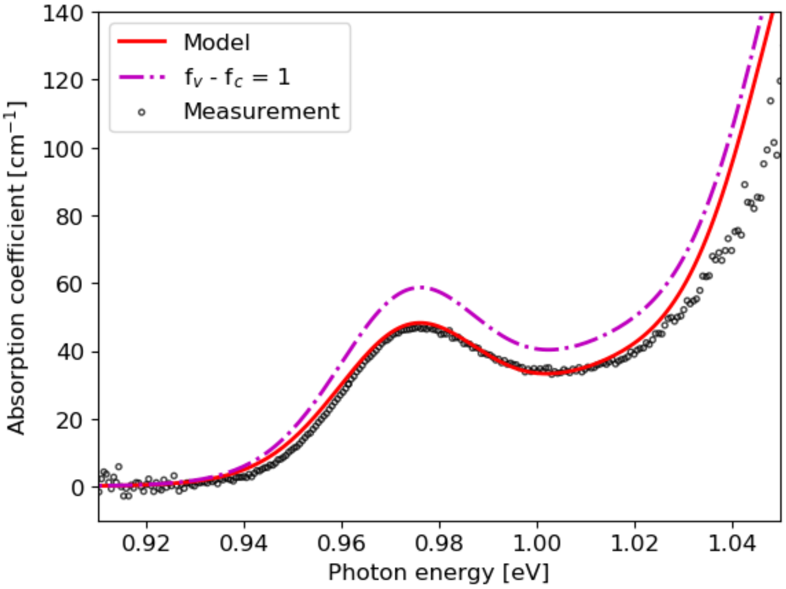

Fig. 5.10 – Modelled and experimentally measured modal absorption coefficient against photon energy for p-doped structure. Model run a second time with fv - fc = 1 to evaluate the role of carrier blocking. Measurements taken by Joe Mahoney.

A negligible change was observed in the undoped structure, signifying that electrons and holes in the conduction and valence bands respectively were almost completely depleted under zero bias. In the p-doped structure there was a difference with an increase in the maximum modal absorption by ≈ 11cm^{-1} when $f_v - f_c = 1$.

However, this was only a fraction of the total difference between p-doped and undoped absorption magnitude. Therefore the larger part of the effect was attributed to greater homogeneous broadening caused by increased carrier scattering rates accounting for the remaining differences in absorption magnitude and broadening. A 41% increase in the carrier scattering rate, calculated from the values of τ, used in the homogeneous broadening term was necessary to describe the remaining difference in the absorption magnitude in the ground state between p-doped and undoped structures.

For full decomposition of the dominant carrier scattering mechanisms in this process a full many-body calculation may be required theoretically to understand the impacts of the p-type modulation doping as in [11]. Further experimental investigation could also assist with the understanding of dominant scattering mechanisms by growing a series of structures with a variety of p-doping placement, layer thickness, and impurity concentrations, and with characterisation under a variety of temperatures. However, Alexander et al. have attributed an increase in the ground state saturated gain to increased carrier-carrier scattering with increasing p-doping[152] which has been corroborated by ultrafast measurements[153].

When a reverse bias was applied we calculated further depletion of the QD layers in the p-doped structure. This led to an increase in the effective absorption with applied reverse bias, an uncommon but beneficial phenomenon for modulating devices. This increase overcame the small predicted reduction of the wavefunction overlap. The band diagrams, shown in fig. 5.11 and 5.12, demonstrated increased deformation in the active region of the p-doped structure, signifying a non-uniformity of carrier depletion across the QD layers.

Qualitatively, under a reverse bias of 5V, the relevant quasi-Fermi levels in the undoped structure were always distant from the dot potential signifying minimum carrier-blocking. Whereas, the hole quasi-Fermi level in the p-doped structure remained very close to two dot layers under a 5V reverse bias. This signifies appreciable population of holes in valence states, with some continued blocking of absorption compared to the undoped structure, indicating potential continued increase of absorption magnitude with reverse bias.

The calculated absorption spectra for undoped and p-doped structures are shown in fig. 5.13 under a zero and 5V reverse bias respectively. Stark shifts of 7.5nm and 5.4nm are observed in undoped and p-doped structures respectively, suggesting enhanced ER in the undoped structure. The reduced broadening and higher magnitude in absorption coefficient in the undoped structure shown in fig. 5.13 gives a sharper absorption edge and is indicative of potentially higher peak ERs. The p-doped data derived from an absorption spectrum that is significantly broader than the undoped spectrum and increases in magnitude under bias, resulting from growing depletion in the conduction band, reducing carrier blocking, may have benefits for modulating devices, with a low IL and improved temperature stability as suggested by Mahoney et al.[13].

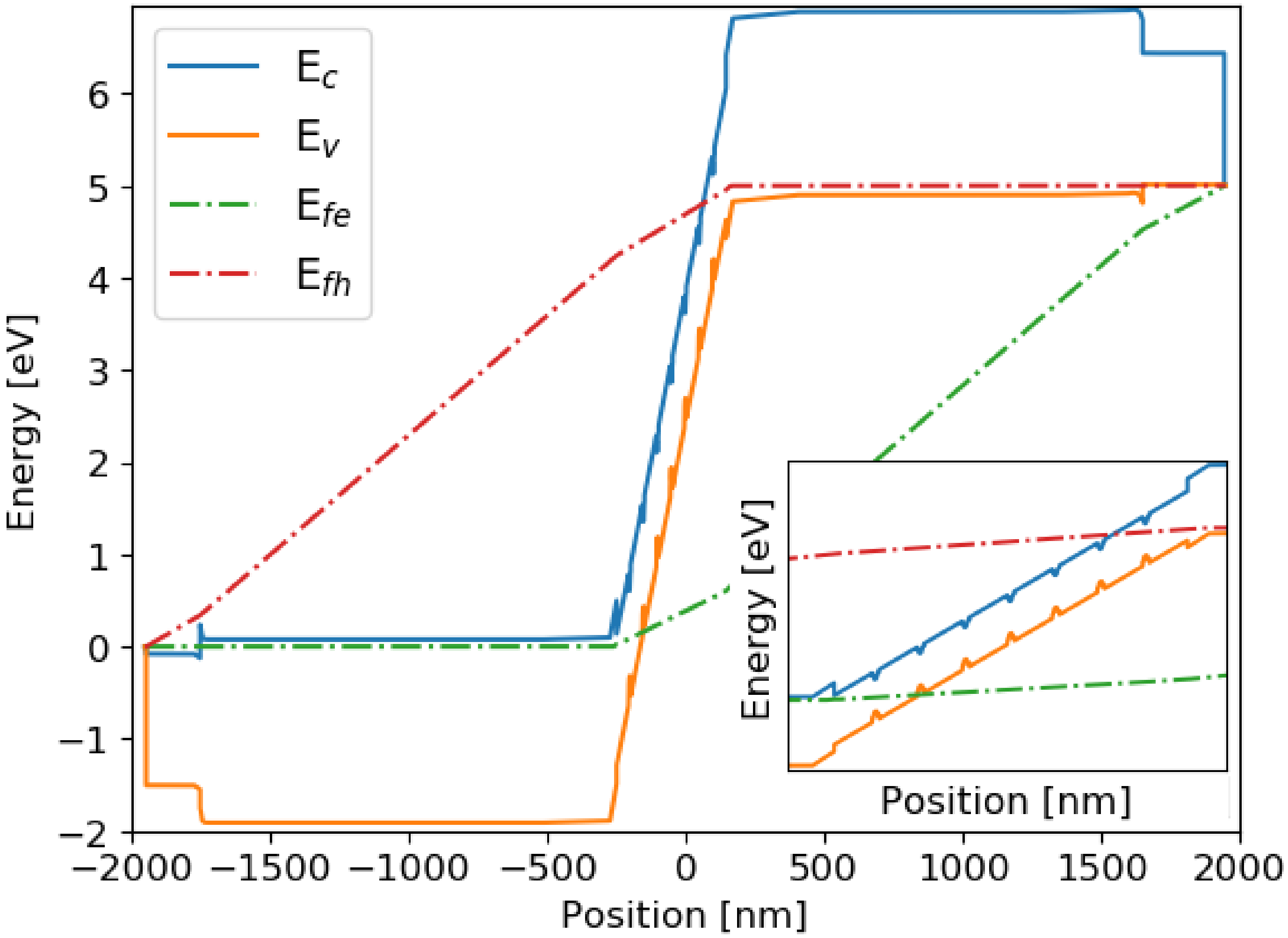

Fig. 5.11 – Full device band diagram calculated for undoped structure under reverse bias, with active region shown in inlay.

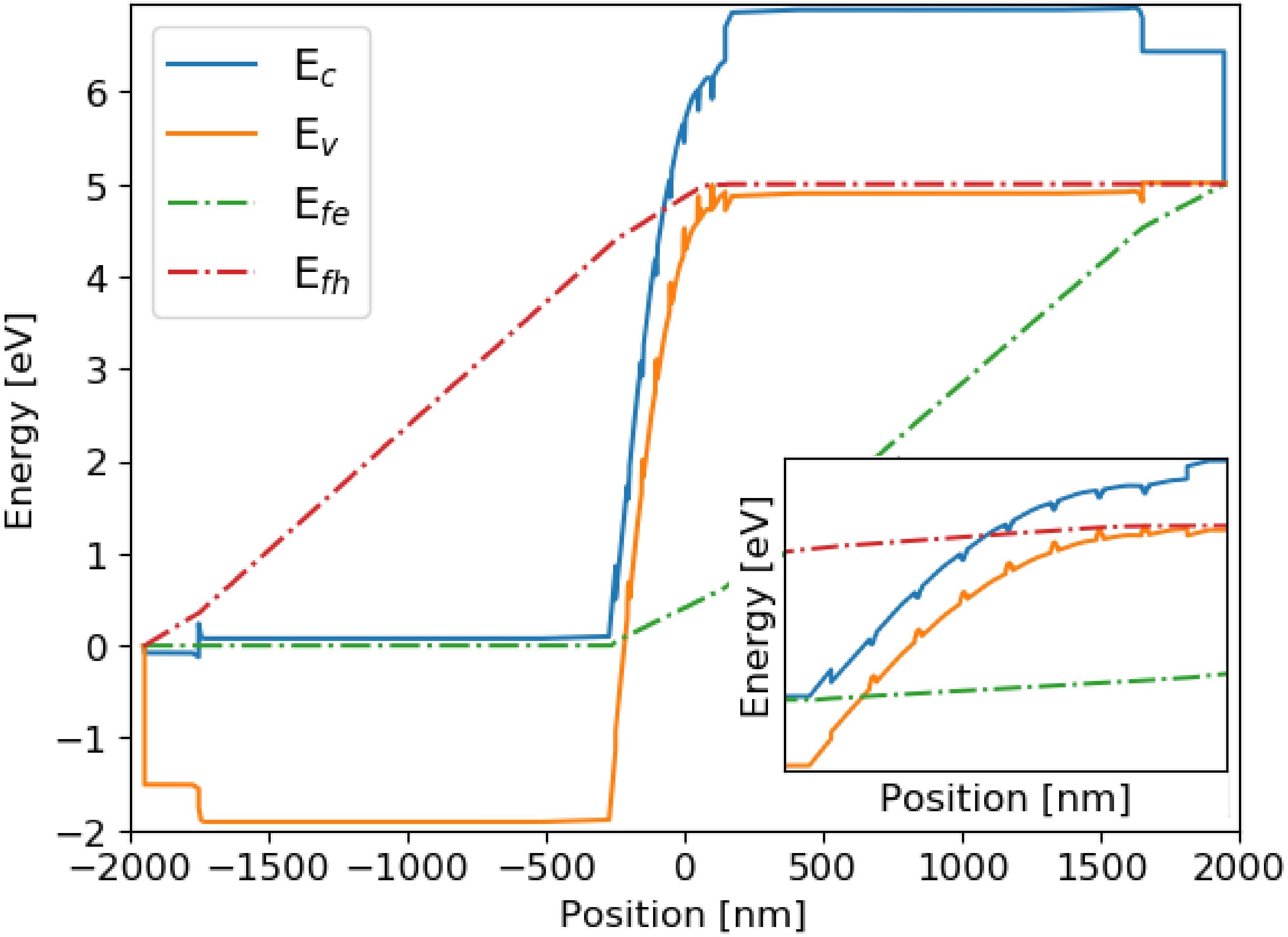

Fig. 5.12 – Full device band diagram calculated for p-doped structure under reverse bias, with active region shown in inlay.

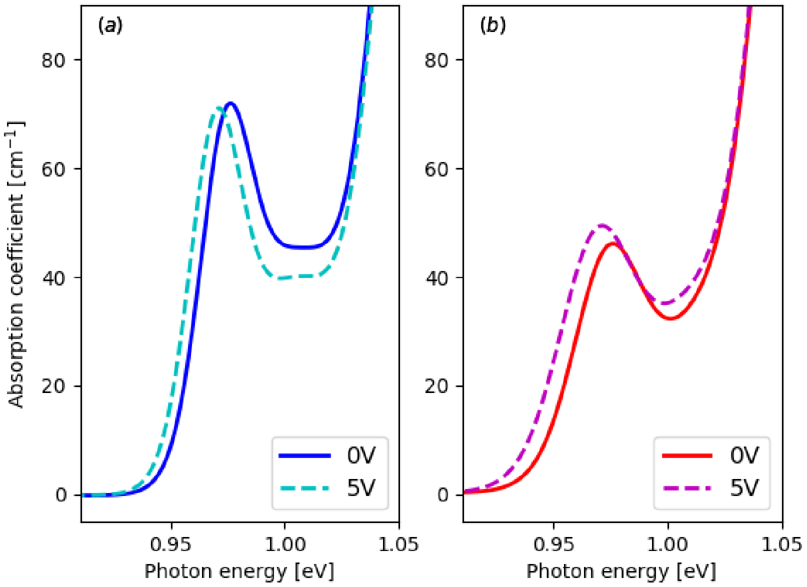

Fig. 5.13 – Calculated absorption spectra shown as solid and dashed lines under 0V and 5V reverse bias respectively for (a) undoped, and (b) p-doped structures.

To assess the relative potential of the undoped and p-doped material for electro-absorption modulation the ER and the IL, calculated in eq. 5.6 and 5.7, are plotted in fig. 5.14 and 5.15. The FoM defined in the literature as the ratio between ER and IL, (equivalent to $\Delta\alpha/\alpha_0$) , was used to compare potential modulator performance[54], [55] and is plotted in fig. 5.16. The mean electric field strength between structures was comparable.

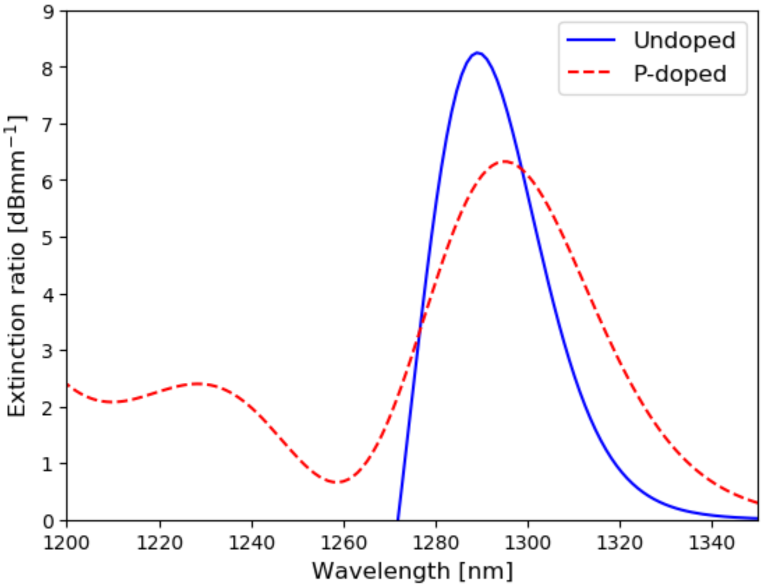

Fig. 5.14 – Predicted ER for undoped and p-doped structures respectively.

Considering the ER, the undoped structure exhibited the highest peak ER of over 8dBmm^{-1}, though an increase in the ER for the p-doped structure was predicted at wavelengths higher than 1300nm. The ER predicted in the p-doped structure is at its maximum at 1300nm with ER of 6 dBmm^{-1}. Nevertheless, due to the additional homogeneous broadening associated with the p-doped structure, the FoM is limited by the IL between wavelengths 1300-1311nm. This finding is contrary to Mahoney et al. who found reduced IL beneficial to the FoM[13], though this appears to be due to a further increase in the level of broadening in the presented samples, with the relative position of the ground state peak, corresponding to a different mean dot size. It may also indicate the importance of a better understanding of the broadening mechanisms and careful selection of the doping concentration to yield full benefits. Although there is a reduction in the peak of the IL, this is not necessarily an improvement to the modulator performance, as the increased broadening caused significant absorption at longer wavelengths where the effects due to the QCSE are most pronounced.

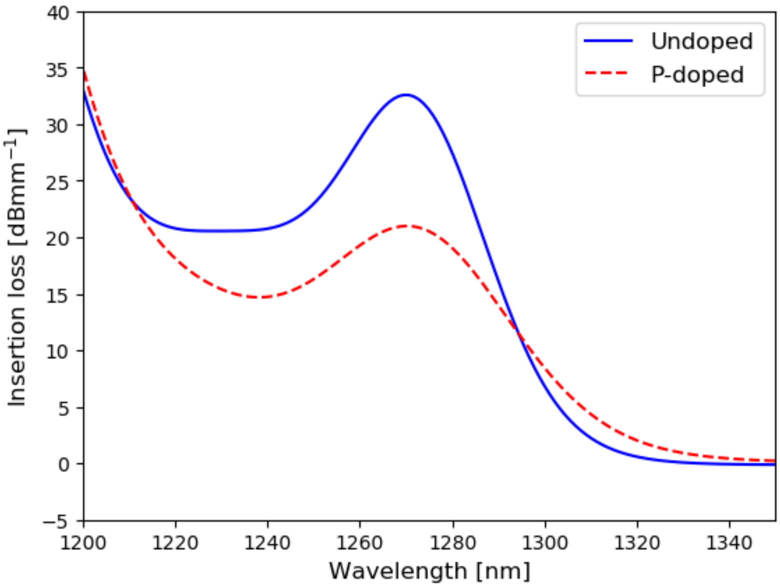

Fig. 5.15 – Predicted IL for undoped and p-doped structures respectively.

Fig. 5.16 shows enhanced amplitude and breadth of the FoM in the p-doped structure, although a lower peak ER was observed in the p-doped structure as with [13], with a greater FoM achieved for wavelengths >1310nm. For operation at the peak FoM wavelength of 1336nm a very low modulation of an incident beam would be achieved for the current structure and for practical use a greater interaction length or additional dot layers would be required for this epistructure.

However, as shown in fig. 5.14 and 5.15, the p-doped structure has ERs>4dBmm^{-1} with ILs<4dBmm^{-1} at 1310nm still offering improvements. Though these structures have not been optimised for electroabsorption, this result suggests potential benefits which may become significant at appropriate levels and positioning of the p-modulation doping layer. The breadth in the p-doped FoM in fig. 5.16 is also suggestive of enhanced temperature stability. Furthermore, for enhanced operation at 1310nm, smaller dot sizes may yield better results for this level of p-doping, with increased confinement blue shifting the absorption spectra.

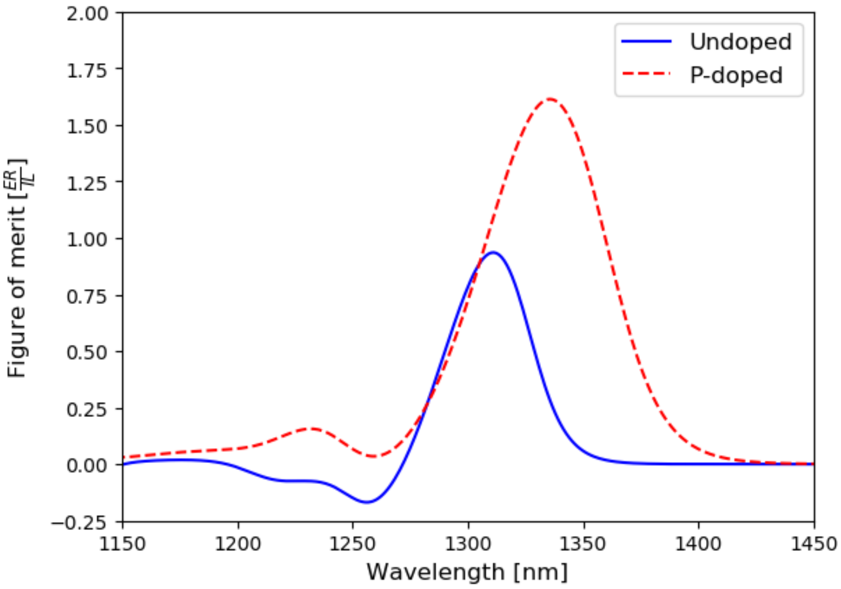

Fig. 5.16 – Predicted FoM for undoped and p-doped structures.

5.4 Modal gain predictions

The laser performance of the structures was predicted under forward bias to calculate modal gain and peak modal gain. Modal gain spectra are shown in fig. 5.17 and 5.18 with corresponding band diagrams shown in fig. 5.19 and 5.20, for undoped and p-doped structures respectively.

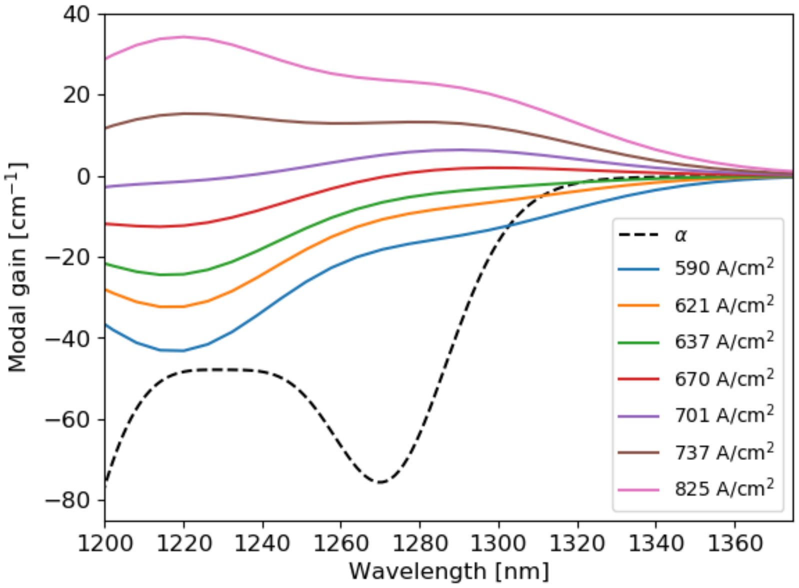

Fig. 5.17 – Modal gain spectra for undoped structure. Modal absorption shown by dashed line, and gain spectra shown with increasing current density.

A linearly increasing carrier scattering rate was included due to an increasing carrier density arising with carrier injection. This has been shown in [11] to depend on the level of doping. Following [11] this led to a carrier scattering rate in the p-doped structure three times that of the undoped structure at the highest value of carrier injection under predicted forward bias (for a 10 hpd doping level).

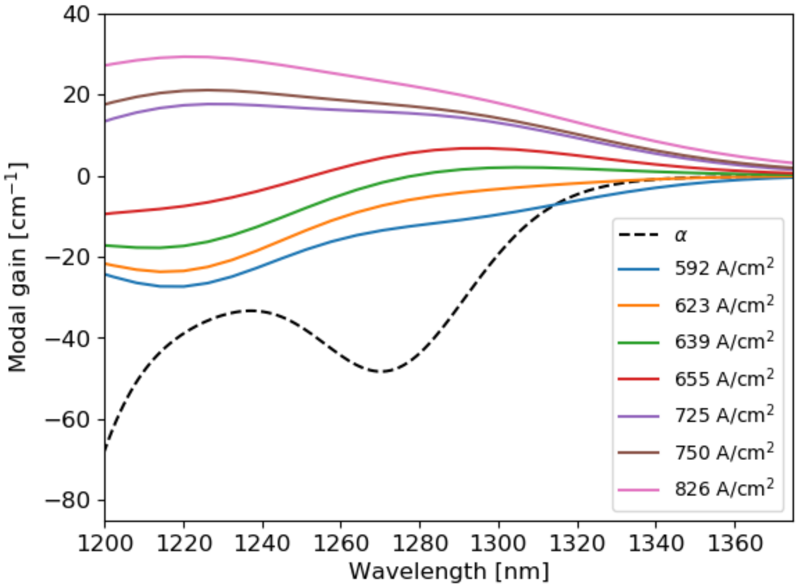

Fig. 5.18 – Modal gain spectra for p-doped structure. Modal absorption shown by dashed line, and gain spectra shown with increasing current density.

The detrimental effect of the increased carrier scattering rate is apparent in fig. 5.17 and 5.18 from the broadened spectra of the p-doped structure. Increased broadening also led to a reduced contribution of the excited state, leading to ground state operation up to higher values of carrier injection. Although, the p-doped structure also has an increased number of LDs which produced lower confinement energy and occupied longer wavelengths. The peak gain can be described by $G_{pk} = g_{max}(f_c - f_v)$, where g_{max} is the maximum potential modal gain achieved in eq. 5.3 at full inversion, $(f_c - f_v) = 1$.

Therefore, the occupation probabilities, calculated from the global quasi-Fermi levels, indicate the impact of p-modulation doping on the population of the valence and conduction states, and the modal gain. The calculated occupation probabilities in the conduction state f_c and valence state f_v using Fermi-Dirac statistics are shown in fig. 5.21 and 5.22, and the degree of inversion in fig. 5.23.

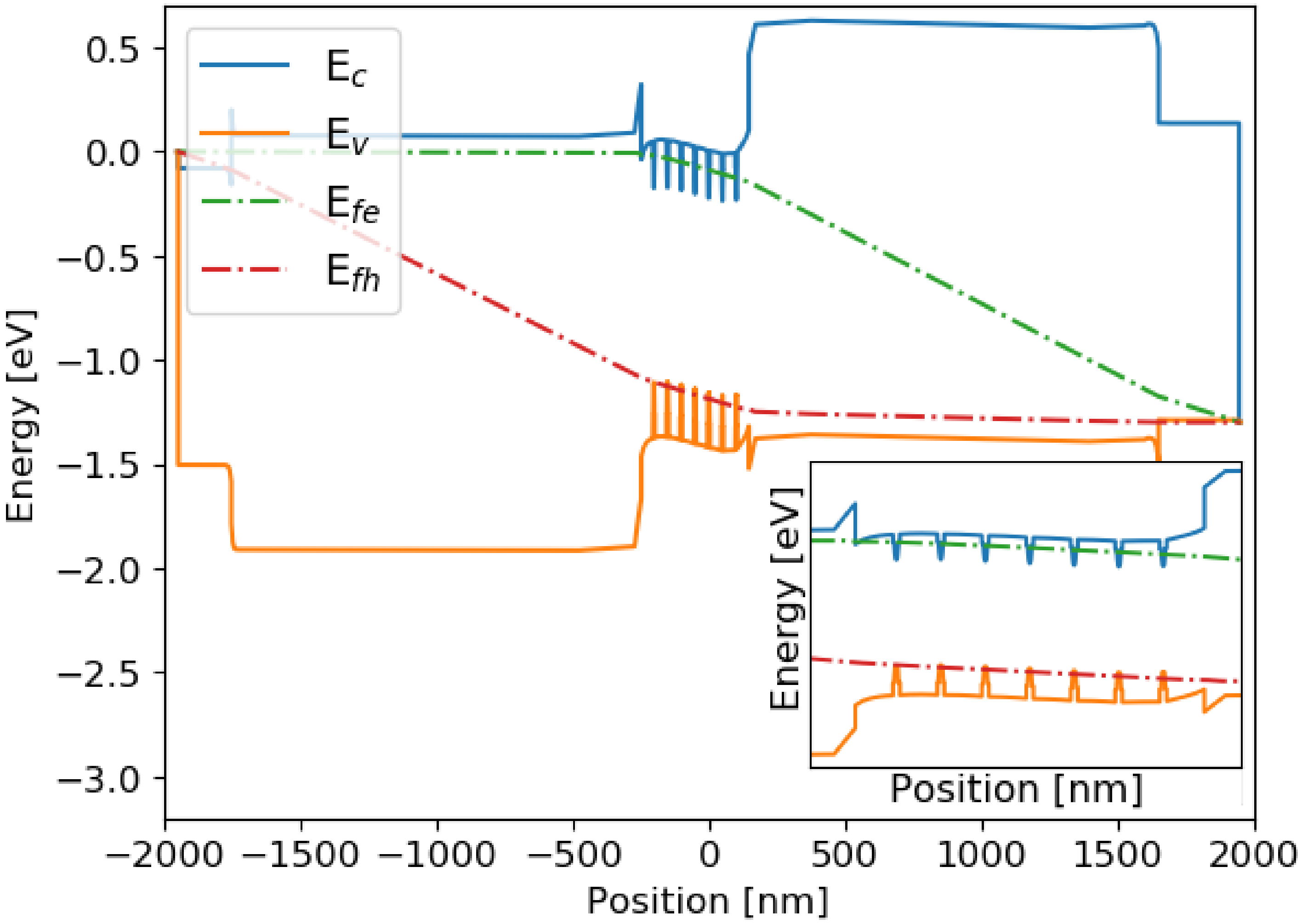

Fig. 5.19 – Full device band diagram calculated for undoped structure under forward bias, with active region shown in inlay.

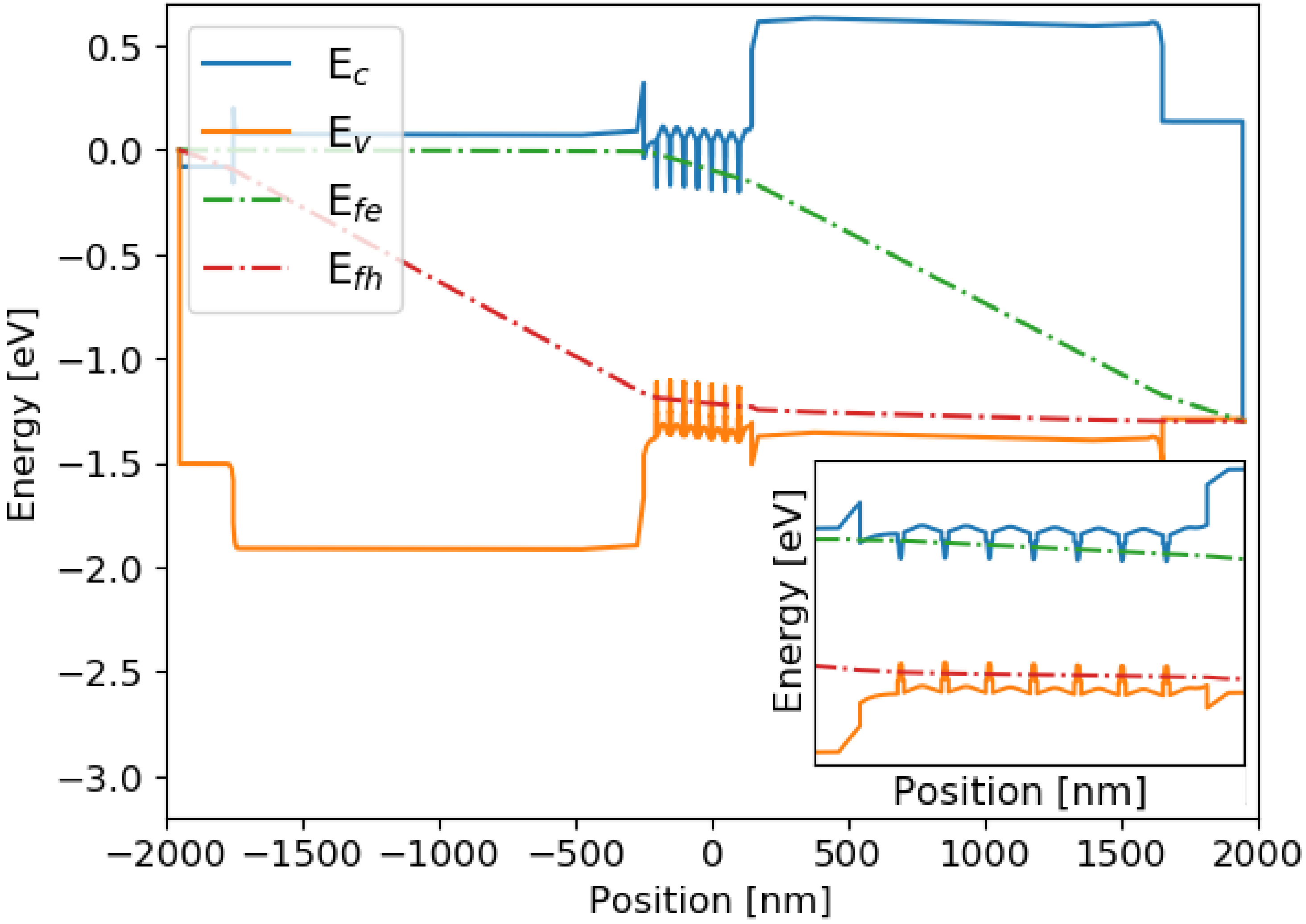

Fig. 5.20 – Full device band diagram calculated for p-doped structure under forward bias, with active region shown in inlay.

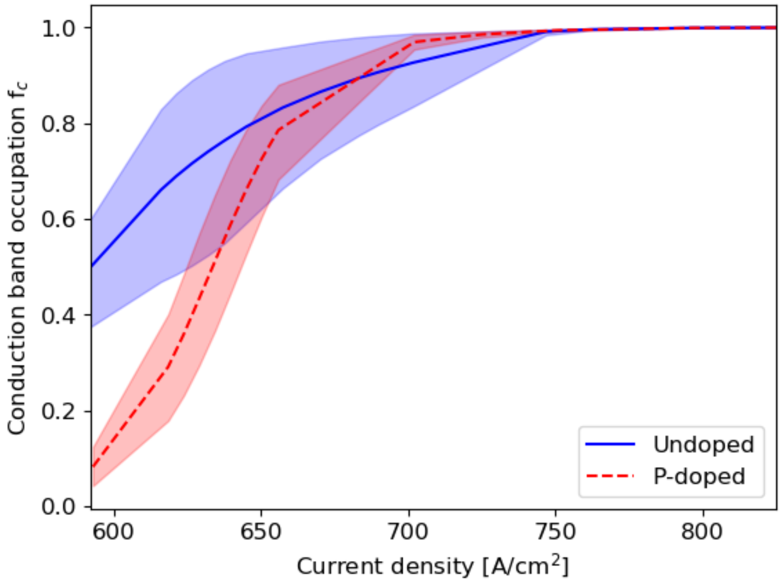

Fig. 5.21 – Conduction band ground state occupation. Solid and translucent lines represent the mean, and the minimum to maximum between the seven layers respectively.

Fig. 5.21 demonstrates reduced population of electrons in the conduction band ground state across all layers of the p-doped structure, though there is less variance between the minimum and maximum contributions across those layers. At a calculated current density of 680A/cm^{-2} the mean occupation probability in the conduction band of the p-doped structure is equal to the undoped structure and surpasses it at higher current densities, suggesting only a minimal reduction in potential gain due to inhibited electron injection.

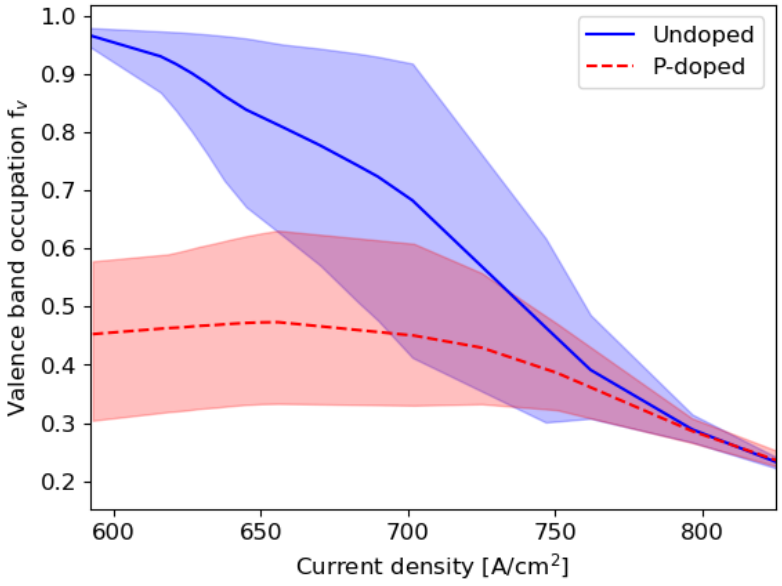

Fig. 5.22 – Valence band ground state occupation. Solid and translucent lines represent the mean, and the minimum to maximum between the seven layers respectively.

Thus at this doping level, we do not attribute saturation in the ground state gain to inhibited electron injection, though the impact of these electrostatic effects may drastically increase with surplus doping. Above given levels of doping significant increases in potential barriers between dot layers may occur, as suggested by Saldutti et al.[101].

Fig. 5.22 shows the valence band occupation probability, exhibiting the effect of state filling for holes as a result of p-doping. The significance of this reduction in electron population in the valence band is that it can be clearly linked to potential decreases in the threshold current density of p-doped laser diodes.

Fig. 5.23 shows the degree of inversion. An increased degree of inversion at a fixed current density leading to a reduced transparency current density in the p-doped structure, with a reduced variance across all dot layers. Additionally, the gradient by which the degree of inversion increases past transparency and threshold, is suggestive of greater differential gain associated with p-doped QD laser diodes, as shown in [47]. The increase in differential gain paired with improved linewidth enhancement factor is desirable for high speed modulated laser diodes. Beneficial effects of the state-filling effect are evident in fig. 5.23 through the degree of inversion, and translate directly to the peak modal gain shown in fig. 5.24.

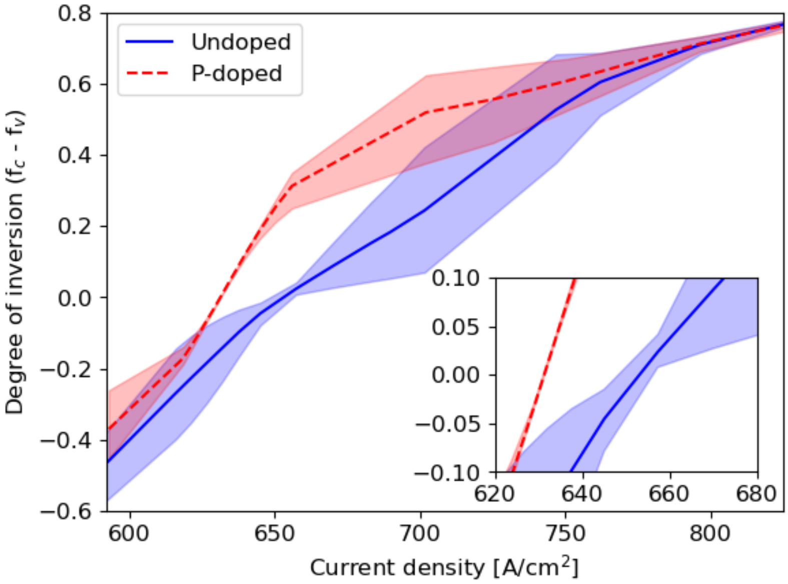

Fig. 5.23 – Degree of inversion for the first bound state in each dot layer for undoped and p-doped structures. Solid and translucent lines represent the mean, and the minimum to maximum between the seven layers respectively.

Increased gain amplitude and differential gain at lower current densities are advantageous although gain saturation is more evident at high current densities for the p-doped case, associated with increased carrier scattering causing more broadening of the gain spectrum. These characteristics are beneficial where the threshold gain requirement is relatively low as for long cavity laser diodes. Combining such lasers with the predicted EAMs would provide an efficient externally modulated laser diode, though additional analysis to optimally tune the doping is required. We note that the operational wavelength of these structures is not optimal for simple integration with the EAM described above. To combine the functionality on a single chip would require a further processing step perhaps via ion-implantation induced intermixing in localised regions to shift the absorber wavelength.

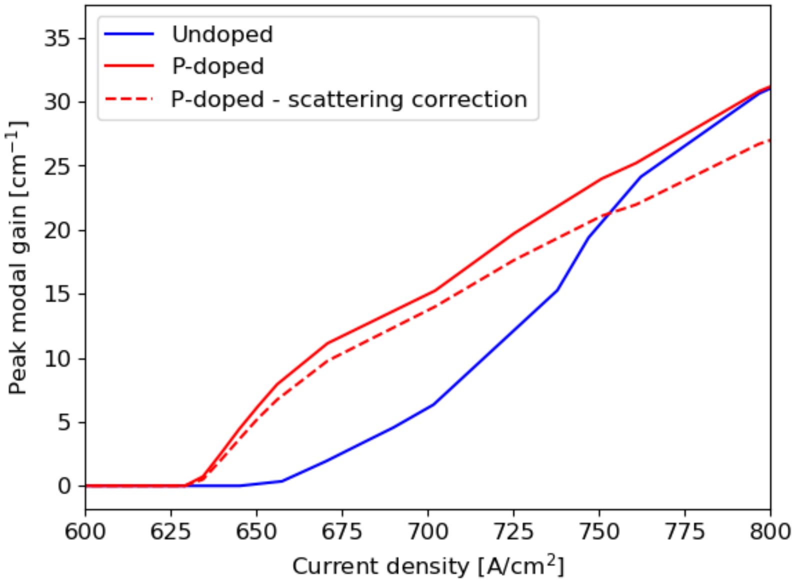

Fig. 5.24 – Peak modal gain versus current density for undoped and p-doped structures.

5.5 P-type modulation doping proximity

Laser performance remains sensitive to variations in the doping concentration with elevated levels limiting successful monolithic integration of high quality light sources on silicon substrates. The variation in doping concentration has been studied previously in [11], [101], [105], with a consensus of finite benefits related to increasing doping level, though the dominant mechanism for this is still disputed.

Design improvements may be possible by considering the positioning of the p-doping relative to the dot layer. A better understanding of this relationship may help understand the literature data on laser performance as a function of doping concentration, which is itself often difficult to accurately quantify in grown structures[102].

While a range of studies, such as many-body models, low temperature photoluminescence, and absorption characterisation, will be important to decouple homogeneous and inhomogeneous broadening mechanisms from p-doping, considering the broader impacts on the global quasi-Fermi level positions can provide insights on the occupation probability changes, and influence short term epitaxial design choices.

The proximity to the dot layer is often not disclosed and in the samples characterised in this chapter is positioned approximately centrally between two adjacent dot layers. This may limit the diffusion of holes into the dot valence potential. Additionally, the doping has significant effects on the band structure and benefits may be possible from increasing the uniformity between the different layers.

The effect of the proximity of the doping layer was calculated using 5nm increment steps between adjacent dot layers. There are limitations in how close the p-type dopant can be grown to the dot layer with a diffusion length of the scale of 5nm for beryllium dopant[152].

A further layer of doping was included as a precursor to the dot layers, with the purpose of increasing the uniformity between the layers particularly adjacent to the n-type cladding (shown in fig. 5.3). It is uncertain how carrier scattering mechanisms will be affected by these changes, therefore calculations of carrier occupation probability and band structure changes are used to infer benefits and inform further designs for growth.

The transparency (f_c-f_v=0) current density for a fixed degree of inversion is plotted as a function of proximity in fig. 5.25. Fig. 5.26 and 5.27 show the degree of inversion as a function of current density at each proximity above and below the dot layer with the undoped structure and centrally positioned doping (at 16.25nm). In all cases p-doping shows benefits in transparency current. All p-doped structures except with doping 31.25nm below the dot layer show a greater rate of increase in the degree of inversion, which may be due to proximity to the n-type cladding layer.

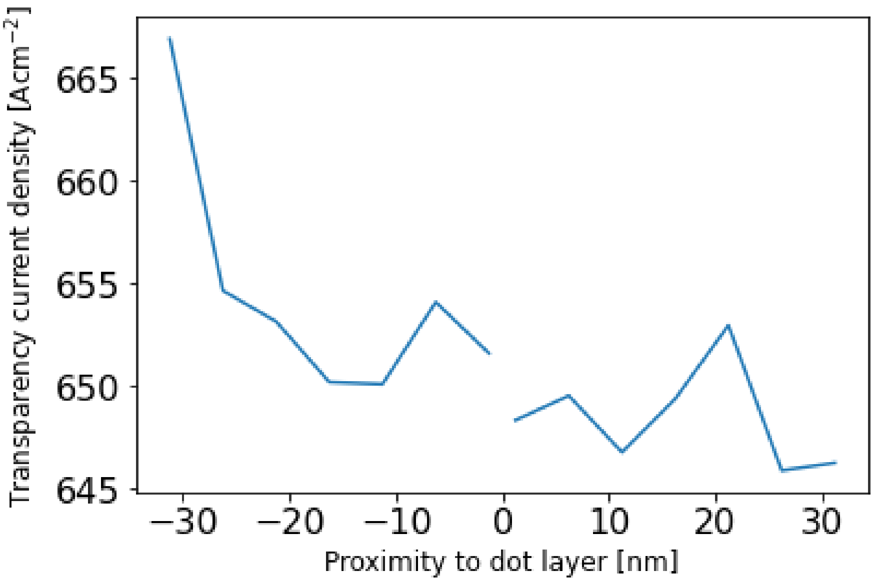

Fig. 5.25 – Calculated transparency current density versus p-type modulation doping layer proximity above and below dot layer.

There is a general trend in fig. 5.25, with the proximity above the dot resulting in lower transparency current densities, though changes between these above the dots are small. Growing p-doping above the dot may marginally increase its effectiveness due to the direction of the electric field across the intrinsic region of the p-i-n diode acting on the movement of carriers. Nevertheless calibration of the model through absorption characterisation is needed for further progression.

Fig. 5.28 shows the band structure calculated using a precursory layer. This was suggested to increase the symmetry of the quasi-Fermi level positions across the layers, particularly in n-type cladding adjacent layers. Though the hole quasi-Fermi level is closer to the valence band in the n-type cladding adjacent layer, the transparency current density at fixed degree of inversion is degraded by small reductions in the quasi-Fermi level separation in other layers. This is attributed to increased nonradiative recombination associated with an increase in the overall level of doping.

Including an extra pre-layer has a minimal effect under reverse bias, with small increases in the Stark shift but a negligible increase in carrier-blocking. Although, the additional doping layer is anticipated to increase homogeneous broadening, with the magnitude determining whether this is advantageous or not. Nevertheless, utilising a pre-layer, with reduced doping concentration may increase the symmetry of the quasi-Fermi level positions across all layers and provide some benefit. Further measurements of samples grown to these designs will be required to verify this, and to determine the effects of the additional layer of doping on the homogeneous broadening.

.

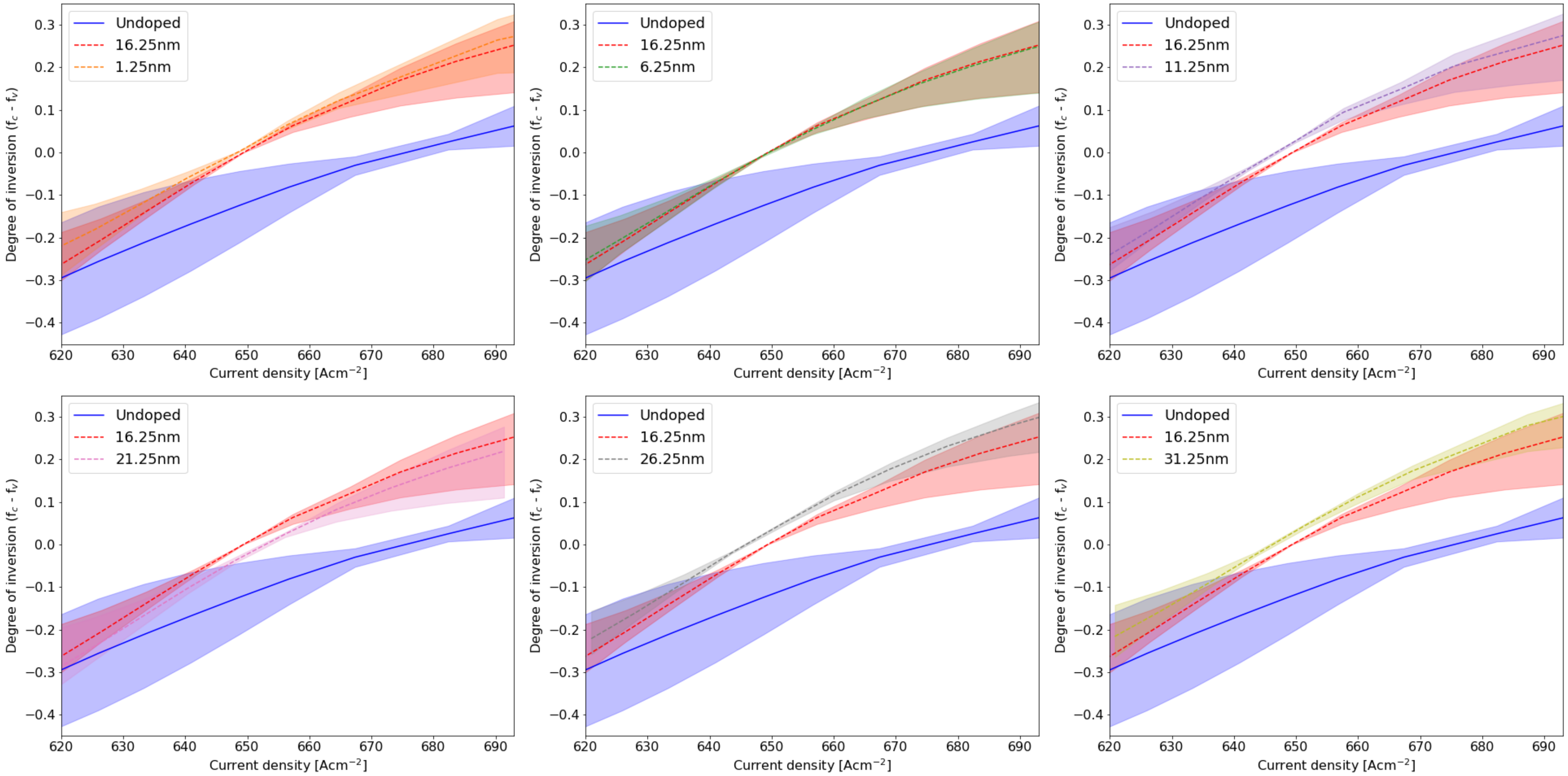

Fig. 5.26 – Degree of inversion as a function of current density calculated for p-doping at varying proximity above dot layer.

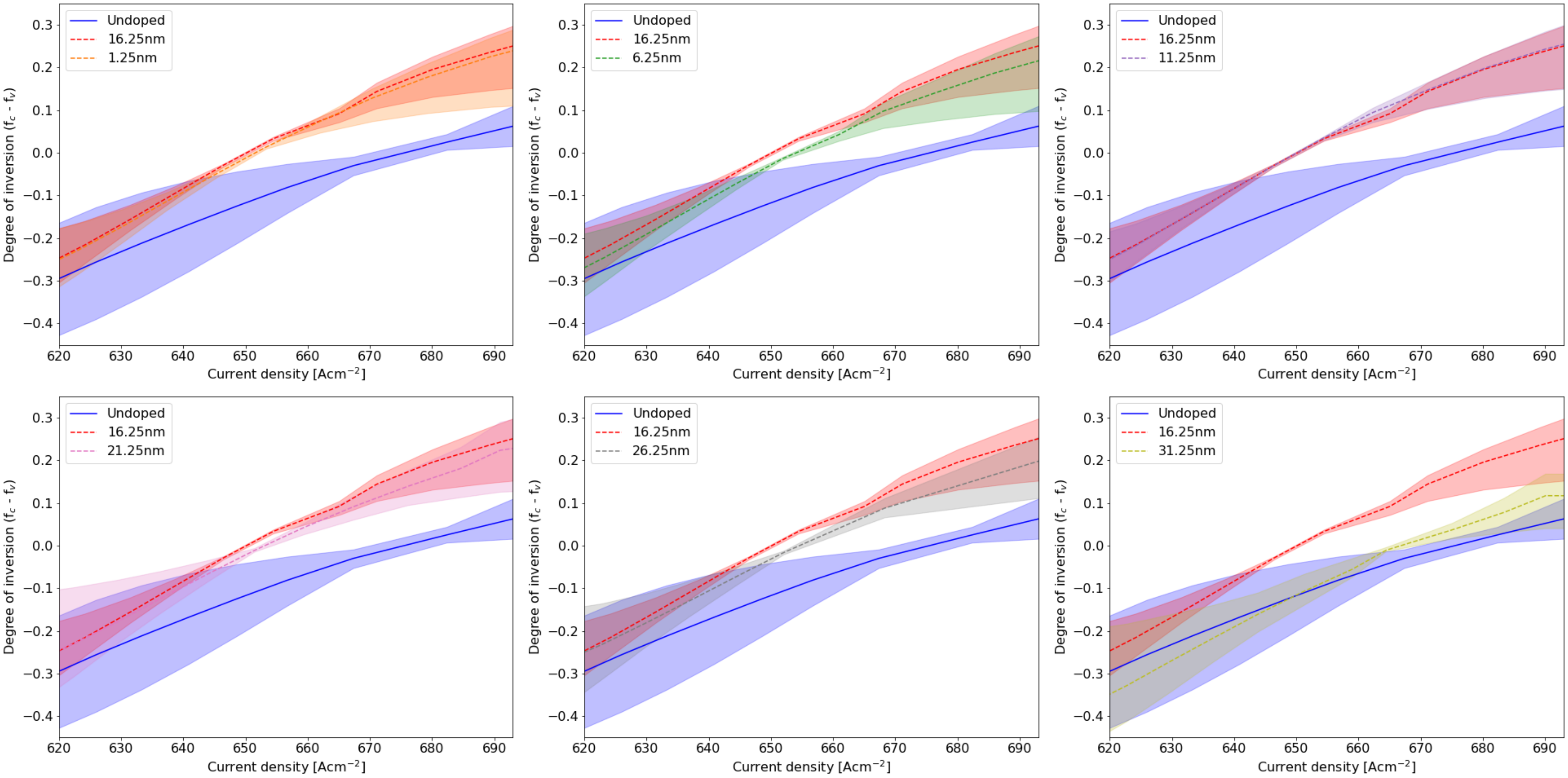

Fig. 5.27 – Degree of inversion as a function of current density calculated for p-doping at varying proximity below dot layer.

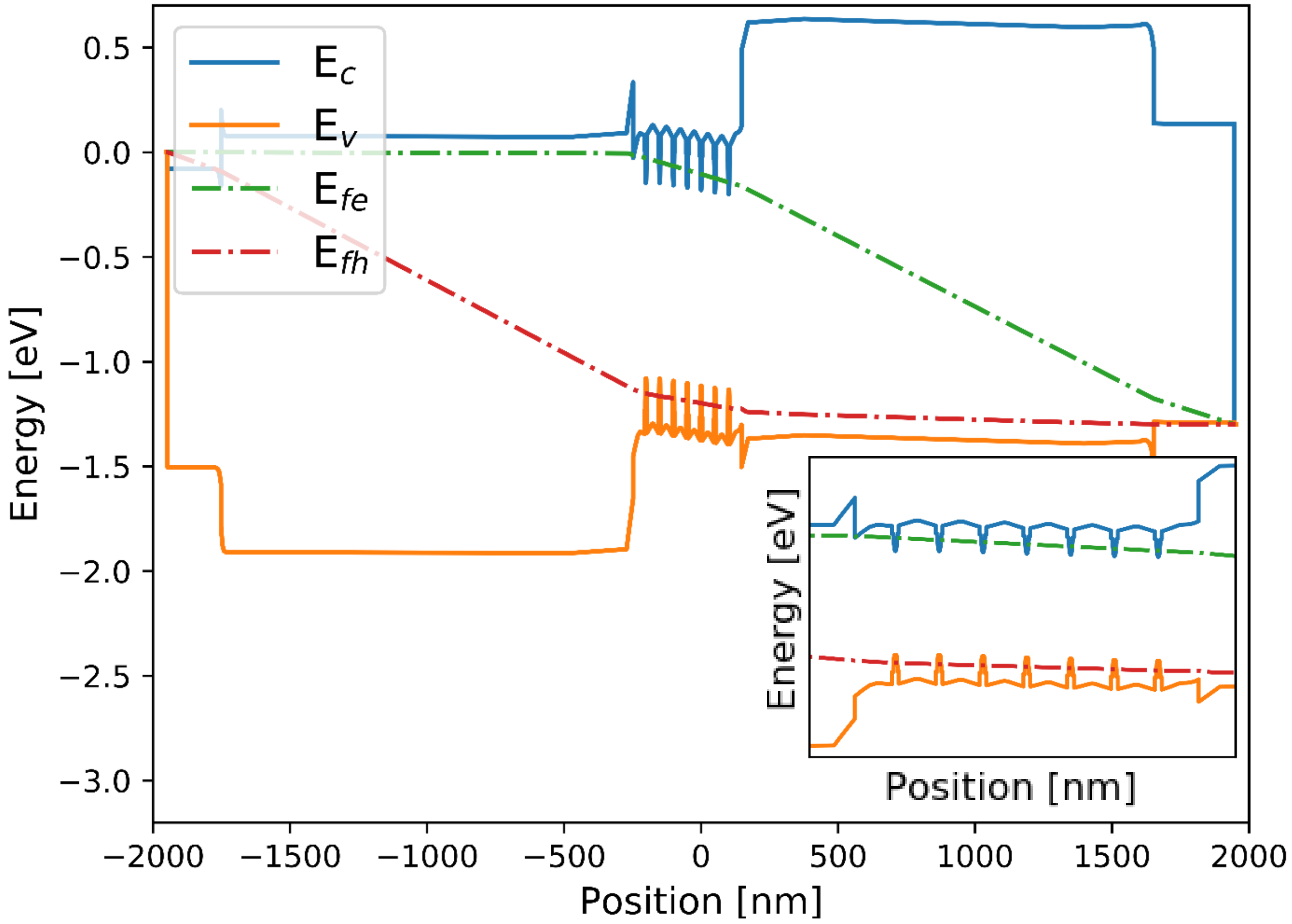

Fig. 5.28 – Full device band diagram calculated with p-type modulation doping and pre-layer.

5.6 Preliminary n-type direct doping calculations

The incorporation of n-type direct doping in QDs has shown benefits in many aspects of laser performance including linewidth enhancement factor, threshold current density, and differential gain[10], [12], [113]. Using the same modelling procedure as described above the effects of n-type direct doping on the band structure, bound energy levels and wavefunctions is considered.

Here, the number of electrons per dot (epd) was approximated through the corrected effective density of states. In measured samples, benefits have been demonstrated with as little as 1.2 epd, though it is indicated that further advantages may be achieved with higher concentrations[154]. Therefore, fully ionised n-type dopant was simulated within the dot layers using the equivalent of 0 – 10 epd, to examine the effects on the band structure and bound states. The dot potential at each doping level is shown in fig. 5.29.

Fig. 5.29 shows that as the doping concentration is increased there are strong distortions to the band structure, with the effects being largest at the highest level of doping. At 10 epd the conduction band potential is significantly deeper, increasing the confinement of electrons, with the valence potential noticeably shallower. In addition to reduced hole confinement there is strong band bending of the dot valence potential.

There is a distinct increase in the height of the potential barriers in the valence band either side of the dot potential which may limit the injection of holes into the dots under forward bias. This latter effect may limit the beneficial effects of direct n-doping at higher levels of doping when operated as lasers. Considering the ground state hole wavefunctions shown in fig. 5.29 there is broadening followed by a splitting of the wavefunction at higher doping levels. This is due to the severe band bowing at the center of the dot valence potential.

Finally, the quasi-Fermi level suggests high population of the conduction states, blocking absorption, though may cause increases in absorption magnitude as a reverse bias is applied. Decreasing of carrier-blocking through removing electrons from the conduction potential, following a similar mechanism to that shown for p-type modulation dopig in section 5.3. Nevertheless, this assumes the electrons incorporated through n-doping are in a thermal equilibrium. Further sample characterisation is required to confirm these processes.

Grown samples with 1.2, 2.4, 4.8 epd, have shown promise, with reduced threshold current density reductions in all samples compared to undoped material and 2.4 epd demonstrating the best performance. A comparison of the calculated energy levels for these doping levels and with 10 epd, is shown in fig. 5.30. The calculated electron states change their position as the potential deepens, with an extra electron state in the dot occurring at the highest doping concentration.

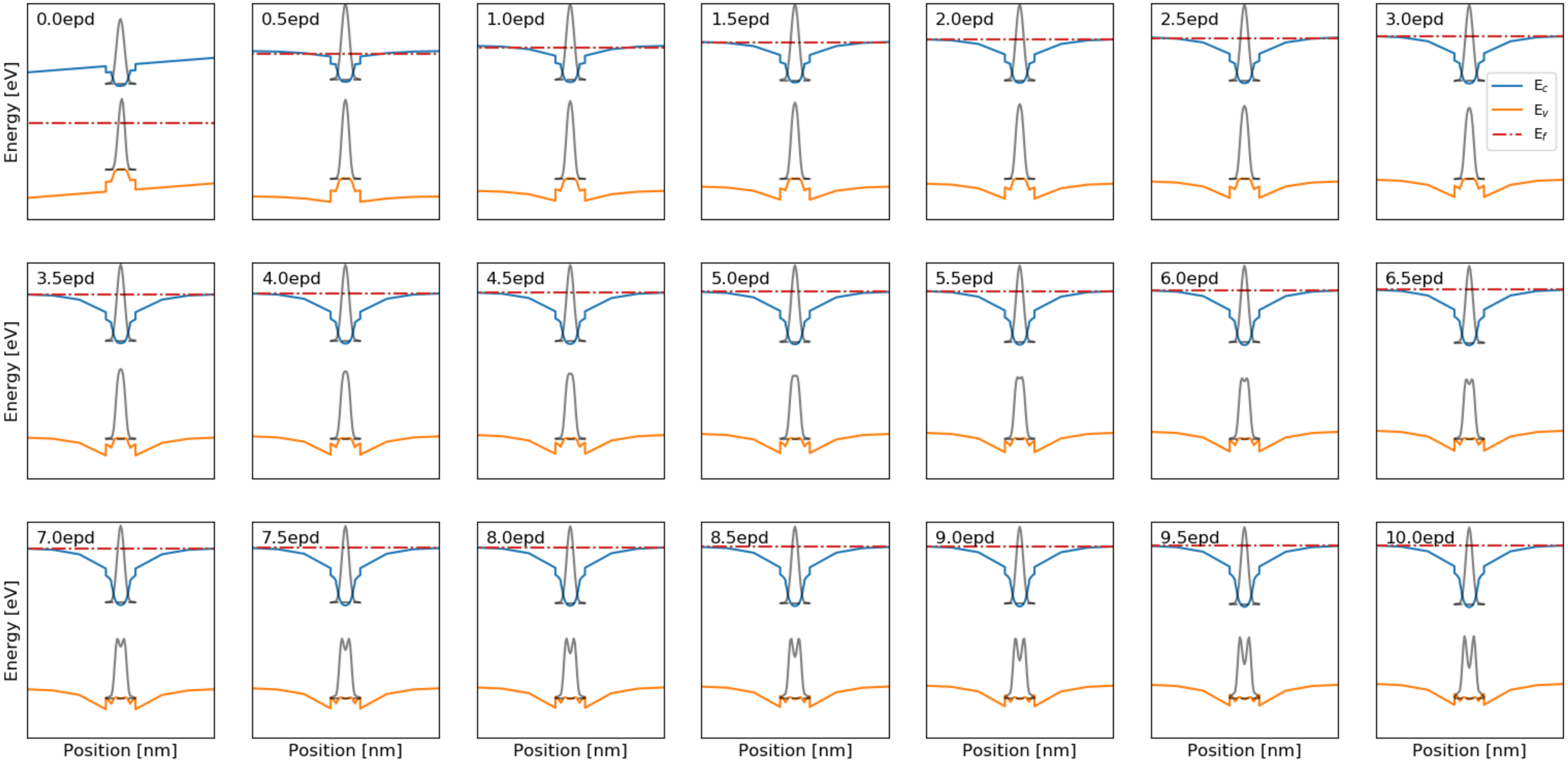

Fig. 5.29 – Central dot potential with n-type direct doping concentration from 0 – 10 epd. Ground state electron and hole wavefunctions are shown.

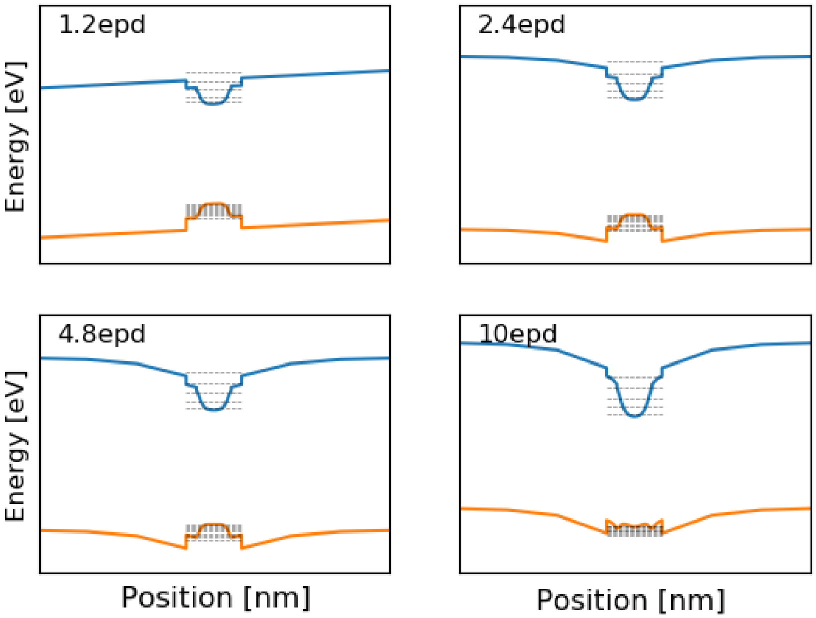

Fig. 5.30 – Calculated dot potential for the numbers of epd grown and highly doped (10 epd) structures. Electron and hole energy levels shown by dashed lines.

The calculated wavefunctions for the ground state are shown in fig. 5.31, for 2.4 and 10 epd respectively. The effects of the band bending in the valence band are apparent, with only minor changes at 2.4 epd, but drastic effects on the hole wavefunction at 10 epd. The band bending results in distortion of the wavefunction, reducing the overlap at higher doping levels, and may lead to separate states arising if the doping level is further increased.

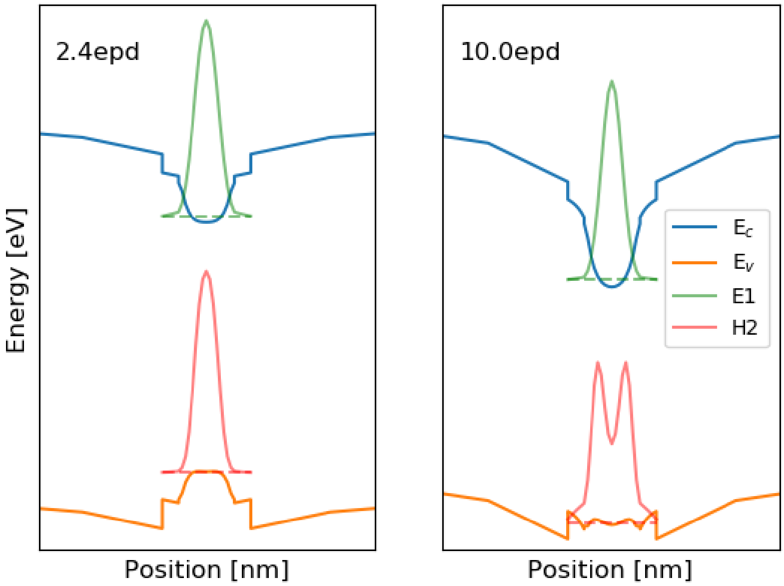

Fig. 5.31 – Calculated potential with ground state energy levels and wavefunctions for electrons and holes respectively at 2.4 and 10 epd.

The variations in the depth of the potentials, calculated bound states, and transition energy separation are shown in fig. 5.32-5.34.

Fig. 5.32 shows a linear increase in the potential depth of the conduction potential, and a linear decrease in the potential depth of the valence band after incorporation of around 0.5 epd. The increase in the conduction potential depth results in greater electron confinement and conductivity. Decreases in the valence potential depth reduce hole confinement and lower the separation between already closely spaced energy levels.

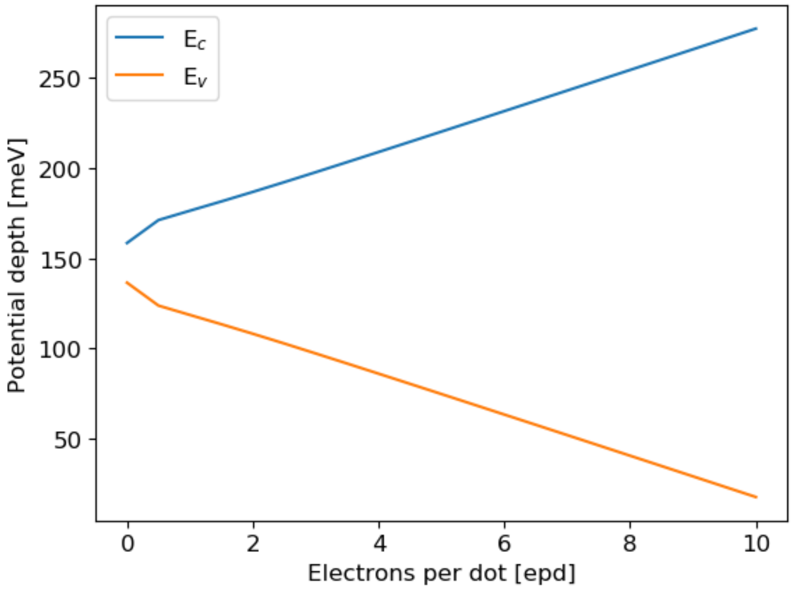

Fig. 5.32 – Calculated conduction and valence band dot potential depth as a function of n-type direct dopant.

The ground and excited state separation for electrons and holes are shown in fig. 5.33, with relation to the potential depth. The hole state separation declines dramatically to < 0.5meV at 10 epd.

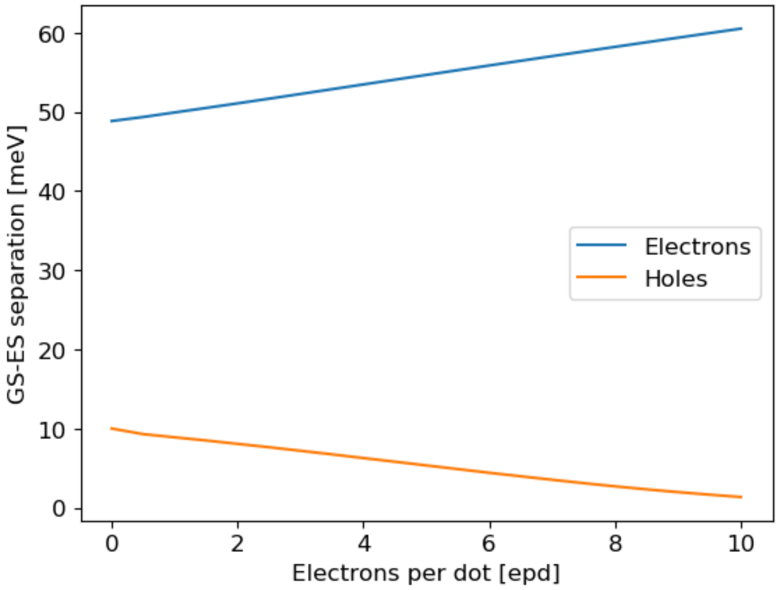

Fig. 5.33 – Calculated energy separation between ground and excited states as a function of n-type direct dopant for electrons and holes respectively.

The increase in the separation between the electron ground and first excited state may have implications for improved ground state lasing at lower doping levels. Fig. 5.34 shows the separation between ground and first excited transition energy as a function of doping. Initially the separation declines to the first simulated doping value of 0.5 epd. Subsequently, the transition energy separation is predicted to continually increase. The increase in transition energy separation is attributed to the increase in electron confinement.

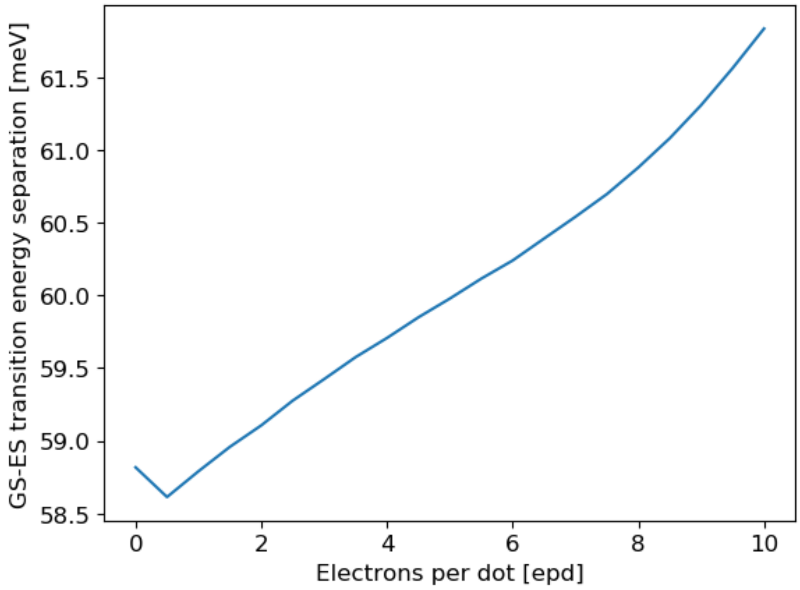

Fig. 5.34 – Calculated separation in ground and excited state transition energy as a function of n-type direct dopant.

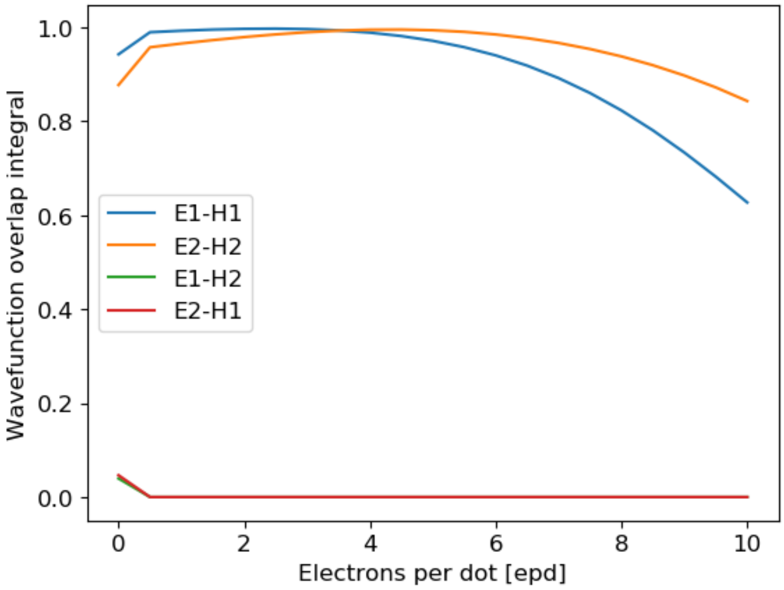

Fig. 5.35 – Wavefunction overlap integral calculated for ground and first excited state transitions and forbidden transitions E1-H2, E2-H1, as a function of n-type direct dopant.

Fig. 5.35 compares the overlap in wavefunctions for ground and first excited states, and shows a peak at around 2 epd, followed by a gradual decline in overlap, particularly in the ground state. The overlap between forbidden transition states (E1-H2 and E2-H1) are suppressed. The decrease in overlap of between ground and first excited state transitions is driven by the distortion in the valence band causing a reduction in the confining potential as well as a shift in the wavefunction which can be seen in fig. 5.31.

Only changes to the band structure have been considered as absorption spectra measurements were unavailable. Thus, as sample dependent parameters could not be extracted, calculation of absorption, peak modal gain and the QCSE would not be valid, due to a lack of data on broadening, internal optical loss, and bimodality. Nevertheless, the results shown above indicate potential benefits from suppression of the excited state in addition to enhanced electron population. Limitations include inhibited hole injection due to increased potential barriers.

Furthermore, combining n-type direct doping with p-type modulation doping, or so-called co-doping has been shown to provide further benefits to laser diodes[155], particularly in reducing threshold current densities. Consequently, the same structures were simulated between 0 – 10 epd, in addition to 10 hpd p-type modulation doping in the barriers. The dot potential at each doping level is shown in fig. 5.36. The dot potential with only p-type modulation doping is shown in fig. 5.36 with the annotation 0.0 epd. This is evident by the lowering of the quasi-Fermi levels with state-filling in the valence band.

The trends are indistinguishable from the purely n-type doping shown in fig. 5.29, showing the n-doping generally dominating the changes to the central dot potential. Similarities are also observed in the dot energy levels and ground state wavefunctions, in fig. 5.37 and 5.38 respectively.

In fig. 5.37 the same number of electron states are confined by the deepening conduction band of the dot potential, and the same number of hole states are lost to the surrounding well. There is also a similar increase and decrease in the height of the surrounding electron and hole barriers respectively. This follows the improvement in electron injection, and inhibition of hole injection. Conversely, with the inclusion of p-type modulation doping, this inhibition should be partially alleviated due to the reservoir of holes in the barrier regions. The enhanced differential gain predicted previously in p-doped structures, combined with the expected improvements in the linewidth enhancement factor in n-direct doped dots could offer high speed modulation devices.

In fig. 5.38 the severe bowing of the dot potential in the valence band causes the splitting of the ground state hole wavefunction. The conduction and valence dot potential depth is shown in fig. 5.39. This follows a linear increase and decrease with conduction and valence bands respectively. The energy separation in ground and first excited state for electrons and holes is shown in fig. 5.40. A similar effect is observed with the same increase and decrease for electrons and holes respectively.

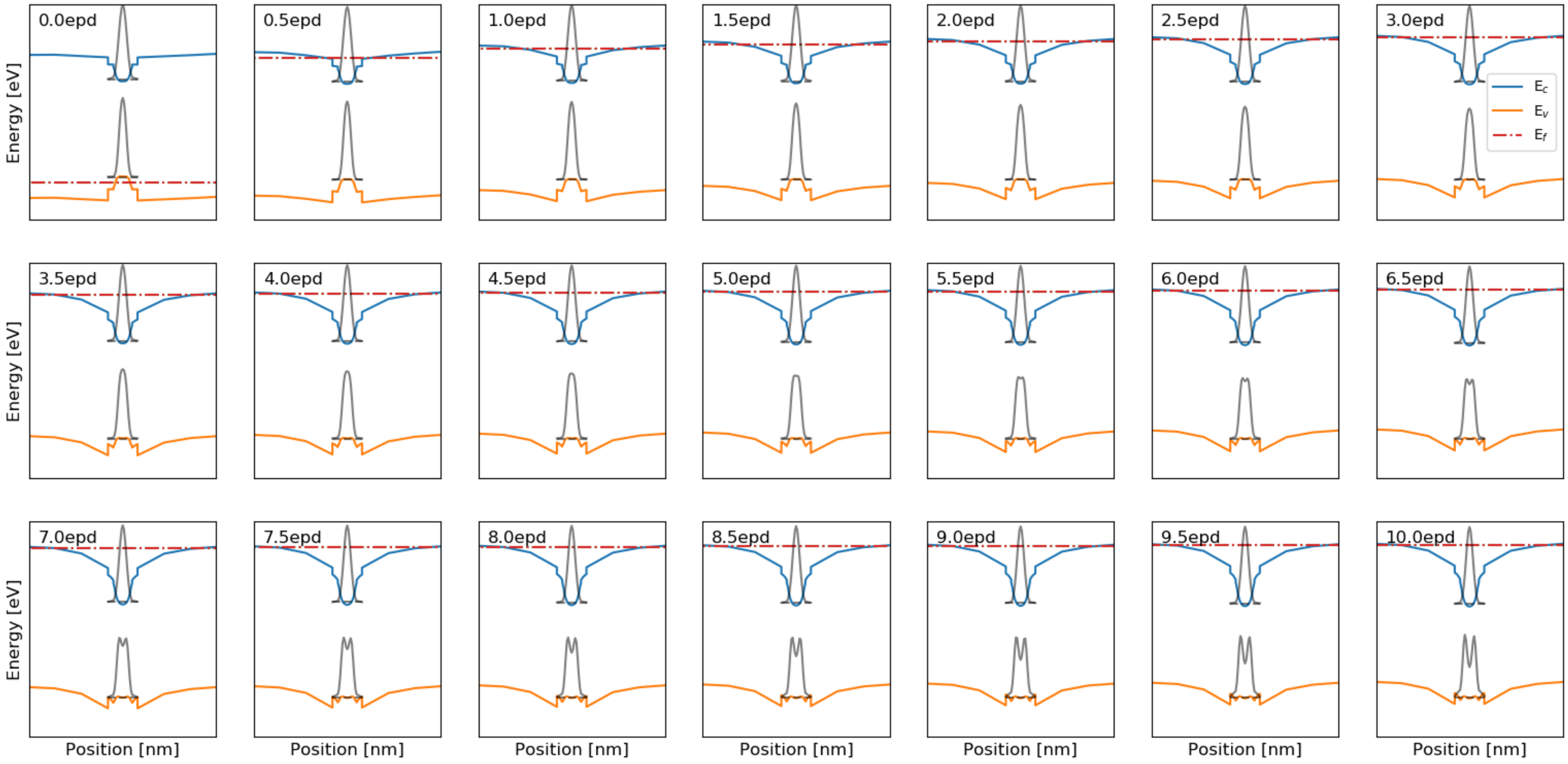

Fig. 5.36 – Central dot potential with 10 hpd p-type modulation doping in the barriers and n-type direct doping concentration from 0 – 10 epd. Ground state electron and hole wavefunctions are shown.

The large increase in the separation of the electron ground and first excited state is expected to suppress excited state operation while further decreasing threshold current densities in co-doped laser structures.

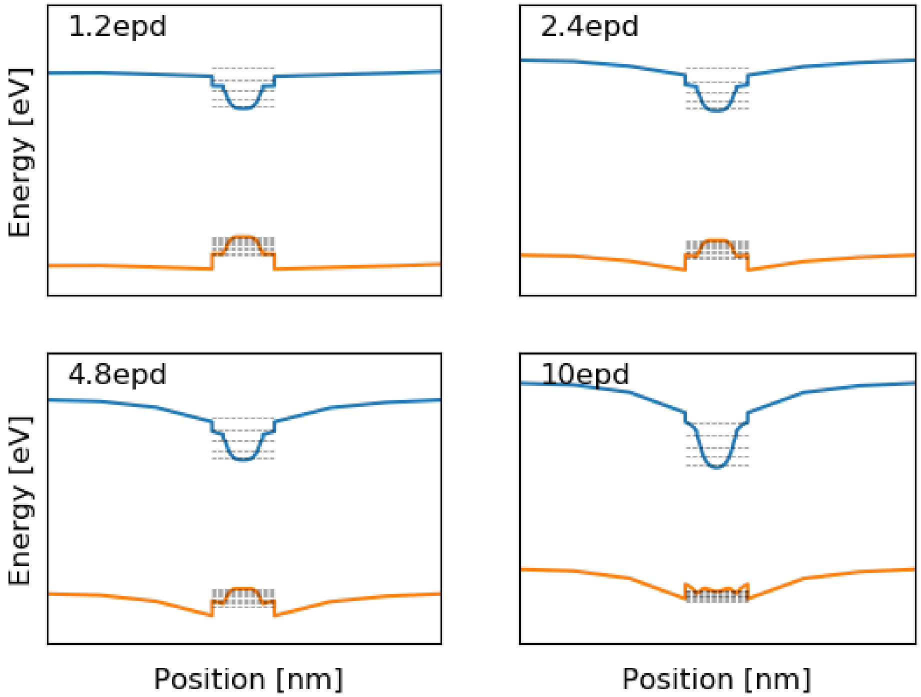

Fig. 5.37 – Calculated dot potential for the numbers of epd grown and highly doped (10 epd) structures with p-type modulation doping in the barrier. Electron and hole energy levels shown by dashed lines.

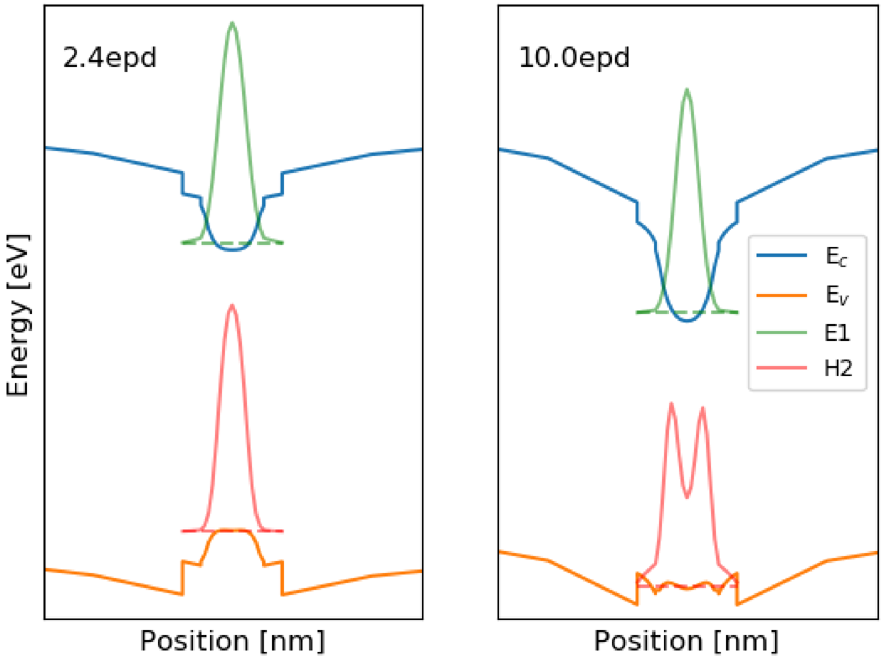

Fig. 5.38 – Calculated potential with ground state energy levels and wavefunctions for electrons and holes respectively at 2.4 and 10 epd with p-type modulation doping.

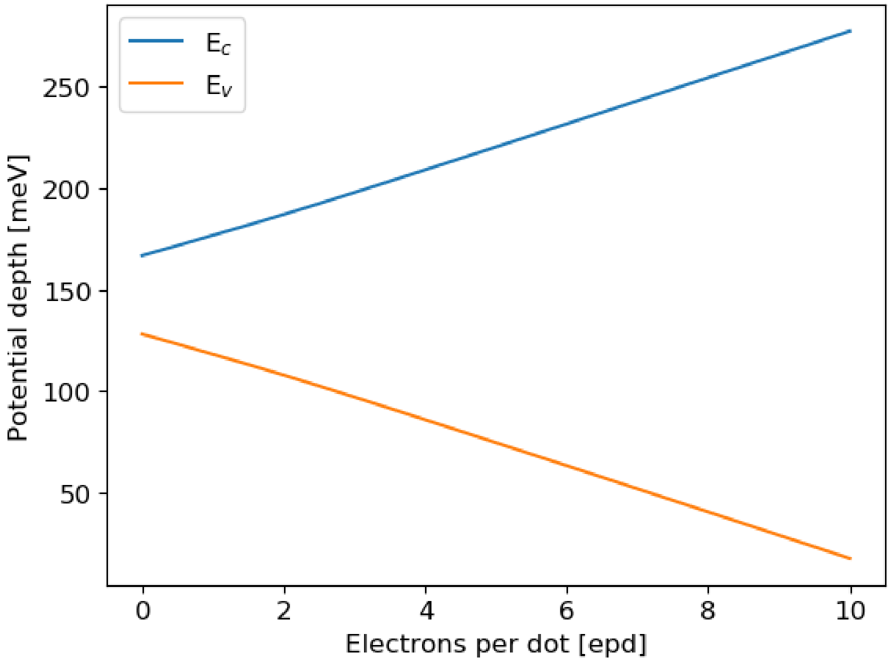

Fig. 5.39 – Calculated conduction and valence band dot potential depth as a function of n-type direct dopant with p-type modulation doping.

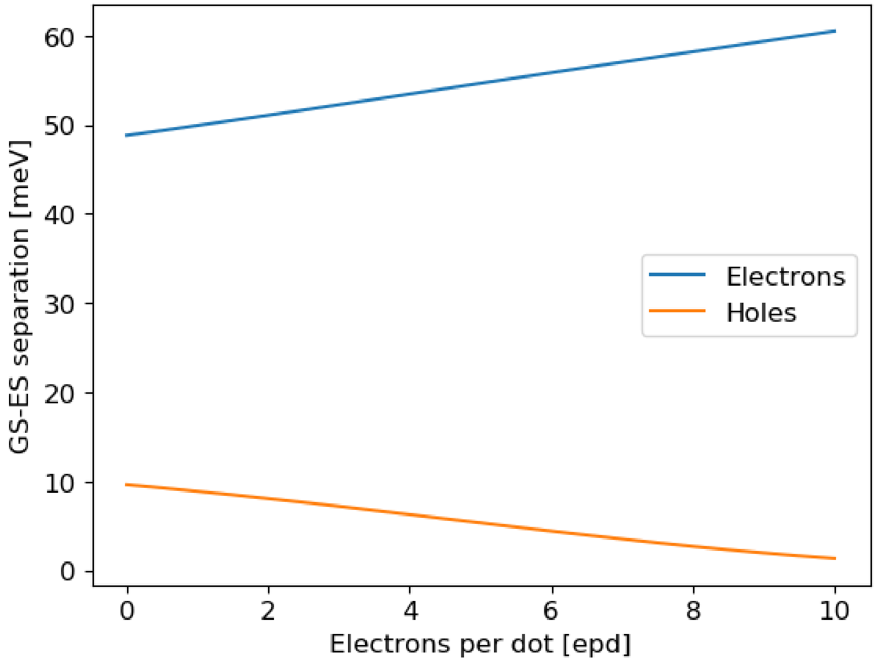

Fig. 5.40 – Calculated energy separation between ground and excited states as a function of n-type direct dopant for electrons and holes respectively with p-type modulation doping.

Fig. 5.41 shows the separation in the ground state and first excited state transition energy as a function of n-type direct doping, with p-type modulation doping. However, this does not have the same initial change as in fig. 5.34, suggesting a slightly reduced transition energy with p-doping.

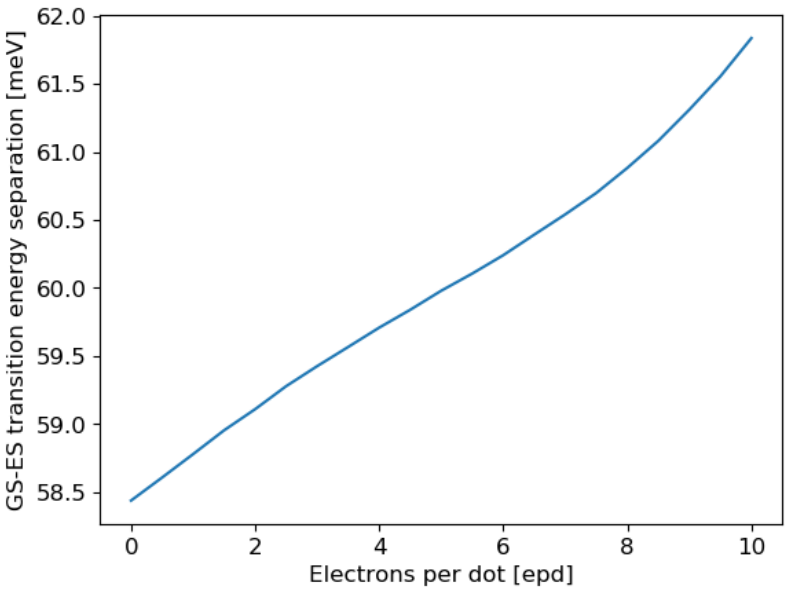

Fig. 5.41 – Calculated separation in ground and excited state transition energy as a function of n-type direct dopant, with p-type modulation doping.

Fig. 5.42 shows the variation in the wavefunction overlap as a function of n-type direct doping concentration with p-type modulation doping. The changes in wavefunction overlap are equivalent to that shown in fig. 5.35, with the exception of the initial point difference between undoped and p-doped.

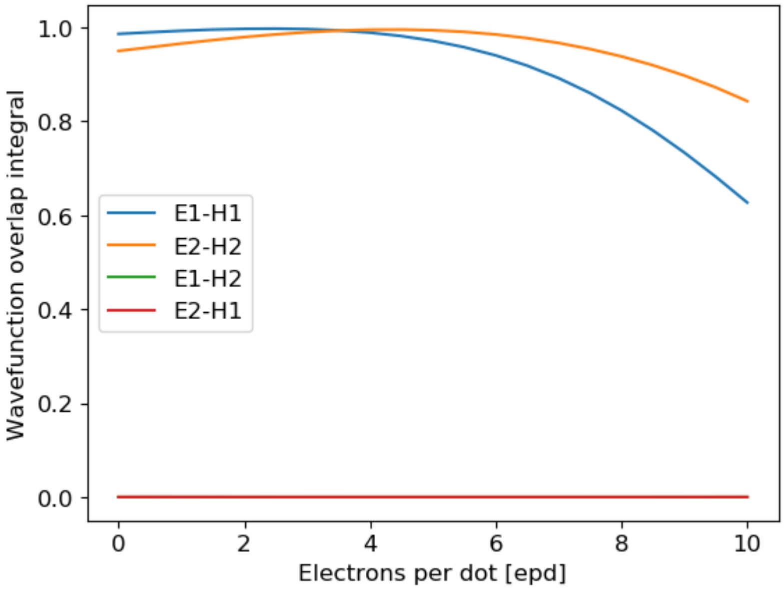

Fig. 5.42 – Wavefunction overlap integral calculated for ground and first excited state transitions and forbidden transitions E1-H2, E2-H1, as a function of n-type direct dopant with p-type modulation doping.

However, the variation in wavefunction overlap will be heavily dependent on the potential created by the dots, and may be impacted by size, shape, and intermixing with the well. Thus further characterisation is required to identify the dominance of these effects.

From these calculations it appears there is little effect on the band diagrams caused by co-doping compared to solely n-direct doping. This may indicate the same benefits possible with n-doping, in addition to those from p-doping, as described in previous sections.

While a simple understanding of the effects of doping might lead one to believe that one form of doping would cancel out the effects of the other the work in this chapter has shown that the mechanisms by which direct n-doping and p-doping may affect the dot potential and occupation of states are quite different and may offer cumulative benefits seen with co-doping. Further work will be necessary to confirm this.

5.7 Summary

We report a semi-empirical model combining full device band structure calculations with a Maxwell equation solver to calculate modal absorption and gain in p-modulation doped InAs/InGaAs QDs. Under reverse and forward bias, the QCSE and peak modal gain were evaluated. Reduced amplitude, broadened absorption spectra were shown to provide increased FoM in p-doped structures, indicating the potential of this structure for use in modulators. We found this to be predominantly caused by increased homogeneous broadening associated with greater carrier scattering rates. There was partial reduction from state filling induced carrier-blocking in p-doped structures, which provided particular benefits through increasing the absorption magnitude with reverse bias.

An increase in the maximum modulator FoM was observed from a bias change of 0 to 5V in p-doped structures. Though additional dot layers or increased cavity lengths may be required for operation at this wavelength where the ER is lower than the undoped structure. An ER>4dB is still present for the p-doped structure at 1311nm. Structures incorporating p-doping slightly outperformed undoped structures at 1311nm, with an increasing benefits at longer wavelengths. Further depletion of holes in p-doped structures with increasing reverse bias led to an increasing absorption amplitude, enhancing the ER at longer wavelengths. There was a reduction in the peak IL but due to increased homogeneous broadening IL was higher in the p-doped above 1300nm. Therefore, enhancements in the FoM were attributed to increased ER in p-doped structures.

Under forward bias, state-filling resulted in reduced threshold current density and increased differential and modal gain for ground state operation. The increased carrier scattering rate in p-doped structures created a severe gain saturation effect at higher current densities. P-doping was shown to offer benefit when carefully used with selection of operating wavelength and operating conditions to mitigate the effects of increased carrier scattering for use in modulators and lasers.

Increasing the proximity of the p-type modulation doping layer above the dot layer may offer minor benefits in terms of the movement of the quasi-Fermi levels. However, at very close proximity or below the corresponding dot layer may have negative effects. Inclusion of a pre-layer may assist laser structures through increasing the uniformity in occupation between dot layers, particularly adjacent to the n-type cladding, with minimal effects from carrier-blocking expected under reverse bias. However, the inclusion of additional doping increases the nonradiative recombination, and a lower doping concentration may be required to provide the desired benefits. In both cases significantly more work is required, including absorption characterisation, to confirm impacts to broadening parameters.

Band structure calculations under zero bias indicate the potential benefits of n-type direct doping technique as well as co-doping. N-type dopant directly incorporated into the dots increases the potential depth in the conduction band and reduces that of the valence band. This increases electron injection efficiency while inhibiting hole injection. As the level of n-type direct doping is further increased, growing valence potential barriers negatively impact hole injection.

Co-doping may allow for further enhancement of both electrons and holes simultaneously. It is expected that the reduced hole injection in n-type direct doped dots will be offset by the p-type modulation doping in the barriers, with improvements in both differential gain and linewidth enhancement factor offering high speed modulation devices. Nevertheless, the model described is reliant on sample dependent parameters, and further characterisation of samples exhibiting variation in the p-doping proximity and inclusion of pre-layer, in addition to n and co-doping techniques will be required to form a full theory of this behaviour.

Chapter 6 Conclusions

In this work, III-V compound semiconductor heterostructures have been simulated using a semi-empirical model with only one dimensional inputs to predict, firstly, absorption and the quantum confined Stark effect in quantum well modulator devices for retroreflective free space optical communication data links. Secondly, absorption, gain, and the quantum confined Stark effect in p-type modulation doped InAs quantum dots for 1.3μm operating lasers and modulators for on-chip integration. Finally, band structure calculations were used to discuss n-type direct and co-doping techniques for InAs quantum dot devices.

Experimental measurements of absorption and the quantum confined Stark effect in quantum wells were used to corroborate the model and then design novel epitaxial structures based on type-II band alignment for enhancing the performance of modulating retroreflectors. Additionally, absorption measurements (performed by fellow PhD student Joe Mahoney) in p-modulation doped InAs quantum dots corroborated model predictions of reduced threshold current density and increased differential gain in lasers, and an enhanced figure of merit in modulators.

Furthermore, band structure calculations following the same procedure allowed examination of n-type direct doped InAs quantum dots providing a hypothesis for improved performance in lasers. Combining n-type direct doping and p-type modulation doping in these calculations, mutual benefits are proposed through the so-called “co-doping” strategy.

6.1 Conclusion to this work

Normal incidence quantum well electroabsorption modulators for retroreflective free space optical communication systems were considered. Through analysis of state of the art devices, limitations of high insertion loss, low extinction ratio, and temperature sensitivity were observed. Asymmetric heterostructures based on type-II band alignment have been proposed as an alternative. A design composed of 2.7nm $In_{(0.43)}GaAs$ and 1.5nm $GaAsSb_{(0.40)}$ quantum wells, with a 6.5nm $In_{(0.60)}AlAs$ strain compensating barrier grown on InP substrate offers benefits, provided challenges in epitaxy can be overcome.

By utilizing the type-II band alignment, it was possible to confine electrons and holes in different material layers, spatially separating them and reducing the wavefunction overlap integral. This yielded significant reductions in the optical insertion loss (valuable to long range communication systems) and altered the zero-field modulation state to ON, which is energetically favourable. Additionally, through careful tuning of the band structure up to double the extinction ratio was predicted. This resulted in a significant increase in the figure of merit, with a design incorporating moderate to higher indium content InAlAs barrier regions to provide strain-balancing.

The asymmetry between the electron and hole confining layers was exploited to increase the separation between transition energies. This suppressed the impact of closely spaced energy levels and forbidden transitions occurring under a reverse bias observed in the state of the art structures. A broader extinction ratio peak was calculated with less reliance on only a narrow wavelength region of the absorption spectrum for operation. The suppression of the closely spaced and forbidden transitions resulted in fewer intersections between the biased and unbiased absorption spectra over the C-band, and hence fewer wavelengths where the extinction ratio may degrade to zero.

The increased broadening of the absorption spectrum and extinction ratio peak is suggested to be more resilient than the current state of the art structure to variations in temperature. The quantum confined Stark effect was predominantly driven by a strong redshift in the band edge absorption resulting in nearly a factor of 10 increase in the figure of merit over current state of the art devices. Further work will be required in the epitaxy of the required combinations of materials to produce narrow well dimensions and manage changes in growth temperature between indium-based and antimony-based alloys. The modelling work done here demonstrates that this is worthwhile.

Edge coupled quantum dot electroabsorption modulators and laser diodes were considered with the inclusion of p-type modulation doping and n-type direct doping techniques. Through a modelling procedure including only one degree of confinement, calculated band edge absorption spectra were produced which matched measurements. A simple transport model was used to calculate the global quasi-Fermi levels across the full device band structures and the carrier occupation probability at each quantum dot layer was evaluated. A reduction in the absorption magnitude in p-type modulation doped structures was attributed predominantly to increased homogeneous broadening via carrier scattering processes. Further reductions in absorption were attributed to carrier-blocking through the comparison of calculated and experimental data.

Under reverse bias an increase in absorption magnitude was calculated in p-doped structures arising from reductions of carrier-blocking with a growing depletion region from the applied electric field. A greatly increased figure of merit was associated with p-doped structures though with a significant redshift from the desired wavelength of operation. However, other changes such as increased device length, a greater number of quantum dot layers, or selective intermixing to shift the operation wavelength, will be required to achieve useful integration.

Carrier injection was modelled to observe behaviour relating to laser diodes. Reductions in threshold current density and increases in differential gain were observed for p-type modulation doping at a variety of positions in the barrier regions of the waveguide core. However, a lower value of maximum gain at the highest current densities was attributed to broadening through increased carrier scattering. Through band structure analysis, the inclusion of a p-doping pre-layer was shown to be advisable if the doping level was reduced, increasing symmetries in the quasi-Fermi levels across all quantum dot layers.

Band structure calculations for n-type direct doped InAs quantum dots showed potential improvements through increased electron confinement, wavefunction overlap, and a reduced number of hole states in the dot potential, though hole injection was predicted to be inhibited at higher doping levels due to increased potential barriers in the valence band. These benefits occur due to the increased depth in the dot conduction potential. Enhanced electron confinement increased the energy separation between ground and first excited state transitions, which should lead to lasing at the ground state wavelength up to higher gain. Though the reduced dot valence potential depth lowered the large number of hole states, the energy separation between them was also significantly reduced. There were also significant increases in the valence potential barriers which will inhibit hole injection.

Calculations including both n-type direct doping and p-type modulation doping indicate direct doping has dominant effects on the dot potential. However, the state filling associated with p-type modulation doping may act complementarily, overcoming the potential barriers which otherwise inhibit hole injection. Therefore, so-called “co-doping” is predicted to have significant implications for improvement to quantum dot laser devices grown on silicon substrates in the future.

6.2 Future study

Further research will be needed as epitaxy develops towards the required type-II quantum well modulator structures. Due to the low dimension, particularly of the hole confining GaAsSb layer, and the high growth temperature required for indium based alloys, achieving sharp interfaces will be a challenge. Nevertheless, appropriate consideration of the profile of the interface may be included into a more complex model, with the potential of mitigating increased broadening or changes to the peak operating wavelength. Additional consideration of the full p-i-n structure will be necessary before a final product design.

Calculation of the p-type and n-type cladding concentrations combined with the appropriate number of quantum well periods can be tuned for application specific extinction ratio, insertion loss, data rate or a data link distance requirements. In type-II structures as well as the current state of the art, further characterization of temperature dependence is needed. Measurement of direct temperature changes on the pixels, with independent heat and electric field sources, will be key in describing modulator performance for aerospace applications.

For continuation of work with p-type modulation doped, n-type direct doped, and co-doped InAs quantum dots, significantly more experimental characterization will be required. This will be necessary to validate predictions of the quantum confined Stark effect and to empirically confirm the theorized mechanisms of n-type direct and co-doped lasers. Moreover, characterization of the absorption spectrum of structures with a variety of doping strategies and doping parameters (such as proximity of p-type modulation doping) will provide sample dependent parameters which may be used within the model to further understand the operation of each approach when devices are used as modulators and lasers.

A1 Exciton Green’s-function approach

The equations for absorption presented in the background theory (chapter 2) are based on solutions derived with an exciton Green’s-function approach in momentum space, as presented by Chuang et al. in [15]. This was introduced as the Coulomb Green’s function in real space by Hostler in [156] for calculating Hydrogen atom ground state perturbations. The method was applied to exciton problems in [157], [158], with calculations in momentum spaced used for consideration of the quantum confined Stark effect (QCSE)[158]–[161].

In [15], Chuang et al. derive the Green’s function for the linear optical susceptibility of a quantum well (QW) and report numerical results with comparison to the variational method. Later in [130], Chuang presents expressions for bound and continuum of states contributions to the absorption coefficient of a QW (as quoted in chapter 2).

Chuang reports the linear optical susceptibility in eq. A1.1 in SI units following a density-matrix approach from Shen[162].

$$\epsilon_0 \chi_{ij}(\omega) = \frac{2}{V} \sum_{a,b} \frac{M_{ab}^{i} M_{ba}^{j}}{E_b - E_a - \hbar\omega - i\Gamma} \tag{A1.1}$$

The susceptibility is found by summing over all electrons in the crystal volume V, where a factor of 2 accounts for spins. M_{ab}^{i} and M_{ba}^{j} the ith and jth spatial components of the dipole matrix elements M_{ab} and M_{ba} respectively. a and b are the ground and excited states with energy difference $E_b - E_a$. The dipole matrix element $\boldsymbol{M}_{ab}$ can be defined as $\langle a|e\boldsymbol{R}|b\rangle$. $\hbar\omega$ is the photon energy and Γ is the half-linewidth resulting from homogeneous broadening.

For a QW, $E_b - E_a$ is replaced by $E_x = E_g + E_n^e + E_m^h - E_B$. Where E_g is the band gap energy. E_n^e and E_m^h are the subband energies (with indices n and m) of the conduction and valence band respectively. E_B is the exciton binding energy separating the bound and free electron and hole pairs, as shown in fig. A1.1.

The N-particle form dipole matrix element can be reduced to a single-particle form, $\langle nm\boldsymbol{k}|e\boldsymbol{R}|g\rangle = \left\langle \Psi_{n\boldsymbol{k}}^{c} \middle| e\boldsymbol{r} \middle| \Psi_{m\boldsymbol{k}}^{\boldsymbol{h}} \right\rangle = \mu_{nm}(\boldsymbol{k})$. Where $\boldsymbol{k}$ is the in-plane wave vector, $\langle nm\boldsymbol{k}|$ is the state obtained by replacing a single electron in the valence band by an electron in the conduction band, and $|g\rangle$ is the ground state of the system. Exciton states can be given as a linear combination of these states $|X\rangle = \sum_{n,m,\boldsymbol{k}} \phi_{nm}^{X}(\boldsymbol{k})|nm\boldsymbol{k}\rangle$.

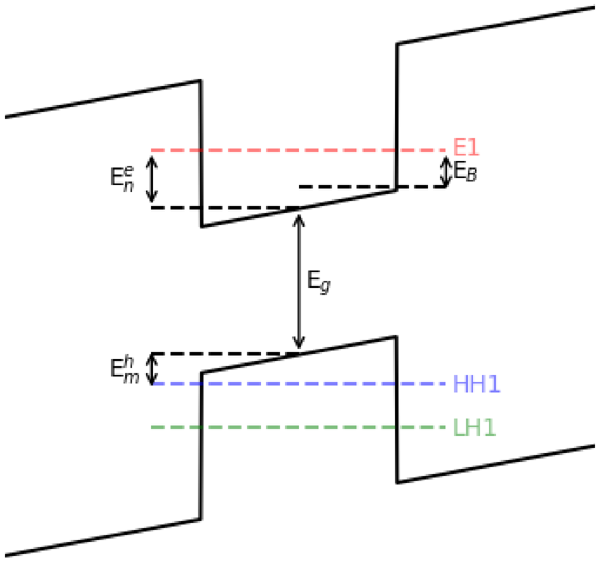

Fig. A1.1 – Quantum well under reverse bias with electron level (E1), heavy hole level (HH1), and light hole level (LH1). Band gap energy (Eg), the confinement energies for electrons and holes (E_n^e and E_m^h), and the exciton binding energy (E_B).

$\Psi_{n\boldsymbol{k}}^{c}$ and $\Psi_{m\boldsymbol{k}}^{\boldsymbol{h}}$ are the electron and hole single particle states satisfying the inhomogeneous Schrödinger equation in eq. A1.2.

$$\left[-\frac{\hbar^2}{2m_{eh}^*}\nabla^2 + V_{eh}(z) + |e|Fz\right]\Psi_{nm\boldsymbol{k}}^{eh}(\boldsymbol{r}) = E_{nm}^{eh}(\boldsymbol{k})\Psi_{nm\boldsymbol{k}}^{eh}(\boldsymbol{r}) \tag{A1.2}$$

$V_{eh}(z)$ is the electron or hole confining potential and F is the electric field. The single-particle dipole matrix element can then be related to the momentum matrix element following the effective mass approximation following eq. A1.3.

$$\langle|\mu_{nm}(k)|^2\rangle = \left[\frac{e\hbar}{mE_{nm}(k)}\right]^2 \left|I_{nm}^{eh}\right|^2 2M_b^2\gamma_{cv} \tag{A1.3}$$

Where $\left|I_{nm}^{eh}\right|^2$ is the wavefunction overlap integral, M_b^2 is the bulk momentum matrix element related to Kane's energy parameter by $\frac{m_0}{6}E_p$[39], and γ_{cv} is a band and polarization dependent multiplier. This is discussed in chapter 2 following [16].

Wavefunctions for the electron and hole can be written in the form given in eq. A1.4 and A1.5.

$$\Psi_{nk}^{e}(\boldsymbol{r}) = f_n(z)\frac{e^{ik\cdot\rho}}{\sqrt{A}}u_c(\boldsymbol{r}) \tag{A1.4}$$

$$\Psi_{mk}^{h}(\boldsymbol{r}) = g_m(z)\frac{e^{ik\cdot\rho}}{\sqrt{A}}u_v(\boldsymbol{r}) \tag{A1.5}$$

A is the in-plane interface area, with $u_c(\boldsymbol{r})$ and $u_v(\boldsymbol{r})$ the periodic parts of the Bloch functions. The optical matrix element $\langle X|e\boldsymbol{R}|g\rangle = \sum_{n,m,\boldsymbol{k}}\phi_{nm}^{X*}(\boldsymbol{k})\mu_{nm}(\boldsymbol{k})$, with the amplitude

$\phi_{nm}^{X}(\boldsymbol{k})$ satisfying the effective mass equation for excitons in a quantum well[163] through eq. A1.6.

$$E_{nm}(k)\phi_{nm}^{X}(\boldsymbol{k}) - \sum_{n',m',\boldsymbol{k}'}\langle nm|V_{\boldsymbol{k}-\boldsymbol{k}'}|n'm'\rangle\phi_{n'm'}^{X*}(\boldsymbol{k}') = E_X\phi_{nm}^{X}(\boldsymbol{k}) \qquad (\mathrm{A1.6})$$

$E_{nm}(k) = E_g + E_n^e(k) + E_m^h(k)$ following fig. A1.1, with states $E_n^e(k)$ and $E_m^h(k)$ in the form $E_{nm}^{eh}(k) = E_{nm}^{eh} + \frac{\hbar^2k^2}{2m_{eh}^*}$. Chuang then expresses the Coulomb potential with quantum-well size effects, as shown in eq. A1.7.

$$\langle nm|V_{\boldsymbol{k}-\boldsymbol{k}'}|n'm'\rangle = \frac{e^2}{2\epsilon|\boldsymbol{k}-\boldsymbol{k}'|A}\int dz_e \int dz_h\, f_n^*(z_e)g_m^*(z_h)e^{-|\boldsymbol{k}-\boldsymbol{k}'||z_e-z_h|}f_{n'}(z_e)g_{m'}(z_h) \qquad (A1.7)$$

The exciton Green’s function is expressed in eq. A1.8 from [158], [159].

$$G_{nm}^{j}(\boldsymbol{k}, \hbar\omega + i\Gamma) = \sum_X \phi_{nm}^{X}(\boldsymbol{k})\left[\frac{\sum_{n',m',\boldsymbol{k}'}\phi_{n'm'}^{X*}(\boldsymbol{k}')\mu_{n'm'}^{j}(\boldsymbol{k}')}{E_X-\hbar\omega-i\Gamma}\right] \qquad (A1.8)$$

Here j refers to the jth spatial component of the dipole moment. The susceptibility defined in eq. A1.1, can then be rewritten in terms of the exciton Green’s function, shown in eq. A1.9.

$$\epsilon_0\chi_{ij}(\omega) = \frac{2}{V}\sum_{n,m,\boldsymbol{k}}\mu_{nm}^{i*}(\boldsymbol{k})G_{nm}^{j}(\boldsymbol{k}, \hbar\omega + i\Gamma) \qquad (A1.9)$$

$\hbar\omega + i\Gamma$ is set as Ω, and G_{nm}^{j} is said to satisfy the integral equation in momentum space for the exciton envelope function in eq. A1.10, similarly to eq. A1.6.

$$[E_{nm}(k) - \Omega]G_{nm}^{j}(\boldsymbol{k}, \Omega) - \sum_{n',m',\boldsymbol{k}'}\langle nm|V_{\boldsymbol{k}-\boldsymbol{k}'}|n'm'\rangle G_{nm}^{j}(\boldsymbol{k}', \Omega) = \mu_{nm}^{j}(\boldsymbol{k}) \qquad (A1.10)$$

The eigenvalues and eigenfunctions can be solved for using eq. A1.6, whereas the dipole moment must be solved for the exciton Green’s function in eq. A1.10. Chuang then shows the exciton Green’s function satisfies eq. A1.10 by expanding G_{nm}^{j} in terms of the exciton envelope functions with the assumption that they form a complete set. This is shown through eq. A1.11.

$$G_{nm}^{j}(\boldsymbol{k}, \Omega) = \sum_X \phi_{nm}^{X}(\boldsymbol{k})\, c_X^j \qquad (A1.11)$$

$$\sum_{n,m,\boldsymbol{k}}\mu_{nm}^{X*}(\boldsymbol{k})\phi_{nm}^{X'}(\boldsymbol{k}) = \delta_{XX'} \qquad (A1.12)$$

By substituting eq. A1.11 into eq. A1.10, multiplying the complex conjugate of the envelope function ϕ_{nm}^{X*} and summing over n, m, and $\boldsymbol{k}$, Chuang shows c_X^j is given by the expression in eq. A1.8 $\left[\frac{\sum_{n',m',\boldsymbol{k}'}\phi_{n'm'}^{X*}(\boldsymbol{k}')\mu_{n'm'}^{j}(\boldsymbol{k}')}{E_X-\hbar\omega-i\Gamma}\right]$proving A1.11. The absorption coefficient was then calculated from the imaginary part of the susceptibility $\alpha = \omega\epsilon_2/(n_r c\epsilon_0)$, where $\epsilon_2 = Im[\epsilon_0\chi(\omega)]$.

Subsequently, Chuang describes the process of solving for the exciton Green's function, in which the singularity of the Coulomb potential is properly taken into account. This is not reported here as though [15] provides sufficient detail.

The solutions of the exciton Green's function can then be applied to find the bound and continuum of states contributions of susceptibility or absorption utilizing appropriate material and structure dependent parameters described in this thesis. The final expressions for bound and continuum of states absorption coefficient contributions (in chapter 2) are reported in [130], and shown in eq. A1.13 and A1.14 respectively.

$$\alpha_B(\hbar\omega) = C_0 \frac{2}{L} \sum_X |\phi_{nm}^{x}(\rho = 0)|^2 \, |\hat{e} \cdot \boldsymbol{p}_{cv}|^2 |I_{nm}^{en}|^2 \frac{\Gamma/\pi}{(E_X - \hbar\omega)^2 + \Gamma^2} \qquad (A1.13)$$

$$\alpha_C(\hbar\omega) = C_0 \frac{m_r^*}{\pi\hbar^2 L} |\hat{e} \cdot \boldsymbol{p}_{cv}|^2 \left|I_{nm}^{eh}\right|^2 \int_0^\infty dE_t |\phi^x(\rho = 0)|^2 \frac{\Gamma/\pi}{\left(E_{nm}^{eh} - \hbar\omega\right)^2 + \Gamma^2} \qquad (A1.14)$$

Where, $C_0 = \frac{\pi e^2}{n_r c \epsilon_0 m_0^2 \omega}$, with n_r the real part of the refractive index. L is the width of the QW. $|\phi_{nm}^{x}(\rho = 0)|^2$ is the oscillator strength evaluated at the band edge. $|\hat{e} \cdot \boldsymbol{p}_{cv}|^2$ is the momentum matrix element $M_b^2 \gamma_{cv}$. $|I_{nm}^{en}|^2$ is the wavefunction overlap integral. m_r^* is the reduced mass related to the electron and hole effective masses by $1/m_r^* = 1/m_e^* + 1/m_h^*$.

Bibliography

[1] B. E. A. Saleh and M. C. Teich, *Fundamentals of Photonics*. John Wiley & Sons, Inc., 1991.

[2] Y. Thueux, N. Avlonitis, and G. Erry, “DAZZLE project: UAV to ground communication system using a laser and a modulated retro-reflector,” Amsterdam, Netherlands, Oct. 2014, p. 92480P. doi: 10.1117/12.2062610.

[3] C. Quintana *et al.*, “High Speed Electro-Absorption Modulator for Long Range Retroreflective Free Space Optics,” *IEEE Photonics Technology Letters*, vol. 29, no. 9, pp. 707–710, May 2017, doi: 10.1109/LPT.2017.2680842.

[4] C. Quintana *et al.*, “A High Speed Retro-Reflective Free Space Optics Links With UAV,” *J. Lightwave Technol.*, vol. 39, no. 18, pp. 5699–5705, Sep. 2021, doi: 10.1109/JLT.2021.3091991.

[5] W. S. Rabinovich, “45-Mbit/s cat’s-eye modulating retroreflectors,” *Opt. Eng*, vol. 46, no. 10, p. 104001, Oct. 2007, doi: 10.1117/1.2789634.

[6] W. S. Rabinovich *et al.*, “Free space quantum key distribution using modulating retro-reflectors,” *Optics Express*, vol. 26, no. 9, p. 11331, Apr. 2018, doi: 10.1364/OE.26.011331.

[7] P. M. Smowton, I. C. Sandall, H. Y. Liu, and M. Hopkinson, “Gain in p-doped quantum dot lasers,” *Journal of Applied Physics*, vol. 101, no. 1, p. 013107, Jan. 2007, doi: 10.1063/1.2405738.

[8] K. Otsubo *et al.*, “Temperature-Insensitive Eye-Opening under 10-Gb/s Modulation of 1.3-µm P-Doped Quantum-Dot Lasers without Current Adjustments,” *Jpn. J. Appl. Phys.*, vol. 43, no. No. 8B, pp. L1124–L1126, Jul. 2004, doi: 10.1143/JJAP.43.L1124.

[9] S. S. Mikhrin *et al.*, “High power temperature-insensitive 1.3 µm InAs/InGaAs/GaAs quantum dot lasers,” *Semicond. Sci. Technol.*, vol. 20, no. 5, pp. 340–342, May 2005, doi: 10.1088/0268-1242/20/5/002.

[10] T. Kita, R. Hasagawa, and T. Inoue, “Suppression of nonradiative recombination process in directly Si-doped InAs/GaAs quantum dots,” *Journal of Applied Physics*, vol. 110, no. 10, p. 103511, Nov. 2011, doi: 10.1063/1.3660794.

[11] Z. Zhang, D. Jung, J. C. Norman, P. Patel, W. W. Chow, and J. E. Bowers, “Effects of modulation *p* doping in InAs quantum dot lasers on silicon,” *Appl. Phys. Lett.*, vol. 113, no. 6, p. 061105, Aug. 2018, doi: 10.1063/1.5040792.

[12] Z.-R. Lv, Z.-K. Zhang, X.-G. Yang, and T. Yang, “Improved performance of 1.3-um InAs/GaAs quantum dot lasers by direct Si doping,” *Applied Physics Letters*, vol. 113, 2018.

[13] J. Mahoney *et al.*, “QCSE and Carrier Blocking in P-modulation Doped InAs/InGaAs Quantum Dots,” p. 2, 2021.

[14] S. Birner *et al.*, “nextnano: General Purpose 3-D Simulations,” *IEEE Transactions on Electron Devices*, vol. 54, no. 9, pp. 2137–2142, Sep. 2007, doi: 10.1109/TED.2007.902871.

[15] S.-L. Chuang, S. Schmitt-Rink, D. A. B. Miller, and D. S. Chemla, “Exciton Green’s-function approach to optical absorption in a quantum well with an applied electric field,” *Physical Review B*, vol. 43, no. 2, pp. 1500–1509, Jan. 1991, doi: 10.1103/PhysRevB.43.1500.

[16] P. Blood, *Quantum confined laser devices: optical gain and recombination in semiconductors*, First edition. Oxford: Oxford University Press, 2015.

[17] S. L. Chuang, “Physics of Photonic Devices,” p. 841.

[18] S. Birner, S. Hackenbuchner, J. Majewski, D. Mamaluy, G. Zandler, and P. Vogl, “nextnano3 – a state-of-the-art simulation tool for 3D quantum nanodevices,” p. 2.

[19] C. G. Van de Walle and R. M. Martin, “Theoretical calculations of semiconductor heterojunction discontinuites,” *J. Vac. Sci. Technol. B*, vol. 4, 1986.

[20] C. G. Van de Walle, “Band Offsets at Strained-Layer Interfaces,” *MRS Proceedings*, vol. 102, Jan. 1987, doi: 10.1557/PROC-102-565.

[21] C. G. Van de Walle, “Band lineups and deformation potentials in the model-solid theory,” *Physical Review B*, vol. 39, no. 3, 1989.

[22] M. P. C. M. Krijn, “Heterojunction band offsets and effective masses in III-V quaternary alloys,” *Semiconductor Science and Technology*, vol. 6, no. 1, pp. 27–31, Jan. 1991, doi: 10.1088/0268-1242/6/1/005.

[23] I. Vurgaftman, J. R. Meyer, and L. R. Ram-Mohan, “Band parameters for III–V compound semiconductors and their alloys,” *Journal of Applied Physics*, vol. 89, no. 11, pp. 5815–5875, Jun. 2001, doi: 10.1063/1.1368156.

[24] D. S. Chemla, B. Miller, P. W. Smith, A. C. Gossard, and W. Wiegmann, “Room Temperature Excitonic Nonlinear Absorption and Refraction in GaAs/AlGaAs Multiple Quantum Well Structures,” p. 11.

[25] D. Miller, J. Weiner, and D. Chemla, “Electric-field dependence of linear optical properties in quantum well structures: Waveguide electroabsorption and sum rules,” *IEEE J. Quantum Electron.*, vol. 22, no. 9, pp. 1816–1830, Sep. 1986, doi: 10.1109/JQE.1986.1073167.

[26] T. Zibold, “Semiconductor based quantum information devices: Theory and simulations,” Technische Universität München, 2007.

[27] T. Andlauer, “Optoelectronic and spin-related properties of semicanductor nanostructures in magnetic fields,” Technische Universität München, 2009.

[28] J. E. Ayers, “Mismatched Heteroepitaxial Growth and Strain Relaxation,” *Heteroepitaxy of Semiconductors*, p. 88, 2007.

[29] I. Demir and S. Elagoz, “Interruption time effects on InGaAs/InAlAs superlattices of quantum cascade laser structures grown by MOCVD,” *Superlattices and Microstructures*, vol. 100, pp. 723–729, Dec. 2016, doi: 10.1016/j.spmi.2016.10.027.

[30] C. A. Wang *et al.*, “OMVPE growth of highly strain-balanced GaInAs/AlInAs/InP for quantum cascade lasers,” *Journal of Crystal Growth*, vol. 310, no. 23, pp. 5191–5197, Nov. 2008, doi: 10.1016/j.jcrysgro.2008.07.100.

[31] N. J. Ekins-Daukes *et al.*, “Strain-balanced GaAsP/InGaAs quantum well solar cells,” *Appl. Phys. Lett.*, vol. 75, no. 26, pp. 4195–4197, Dec. 1999, doi: 10.1063/1.125580.

[32] Y. P. Wang, S. J. Ma, K. Watanabe, M. Sugiyama, and Y. Nakano, “Management of highly-strained heterointerface in InGaAs/GaAsP strain-balanced superlattice for photovoltaic application,” *Journal of Crystal Growth*, vol. 352, no. 1, pp. 194–198, Aug. 2012, doi: 10.1016/j.jcrysgro.2011.12.049.

[33] E. D. Palik, *Handbook of Optical Constants of Solids*, vol. Volume IV. Elsevier Inc., 1997.

[34] S. Adachi, “Refractive indices of III–V compounds: Key properties of InGaAsP relevant to device design,” *Journal of Applied Physics*, vol. 53, no. 8, pp. 5863–5869, Aug. 1982, doi: 10.1063/1.331425.

[35] Z. Zhu and T. Brown, “Full-vectorial finite-difference analysis of microstructured optical fibers,” *Opt. Express*, vol. 10, no. 17, p. 853, Aug. 2002, doi: 10.1364/OE.10.000853.

[36] M. Fox, *Optical properties of solids*. Oxford ; New York: Oxford University Press, 2001.

[37] A. C. MacGillivray *et al.*, “Band-edge absorption characteristics of semi-insulating indium phosphide under unified Franz-Keldysh and Einstein models,” *Phys. Rev. B*, vol. 105, no. 15, p. 155203, Apr. 2022, doi: 10.1103/PhysRevB.105.155203.

[38] M. Hutchings, I. O’Driscoll, P. M. Smowton, and P. Blood, “Fermi-dirac and random carrier distributions in quantum dot lasers,” *Appl. Phys. Lett.*, vol. 104, no. 3, p. 031103, Jan. 2014, doi: 10.1063/1.4862813.

[39] E. O. Kane, “Band structure of indium antimonide,” *Journal of Physics and Chemistry of Solids*, vol. 1, no. 4, pp. 249–261, Jan. 1957.

[40] K. S. Potter and J. H. Simmons, “Optical properties of semiconductors,” in *Optical Materials*, Elsevier, 2021, pp. 229–307. doi: 10.1016/B978-0-12-818642-8.00005-3.

[41] P. J. Stevens, M. Whitehead, G. Parry, and K. Woodbridge, “Computer modeling of the electric field dependent absorption spectrum of multiple quantum well material,” *IEEE Journal of Quantum Electronics*, vol. 24, no. 10, pp. 2007–2016, Oct. 1988, doi: 10.1109/3.8536.

[42] R. K. Schaevitz *et al.*, “Simple electroabsorption calculator for germanium quantum well devices,” in *8th IEEE International Conference on Group IV Photonics*, London, United Kingdom, Sep. 2011, pp. 139–141. doi: 10.1109/GROUP4.2011.6053742.

[43] P. Blood, “On the dimensionality of optical absorption, gain, and recombination in quantum-confined structures,” *IEEE J. Quantum Electron.*, vol. 36, no. 3, pp. 354–362, Mar. 2000, doi: 10.1109/3.825883.

[44] A. Baskaran and P. Smereka, “Mechanisms of Stranski-Krastanov growth,” *Journal of Applied Physics*, vol. 111, no. 4, p. 044321, Feb. 2012, doi: 10.1063/1.3679068.

[45] C. Z. Tong, S. F. Yoon, C. Y. Ngo, C. Y. Liu, and W. K. Loke, “Rate Equations for 1.3-mum Dots-Under-a-Well and Dots-in-a-Well Self-Assembled InAs–GaAs Quantum-Dot Lasers,” *IEEE J. Quantum Electron.*, vol. 42, no. 11, pp. 1175–1183, Nov. 2006, doi: 10.1109/JQE.2006.883471.

[46] A. A. Dikshit and J. M. Pikal, “Carrier Distribution, Gain, and Lasing in 1.3micron InAs–InGaAs Quantum-Dot Lasers,” *IEEE J. Quantum Electron.*, vol. 40, no. 2, pp. 105–112, Feb. 2004, doi: 10.1109/JQE.2003.821532.

[47] J. Kim and S. L. Chuang, “Theoretical and Experimental Study of Optical Gain, Refractive Index Change, and Linewidth Enhancement Factor of p-Doped Quantum-Dot Lasers,” *IEEE Journal of Quantum Electronics*, vol. 42, no. 9, pp. 942–952, Sep. 2006, doi: 10.1109/JQE.2006.880380.

[48] H. Kissel *et al.*, “Size distribution in self-assembled InAs quantum dots on GaAs (001) for intermediate InAs coverage,” *Phys. Rev. B*, vol. 62, no. 11, pp. 7213–7218, Sep. 2000, doi: 10.1103/PhysRevB.62.7213.

[49] M. V. Maximov *et al.*, “Optical properties of quantum dots formed by activated spinodal decomposition for GaAs-based lasers emitting at | 1.3 mm,” *Microelectronic Engineering*, p. 12, 2000.

[50] I. O’Driscoll, P. M. Smowton, and P. Blood, “Low-Temperature Nonthermal Population of InAs–GaAs Quantum Dots,” *IEEE J. Quantum Electron.*, vol. 45, no. 4, pp. 380–387, Apr. 2009, doi: 10.1109/JQE.2009.2013869.

[51] E. E. Mendez, G. Bastard, L. L. Chang, L. Esaki, H. Morkoc, and R. Fischer, “Effect of an electric field on the luminescence of GaAs quantum wells,” *Phys. Rev. B*, vol. 26, no. 12, pp. 7101–7104, Dec. 1982, doi: 10.1103/PhysRevB.26.7101.

[52] P. Holmström and L. Thylén, “Electro-optic switch based on near-field-coupled quantum dots,” *Appl. Phys. A*, vol. 115, no. 4, pp. 1093–1101, Jun. 2014, doi: 10.1007/s00339-014-8420-5.

[53] T. H. Wood, “Multiple quantum well (MQW) waveguide modulators,” *J. Lightwave Technol.*, vol. 6, no. 6, pp. 743–757, Jun. 1988, doi: 10.1109/50.4063.

[54] S. Nojima and K. Wakita, “Optimization of quantum well materials and structures for excitonic electroabsorption effects,” *Appl. Phys. Lett.*, vol. 53, no. 20, pp. 1958–1960, Nov. 1988, doi: 10.1063/1.100335.

[55] M. K. Chin, “On the figures of merit for electroabsorption waveguide modulators,” *IEEE Photon. Technol. Lett.*, vol. 4, no. 7, pp. 726–728, Jul. 1992, doi: 10.1109/68.145252.

[56] E. Bigan, M. Allovon, M. Carre, C. Braud, A. Carenco, and P. Voisin, “Optimization of optical waveguide modulators based on Wannier-Stark localization: an experimental study,” *IEEE J. Quantum Electron.*, vol. 28, no. 1, pp. 214–223, Jan. 1992, doi: 10.1109/3.119516.

[57] T. H. Stievater, W. S. Rabinovich, P. G. Goetz, R. Mahon, and S. C. Binari, “A Surface-Normal Coupled-Quantum-Well Modulator at 1.55<tex>mu</tex>m,” *IEEE Photonics Technology Letters*, vol. 16, no. 9, pp. 2036–2038, Sep. 2004, doi: 10.1109/LPT.2004.831981.

[58] P. Luo *et al.*, “Experimental Demonstration of a 1024-QAM Optical Camera Communication System,” *IEEE Photon. Technol. Lett.*, vol. 28, no. 2, pp. 139–142, Jan. 2016, doi: 10.1109/LPT.2015.2487544.

[59] I. R. Hristovski, N. I. Lesack, L. A. Herman, and J. F. Holzman, “Urbach-edge-assisted electro-absorption for enhanced free-space optical modulation,” *Opt. Lett.*, vol. 45, no. 9, p. 2478, May 2020, doi: 10.1364/OL.388915.

[60] W. S. Rabinovich *et al.*, “A cat’s eye multiple quantum-well modulating retro-reflector,” *IEEE Photon. Technol. Lett.*, vol. 15, no. 3, pp. 461–463, Mar. 2003, doi: 10.1109/LPT.2002.807904.

[61] S. Junique, D. Agren, Qin Wang, S. Almqvist, B. Noharet, and J. Y. Andersson, “A Modulating retro-reflector for free-space optical communication,” *IEEE Photon. Technol. Lett.*, vol. 18, no. 1, pp. 85–87, Jan. 2006, doi: 10.1109/LPT.2005.860388.

[62] G. C. Gilbreath, “Progress in development of multiple-quantum-well retromodulators for free-space data links,” *Opt. Eng*, vol. 42, no. 6, p. 1611, Jun. 2003, doi: 10.1117/1.1572155.

[63] M. Achour, C. Sandoval, and S. Diego, “Free-Space Optical Communication by Retro-Modulation: Concept, Technologies and Challenges.,” p. 13.

[64] W. S. Rabinovich *et al.*, “Performance of cat’s eye modulating retro-reflectors for free-space optical communications,” Denver, CO, Oct. 2004, p. 104. doi: 10.1117/12.561604.

[65] S. Junique *et al.*, “Multiple quantum well spatial light modulators: design,fabrication,characterization,” San Diego, CA, Nov. 2001, pp. 62–71. doi: 10.1117/12.447739.

[66] Q. Wang *et al.*, “Wide-aperture GaAs/AlGaAs multiple quantum well electro-optic modulators,” Brugge, Belgium, Mar. 2003, p. 59. doi: 10.1117/12.470177.

[67] Q. Wang, S. Junique, D. Agren, B. Noharet, and J. Y. Andersson, “Fabry–PÉrot Electroabsorption Modulators for High-Speed Free-Space Optical Communication,” *IEEE Photon. Technol. Lett.*, vol. 16, no. 6, pp. 1471–1473, Jun. 2004, doi: 10.1109/LPT.2004.827855.

[68] G. C. Gilbreath, “Large-aperture multiple quantum well modulating retroreflector for free-space optical data transfer on unmanned aerial vehicles,” *Opt. Eng*, vol. 40, no. 7, p. 1348, Jul. 2001, doi: 10.1117/1.1383783.

[69] W. S. Rabinovich *et al.*, “45 Mbps cat’s eye modulating retro-reflector link over 7 Km,” San Diego, California, USA, Sep. 2006, p. 63040Q. doi: 10.1117/12.688407.

[70] Q. Wang, S. Junique, S. Almqvist, D. Ågren, B. Noharet, and J. Y. Andersson, “1550 nm surface normal electroabsorption modulators for free space optical communications,” Bruges, Belgium, Oct. 2005, p. 598610. doi: 10.1117/12.630395.

[71] S. R. Andrews, C. M. Murray, R. A. Davies, and T. M. Kerr, “Stark effect in strongly coupled quantum wells,” *Physical Review B*, vol. 37, no. 14, pp. 8198–8204, May 1988, doi: 10.1103/PhysRevB.37.8198.

[72] M. K. Chin, “Modeling of InGaAs/InAlAs coupled double quantum wells,” *Journal of Applied Physics*, vol. 76, no. 1, pp. 518–523, Jul. 1994, doi: 10.1063/1.357104.

[73] Q. Wang, B. Noharet, S. Junique, S. Almqvist, D. Ågren, and J. Y. Andersson, “1550 nm transmissive⁄reflective surface-normal electroabsorption modulator arrays,” *Electron. Lett.*, vol. 42, no. 1, p. 47, 2006, doi: 10.1049/el:20063504.

[74] Y. K. Hong, R. R. A. Syms, K. S. J. Pister, and L. X. Zhou, “Design, fabrication and test of self-assembled optical corner cube reflectors,” *J. Micromech. Microeng.*, vol. 15, no. 3, pp. 663–672, Mar. 2005, doi: 10.1088/0960-1317/15/3/030.

[75] Lixia Zhou, J. M. Kahn, and K. S. J. Pister, “Corner-cube retroreflectors based on structure-assisted assembly for free-space optical communication,” *J. Microelectromech. Syst.*, vol. 12, no. 3, pp. 233–242, Jun. 2003, doi: 10.1109/JMEMS.2003.809956.

[76] L. Ziph-Schatzberg, T. Bifano, S. Cornelissen, J. Stewart, and Z. Bleier, “Secure optical communication system utilizing deformable MEMS mirrors,” San Jose, CA, Feb. 2009, p. 72090C. doi: 10.1117/12.812145.

[77] T. Bifano, L. Schatzberg, J. Stewart, and S. Cornelissen, “MEMS Modulated Retroreflectors for Secure Optical Communication,” in *Volume 13: Nano-Manufacturing Technology; and Micro and Nano Systems, Parts A and B*, Boston, Massachusetts, USA, Jan. 2008, pp. 395–399. doi: 10.1115/IMECE2008-66795.

[78] W. C. Cox, K. F. Gray, J. A. Simpson, B. Cochenour, B. L. Hughes, and J. F. Muth, “A MEMS blue/green retroreflecting modulator for underwater optical communications,” in *OCEANS 2010 MTS/IEEE SEATTLE*, Seattle, WA, Sep. 2010, pp. 1–4. doi: 10.1109/OCEANS.2010.5664432.

[79] M. J. Moghimi, “MOEMS deformable mirrors for focus control in vital microscopy,” *J. Micro/Nanolith. MEMS MOEMS*, vol. 10, no. 2, p. 023005, Apr. 2011, doi: 10.1117/1.3574129.

[80] M. J. Moghimi, K. N. Chattergoon, C. R. Wilson, and D. L. Dickensheets, “High Speed Focus Control MEMS Mirror With Controlled Air Damping for Vital Microscopy,” *J. Microelectromech. Syst.*, vol. 22, no. 4, pp. 938–948, Aug. 2013, doi: 10.1109/JMEMS.2013.2251320.

[81] T. K. Chan and J. E. Ford, “Retroreflecting optical modulator using an MEMS deformable micromirror array,” *J. Lightwave Technol.*, vol. 24, no. 1, pp. 516–525, Jan. 2006, doi: 10.1109/JLT.2005.859853.

[82] T. Yamada, Y. Sakamaki, T. Shibata, A. Kaneko, A. Sano, and Y. Miyamoto, “Compact 111-Gbit/s integrated RZ-DQPSK modulator using hybrid assembly technique with silica-based PLCs and LiNbO3 devices,” in *OFC/NFOEC 2008 - 2008 Conference on Optical Fiber Communication/National Fiber Optic Engineers Conference*, San Diego, CA, USA, Feb. 2008, pp. 1–3. doi: 10.1109/OFC.2008.4528437.

[83] X. Li *et al.*, “AlInGaAs MQW Transceiver with Electro-optic Modulation Characteristics for Free-Space Optical Communication and Sensing,” *ACS Omega*, vol. 6, no. 36, pp. 23614–23620, Sep. 2021, doi: 10.1021/acsomega.1c03865.

[84] E. Rosenkrantz and S. Arnon, “Tunable electro-optic filter based on metal-ferroelectric nanocomposite for VLC,” *Opt. Lett.*, vol. 39, no. 16, p. 4954, Aug. 2014, doi: 10.1364/OL.39.004954.

[85] E. Rosenkrantz and S. Arnon, “1550 nm modulating retroreflector based on coated nanoparticles for free-space optical communication,” *Appl. Opt.*, vol. 54, no. 17, p. 5309, Jun. 2015, doi: 10.1364/AO.54.005309.

[86] E. Rosenkrantz and S. Arnon, “Electro-optic modulator based on a metal-ferroelectric nanocomposite,” San Diego, California, United States, Sep. 2013, p. 88090T. doi: 10.1117/12.2022743.

[87] E. Rosenkrantz and S. Arnon, “Modulating Light by Metal Nanospheres-Embedded PZT Thin-Film,” *IEEE Trans. Nanotechnology*, vol. 13, no. 2, pp. 222–227, Mar. 2014, doi: 10.1109/TNANO.2013.2297833.

[88] J.-H. Park and J. Akedo, “Transparent Metal-Ferroelectric nanocomposite thick films prepared by Aerosol Deposition Method,” in *2007 Sixteenth IEEE International Symposium on the Applications of Ferroelectrics*, Nara-city, Japan, May 2007, pp. 840–842. doi: 10.1109/ISAF.2007.4393421.

[89] N. A. Razilam, N. Juhari, and P. Poopalan, “Metal-Ferroelectric-Metal Characterization for Optical Modulator,” *J. Phys.: Conf. Ser.*, vol. 1962, no. 1, p. 012067, Jul. 2021, doi: 10.1088/1742-6596/1962/1/012067.

[90] A. Korpel, “Acousto-optics—A review of fundamentals,” *Proc. IEEE*, vol. 69, no. 1, pp. 48–53, 1981, doi: 10.1109/PROC.1981.11919.

[91] L. H. Gesell, R. E. Feinleib, J. L. Lafuse, and T. M. Turpin, “Acousto-optic control of time delays for array beam steering,” Los Angeles, CA, Jun. 1994, pp. 194–204. doi: 10.1117/12.177401.

[92] J. Mur, B. Kavčič, and I. Poberaj, “Fast and precise Laguerre–Gaussian beam steering with acousto-optic deflectors,” *Appl. Opt.*, vol. 52, no. 26, p. 6506, Sep. 2013, doi: 10.1364/AO.52.006506.

[93] N. Savage, “Acousto-optic devices,” *Nature Photon*, vol. 4, no. 10, pp. 728–729, Oct. 2010, doi: 10.1038/nphoton.2010.229.

[94] J. A. Coy, “Characterization of a liquid crystal television as a programmable spatial light modulator,” *Opt. Eng*, vol. 35, no. 1, p. 15, Jan. 1996, doi: 10.1117/1.600886.

[95] W. H. De Jeu, “Physical Properties of Liquid Crystalline Materials in Relation to Their Applications,” *Molecular Crystals and Liquid Crystals*, vol. 63, no. 1, pp. 83–109, Jan. 1981, doi: 10.1080/00268948108071988.

[96] Y. Gong *et al.*, “Current control of light by nonreciprocal magnetoplasmonics,” *Appl. Phys. Lett.*, vol. 106, no. 19, p. 191104, May 2015, doi: 10.1063/1.4921208.

[97] J.-S. Park, M. Tang, S. Chen, and H. Liu, “Heteroepitaxial Growth of III-V Semiconductors on Silicon,” *Crystals*, vol. 10, no. 12, p. 1163, Dec. 2020, doi: 10.3390/cryst10121163.

[98] Y. Arakawa and H. Sakaki, “Multidimensional quantum well laser and temperature dependence of its threshold current,” *Appl. Phys. Lett.*, vol. 40, no. 11, pp. 939–941, Jun. 1982, doi: 10.1063/1.92959.

[99] C. Zhao *et al.*, “Novel III-V semiconductor epitaxy for optoelectronic devices through two-dimensional materials,” *Progress in Quantum Electronics*, vol. 76, p. 100313, Mar. 2021, doi: 10.1016/j.pquantelec.2020.100313.

[100] E. Yablonovitch and E. Kane, “Reduction of lasing threshold current density by the lowering of valence band effective mass,” *J. Lightwave Technol.*, vol. 4, no. 5, pp. 504–506, 1986, doi: 10.1109/JLT.1986.1074751.

[101] M. Saldutti, A. Tibaldi, F. Cappelluti, and M. Gioannini, “Impact of carrier transport on the performance of QD lasers on silicon: a drift-diffusion approach,” *Photon. Res.*, vol. 8, no. 8, p. 1388, Aug. 2020, doi: 10.1364/PRJ.394076.

[102] T. Inoue, S. Kido, K. Sasayama, T. Kita, and O. Wada, “Impurity doping in self-assembled InAs/GaAs quantum dots by selection of growth steps,” *Journal of Applied Physics*, vol. 108, no. 6, p. 063524, Sep. 2010, doi: 10.1063/1.3483252.

[103] Y.-Q. Qiu, Z.-R. Lv, H. Wang, H.-M. Wang, X.-G. Yang, and T. Yang, “Improved linewidth enhancement factor of 1.3- *μ* m InAs/GaAs quantum dot lasers by direct Si doping,” *AIP Advances*, vol. 11, no. 5, p. 055002, May 2021, doi: 10.1063/5.0044313.

[104] I. C. Sandall *et al.*, “The effect of p doping in InAs quantum dot lasers,” *Appl. Phys. Lett.*, vol. 88, no. 11, p. 111113, Mar. 2006, doi: 10.1063/1.2186078.

[105] V. V. Korenev *et al.*, “Effect of modulation *p* -doping level on multi-state lasing in InAs/InGaAs quantum dot lasers having different external loss,” *Appl. Phys. Lett.*, vol. 111, no. 13, p. 132103, Sep. 2017, doi: 10.1063/1.5004268.

[106] J. Rihani, V. Sallet, N. Yahyaoui, J. C. Harmand, M. Oueslati, and R. Chtourou, “Interdot carrier’s transfer via tunneling pathway studied from photoluminescence spectroscopy,” *Journal of Luminescence*, vol. 129, no. 3, pp. 251–255, Mar. 2009, doi: 10.1016/j.jlumin.2008.10.004.

[107] O. B. Shchekin, D. G. Deppe, and D. Lu, “Fermi-level effect on the interdiffusion of InAs and InGaAs quantum dots,” *Appl. Phys. Lett.*, vol. 78, no. 20, pp. 3115–3117, May 2001, doi: 10.1063/1.1372362.

[108] J. C. Norman *et al.*, “A Review of High-Performance Quantum Dot Lasers on Silicon,” *IEEE J. Quantum Electron.*, vol. 55, no. 2, pp. 1–11, Apr. 2019, doi: 10.1109/JQE.2019.2901508.

[109] Y. Chu, M. G. Thompson, R. V. Penty, I. H. White, and A. R. Kovsh, “1.3 μm quantum-dot electro-absorption modulator,” in *2007 Conference on Lasers and Electro-Optics (CLEO)*, Baltimore, MD, USA, May 2007, pp. 1–2. doi: 10.1109/CLEO.2007.4452614.

[110] J. Mahoney, M. Tang, H. Liu, and N. Abadía, “Measurement of the quantum-confined Stark effect in InAs/In(Ga)As quantum dots with p-doped quantum dot barriers,” *Opt. Express*, vol. 30, no. 11, p. 17730, May 2022, doi: 10.1364/OE.455491.

[111] C. Y. Ngo *et al.*, “Characteristics of 1.3 µm InAs/InGaAs/GaAs quantum dot electroabsorption modulator,” *Appl. Phys. Lett.*, vol. 94, no. 14, p. 143108, Apr. 2009, doi: 10.1063/1.3119186.

[112] X. Yang *et al.*, “Improved efficiency of InAs/GaAs quantum dots solar cells by Si-doping,” *Solar Energy Materials and Solar Cells*, vol. 113, pp. 144–147, Jun. 2013, doi: 10.1016/j.solmat.2013.02.005.

[113] H. Wang *et al.*, “Enhanced performance of InAs/GaAs quantum dot superluminescent diodes by direct Si-doping,” *AIP Advances*, vol. 10, no. 4, p. 045202, Apr. 2020, doi: 10.1063/1.5141160.

[114] M. V. Maximov *et al.*, “A 1.33 µm InAs/GaAs quantum dot laser with a 46 cm $^{-1}$ modal gain,” *Semicond. Sci. Technol.*, vol. 23, no. 10, p. 105004, Oct. 2008, doi: 10.1088/0268-1242/23/10/105004.

[115] T. Amano, S. Aoki, T. Sugaya, K. Komori, and Y. Okada, “Laser Characteristics of 1.3-μm Quantum Dots Laser With High-Density Quantum Dots,” *IEEE J. Select. Topics Quantum Electron.*, vol. 13, no. 5, pp. 1273–1278, 2007, doi: 10.1109/JSTQE.2007.903845.

[116] A. Salhi, L. Fortunato, L. Martiradonna, R. Cingolani, M. De Vittorio, and A. Passaseo, “Enhanced modal gain of multilayer InAs⁄InGaAs⁄GaAs quantum dot lasers emitting at 1300nm,” *Journal of Applied Physics*, vol. 100, no. 12, p. 123111, Dec. 2006, doi: 10.1063/1.2402744.

[117] R. Nagarajan and J. E. Bowers, “High-Speed Lasers,” in *Semiconductor Lasers I*, Academic Press, 1999, pp. 177–290.

[118] P. L. Derry, L. Figueroa, and C.-S. Hong, “SEMICONDUCTOR LASERS,” p. 55.

[119] Xiaodong Huang, A. Stintz, C. P. Hains, G. T. Liu, J. Cheng, and K. J. Malloy, “Very low threshold current density room temperature continuous-wave lasing from a single-layer InAs quantum-dot laser,” *IEEE Photon. Technol. Lett.*, vol. 12, no. 3, pp. 227–229, Mar. 2000, doi: 10.1109/68.826896.

[120] D. G. Deppe, K. Shavritranuruk, G. Ozgur, H. Chen, and S. Freisem, “Quantum dot laser diode with low threshold and low internal loss,” *Electron. Lett.*, vol. 45, no. 1, p. 54, 2009, doi: 10.1049/el:20092873.

[121] C. Lin, J. Wu, Y. Kuo, Y. Chiu, T. E. Tzeng, and T. S. Lay, “InGaAs self-assembly quantum dot for high-speed 1300nm electroabsorption modulator,” *Journal of Crystal Growth*, vol. 323, no. 1, pp. 473–476, May 2011, doi: 10.1016/j.jcrysgro.2011.01.024.

[122] D. B. Malins, A. Gomez-Iglesias, E. U. Rafailov, W. Sibbett, and A. Miller, “Electroabsorption and Electrorefraction in an InAs Quantum-Dot Waveguide

Modulator,” *IEEE Photon. Technol. Lett.*, vol. 19, no. 15, pp. 1118–1120, Aug. 2007, doi: 10.1109/LPT.2007.901093.

[123] C. Y. Ngo *et al.*, “Electroabsorption Characteristics of Single-Mode 1.3-μm InAs–InGaAs–GaAs Ten-Layer Quantum-Dot Waveguide,” *IEEE Photon. Technol. Lett.*, vol. 22, no. 23, pp. 1717–1719, Dec. 2010, doi: 10.1109/LPT.2010.2083642.

[124] E. D. Le Boulbar *et al.*, “Temperature Dependent Behavior of the Optical Gain and Electroabsorption Modulation Properties of an InAs/GaAs Quantum Dot Epistructure,” in *2019 21st International Conference on Transparent Optical Networks (ICTON)*, Angers, France, Jul. 2019, pp. 1–4. doi: 10.1109/ICTON.2019.8840542.

[125] D. Atkinson, G. Parry, and E. J. Austin, “Modelling of electroabsorption in coupled quantum wells with applications to low voltage optical modulation,” *Semicond. Sci. Technol.*, vol. 5, no. 6, pp. 516–524, Jun. 1990, doi: 10.1088/0268-1242/5/6/009.

[126] N. Dai, F. Brown, R. E. Doezema, S. J. Chung, and M. B. Santos, “Temperature dependence of exciton linewidths in InSb quantum wells,” *Phys. Rev. B*, vol. 63, no. 11, p. 115321, Mar. 2001, doi: 10.1103/PhysRevB.63.115321.

[127] C. Quintana *et al.*, “High Speed Electro-Absorption Modulator for Long Range Retroreflective Free Space Optics,” *IEEE Photon. Technol. Lett.*, vol. 29, no. 9, pp. 707–710, May 2017, doi: 10.1109/LPT.2017.2680842.

[128] A. K. Viswanath, J. I. Lee, D. Kim, C. R. Lee, and J. Y. Leem, “Exciton-phonon interactions, exciton binding energy, and their importance in the realization of room-temperature semiconductor lasers based on GaN,” *Phys. Rev. B*, vol. 58, no. 24, pp. 16333–16339, Dec. 1998, doi: 10.1103/PhysRevB.58.16333.

[129] Y. J. Chen, E. S. Koteles, J. Lee, J. Y. Chi, and B. S. Elman, “Temperature dependent optical studies of GaAs/AlGaAs single quantum wells,” p. 7.

[130] S. L. Chuang, “Physics of Photonic Devices,” p. 841, 2009.

[131] J. D. Thomson, P. M. Smowton, P. Blood, and J. F. Klem, “Optical Gain and Spontaneous Emission in GaAsSb–InGaAs Type-II ‘W’ Laser Structures,” *IEEE J. Quantum Electron.*, vol. 43, no. 7, pp. 607–613, Jul. 2007, doi: 10.1109/JQE.2007.899499.

[132] B. Tossoun *et al.*, “High-Speed InP-Based p-i-n Photodiodes With InGaAs/GaAsSb Type-II Quantum Wells,” *IEEE Photon. Technol. Lett.*, vol. 30, no. 4, pp. 399–402, Feb. 2018, doi: 10.1109/LPT.2018.2793663.

[133] J. Vijay, R. krishan Yadav, P. A. Alvi, K. Singh, and A. Rathi, “Design and modeling of InGaAs/GaAsSb nanoscale heterostructure for application of optical fiber communication system,” *Materials Today: Proceedings*, vol. 30, pp. 128–131, 2020, doi: 10.1016/j.matpr.2020.05.097.

[134] B. Chen, “Optical gain analysis of GaAs-based InGaAs/GaAsSbBi type-II quantum wells lasers,” *Opt. Express*, vol. 25, no. 21, p. 25183, Oct. 2017, doi: 10.1364/OE.25.025183.

[135] N. Tansu and L. J. Mawst, “Design analysis of 1550-nm gaassb-(in)gaasn type-II quantum-well laser active regions,” *IEEE J. Quantum Electron.*, vol. 39, no. 10, pp. 1205–1210, Oct. 2003, doi: 10.1109/JQE.2003.817235.

[136] P. Dowd *et al.*, “Long wavelength (1.3 and 1.5 μm) photoluminescence from InGaAs/GaPAsSb quantum wells grown on GaAs,” *Appl. Phys. Lett.*, vol. 75, no. 9, pp. 1267–1269, Aug. 1999, doi: 10.1063/1.124663.

[137] E. A. Plis, “InAs/GaSb Type-II Superlattice Detectors,” *Advances in Electronics*, vol. 2014, pp. 1–12, Apr. 2014, doi: 10.1155/2014/246769.

[138] H. Kobayashi, Y. Kawamura, and H. Iwamura, “Electroabsorption in an AlInAs/InP Type II Superlattice,” *Jpn. J. Appl. Phys.*, vol. 32, no. Part 1, No. 1B, pp. 548–551, Jan. 1993, doi: 10.1143/JJAP.32.548.

[139] F. Xie *et al.*, “3.5 μm strain balanced GaInAs/AlInAs quantum cascade lasers operating at room temperature,” San Francisco, California, Feb. 2011, p. 79531A. doi: 10.1117/12.882762.

[140] M. A. Steiner *et al.*, “High Efficiency Inverted GaAs and GaInP/GaAs Solar Cells With Strain-Balanced GaInAs/GaAsP Quantum Wells,” *Advanced Energy Materials*, vol. 11, no. 4, p. 2002874, 2021, doi: https://doi.org/10.1002/aenm.202002874.

[141] U. Seidel, H.-J. Schimper, Z. Kollonitsch, K. Möller, K. Schwarzburg, and T. Hannappel, “Growth of an InGaAs/GaAsSb tunnel junction for an InP-based low band gap tandem solar cell,” *Journal of Crystal Growth*, vol. 298, pp. 777–781, Jan. 2007, doi: 10.1016/j.jcrysgro.2006.10.132.

[142] B. N. Zvonkov, S. M. Nekorkin, O. V. Vikhrova, and N. V. Dikareva, “Emission properties of heterostructures with a (GaAsSb-InGaAs)/GaAs bilayer quantum well,” *Semiconductors*, vol. 47, no. 9, pp. 1219–1223, Sep. 2013, doi: 10.1134/S1063782613090261.

[143] P. Blood, G. M. Lewis, P. M. Smowton, H. Summers, J. Thomson, and J. Lutti, “Characterization of semiconductor laser gain media by the segmented contact method,” *IEEE JOURNAL OF SELECTED TOPICS IN QUANTUM ELECTRONICS*, vol. 9, no. 5, p. 8, 2003.

[144] C. G. Van de Walle, “Theoretical calculations of semiconductor heterojunction discontinuities,” *J. Vac. Sci. Technol. B*, vol. 4, no. 4, p. 1055, Jul. 1986, doi: 10.1116/1.583580.

[145] C. G. Van De Walle, “Band Offsets at Strained-Layer Interfaces,” *MRS Proc.*, vol. 102, p. 565, 1987, doi: 10.1557/PROC-102-565.

[146] A. Trellakis *et al.*, “The 3D nanometer device project nextnano: Concepts, methods, results,” *J Comput Electron*, vol. 5, no. 4, pp. 285–289, May 2007, doi: 10.1007/s10825-006-0005-x.

[147] M. Gioannini, “Ground-state power quenching in two-state lasing quantum dot lasers,” *Journal of Applied Physics*, vol. 111, no. 4, p. 043108, Feb. 2012, doi: 10.1063/1.3682574.

[148] Y. Nabetani, T. Matsumoto, G. Sasikala, and I. Suemune, “Theory of strain states in InAs quantum dots and dependence on their capping layers,” *Journal of Applied Physics*, vol. 98, no. 6, p. 063502, Sep. 2005, doi: 10.1063/1.2041846.

[149] E. O. Chukwuocha, M. C. Onyeaju, and T. S. T. Harry, “Theoretical Studies on the Effect of Confinement on Quantum Dots Using the Brus Equation,” *WJCMP*, vol. 02, no. 02, pp. 96–100, 2012, doi: 10.4236/wjcmp.2012.22017.

[150] I. O’Driscoll, P. Blood, and P. M. Smowton, “Random Population of Quantum Dots in InAs–GaAs Laser Structures,” *IEEE J. Quantum Electron.*, vol. 46, no. 4, pp. 525–532, Apr. 2010, doi: 10.1109/JQE.2009.2039198.

[151] M. V. Maximov *et al.*, “Optical Properties of Quantum Dots Formed by Activated Spinodal Decomposition for GaAs-Based Lasers Emitting at ∼ 1.3 μm,” in *Proceedings of the Third International Conference on on Low Dimensional Structures & Devices*, NLD, 2000, pp. 61–72.

[152] R. R. Alexander *et al.*, “Systematic Study of the Effects of Modulation p-Doping on 1.3-$\mu{\hbox {m}}$ Quantum-Dot Lasers,” *IEEE J. Quantum Electron.*, vol. 43, no. 12, pp. 1129–1139, Dec. 2007, doi: 10.1109/JQE.2007.907213.

[153] K. W. Sun, A. Kechiantz, B. C. Lee, and C. P. Lee, “Ultrafast carrier capture and relaxation in modulation-doped InAs quantum dots,” *Appl. Phys. Lett.*, vol. 88, no. 16, p. 163117, Apr. 2006, doi: 10.1063/1.2197309.

[154] H. Deng *et al.*, “The role of different types of dopants in 1.3 μm InAs/GaAs quantum-dot lasers,” *J. Phys. D: Appl. Phys.*, vol. 55, no. 21, p. 215105, May 2022, doi: 10.1088/1361-6463/ac55c4.

[155] L. Jarvis *et al.*, “Co-doping 1.3um InAs Quantum Dot Lasers with P-type modulation doping and direct N-type doping,” *Semiconductor & Integrated Opto-electronics Conference SIOE 2022*.

[156] L. C. Hostler, “Reduced Coulomb Green’s Function for Bound-State Calculations,” *Phys. Rev.*, vol. 178, no. 1, pp. 126–131, Feb. 1969, doi: 10.1103/PhysRev.178.126.

[157] A. Stahl, “Polariton structure of interband transitions in semiconductors,” *Phys. Stat. Sol. (b)*, vol. 94, no. 1, pp. 221–230, Jul. 1979, doi: 10.1002/pssb.2220940125.

[158] R. Zimmermann, “Excitonic spectra in 1, 2, 3 dimensions a numerical approach,” *phys. stat. sol. (b)*, vol. 135, no. 2, pp. 681–690, Jun. 1986, doi: 10.1002/pssb.2221350227.

[159] R. Zimmermann and M. Hartmann, “Theory of the dynamical stark effect of excitons in CdS,” *Journal of Crystal Growth*, vol. 101, no. 1–4, pp. 341–345, Apr. 1990, doi: 10.1016/0022-0248(90)90992-T.

[160] S. Schmitt-Rink, D. S. Chemla, and H. Haug, “Nonequilibrium theory of the optical Stark effect and spectral hole burning in semiconductors,” *Phys. Rev. B*, vol. 37, no. 2, pp. 941–955, Jan. 1988, doi: 10.1103/PhysRevB.37.941.

[161] S. Schmitt-Rink and D. S. Chemla, “Collective Excitations and the Dynamical Stark Effect in a Coherently Driven Exciton System,” *Phys. Rev. Lett.*, vol. 57, no. 21, pp. 2752–2755, Nov. 1986, doi: 10.1103/PhysRevLett.57.2752.

[162] Y. R. Shen, “The Principles of Nonlinear Optics, Chap. 2.,” New York: Wiley, 1984.

[163] G. Sanders and Y.-C. Chang, “Theory of photoabsorption in modulation-doped semiconductor quantum wells,” *Phys. Rev. B*, vol. 35, no. 3, pp. 1300–1315, Jan. 1987, doi: 10.1103/PhysRevB.35.1300.